Valery Ya. Rudyak · Vladimir M. Aniskin Anatoly A. Maslov · Andrey V. Minakov Sergey G. Mironov

Micro-and Nanoflows

Modeling and Experiments



Fluid Mechanics and Its Applications

Volume 118

Series editor

André Thess, German Aerospace Center, Institute of Engineering Thermodynamics, Stuttgart, Germany

Founding Editor

René Moreau, Ecole Nationale Supérieure d'Hydraulique de Grenoble, Saint Martin d'Hères Cedex, France

The purpose of this series is to focus on subjects in which fluid mechanics plays a fundamental role. As well as the more traditional applications of aeronautics, hydraulics, heat and mass transfer etc., books will be published dealing with topics which are currently in a state of rapid development, such as turbulence, suspensions and multiphase fluids, super and hypersonic flows and numerical modelling techniques. It is a widely held view that it is the interdisciplinary subjects that will receive intense scientific attention, bringing them to the forefront of technological advancement. Fluids have the ability to transport matter and its properties as well as transmit force, therefore fluid mechanics is a subject that is particulary open to cross fertilisation with other sciences and disciplines of engineering. The subject of fluid mechanics will be highly relevant in such domains as chemical, metallurgical, biological and ecological engineering. This series is particularly open to such new multidisciplinary domains. The median level of presentation is the first year graduate student. Some texts are monographs defining the current state of a field; others are accessible to final year undergraduates; but essentially the emphasis is on readability and clarity.

Springer and Professor Thess welcome book ideas from authors. Potential authors who wish to submit a book proposal should contact Nathalie Jacobs, Publishing Editor, Springer (Dordrecht), e-mail:

Nathalie.Jacobs@springer.com

Indexed by SCOPUS, EBSCO Discovery Service, OCLC, ProQuest Summon, Google Scholar and SpringerLink

More information about this series at http://www.springer.com/series/5980

Valery Ya. Rudyak · Vladimir M. Aniskin Anatoly A. Maslov · Andrey V. Minakov Sergey G. Mironov

Micro- and Nanoflows

Modeling and Experiments



Valery Ya. Rudyak Novosibirsk State University of Architecture and Civil Engineering Novosibirsk Russian Federation

Vladimir M. Aniskin Khristianovich Institute of Theoretical and Applied Mechanics Siberian Branch of Russian Academy of Sciences Novosibirsk Russian Federation

Anatoly A. Maslov Khristianovich Institute of Theoretical and Applied Mechanics Siberian Branch of Russian Academy of Sciences Novosibirsk Russian Federation Andrey V. Minakov Siberian Federal University Krasnoyarsk Russian Federation

Sergey G. Mironov Khristianovich Institute of Theoretical and Applied Mechanics Siberian Branch of Russian Academy of Sciences Novosibirsk Russian Federation

ISSN 0926-5112 ISSN 2215-0056 (electronic) Fluid Mechanics and Its Applications ISBN 978-3-319-75522-9 ISBN 978-3-319-75523-6 (eBook) https://doi.org/10.1007/978-3-319-75523-6

Library of Congress Control Number: 2018932990

© Springer International Publishing AG, part of Springer Nature 2018

This work is subject to copyright. All rights are reserved by the Publisher, whether the whole or part of the material is concerned, specifically the rights of translation, reprinting, reuse of illustrations, recitation, broadcasting, reproduction on microfilms or in any other physical way, and transmission or information storage and retrieval, electronic adaptation, computer software, or by similar or dissimilar methodology now known or hereafter developed.

The use of general descriptive names, registered names, trademarks, service marks, etc. in this publication does not imply, even in the absence of a specific statement, that such names are exempt from the relevant protective laws and regulations and therefore free for general use.

The publisher, the authors and the editors are safe to assume that the advice and information in this book are believed to be true and accurate at the date of publication. Neither the publisher nor the authors or the editors give a warranty, express or implied, with respect to the material contained herein or for any errors or omissions that may have been made. The publisher remains neutral with regard to jurisdictional claims in published maps and institutional affiliations.

Printed on acid-free paper

This Springer imprint is published by the registered company Springer International Publishing AG part of Springer Nature

The registered company address is: Gewerbestrasse 11, 6330 Cham, Switzerland

Preface

Overview

Each century has its own scientific and engineering paradigm. The nineteenth century was the age of steam engines, and the twentieth century was the age of nuclear energy. Both centuries were characterized by extremely fast growth in regard to consumption of energy and resources. At the end of the twentieth century, energy and resource issues became the priorities in the development of all leading fields of industry and economy all over the world. American Cadillac battleships passed into oblivion, and the main interest today is in cost-efficient Japanese cars. Now, in the second decade of the twenty-first century, the priority task can be defined as efficient utilization of resources and energy, which requires significant effort from all branches of economy, industry, and science. One of the main avenues toward reaching this goal is the development of mini- and microtechnologies and devices with improved performance. Nanotechnologies are also within this category.

A typical trend in the worldwide engineering market over the last three decades has been the development of microsystem engineering (MSE) and corresponding technologies. MSE devices ensure the generation, conversion, and transfer of energy and motion, as well as the analysis, processing, compilation, and storage of information. A mere list of already used and developed MSE devices would require a special review. To mention but a small number of examples: heads for hard disk storage drives, heads for jet printers, cardio-pacemakers, in vitro diagnostic tools, deaf-aid devices, pressure transducers, chemical sensors, magnetoresistive sensors, microspectrometers, drug delivery systems, on-chip laboratories, high-resolution DNA liquid chromatography, injectors, micronozzles (thrusters) for space vehicles, and various microelectromechanical system (MEMS), which are followed by nanoelectromechanical systems (NEMS). This list is far from complete. It should be emphasized that rapid diversification of this field has been observed since the 1990s. Many new applications have been developed for medicine, pharmacology, biology, thermal engineering, catalysis, etc. The advantages of MSE devices and

vi Preface

technologies are their high operational characteristics (mass, size, weight, energy, etc.). The MSE market has been intensely developed all over the world, though it is still not yet completely formed. The cost of this market increases by approximately 20 percent every year and now reaches more than 100 billion dollars.

In practice, many MSE devices and technologies involve fluid flows in microchannels. Nanoflows have already become a focus of interest in this century. This is not only due to the development of nanotechnologies for various purposes, but also due to research in fairly traditional fields, such as biology, geophysics, thermal engineering. Up to now, transportation of nutrients in plants and living organisms is still one of the most mysterious of processes. Investigations into various microporous coatings and the flows in such coatings are intensely performed. The pore size in typical oil- and gas-bearing formations varies from tens of nanometers to tens of micrometers, which means that both nanoflows and microflows occur in these media.

Nevertheless, this topic also has an important basic research component. There are two reasons for that. First, some phenomena that are not typical for macroflows are observed in microflows. Therefore, a correct interpretation and description of these phenomena are needed. On the other hand, almost all methods for studying fluid flows were developed for macroscopic systems. Are these methods applicable to the description of micro- and nanoflows? This is not an idle inquiry, because micro- and nanofluidics have become extremely important fields of mechanics. Moreover, such flows cannot be treated within the framework of mechanics alone. At small scales, it is necessary to revise the concepts of transportation and relaxation processes, because there is no reason to believe that the viscosity and the thermal conductivity of a fluid in bulk and in a sufficiently small channel are identical. Thus, it is necessary to study thermophysical properties of fluids in microand nanochannels to provide a correct interpretation and description of the experimental data.

The use of nanofluids as working fluids in some facilities and devices seems to be fairly promising: it allows for heat removal at room temperature of the coolant, in contrast to traditional low-temperature coolers. The thermal conductivity of currently available nanofluids of different compositions with a sufficiently small volume fraction of nanoparticles might exceed the thermal conductivity of a carrier fluid by tens of percent. At the same time, the character of nanofluid flows is still almost unexplored for several reasons, many involving lack of reliable data (on transport coefficients, on formulation of boundary conditions, etc.). The situation is aggravated by the fact that none of the thermophysical properties of nanofluids, in particular, their viscosity and thermal conductivity, are described by the classical theories. Moreover, these properties are not universal, in contrast to fluids with coarse particles. Therefore, simulations of nanofluid flows should be performed carefully, based on consideration of particular fluids. In the general case, it is difficult here to use even the similarity criteria typically applied in fluid dynamics.

The problems of experimental investigations of microflows are fairly obvious. First, the small sizes of examined systems require appropriate measurement tools. In principle, such tools have been actively developed over the last three decades,

Preface vii

and it can be stated that many of these tools are fairly adequate. However, to characterize the flow, it is usually necessary to measure the flow rate, pressure difference, pressure in the channel, velocity profile, velocity at the wall, stress at the wall, hydraulic resistance coefficient, temperatures of the channel walls and fluid, temperature profile, transport coefficients in the channel, surface distribution of the charge, etc. Moreover, the level of roughness of the channel walls and the exact size of the channel should be carefully monitored, because they can change over the course of the experiment, owing to the compliance and elasticity of the channel walls. Nevertheless, most researchers manage to measure the integral characteristics of the flow: flow rate, pressure drop, temperature, etc. Local and, moreover, fluctuating characteristics are actually unmeasurable. On the other hand, it should be borne in mind that perturbations excited in microflows, and especially nanoflows, by the measurement instrument in the course of measurements may be of the same order or even greater than the measured variable. The situation is similar to that in quantum mechanics, a field of knowledge for which a theory of measurements was specially developed. Something like that is needed for interpreting experimental data in microflows, and especially nanoflows. This is important because the interpretation techniques of almost all currently available methods are based on theoretical relations derived for macroscopic flows.

As was already mentioned, micro- and nanofluidics have become rapidly developing fields of economy. Naturally, this is supported and stimulated by intense development of research all over the world. All industrial companies actively collaborate with various research centers. It should be mentioned that almost every high-ranking university has a laboratory dealing with this topic.

There are dozens of monographs that describe microflows. The difficult task is choosing the material, because the area of micro- and nanofluidics is unbounded. In May 2012, the fourth session of the Russian conference entitled "Fundamentals of MEMS and nanotechnologies" was held, arousing significant interest from the academic community. Based on presentations at this conference, the monograph entitled "Modeling of micro- and nanoflows" was published in Russia in 2014. The revised and supplemented version of that monograph is the basis of the present book. Priority is given to the modeling of micro- and nanoflows. The book describes two cycles of experimental activities aimed at studying microjets and microflows and to develop unique tools for these purposes. Both subsonic and supersonic jets are considered. The remaining chapters in the book describe various methods of numerical simulation of micro- and nanoflows. Much attention is paid to the systematic description of the area of applicability of particular methods, hydrodynamic modeling of micromixers, and molecular dynamics modeling of nanoflows. Algorithms of molecular dynamics modeling of flows without involving an external force of thermostats for controlling molecular velocities are comprehensively described for the first time. The last chapter provides a systematic description of the statistical theory of fluid transport processes under confined conditions. It is demonstrated that both the viscosity and thermal conductivity of such a fluid are no longer the properties of the fluid itself alone. These properties are determined to a large extent by interaction of fluid molecules with atoms viii Preface

(or molecules) of the channel walls where the flow occurs. Moreover, by varying the wall material, it is possible to control the hydraulic resistance in such a channel by means of increasing or, vice versa, decreasing the viscosity.

Organization of the Book

Chapter 1 is devoted to problems of methods of numerical simulation of micro- and nanoflows. The chapter begins with a brief classification of these flows, and it is arranged in a manner that allows for consecutive consideration of all situations. The methods of simulating flows of the rarefied and dense gases, liquids, and disperse liquids, including nanofluids are repeatedly considered.

The goal of Chap. 2 is to study the structure and stability of microjets. The overview of the works on the study of the gas dynamics of subsonic and supersonic mini- and microjets is given in Sect. 2.1. As the tools used in experimental investigations are also very important, they are described in great detail. Diagnostic methods and the results of studying subsonic plane jet stability are described in Sect. 2.2. Experiments aimed at studying the structure and stability of supersonic axisymmetric microjets and the results obtained therein are discussed in Sect. 2.3. Much attention is paid to the techniques used to obtain experimental data. Finally, the problem of microjet modeling with the use of commonly used similarity parameters is discussed in Sect. 2.4.

Chapter 3 describes the results of measurements of hydraulic resistance coefficients in microchannels of various shapes and various diameters for laminar and turbulent flows, as well as these same coefficients for input regions.

Chapter 4 describes the results of CFD simulations of micromixers of Y- and T-types. The method used to solve the Navier–Stokes equations is described in the first section, followed by consideration of flows with low and then moderate Reynolds numbers. The regimes of the flows and mixing are analyzed.

In Chap. 5, we propose new molecular dynamics algorithms, which allow one to simulate a real plane Poiseuille-type flow characterized by a certain pressure gradient, and discuss specific features of plane flows in nanochannels. This is the subject of the first four sections of the chapter. In Sects. 5.5 and 5.6, the self-diffusion of the fluid molecules in nanochannels and porous media is studied. Finally, the last section deals with the modeling of the separation of nanofluids through the use of nanomembranes.

In Chap. 6, we propose the statistical theory of transport processes under confined conditions. The new constitutive relation and formulas for transport coefficients are obtained. Using the molecular dynamics method, the viscosity of the fluids in nanochannels with walls of different materials is simulated.

In conclusions, the main inferences are formulated.

The preface, Chaps. 1, 5, and 6, and the conclusion were written by V. Ya. Rudyak. The authors of Chap. 2 are V. M. Aniskin, A. A. Maslov, and S. G. Mironov. Chapter 3 was written by V. M. Aniskin and A. A. Maslov. Finally, the authors of Chap. 4 are

Preface

A. V. Minakov and V. Ya. Rudyak. The overall editing of the book was also performed by V. Ya. Rudyak.

Acknowledgements

The authors are grateful to Prof. Fomin V. M., who initiated the writing of this book. This work was supported by the Russian Foundation for Basic Research (Grants #17-01-00040, #17-58-45023), Russian Science Foundation (Grant #17-19-01157), and Project of the President of Russian Federation (Project # RF HS-8788.2016.1).

The results presented in the monograph were obtained using the experimental and computing equipment of the Novosibirsk State University of Architecture and Civil Engineering, the Siberian Federal University, and the Khristianovich Institute of Theoretical and Applied Mechanics Siberian Branch of Russian Academy of Sciences.

Novosibirsk, Russian Federation September 2017



Valery Ya. Rudyak



Vladimir M. Aniskin

x Preface



Anatoly A. Maslov



Andrey V. Minakov



Sergey G. Mironov

Contents

1	Met	hods of	Modeling of Microflows and Nanoflows	1
	1.1	Consid	dered Systems and Their Classification	1
	1.2	Model	ing of Rarefied Gas Microflows	5
	1.3	Model	ing of Moderately Dense Gases	13
	1.4	Model	ling of Dense Gas and Liquid Flows	15
	1.5			17
	1.6	.6 Modeling of Nanofluid Microflows		28
		1.6.1	Methods of Modeling of Nanofluid Flows	28
		1.6.2	Diffusion of Nanoparticles in Gases and Liquids	31
		1.6.3	Viscosity of Gas Suspensions of Nanoparticles	36
		1.6.4	Viscosity of Nanosuspensions	39
		1.6.5	Thermal Conductivity of Nanofluids	42
		Molec	ular Dynamics Method	44
		1.7.1	Continuous Potentials	46
		1.7.2	Smooth Hard Spheres	48
		1.7.3	Boundary and Initial Conditions	48
		1.7.4	Reaching Equilibrium in Molecular Systems	50
		1.7.5	Statistical Ensemble	51
	Refe	erences		53
2	Gas	-Dynan	nic Structure and Stability of Gas Microjets	57
	2.1	Invest	igation and Application of Microjets	57
	2.2	• • • • • • • • • • • • • • • • • • • •		60
	2.3 Structure and Characteristics of Stability of Supersonic		ure and Characteristics of Stability of Supersonic	
		Axisymmetric Microjets		70
		2.3.1	Experimental Equipment	70
		2.3.2	Experimental Arrangement and Measurement	
			Conditions	74

xii Contents

	2.4 Refe	2.3.3 Measurement Results	76 87 94		
3	Fluid Flows in Microchannels				
3			97 97		
	3.1 3.2	Methods of Determining the Friction Factor in Tubes	101		
		Fabrication Technology and Characteristics of Microchannels	101		
	3.3 3.4	Experimental Arrangement			
	3.4	Errors in Microchannel Measurement	111 113		
		Fluid Flow in Straight Tubes			
	3.6	Fluid Flows in Curved Tubes	120		
	кете	erences	124		
4	Mod	leling of Micromixers	127		
	4.1	Algorithm for Solving the Navier-Stokes Equations	127		
	4.2	Testing of the Algorithm	134		
	4.3	Mixing of Fluids in a Y-Type Mixer at Low			
		Reynolds Numbers	139		
	4.4	Mixing of Fluids in a T-Type Micromixer at Moderate			
		Reynolds Numbers	145		
	4.5	Experimental Study of Flow Regimes in a T-Type			
		Micromixer	159		
	4.6	Modeling of Two-Phase Flows in a T-Type Micromixer	166		
	4.7	Heat Transfer in a T-Type Micromixer	173		
	4.8	Active Method of Mixing	179		
	Refe	erences	182		
_	3.7	LP CN G	105		
5		leling of Nanoflows	185		
	5.1	Molecular Dynamics Simulation of a Channel Flow Generated	105		
	<i>-</i> -	by an External Force	185		
	5.2	Algorithm of Modeling a Plane Nanoflow Under Pseudo-periodic	1.00		
	5 0	Conditions	188		
	5.3	Algorithm of Modeling a Plane Nanoflow with a Prescribed	100		
		Flow Rate	189		
	5.4	Specific Features of Nanoflows in MD Simulations	191		
		5.4.1 Flow Velocity Profile	192		
		5.4.2 Decrease in Pressure	193		
		5.4.3 Resistance Coefficient	195		
		5.4.4 Compressibility of the Fluid in Nanochannels	196		
		5.4.5 Fluid Structure in a Plane Channel	197		
	5.5	Diffusion of Molecules in Nanochannels	200		
	5.6	Self-diffusion of Molecules in Porous Media	204		

Contents xiii

	5.7	Modeling of Nanofluid Separation with the Use	
		of Nanomembranes	209
	Refe	erences	213
6	Fluid Transport Under Confined Conditions		
	6.1	Physics of the Transport Processes in Fluid	217
	6.2	Statistical Theory of Transport Processes	220
		6.2.1 Dynamic Description of the Fluid-Surface System	220
		6.2.2 Nonequilibrium Distribution Function	222
		6.2.3 Constitutive Relations and Transport Coefficients	225
	6.3	On Fluid Viscosity in the Nanochannel	232
	Refe	erences	236
7	Con	clusions	237
	Refe	prences	240
In	dex		241

Nomenclature

D Diffusion coefficientD Strain rate tensor

 F_N N-particle distribution function

 f_{10W} Local Maxwell distribution function with wall temperature f_{1W} Distribution function of molecules reflected from wall

 f_1 Single-particle distribution function

 J_2 Stress tensor J_3 Heat flux vectorKnKnudsen number κ_m Normalization factor

 l_p Mean free path of particles

n Normal to surface

p* Momentum of molecule incident onto surface

qHeat flux vectorRGas constant

 \mathbf{r}_i Radius-vector of particle iTTemperature of gas T_W Temperature on wall \mathbf{u} Velocity of gas \mathbf{u}_W Velocity on the wall

 \mathbf{u}_{τ} Tangential (to the surface) component of gas velocity

V, R Velocity and coordinate of center of mass of disperse particle

 $\mathbf{v}_1, \, \mathbf{v}_2$ Velocities of molecules 1 and 2

 $w(\mathbf{p}^*, \mathbf{p})$ Scattering kernel

 x_1, x_2 Molar fractions of components 1 and 2 α_p Accommodation coefficients for momentum α_E Accommodation coefficients for energy

χ Correlation function

 Φ_1 Potential energy of external fields applied onto system

 ϕ Volume concentration of disperse particles

xvi Nomenclature

 η Viscosity coefficient

 $\varphi(\mathbf{p})$ Certain function of molecular momentum

 λ Thermal conductivity coefficient μ Shear viscosity coefficient ν Volume viscosity coefficient

 ρ Mass density

 $\sigma(v_{ii})$ Scattering cross section of colliding molecules i and j

D Real micronozzle diameter D_{eff} Model micronozzle diameter

f Frequencyh Nozzle widthJPR Jet pressure ratio

k x/D

LLength, amplitude of acoustic wave L_s Length of wave structure cellLcLength of supersonic coreNPRNozzle pressure ratio p_0 Stagnation pressure p_a Atmospheric pressure

 p_0' Pitot pressure

 u_0 Velocity of gas exhaustion

 Δ Maximum deviation of nozzle exit δ Maximum roughness level of nozzle C^* Hydraulic resistance coefficients D Hydraulic diameter of channel

Dn Dean number

f Coefficient of proportionality between the pressure drop in

microchannel Channel length

L Channel leng
P Pressure

 ΔP Pressure drop

Q Volume flow rate of fluid

V Mean mass velocity of fluid in channel

bSlip lengthCaCapillary number c_p Specific heatDnDean numberEtEotyos number

Et Eotvos number F(x, y, z, t) Special marker function h Computational grid step

k Kinetic energy of turbulent fluctuations

L Reference input number

L Channel length
M Mixing efficiency

Nomenclature xvii

 \mathbf{n} Vector of external normal to computational domain \mathbf{n}_w Normal vectors to wall

Pe Peclet number

p Pressure Q Flow rate

 \mathbf{q}_{w} Specific heat flux through body surface S Cross-sectional area of microchannel

 S_{ik} Strain rate tensor T_0 Room temperature

U Value of flow velocity in section

 U_m Maximum value of flow velocity in section

u Velocity vector

 u_K , v_K , w_K Velocity vector components at Kth face of control volume

 β Thermal expansion coefficient ε Turbulence dissipation rate

Φ Arbitrary variable λ Thermal conductivity

 μ_1 Viscosity coefficient of liquid
Viscosity coefficient of gas $v = \mu/\rho$ Kinematic coefficient of viscosity

ρ Fluid density

 ρ_0 Fluid density at room temperature

τ Computational time step

τ Viscous stress tensor components

 τ_w Tangential vectors to wall

 Ω_{ik} Vorticity tensor

 $\Psi(r)$ Limiter

D Self-diffusion coefficient E_K kinetic energy of molecules

 \mathbf{F}_{e} Mass force

 $g_2(r, h)$ Radial distribution function in bulk

H Membrane thicknessh Channel heightKn Knudsen numbers

 Δp_{ij} Change in the absolute value of momentum of *i*th molecule

during time Δt owing to its σ_{11}

Q Fluid flow rate Q_d Diffusive flux Q_c Convective flux

 r_{ij}^* Distance between molecules

 $\langle \mathbf{r}_{ij} \cdot \mathbf{F}_{ij} \rangle$ Virial of force collision with *j*th molecule *n* Number of molecules in unit volume

 \bar{u} Flow velocity

V Total volume of the medium

xviii Nomenclature

V_p	Pore volume
w	Channel width
χ	Autocorrelation function of velocity
ε_{11}	Parameters of interaction of fluid molecules
$arepsilon_V$	Van der Waals parameter
ϕ	Membrane porosity
φ	Matrix porosity
λ	Hydraulic resistance coefficient
θ	Accommodation coefficient
ho	Density of molecules
$\sigma_{22}, \varepsilon_{22}$	Parameters of interaction of wall molecules
E_{α}	Energy of particles of phase α
$E_{\alpha}(\mathbf{r}, t)$	Macroscopic values of energy obtained by averaging over ensemble F_N
N	Particle distribution function F_N
F_{N0}	Quasi-equilibrium distribution function
F_{N1}	Dissipative function
\mathbf{F}_{ij}	Force of intermolecular interaction
$g_{k\alpha}$	Lagrangian multipliers
h	Channel height
L_N	Liouville operator
$\mathbf{\hat{I}}_{klpha}$	Fluxes
\mathbf{J}_{1lpha}	Diffusion vector
J_2	Stress tensor
J_3	Heat flux vector
$\hat{\mathbf{J}}_{1\alpha}$	Operators of flux of number of molecules
$\mathbf{\hat{J}}_{1lpha}$ $\mathbf{\hat{J}}_{2lpha}$	Operators of momentum flux
$\hat{\mathbf{J}}_{3\alpha}$	Operators of energy flux
$\hat{\mathbf{j}}_{2\alpha},\ \hat{j}_{3\alpha}$	Operators of interphase forces
L	Plate length
l_c	Correlation length
m_i	Mass of <i>i</i> th molecule of phase α
n_{α}	Number density of particles of phase α
$n_{\alpha}(\mathbf{r}, t)$	Macroscopic values of density obtained by averaging over ensemble F_N
\mathbf{p}_{lpha}	Momentum of particles of phase α
\mathbf{p}_i	Momentum of <i>i</i> th molecule of phase α
$\mathbf{p}_{\alpha}(\mathbf{r}, t)$	Macroscopic values of momentum obtained by averaging over
1 4 ()	ensemble F_N
\mathbf{r}_i	Coordinate of center of mass of <i>i</i> th molecule of phase α
S	Information entropy
$S_{-(t-t_1)}^{(N)}$	Displacement operator over trajectory of N particles
T	Temperature

Nomenclature xix

U	Unit tensor of second rank
u	Macroscopic velocity
$\mathbf{\hat{Y}}_{klpha}$	Thermodynamic forces
α_{ieta}	Lagrangian multipliers
μ_{ij}	Transport coefficients
$\mu_{e\!f\!f}$	Effective viscosity coefficient
μ_{ff}^s , μ_{fb}^s , μ_{bf}^s , μ_{bb}^s	Tensors of fourth rank
$\mathbf{v}_{fb},~\lambda_{ff},~\mathbf{\sigma}_{fb}$	Tensors of second rank

 ζ_{α} Chemical potential of component α $\langle \rangle$ Averaging over ensemble F_N

Chapter 1 Methods of Modeling of Microflows and Nanoflows



1

Abstract The development and application of methods of numerical simulation of micro- and nanoflows are urgent tasks because of the lack and inconsistency of systematic experimental data. However, interpretation of results and determination of the applicability area of particular methods of modeling such flows should also be treated carefully and cautiously. In addition, precise terminology is important, because inadequate usage of terms can lead not only to misunderstanding, but even to erroneous ideas about the physics of the phenomena being considered. The usual flows of liquids and gases are rather difficult in the general case. This is even more so for micro- and nanoflows. Therefore, such flows should be treated with different methods. The situation becomes even more complicated if multiphase fluid flows are studied. In the present chapter, all of these situations were considered consecutively. It begins with a brief classification of these flows. After that, the methods of the modeling flows of the rarefied and dense gases and liquids are described. In the following two sections, the modeling of dispersed fluids, including nanofluids, is analyzed. The last section is devoted to a brief description of the method of molecular dynamics, the application of which is necessary for the modeling of nanoflows.

Keywords Microflows • Rarefied and dense gases • Kinetic theory Boltzmann equation • DSMC • Model kinetic equation • Dispersed fluids Nanofluids • Nanoparticles • Viscosity • Thermal conductivity • Diffusion Molecular dynamics method

1.1 Considered Systems and Their Classification

Microflows are usually understood as flows whose characteristic linear size (e.g., diameter of a cylindrical channel or distance between the plates in a plane channel) is $d \le 5 \times 10^{-4}$ m. The channel length L, however, is usually much greater than the characteristic linear size: $L \gg d$. It can reach dozens of centimeters in micromixers and several meters in microreactors. The characteristic Reynolds number for such flows of a homogeneous liquid or gas, $Re = (\rho Ud)/\mu$, usually varies in the interval

 $10^{-3} \le \text{Re} \le 10^3$, where ρ , U, and μ are the fluid density, velocity, and shear viscosity, respectively. The Knudsen number Kn = l/d (l is the mean free path of gas molecules) of the gas in microflows at standard pressure varies in the interval $10^{-4} \le Kn \le 1$. However, the gas flow can actually already be considered as free-molecular at pressures on the order of one hundredth of atmospheric pressure, i.e., as a flow with no molecular collisions.

The characteristic size of nanochannels varies from 100 to 1 nm. Channels with the characteristic size on the order of 1 nm are carbon nanotubes. However, the length of such channels can reach several millimeters and even centimeters. Carbon nanotubes form a very durable material; one of the space elevator projects implies the use of fibers made of such tubes, and the length of these fibers is expected to reach several kilometers.

In nanoflows obtainable today, the Reynolds number is always smaller, or even much smaller, than unity. In gas flows in nanochannels, the Knudsen number is usually greater than or on the order of unity. Formally, the Knudsen number in liquids with the mean free path of molecules of about 10^{-10} m is almost always smaller than unity, because in channels with the characteristic size on the order of 100 nm, it has the values $Kn \sim 10^{-2} \div 10^{-3}$. Standard hydrodynamic description becomes valid at the lower limit of these values; however, the following fact should be noted. The respective processes of viscous dissipation in gases and liquids are principally different. In gases, the momentum is leveled off, basically due to its transfer in molecular collisions; therefore, $\mu \sim l$ in rarefied gases. This manner of momentum redistribution also occurs in liquids, but it has little effect, because each molecule in a liquid always interacts with several neighbors simultaneously. In fact, viscous dissipation is associated with violation of the short-range order whose characteristic scale δ is on the order of nanometers. Thus, the viscous fluid concept becomes valid only at scales $L > \delta$. Dissipative coefficients are formed at mesoscales.

To identify similarity parameters in heterogeneous fluid flows, it is necessary to determine the characteristic scales for these flows. There are three scales in homogeneous fluids: characteristic scale of the flow, mean free path, and size of fluid molecules. The internal structure of heterogeneous fluids is much more complicated. In the general case, the set of the characteristic scales for a heterogeneous fluid is determined not only by the sizes of the internal structural elements of the medium, carrier medium molecules, and disperse particles, but also by other parameters: mean free path of molecules or particles in gases, Debye radius in plasmas, etc.

Heterogeneous or disperse fluids are multiphase media. A simple example of such media is a two-phase fluid consisting of a carrier liquid (gas) and solid, liquid, or gaseous particles suspended in the carrier fluid. These particles are considered a disperse phase. If disperse phase particles have an identical size and identical physical nature, the medium is monodisperse; otherwise, it is a polydisperse medium.

The most popular classification of disperse fluids is based on their aggregate state (Soo 1990). However, this classification is obviously insufficient. In some cases, e.g., mixtures of solid particles with liquids and gases, the behavior is the same; in other situations, even the behaviors of disperse media of the same class can

be different. The variety of heterogeneous fluids does not give a chance for creating a universal model suitable to describe all of them. One can only speak about the development of models that can describe certain classes of such media. So, the task of the classification of heterogeneous fluids is to identify such classes. An appropriate classification was developed in Rudyak (1996); here, we mention only some of its principal postulates that are important for further considerations.

Heterogeneous fluids are media with a developed internal structure. Therefore, in addition to the aggregate state, another important classification attribute should be the relationship of internal structural elements of the medium. Moreover, the heterogeneous medium properties substantially depend on the disperse phase density. Thus, the following triad can be selected for classifying heterogeneous media:

- Classification in terms of the aggregate state of the carrier fluid;
- Classification in terms of the relationship of internal structural elements of the medium;
- Classification in terms of the disperse phase density.

In the development of the classification of heterogeneous media in terms of the aggregate state, the aggregate states of both the carrier and disperse phases are taken into account. For simplicity, only monodisperse media are considered in this section. In the commonly used terminology (Soo 1990), gas suspensions and aerosols are understood as gas mixtures with solid and liquid particles, respectively. Suspensions are mixtures of the carrier liquid with solid particles, and emulsions are mixtures of the carrier liquid with droplets of another liquid. There are also gas-liquid media, which are sometimes called bubbly media.

Certainly, this classification is rather conventional. In practice, even in academic publications, the term "aerosol" is used for both suspensions and emulsions. In meteorology, aerosols are understood as particles dispersed in the atmosphere. Hence, specific classifications and terminology are used in this branch of science (dust, water dust, smoke, smog, etc.). There is also a certain classification in terms of the optical properties of the disperse phase. In a very good monograph (Friedlander 2000), aerosols are defined as gas suspensions. Simultaneously, aerosols are understood as all systems consisting of disperse particles (regardless of their nature) and carrier air or another gas.

Finally, referring to the classification of heterogeneous media in terms of their aggregate state, we have to recall one more specific state of the media. Today, both engineering applications and natural conditions involve heterogeneous media whose carrier component is the plasma. Such media are encountered, e.g., in the upper layers of the atmosphere, in facilities for plasma-enhanced deposition, etc. Thus, it seems reasonable to identify two more types of heterogeneous medium: plasma suspensions and plasmasols with solid and liquid particles as disperse components, respectively.

The complete set of characteristic scales is different for different heterogeneous fluids and is determined by the aggregate state of the carrier phase. Therefore, in constructing a classification of heterogeneous media in terms of the sizes of internal

structural elements, the above-mentioned classes of medium should be considered separately. The scales in monodisperse gas suspensions can be the characteristic radii of molecules r_0 and particles R_0 , mean free paths of molecules l_f and particles l_p , and mean free paths of particles with respect to molecules l_{pf} . If the virial parameter $\varepsilon_f = n_{\rm vf} r_0^3$ ($n_{\rm vf}$ is the number density of molecules) of the carrier gas or, identically, the volume concentration of molecules is small, then the gas can be considered rarefied, and its evolution is determined by the Boltzmann equation for a single-particle distribution function.

Models that describe the behavior of gas suspensions are qualitatively different depending on the ratio of the disperse particle size and the characteristic linear scale of the carrier gas. Depending on this ratio, the following classes of gas suspension can be identified: ultrafine suspension with nanoparticles as the disperse phase and suspensions of fine, medium-size, and coarse particles in a gas. In the general case, the dynamics of these suspensions is described by different models.

A necessary condition for a pseudo-gas of suspended particles to be considered as rarefied is a small value of the corresponding virial parameter (volume concentration); moreover, the coarser the disperse particles, the more rarefied the carrier gas should be. Finally, all mean free paths in a rarefied gas suspension should be significantly greater than the sizes of internal structural elements of the medium. Depending on the degree of rarefaction of the disperse phase, it is possible to identify strongly rarefied gas suspensions, rarefied gas suspensions, moderately dense gas suspensions, and dense gas suspensions. In suspensions of the last type, the molecular component occupies a comparatively small volume; these suspensions are usually called granular media in the literature.

The classification developed above for gas suspensions is inapplicable for liquid suspensions, because the kinetic stage of evolution is practically absent in liquids. Therefore, there are only three characteristic linear scales in suspensions: r_0 , R_0 , and L. At the next stage, liquid suspensions are divided in terms of particle size: ultrafine, fine, medium-size, and coarse particles. With certain restrictions, this classification can also be used for aerosols and emulsions. In regard to aerosols and emulsions, however, it should always be borne in mind that coagulation is an important process in such media, and neither aerosols nor emulsions (generally speaking, suspensions as well) can be considered as mixtures containing one fraction of particles. Moreover, because of nucleation and coagulation, which always proceed in aerosols and emulsions, most mixtures have particles of almost all possible sizes. Depending on the disperse phase density, it is possible to identify strongly rarefied, rarefied, moderately dense, and dense suspensions. It should be noted that suspensions can change their rheology depending on the disperse phase density.

1.2 Modeling of Rarefied Gas Microflows

A rarefied gas is usually defined as a gas where collisions occur only between pairs of molecules. This corresponds to the pressures ranging approximately from ten atmospheres to several hundredths of a percent of the atmosphere. In more rarefied flows, there may be practically zero collisions of molecules within the characteristic time of process observation; in this case, a free-molecular flow is formed. At pressures above ten atmospheres, the gas is no longer ideal, and corrections for density should be made both in the equation of state and in transport coefficients.

The method that can be used for modeling a gas flow is determined by the Knudsen number of this flow. The flow of a rarefied gas, i.e., a gas with only paired collisions of molecules and with no multiparticle collisions, is described by the Boltzmann equation (Chapman and Cowling 1990) for the single-particle distribution function f_1 as

$$\frac{\partial f_1}{\partial t} + \mathbf{v}_1 \cdot \frac{\partial f_1}{\partial \mathbf{r}_1} = J_B, \tag{1.1}$$

$$J_B = \int d\mathbf{v}_2 d\kappa \mathbf{v}_{21} \left[f_1(\mathbf{r}_1, \mathbf{v}_1', t) f_1(\mathbf{r}_1, \mathbf{v}_2', t) - f_1(\mathbf{r}_1, \mathbf{v}_1, t) f_1(\mathbf{r}_1, \mathbf{v}_2, t) \right], \tag{1.2}$$

where \mathbf{v}_1 and \mathbf{v}_2 are the velocities of molecules 1 and 2 before the collision, \mathbf{v}_1' and \mathbf{v}_2' are the velocities of these particles after the collision, $\mathbf{v}_{21} = \mathbf{v}_2 - \mathbf{v}_1$, $d\kappa = d\varepsilon dbb$, b is the impact parameter, and ε is the azimuth angle.

Nevertheless, the description at the level of the single-particle distribution function (kinetic description) is necessary only if the Knudsen number is not too low. A continuum flow regime is formed as $Kn \to 0$, and a free-molecular flow is observed as $Kn \to \infty$.

Experiments and investigations of the areas of applicability of various methods show that the Navier-Stokes equations

$$\frac{\partial \rho}{\partial t} = -\nabla \cdot \rho \mathbf{u}, \quad \rho \frac{\partial \mathbf{u}}{\partial t} = -\rho \mathbf{u} \cdot \nabla \mathbf{u} - \nabla \cdot \mathbf{J}_{2},
\frac{\partial T}{\partial t} = -\mathbf{u} \cdot \nabla T - \frac{2}{3\rho R} (\mathbf{J}_{2} : \nabla \mathbf{u} + \nabla \cdot \mathbf{J}_{3})$$
(1.3)

ensure an accurate description of gas flows up to Knudsen numbers on the order of 10^{-3} . Here, ρ , \mathbf{u} , and T are the mass density, velocity, and temperature of the gas, R is the gas constant, and \mathbf{J}_2 and \mathbf{J}_3 are the stress tensor and the heat flux vector, which are defined in the Navier-Stokes approximation by the expressions

$$\mathbf{J}_2 = \rho RT\mathbf{U} - \mu \mathbf{D} - \mu_V (\nabla \cdot \mathbf{u}) \mathbf{U}, \quad \mathbf{J}_3 = -\lambda \nabla T, \tag{1.4}$$

where μ and μ_V are the shear and volume viscosity coefficients, respectively, λ is the thermal conductivity coefficient, and **D** is the strain rate tensor:

$$\mathbf{D} \equiv D_{ij} = \frac{1}{2} \left(\frac{\partial u_i}{\partial x_i} + \frac{\partial u_j}{\partial x_i} \right).$$

When the Navier-Stokes equations are used, the channel walls are usually subjected to the no-slip boundary conditions

$$\mathbf{u}(\mathbf{r} = \mathbf{r}_W) = \mathbf{u}_W, \ T(\mathbf{r} = \mathbf{r}_W) = T_W,$$

where \mathbf{u}_W and T_W are the velocity and temperature on the wall. However, beginning from the Knudsen number $Kn \sim 5 \times 10^{-3}$, it is necessary to apply the velocity slip and temperature jump conditions

$$\mathbf{u}(\mathbf{r} = \mathbf{r}_W) = \mathbf{u}_W + \gamma_1 \mathbf{n} \cdot \nabla \mathbf{u}_{\tau} + \gamma_2 \nabla_{\tau} T,$$

$$T(\mathbf{r} = \mathbf{r}_W) = T_W + \gamma_3 \mathbf{n} \cdot \nabla T + \gamma_4 (\nabla \cdot \mathbf{u}_{\tau} - \mathbf{n}\mathbf{n} : \nabla \mathbf{u}_{\tau}),$$
(1.5)

where \mathbf{u}_{τ} is the tangential (to the surface) component of the gas velocity, ∇_{τ} is the tangential component of the gradient, and \mathbf{n} is the normal to the surface. The coefficients γ_i used here are proportional to the mean free path of molecules.

The Navier-Stokes equations with the boundary conditions (1.5) make it possible to move approximately by an order of magnitude toward higher Knudsen numbers; after that, higher-order transport equations with appropriate boundary conditions can apparently be used. It should be borne in mind in regard to this particular situation that the traditionally recommended Burnett equations are incomplete, strictly speaking, because they ignore memory effects; therefore, these equations can only be used for steady flows (Rudyak 1995).

The so-called transitional flow regime begins at Knudsen numbers on the order of unity. At Kn > 10, the flow can be considered as free-molecular, though, strictly speaking, the free-molecular flow regime corresponds to an infinite Knudsen number. The Boltzmann collision integral (1.2) is equal to zero in this case, and the flow is described by a homogeneous kinetic equation.

This discussion refers to the class of rarefied flows as a whole, but flows in microchannels have some specific features. First, it is a typical situation that the Knudsen numbers based on the channel length Kn_L , channel width Kn_w , and channel height (depth) Kn_d can differ by orders of magnitude. For example, a typical case is $Kn_L \ll 1$, $Kn_w \sim 10^{-1}$, but $Kn_d \sim 1$. The flow in such a channel cannot be described hydrodynamically; it is necessary to use the kinetic Boltzmann equation (1.1). Regular methods for its solution have been developed fairly successfully (see, e.g., Aristov et al. 2007), but practically no specific problems have yet been solved.

In practice, rarefied gas dynamic simulations are usually performed by the Direct Simulation Monte Carlo (DSMC) method. The principal scheme of the DSMC method for rarefied gases was formulated by Bird and was described in detail in his monograph (Bird 1976). The method is based on dividing the molecular motion process into free flight and collisions. In the scheme of the collision process, the

physical volume is split into cells $\Delta \mathbf{r}$ of such a size that the variations of flow parameters in each cell are small. The time is measured in discrete steps Δt_m , which are small when compared to the mean time of free flight of gas molecules. The computational domain is filled with N particles (molecules). The particle state is defined by its coordinate \mathbf{r}_i and velocity \mathbf{v}_i . Thus, the state of the modeled system at each time instant is characterized by a 6N-dimensional vector $\{\mathbf{r}_1, \mathbf{v}_1, \dots, \mathbf{r}_N, \mathbf{v}_N\} \equiv \{\mathbf{r}^N, \mathbf{v}^N\}$. The motion of molecules and their collisions at each time step are calculated in two consecutive stages. At the first stage, particle collisions in each cell are simulated independently. In choosing a pair of colliding particles, their mutual distances are ignored. It is only the particle velocities that change after collision, while the particle coordinates remain unchanged.

At the second stage, convective transfer of all molecules to distances proportional to their velocities and the time $\Delta t_m = \Delta t$ is performed. Thus, if the coordinate and velocity of the *i*th molecule at the time t_k are $\mathbf{r}_i(t_k)$ and $\mathbf{v}_i(t_k)$, then its coordinate at the time $t_{k+1} = t_k + \Delta t$ is determined by the formula $\mathbf{r}_i(t_{k+1}) = \mathbf{r}_i(t_k) + \mathbf{v}_i(t_k)\Delta t$. Interaction with physical boundaries (body surfaces) is also simulated at this stage. New particles are generated on the boundaries of the computational domain, whereas particles intersecting these boundaries are eliminated from the computation.

The most important aspect of this scheme is the simulation of particle collisions in the cell. This problem is of independent significance, because this process defines the process of relaxation in a spatially homogeneous system. To clarify the basic features of this stage, let us consider a cell α with the number of molecules N_{α} . The state of these molecules is characterized in the phase space by the vector $\{\mathbf{r}_{1_{\alpha}},\mathbf{v}_{1_{\alpha}},\dots,\mathbf{r}_{N_{\alpha}},\mathbf{v}_{N_{\alpha}}\} \equiv \{\mathbf{r}^{N_{\alpha}},\mathbf{v}^{N_{\alpha}}\}$. As the molecule positions are ignored when collision partners are chosen, the state inside the cell can be characterized only by the vector $\mathbf{v}^{N_{\alpha}}$. The next important assumption implies that the transition of a particle from the state $\mathbf{v}^{N_{\alpha}}(t_k)$ to the state $\mathbf{v}^{N_{\alpha}}(t_{k+1})$ is performed by means of paired collisions. Therefore, to study the process of spatially homogeneous relaxation of N_{α} molecules within the time interval Δt , it is necessary to determine the total number of collisions during this time interval $N_{\Delta t}$ and to establish pairs of colliding molecules.

The frequency of molecular collisions in the cell v is proportional to the scattering cross-section $\sigma(v_{ij})$ of the colliding molecules i and j, their density n, and relative velocity $v_{ij}: v = n\sigma(v_{ij})v_{ij}$. The mean collision frequency is obtained by summation over all molecules. To find the number of collisions during the time interval Δt , the thus-obtained frequency should be multiplied by the number of pairs in the system and the time interval: $N_{\Delta t} = n[(N_{\alpha} - 1)/2] < \sigma(v_{ij})v_{ij} > \Delta t$. The angular brackets here mean averaging over all pairs of molecules. The number of collisions of the pair of molecules i and j within the time interval is determined by the expression

$$\mathsf{N}_{\Lambda t}^{\mathrm{i}\mathrm{j}} = (n/N_{\alpha})\sigma(\mathsf{v}_{ij})\mathsf{v}_{ij}\Delta t,\tag{1.6}$$

and the probability of the collision of this pair is

$$\mathsf{P}_{ij} = \frac{\mathsf{N}_{\Delta t}^{ij}}{\mathsf{N}_{\Delta t}} = \frac{2}{N_{\alpha}(N_{\alpha} - 1)} \frac{\sigma(\mathsf{v}_{ij})\mathsf{v}_{ij}}{\langle \sigma(\mathsf{v}_{ij})\mathsf{v}_{ij} \rangle} \tag{1.7}$$

Thus, for modeling the process of relaxation due to collisions in the cell, it is necessary to simulate $N_{\Delta t}$ collisions between molecule pairs in accordance with Eq. (1.6). When the pair of colliding molecules is chosen, their velocities after the collision are determined on the basis of conservation laws.

The above-described procedure shows that this method, strictly speaking, does not solve the kinetic Boltzmann equation. Instead, it solves the so-called master kinetic equation for the N-particle distribution function F_N (Rudyak 1989a, 1991)

$$\frac{\partial \mathsf{F}_{N}}{\partial t} + \sum_{i=1}^{N} \frac{\mathbf{p}_{i}}{m} \cdot \frac{\partial \mathsf{F}_{N}}{\partial \mathbf{r}_{i}} = J_{N},$$

$$J_{N} = V^{-1} \sum_{j>i}^{N} \int_{0}^{2\pi} \int_{0}^{\infty} d\kappa \, v_{ij} \Big[\mathsf{F}_{N}(\mathbf{r}_{1}, \mathbf{p}_{1}, \dots, \mathbf{r}_{i}, \mathbf{p}'_{i}, \dots, \mathbf{r}_{i}, \mathbf{p}'_{j}, \dots, \mathbf{r}_{N}, \mathbf{p}_{N}, t) - \mathsf{F}_{N}(\mathbf{r}_{1}, \mathbf{p}_{1}, \dots, \mathbf{r}_{i}, \mathbf{p}_{i}, \dots, \mathbf{r}_{i}, \mathbf{p}_{j}, \dots, \mathbf{r}_{N}, \mathbf{p}_{N}, t) \Big].$$
(1.8)

The master kinetic equations (1.8) are equations for the *N*-particle distribution function, similar to the Liouville equation. In contrast to the latter, however, the master kinetic equation is irreversible and non-invariant with respect to time inversion. It can be demonstrated (Rudyak 1989a, 1991) that the master kinetic equation (1.8) yields the following kinetic equation for the single-particle distribution function:

$$\frac{\partial f_1}{\partial t} + \mathbf{v}_1 \cdot \frac{\partial f_1}{\partial \mathbf{r}_1} = \frac{N-1}{N} \int d\mathbf{v}_2 \int d\kappa_{12} \mathbf{v}_{12} (f_1' f_1' - f_1 f_1)
+ \frac{N-1}{N} \int d\mathbf{v}_2 \int d\kappa_{12} \mathbf{v}_{12} (g_2' - g_2), \tag{1.9}$$

which is drastically different from the Boltzmann equation (1.1), (1.2) and reduces to it only in the limit as $N \to \infty$ and under the assumption of multiplicativity of the pair (two-particle) distribution function $f_2 = f_1 f_1 + g_2$, $g_2 = 0$ (here, f_2 is the pair distribution function). Equation (1.9) depends on the two-particle correlation function g_2 ; as a consequence, there appear two-particle correlations in the solution, which are absent in the rarefied gas. In particular, they arise owing to a large number of repeated collisions in the simulated cell. Such collisions are typical for dense gases. To eliminate them from consideration, a special procedure using a thermostat was developed (Gimelshtein and Rudyak 1991). As a result, the number

of particles needed for simulations could be reduced by two or three orders for spatially homogeneous problems.

With the capabilities of advanced computers, the DSMC method provides sufficiently accurate solutions for a wide range of problems. In particular, it is possible to simulate supersonic jets and supersonic external flows. However, the velocities of flows in microchannels are usually not very high, and the DSMC method does not ensure satisfactory accuracy. Therefore, the method can hardly be used for modeling such flows in reality.

It is possible to move further in studying rarefied gas microflows by using model kinetic equations, i.e., equations in which the collision integral is presented in a significantly simplified form. The first model equation was developed by Bhatnagar et al. (1954) (the so-called BGK equation). The collision integral in this equation has the form

$$J_{BGK} = v[f_M(\rho, \mathbf{u}, T) - f_1(\mathbf{r}_1, \mathbf{v}_1, t)],$$

where v is the frequency of molecular collisions and $f_M(\rho, \mathbf{u}, T)$ is the local Maxwell distribution function. This model, however, has an important drawback: it does not allow for correct determination of the gas viscosity and thermal conductivity, and yields an incorrect Prandtl number for this reason. This drawback was corrected by Shakhov (1968), whose model equation is called the S-model. The collision integral in this model is determined by the expression

$$J_{S} = \frac{P}{\mu} \left\{ f_{M} \left[1 + \frac{2m}{15n(kT)^{2}} \mathbf{q} \cdot \mathbf{C} \left(\frac{mC^{2}}{2kT} - \frac{5}{2} \right) \right] - f_{1}(\mathbf{r}_{1}, \mathbf{v}_{1}, t) \right\},\,$$

where **q** is the heat flux vector and $\mathbf{C} = \mathbf{v} - \mathbf{u}$.

There are also more complicated models, e.g., the ellipsoidal model, but they can only be applied for solving linearized problems because of an extremely complicated form of the model collision integral. Examples of the description of rarefied gas microflows with the use of model equations can be found in Cercignani and Pagani (1967), Graur and Sharipov (2008a, b).

A principal problem that cannot be resolved by using the above-described methods of rarefied gas modeling is the necessity of taking into account the roughness of the channel wall. This is an extremely important factor for macroscopic flows as well. It is known that the flow in a smooth tube is stable under comparatively small perturbations. This means that the flow in the tube remains laminar at sufficiently high Reynolds numbers. It was experimentally found that this is at least true for Reynolds numbers up to 10^5 . On the other hand, it is usually assumed that a laminar-turbulent transition occurs in a circular tube at Reynolds numbers on the order of 2.200. This transition is usually associated with the roughness of the tube wall. This factor becomes even more important in microflows. The roughness height in sufficiently smooth channels is normally several tens of nanometers. Nevertheless, there are channels where the roughness height can vary from hundreds of nanometers to tens of micrometers. Roughness of this height can drastically change the character of the microflow.

Gas/surface interaction in microflows, and especially in nanoflows, is sometimes a key factor. Indeed, the number of molecules near the cylindrical channel surface. which interact with the latter during mean free flight times, is on the order of $N_S \sim \pi dl L n$. At the same time, the number of molecules interacting with each other in the bulk is $N_R \sim (\pi d^2 L - \pi dl L)n$. It can be easily seen that two thirds of molecules already interact with the wall at Knudsen numbers of about 0.2, and collisions of molecules in the bulk can actually be ignored at Knudsen numbers of 0.4. Under these conditions, the adequacy of the description of interaction of molecules with the wall is the governing factor. The situation, however, is not that simple. In the kinetic description of a gas system, interaction of gas molecules with the surface changes the probability of finding the gas system in a given state. In fact, an additional source term J_W appears in the kinetic equation. The explicit form of this term can be obtained in the following manner. Let us consider a rarefied gas and assume, for simplicity, that molecules incident onto the surface interact with it instantaneously and return to the system, leaving the surface at the point of their incidence. The number of molecules located at the time t near the point (\mathbf{r}, \mathbf{p}) in the phase volume element $d\mathbf{r}d\mathbf{p}$ is $f_1(\mathbf{r},\mathbf{p})d\mathbf{r}d\mathbf{p}$. Let us now determine the number of molecules leaving this group during the time Δt as a result of their incidence onto the surface W. The only molecules capable of colliding are those whose momentum satisfies the condition $\mathbf{p} \cdot \mathbf{n} < 0$. Then, the number of molecules incident onto the surface element dW during the time dt is $d\mathbf{r}d\mathbf{p}dt\Theta(-\mathbf{p}\cdot\mathbf{n})\}|\mathbf{p}\cdot\mathbf{n}|f_1(\mathbf{r},\mathbf{p},t)\delta(\mathbf{r}-\mathbf{p}\cdot\mathbf{n})|f_1(\mathbf{r},\mathbf{p},t)\delta(\mathbf{r}-\mathbf{p}\cdot\mathbf{n})|f_1(\mathbf{r},\mathbf{p},t)\delta(\mathbf{r}-\mathbf{p}\cdot\mathbf{n})|f_1(\mathbf{r},\mathbf{p},t)\delta(\mathbf{r}-\mathbf{p}\cdot\mathbf{n})|f_1(\mathbf{r},\mathbf{p},t)\delta(\mathbf{r}-\mathbf{p}\cdot\mathbf{n})|f_1(\mathbf{r},\mathbf{p},t)\delta(\mathbf{r}-\mathbf{p}\cdot\mathbf{n})|f_1(\mathbf{r},\mathbf{p},t)\delta(\mathbf{r}-\mathbf{p}\cdot\mathbf{n})|f_1(\mathbf{r},\mathbf{p},t)\delta(\mathbf{r}-\mathbf{n})|f_1(\mathbf{r},\mathbf{n},t)\delta(\mathbf{r}-\mathbf{n})|f_1(\mathbf{r},\mathbf{n},t)\delta(\mathbf{r}-\mathbf{n})|f_1(\mathbf{r},\mathbf{n},t)\delta(\mathbf{r}-\mathbf{n})|f_1(\mathbf{r},\mathbf{n},t)\delta(\mathbf{r}-\mathbf{n})|f_1(\mathbf{r},\mathbf{n},t)\delta(\mathbf{r}-\mathbf{n})|f_1(\mathbf{r},\mathbf{n},t)\delta(\mathbf{r}-\mathbf{n})|f_1(\mathbf{r},\mathbf{n},t)\delta(\mathbf{r}-\mathbf{n})|f_1(\mathbf{r},\mathbf{n},t)\delta(\mathbf{r}-\mathbf{n})|f_1(\mathbf{r},\mathbf{n},t)\delta(\mathbf{r}-\mathbf{n})|f_1(\mathbf{r},\mathbf{n},t)\delta(\mathbf{r}-\mathbf{n})|f_1(\mathbf{r},\mathbf{n},t)\delta(\mathbf{r}-\mathbf{n})|f_1(\mathbf{r},\mathbf{n},t)\delta(\mathbf{r}-\mathbf{n})|f_1(\mathbf{r},\mathbf{n},t)\delta(\mathbf{r}-\mathbf{n})|f_1(\mathbf{r},\mathbf{n},t)\delta(\mathbf{r}-\mathbf{n})|f_1(\mathbf{r},\mathbf{n},t)\delta(\mathbf{r}-\mathbf{n})|f_1(\mathbf{r},\mathbf{n},t)\delta(\mathbf{r}-\mathbf{n})|f_1(\mathbf{r},\mathbf{n},t)\delta(\mathbf{r}-\mathbf{n})|f_1(\mathbf{r},\mathbf{n},t)\delta(\mathbf{r}-\mathbf{n})|f_1(\mathbf{r},\mathbf{n},t)\delta(\mathbf{r}-\mathbf{n})|f_1(\mathbf{r},\mathbf{n},t)\delta(\mathbf{r}-\mathbf{n})|f_1(\mathbf{r},\mathbf{n},t)\delta(\mathbf{r}-\mathbf{n})|f_1(\mathbf{r},\mathbf{n},t)\delta(\mathbf{r}-\mathbf{n})|f_1(\mathbf{r},\mathbf{n},t)\delta(\mathbf{r}-\mathbf{n})|f_1(\mathbf{r},\mathbf{n},t)\delta(\mathbf{r}-\mathbf{n})|f_1(\mathbf{r},\mathbf{n},t)\delta(\mathbf{r}-\mathbf{n})|f_1(\mathbf{r}-\mathbf{n},t)\delta(\mathbf{r}-\mathbf{n})|f_1(\mathbf{r}-\mathbf{n},t)\delta(\mathbf{r}-\mathbf{n})|f_1(\mathbf{r}-\mathbf{n},t)\delta(\mathbf{r}-\mathbf{n})|f_1(\mathbf{r}-\mathbf{n},t)\delta(\mathbf{r}-\mathbf{n})|f_1(\mathbf{r}-\mathbf{n},t)\delta(\mathbf{r}-\mathbf{n})|f_1(\mathbf{r}-\mathbf{n},t)\delta(\mathbf{r}-\mathbf{n})|f_1(\mathbf{r}-\mathbf{n},t)\delta(\mathbf{r}-\mathbf{n},t)$ $(\mathbf{R}_W)dW$, where (\mathbf{R}_W) is the radius-vector of the points on the surface (W, Θ) is the Heaviside function, $\delta(\mathbf{r})$ is the Dirac delta function, and \mathbf{n} is the internal normal to the surface.

The total number of molecules colliding with the surface during the time dt is obtained by integration over dW:

$$d\mathbf{r}d\mathbf{p}dt \int dW\Theta(-\mathbf{p}\cdot\mathbf{n})|\mathbf{p}\cdot\mathbf{n}|f_1(\mathbf{r},\mathbf{p},t)\delta(\mathbf{r}-\mathbf{R}_W). \tag{1.10}$$

The number of molecules entering the volume $d\mathbf{r}d\mathbf{p}$ during the time dt due to interaction with the surface is

$$d\mathbf{r}d\mathbf{p}dt \int dW\Theta(\mathbf{p}\cdot\mathbf{n})|\mathbf{p}\cdot\mathbf{n}|f_{1W}(\mathbf{R}_W,\mathbf{p},t)\delta(\mathbf{r}-\mathbf{R}_W). \tag{1.11}$$

Here, f_{1W} is the distribution function of molecules reflected from the wall, which is related in the general case to the distribution function of the incident molecules as

¹Strictly speaking, interaction of gas molecules with the surface is not instantaneous. Moreover, incident gas molecules can be adsorbed on the surface and experience ionization or dissociation. Adsorption, in turn, can lead to the formation of an adsorbed layer on the surface, whose state depends on the ambient gas. In addition, gas/surface interaction depends on the surface state, temperature, roughness, etc.

$$f_{1W}(\mathbf{p} \cdot \mathbf{n})\Theta(\mathbf{p} \cdot \mathbf{n}) = \int d\mathbf{p}^* \Theta(-\mathbf{p}^* \cdot \mathbf{n}) |\mathbf{p}^* \cdot \mathbf{n}| f_{1W}(\mathbf{R}_W, \mathbf{p}^*) w(\mathbf{p}^*, \mathbf{p}), \qquad (1.12)$$

where \mathbf{p}^* is the momentum of the molecule incident onto the surface and $w(\mathbf{p}^*, \mathbf{p})$ is the scattering kernel.

In view of Eqs. (1.10)–(1.12), the source term of the kinetic equation induced by the presence of the surface can be presented as

$$J_{W} = \int dW \, \delta(\mathbf{r} - \mathbf{R}_{W})$$

$$\left[\int d\mathbf{p}^{*} \Theta(-\mathbf{p}^{*} \cdot \mathbf{n}) |\mathbf{p}^{*} \cdot \mathbf{n}| f_{1W}(\mathbf{R}_{W}, \mathbf{p}^{*}) w(\mathbf{p}^{*}, \mathbf{p}) - \Theta(\mathbf{p} \cdot \mathbf{n}) |\mathbf{p} \cdot \mathbf{n}| f_{1}(\mathbf{r}, \mathbf{p}) \right].$$
(1.13)

The calculation of the scattering kernel $w(\mathbf{p}^*, \mathbf{p})$ is extremely complicated in the general case, and its general solution can hardly be obtained (see Cercignani 1975; Goodman and Wachman 1976). In practice, researchers often use model presentations of the scattering kernel, which are based on the specular-diffuse Maxwell model (Maxwell 1879), in which some portion of molecules $(1 - \alpha)$ experience specular reflection from the surface, and the remaining portion of molecules (α) are reflected with the Maxwell distribution at the wall temperature (diffuse reflection). The scattering kernel in this model has the form

$$w(\mathbf{p}^*, \mathbf{p}) = (1 - \alpha)\delta(\mathbf{p} - \mathbf{p}^* + 2\mathbf{n}(\mathbf{p}^* \cdot \mathbf{n})) + \alpha f_{10W}(\mathbf{p}^*)(\mathbf{p}^* \cdot \mathbf{n}). \tag{1.14}$$

Here,

$$f_{10}(\mathbf{p}, \mathbf{r}, t) = \frac{n(\mathbf{p}, \mathbf{r}, t)}{\left[2\pi mkT(\mathbf{p}, \mathbf{r}, t)\right]^{3/2}} \exp\left(-\frac{\mathbf{p} - m\mathbf{u}^2(\mathbf{p}, \mathbf{r}, t)}{2mkT(\mathbf{p}, \mathbf{r}, t)}\right)$$

is a local Maxwell distribution function whose parameters depend on coordinates and time, and f_{10W} is the local Maxwell distribution function with the wall temperature.

Kernel (1.14) is written under the assumption that the surface is at rest. If the surface moves with a velocity V_W , then the momentum \mathbf{p} should be replaced by $(\mathbf{p} - mV_W)$. Thus, reflection of molecules is described by the specular law at $\alpha = 0$ and by the diffuse law at $\alpha = 1$. In this case, the model completely loses the memory of its characteristics before its incidence. The coefficient α is usually called the accommodation coefficient. Nevertheless, some care is needed here, because the molecule interacting with the boundary exchanges both momentum and energy with this boundary. This interaction is inelastic in the general case, but momentum and energy exchange is performed in a different manner. The accommodation coefficient does not take this fact into account. The accommodation coefficients for

momentum α_p or energy α_E for a rarefied gas in the general case are determined by the following relation (Cercignani 1975):

$$\alpha(\varphi) = \frac{\int\limits_{\mathbf{p}\cdot\mathbf{n}<0} \varphi(\mathbf{p})|\mathbf{p}\cdot\mathbf{n}|f_1(\mathbf{p})d\mathbf{p} - \int\limits_{\mathbf{p}\cdot\mathbf{n}>0} \varphi(\mathbf{p})|\mathbf{p}\cdot\mathbf{n}|f_1(\mathbf{p})d\mathbf{p}}{\int\limits_{\mathbf{p}\cdot\mathbf{n}<0} \varphi(\mathbf{p})|\mathbf{p}\cdot\mathbf{n}|f_1(\mathbf{p})d\mathbf{p} - \kappa_m \int\limits_{\mathbf{p}\cdot\mathbf{n}>0} \varphi(\mathbf{p})|\mathbf{p}\cdot\mathbf{n}|f_{10W}(\mathbf{p})d\mathbf{p}}.$$
 (1.15)

Here, $\varphi(\mathbf{p})$ is a certain function of molecular momentum and κ_m is a normalization factor chosen in such a way that $\kappa_m f_{10W}$ provides the same mass flux as the function f_1 . The energy accommodation coefficient is obtained from here by assuming that $\varphi(\mathbf{p}) = p^2/2m$, the tangential momentum accommodation coefficient $\alpha_{p\tau}$ is found at $\varphi(\mathbf{p}) = \mathbf{p} \times \mathbf{n}$, and the normal momentum accommodation coefficient α_{pn} is obtained at $\varphi(\mathbf{p}) = \mathbf{p} \cdot \mathbf{n}$.

Expression (1.15) can be written in macroscopic variables as

$$\alpha_E = \frac{\Im_i - \Im_r}{\Im_i - \Im_W}, \quad \alpha_{p\tau} = \frac{P_{\tau i} - P_{\tau r}}{P_{\tau i} - P_{W\tau}}, \quad \alpha_{pn} = \frac{P_{ni} - P_{nr}}{P_{ni} - P_{Wn}},$$

where \Im_i , \Im_r , \Im_w are the energy fluxes of incident molecules and reflected molecules from the wall per unit time and the energy flux corresponding to the case of diffuse reflection of all molecules incident onto the wall. In two remaining formulas, the subscripts τ and n correspond to tangential and normal momenta of the incident (subscript i) and reflected (subscript r) molecules, and P_W is the momentum acquired by the molecules due to wall motion. Naturally, this momentum is equal to zero for a motionless wall.

The boundary conditions (1.5) can also be rewritten in terms of the accommodation coefficients. For simplicity, we consider only the case with no thermal slipping. In this case, we have (Maxwell 1879; Smoluchowski 1898)

$$\mathbf{u}(\mathbf{r} = \mathbf{r}_{W}) = \mathbf{u}_{W} + \frac{2 - \alpha_{p}}{\alpha_{p}} Kn(\mathbf{n} \cdot \nabla \mathbf{u}_{\tau}),$$

$$T(\mathbf{r} = \mathbf{r}_{W}) = T_{W} + \frac{2 - \alpha_{E}}{\alpha_{F}} \frac{2\gamma Kn}{(\gamma + 1) \operatorname{Pr}} (\mathbf{n} \cdot \nabla T),$$
(1.16)

where $\gamma = c_p/c_V$ is the ratio of specific heats at constant volume and pressure, and $\Pr = (\mu c_p/k)$ is the Prandtl number.

According to Eq. (1.16), the slip coefficients increase almost linearly with an increase in the Knudsen number. Accommodation coefficients have been intensely studied for the last 50 years, because of their various applications in space aerodynamics, vacuum engineering, etc. Experiments aimed at investigating the accommodation coefficients for industrial materials have shown that the momentum accommodation coefficient α_p at room temperature is fairly close to unity. This is primarily related to the roughness of these materials and the adsorption of molecules on them. The accommodation coefficients increase with increasing surface

roughness. Contrastingly, in experiments on carefully treated and cleaned surfaces, it was found that the accommodation coefficients can turn out to be appreciably smaller than unity. Unfortunately, there are no universal relations or even regular features. Moreover, the accommodation coefficients are certainly not universal, because they depend on the surface material, the degree of its purity, gas temperature, pressure, and velocity, and surface temperature. Moreover, the accommodation coefficient depends in the general case on the degree of gas rarefaction, i.e., on the Knudsen number.

1.3 Modeling of Moderately Dense Gases

The Boltzmann kinetic equation is the kinetic equation for rarefied gases. The Boltzmann gas should be rarefied to an extent that it should be possible to neglect all multiparticle collisions except for paired collisions and to assume that the molecules are statistically independent before their collision. A moderately dense gas in which the pressure at standard temperatures varies approximately from ten to 100-200 atmospheres cannot be described by the Boltzmann theory. The mean free path of molecules of a moderately dense gas is $10^{-5} \div 10^{-6}$ cm. Therefore, Knudsen numbers in microchannels can vary from 10^{-4} for the largest channels to 10^{-1} for the smallest channels. As for rarefied gases, there is a range of parameters in which the flow can be described hydrodynamically, but there is also a range of parameters in which the kinetic description should be applied. Flows in nanochannels should almost always be described kinetically.

The first successful attempt to construct the kinetic theory of moderately dense gases was made by Enskog (Chapman and Cowling 1990). He derived an equation that was named after him, which has the form

$$\frac{\partial f_1}{\partial t} + \mathbf{v}_1 \cdot \frac{\partial f_1}{\partial \mathbf{r}_1} = J_E, \tag{1.17}$$

$$J_{E} = d^{2} \int d\mathbf{p}_{12} \int_{\mathbf{p}_{12} \cdot \mathbf{e} > 0} d\mathbf{e} \frac{\mathbf{p}_{12} \cdot \mathbf{e}}{m} \left[\chi(\mathbf{r}_{1} + \frac{1}{2}\sigma\mathbf{e})f_{1}(\mathbf{r}_{1}, \mathbf{p}'_{1})f_{1}(\mathbf{r}_{1} + \sigma\mathbf{e}, \mathbf{p}'_{2}) - \chi(\mathbf{r}_{1} - \frac{1}{2}\sigma\mathbf{e})f_{1}(\mathbf{r}_{1}, \mathbf{p}_{1})f_{1}(\mathbf{r}_{1} - \sigma\mathbf{e}, \mathbf{p}_{2}) \right],$$

$$(1.18)$$

where χ is the correlation function, which takes into account two effects: (i) reduction of the system volume due to screening effects induced by the emergence of overlapping configurations of molecules; (ii) enhancement of the collision frequency due to reduction of the free volume of the system.

The collision integral (1.18) is nonlocal [in contrast to the Boltzmann collision integral (1.2)]. This nonlocality is caused by nonlocal interaction of molecules;

during the collision, their centers are located at a distance σ (molecule diameter). Enskog simulated the molecules by finite-diameter solid spheres and phenomenologically derived a Boltzmann-type equation for them. As a result, the problem could be principally simplified: in a gas consisting of solid spheres, only paired collisions occur, regardless of the gas density. The kinetic Enskog equation (1.17), in contrast to the Boltzmann equation, takes into account momentum and energy transfer in collisions at distances on the order of the molecule's diameter. The denser the gas, the more important it is to take into account this transfer mechanism.

After solving the Enskog equation, the gas description in the first approximation over the gradients of the macroscopic variables reduces to the hydrodynamic Navier-Stokes equations (1.1), where the equation of state and the fluxes are now defined as

$$p = (1 + \rho b \chi) n k T$$
, $\widetilde{\mathbf{J}}_2 = -2 \mu_{22}^{sE} (\nabla \mathbf{u}) - \mu_{22}^{vE} (\nabla \cdot \mathbf{u})$, $\mathbf{J}_3 = -\mu_{33}^E \nabla T$. (1.19)

The transport coefficients involved in these equations are defined by the expressions

$$\mu_{22}^{sE} = \mu_{22}^{0} \left[1 + 0.8\rho b\chi + 0.7614(\rho b\chi)^{2} \right] \chi^{-1}, \quad \mu_{22}^{vE} = 1.002(\rho b\chi)^{2} \chi^{-1},$$

$$b = (2\pi d^{3}/3m), \quad \mu_{33}^{E} = \mu_{33}^{0} \left[1 + 0.6\rho b\chi + 0.7574(\rho b\chi)^{2} \right] \chi^{-1}.$$
(1.20)

Thus, the Enskog theory not only provides density-based corrections to the shear viscosity and thermal conductivity coefficients, but also determines the volume viscosity coefficient, which is absent in the theory of structureless rarefied gases.

The equation of state (1.19) can be expanded in the virial parameter² ρb :

$$(p/nkT) = 1 + \rho b + 0.625(\rho b)^{2} + 0.2869(\rho b)^{3} + \dots$$
 (1.21)

This expansion coincides with the virial expansion of the equation of state in equilibrium statistical mechanics. Thus, the function χ introduced by Enskog is actually the equilibrium two-particle correlation function χ_{20} .

The results predicted by the Enskog theory, with the molecule's diameter being chosen on the basis of calculations of the rarefied gas transport coefficients, ensure a good description of experimental data on the transport coefficients of inert gases up to $\rho b = 0.4$ (Ferziger and Kaper 1972). In this case, however, the molecule's diameter should be a function of temperature.

The derivation of the Enskog equation is based on three model assumptions: (i) the molecules are modeled by hard spheres; (ii) the influence of dynamic correlations can be neglected; (iii) multiparticle collisions are effectively taken into

²This parameter is proportional to the van der Waals parameter and density; therefore, the corresponding expansion can also be called the expansion in terms of density.

account by introducing an equilibrium configuration correlation function. Numerous calculations and comparisons with experiments have shown that the main drawbacks of the theory are caused by the first assumption. Therefore, a model kinetic equation for a dense gas of the Enskog equation type was derived in (Rudyak 1985, 1989b) for real interaction potentials

$$\frac{\partial f_1}{\partial t} + \mathbf{v}_1 \cdot \frac{\partial f_1}{\partial \mathbf{r}_1} = \int dx_2 \frac{\partial U_{12}}{\partial \mathbf{r}_1} \cdot \frac{\partial}{\partial \mathbf{v}_1} \chi_2 S_-^{(2)} f_1(t_0) f_1(t_0). \tag{1.22}$$

Here, U_{12} is the molecular interaction potential.

The kinetic equation (1.22) takes into account imperfection effects associated with nonlocality and the delay of molecular interaction; moreover, multiparticle collisions are taken into account by the quasi-equilibrium two-particle correlation function χ_2 . Thus, this equation, in contrast to the Enskog equation, can be used for gases with real interaction potentials and takes into account the influence of the delay and the correlation between the delay and spatial nonlocality on the transport processes. A detailed solution of this equation in the approximation of a moderately dense gas can be found in Rudyak (1989b).

The kinetic equations (1.17) and (1.22) actually provide a reliable base for the description of moderately dense gases, but they have to be solved at sufficiently high Knudsen numbers, as was demonstrated above. Unfortunately, there are no methods that can be used to solve these equations at such Knudsen numbers. Therefore, the only way out is to use the molecular dynamics method, which will be discussed in the last section of this chapter.

1.4 Modeling of Dense Gas and Liquid Flows

The density of a dense gas is close to liquid density. However, the thermodynamic properties of fluids in these two aggregate states are significantly different. Thus, for example, the viscosity coefficient increases with temperature in gases and, vice versa, decreases with increasing temperature in liquids. This is caused by the fact that the transport processes in gases are mainly induced by kinetic effects, i.e., by transfer in the course of motion of molecules and their interaction. Liquids are governed by the short-range order, and the processes of viscous dissipation, for instance, are caused by violation of the short-range order and by diffusion processes of momentum leveling in the system, in addition to molecular transfer. Naturally, this should be taken into account in simulating dense fluids. However, the simulation methods are actually identical. Indeed, dense fluid molecules are almost always in the sphere of interaction with other molecules. Their mean free path is $l \le \sigma \sim 10^{-8}$ cm, where σ is the effective size of the molecules. The corresponding Knudsen numbers in microchannels are always smaller, or even much smaller, than unity. However, the hydrodynamic description requires a certain degree of care to be used. As was already noted, the concept of a continuum medium is valid if it is

possible to select a physically infinitesimal hydrodynamic scale r_h such that fluctuations inside the corresponding volume could be neglected. For liquids, we have $r_h \sim \sqrt{\sigma d}$ (Rudyak 1995), where d is the characteristic linear scale of the flow (diameter of a cylindrical channel, distance between the plates in a plane Poiseuille flow, etc.). If the microchannel height is $d \sim 1~\mu m$, then $r_h \sim 10^{-4}~m$, which is already comparable with the channel height. Fluctuations of the number of particles in such a volume for a dense fluid in equilibrium are on the order of $1/\sqrt{N_d} \sim 10^{-2}$, which is quite noticeable. Therefore, the hydrodynamic description fails if there are gradients of macroscopic variables in the flow.

Particular problems arise near the channel walls. As was already noted, viscosity in gases is related to momentum transfer by molecules; therefore, it is formed at scales greater than the mean free path of molecules. In liquids, however, the short-range order is observed at scales on the order of 1 nm, and viscosity is formed at mesoscales r_l : $\sigma < r_l < r_h$. Thus, the viscous liquid concept is valid only at scales beginning from tens of nanometers. Therefore, the liquid in sufficiently small microchannels can have different values of viscosity near the walls and in the bulk. Moreover, the transport processes in microchannels are no longer isotropic. For example, diffusion of molecules along and across the channel has different characteristics.

Nevertheless, it should be noted that the hydrodynamic description is rather rough, in the sense that it is valid far beyond the area of its applicability. It should be borne in mind, however, that the existence of roughness on the channel walls can significantly change in the character of the flow, and this fact should be taken into account in simulations. The second problem arising here is the formulation of the boundary conditions. A fairly large slip length is observed on the walls, even in liquid microflows. Correspondingly, the no-slip boundary condition can turn out to be insufficient.

Naturally, all of the above-described problems are aggravated if nanoflows are considered. The Knudsen numbers are still smaller than unity, but have such values that the hydrodynamic description is inapplicable. The physically infinitesimal hydrodynamic scale in such a flow is on the order of $r_h \sim \sqrt{\sigma d} \le 10^{-7}$ cm. In this case, the relative fluctuations in the number of particles, even as predicted by the equilibrium theory, are on the order of $1/\sqrt{N_d} \sim 1 \div 10^{-1}$. It was shown (Rudyak and Kharlamov 2003; Kharlamov and Rudyak 2004) that the fluctuations in the number of particles, momentum, and energy in such small systems are no longer described by the classical relations. In particular, the distribution functions of the fluctuations of the number of particles and energy are appreciably different from the Gaussian curve and do not coincide with the Poisson distribution in the case of an ideal gas. The distribution function of the momentum fluctuations for a small subsystem is Gaussian, but the dispersion of the distribution depends, to a large extent, on the thermostat density, in contrast to the usual equilibrium theory. Molecular dynamics calculations have also shown that autocorrelation functions of the momentum fluctuations decrease nonmonotonically. It was demonstrated that the temperature can be introduced beginning from volumes with the characteristic size of about ten nanometers, i.e., at the mesoscale r_l . All of these circumstances suggest that the only method suitable for modeling dense fluid nanoflows is molecular simulation, and the most appropriate technique here is the molecular dynamics method.

1.5 Modeling of Disperse Fluid Flows

In the general case, disperse fluids are multiphase systems. The method of modeling these fluids is determined by the classification given in Sect. 1.1. A gas suspension is a two-phase system consisting of carrier gas molecules and a pseudo-gas of disperse particles. In what follows, the disperse phase is assumed to consist of solid particles for simplicity, though the majority of conclusions formulated here are also valid for liquid particles. Thus, let the particles in the gas suspension be hard spheres of radius R_0 . Then, in addition to the molecule size σ and particle size R_0 , it is possible to choose three more characteristic scales: mean free path of fluid molecules l_f , mean free path of particles l_p , and mean free path of particles with respect to molecules l_{pf} . The mean free path of molecules is determined by their number density n_{vf} and the scattering cross-section $l_f \sim 1/n_{vf}\sigma^2$. For a gas consisting of hard spheres (Chapman and Cowling 1990), $l_f = 0.177/n_{vf}\pi\sigma^2$. Similarly, $l_p = 0.177/n_{vp}\pi R_0^2$. The mean free path of particles with respect to molecules is

$$l_{pf} \sim \frac{0.177 c_{0p}}{n_{\text{vf}} \pi R_0^2 c_{0f}} \sim \frac{0.177}{n_{\text{vf}} \pi R_0^2} \sqrt{\frac{m}{M}} \sim \frac{0.177}{n_{\text{vf}} \pi R_0^2} \sqrt{\frac{r_0^3}{R_0^3}}, \tag{1.23}$$

where it is also taken into account that $m \sim \sigma^3$, $M \sim R_0^3$, $c_{0p}/c_{0f} \sim \sqrt{m/M}$, and c_{0p} , c_{0f} are the mean thermal velocities of the disperse particles and carrier gas molecules, respectively, $c_{0i} \sim \sqrt{2kT/m_i}$, i = f, p.

Formula (1.23) shows that, if the carrier gas is, e.g., air under standard conditions, then the mean free path for particles with the characteristic size $R_0 \ge 10^{-8}\,$ m is $l_{pf} \ll l_f$. Moreover, $l_{pf} < \sigma$ almost always, i.e., the process of particle collisions with molecules is almost continuous. Naturally, the mean free path l_{pf} increases with an increasing level of carrier gas rarefaction.

In fine disperse gas suspensions, the characteristic particle size is on the order of the infinitesimal (for the carrier gas) kinetic scale (Klimontovich 1974)

$$R_0 \sim r_{kf} \sim \sqrt{\varepsilon_f} l_f,$$
 (1.24)

where $\varepsilon_f = n_{\rm vf} \sigma^3$. For air under standard conditions, we have $l_f \sim 10^{-6}$ m, $\varepsilon_f \sim 10^{-4}$, and $R_0 \leq 10^{-7}$ m. The value of r_{kf} increases with increasing gas rarefaction. For example, at an altitude of 100 km above the Earth's surface, the density of molecules in the atmosphere is $n_{\rm vf} \sim 10^{13}$, $l_f \sim 1$ m, and $\varepsilon_f \sim 10^{-10}$.

Therefore, a fine disperse suspension at this altitude can have molecules with $R_0 \le 10^{-5}$ m. On the other hand, the physically infinitesimal kinetic scale in dense gases and liquids is on the order of nanometers. Therefore, a fine disperse suspension is understood here as a gas or liquid suspension with nanoparticles. Such media are called nanofluids, and they will be discussed in the next section. In all other situations, we have a usual fluid with macroscopic particles. Modeling of this fluid depends, to a large extent, on both the flow regime and the microchannel size. It should be mentioned that such fluid flows in nanochannels are impossible (strictly speaking, it is possible to organize a flow with compliant particles; a well-known example of such a fluid is blood, though disperse particles are not solid).

For the hydrodynamic description of gas suspensions, the Knudsen numbers of the carrier gas Kn_g and the pseudo-gas consisting of particles Kn_p should be small: $Kn_g \sim 1/(n_g\sigma^2d) \ll 1$, $Kn_p \sim 1/(n_pR_0^2d) \ll 1$, where n_g and n_p are the number densities of carrier gas molecules and particles, respectively. The lower boundary of the microchannel size is about $d \geq 10^{-1}$ µm. The upper boundary is smaller than 500 µm. Therefore, the carrier gas can be described hydrodynamically if its density is $n_g \gg 1/(\sigma^2d)$. In fact, this condition is satisfied only for moderately dense and dense gases. Even if the carrier gas is dense, however, the second condition should be also satisfied. It can be easily seen that it is not satisfied, even for the largest microchannels and the finest particles. Thus, it is almost always impossible to describe gas suspensions in microchannels hydrodynamically.

In suspensions, only three characteristic linear scales can be identified: σ , R_0 , and d. An important scale of the liquid flow is the physically infinitesimal hydrodynamic scale $r_{hf} = \sqrt{\sigma d}$. The corresponding physically infinitesimal hydrodynamic volume is $v_{hf} \sim (\sigma d)^{3/2}$. In the equilibrium state, the fluctuations of macroscopic variables are inversely proportional to the square root from the number of particles in the system. As the number of molecules in this volume is $N_{hf} = n_{vf} v_{hf} \sim n_{vf} (r_0 L)^{3/2}$, then the condition $\sqrt{N_{hf}} = \sqrt{n_{vf}} (\sigma d)^{3/4} \gg 1$ should be satisfied for the fluctuations of macroscopic variables to be small in this volume. This relation is almost always valid for liquids.

A fine disperse suspension is understood as one with the particle size

$$R_0 \ll r_{hf} \sim \sqrt{\sigma d},$$
 (1.25a)

a medium disperse suspension has particles with the size

$$R_0 \sim r_{hf} \sim \sqrt{\sigma d}$$
, (1.25b)

³At the boundary of applicability of the hydrodynamic description, one can try to study a microflow of a moderately dense or dense gas with particles on the order of one micrometer. However, the boundary conditions here should be imposed carefully, because the usual hydrodynamic boundary conditions are invalid for the pseudo-gas of particles (see below).

and the particle size in a coarse disperse suspension are determined by the inequality

$$d \gg R_0 > r_{hf}$$
 or $d \gg R_0 \gg r_{hf}$. (1.25c)

As the suspension characteristics are different depending on the particle and channel sizes, they have to be described by different models. In a microchannel with the characteristic size on the order of several micrometers, a fine or medium disperse suspension is a nanofluid, i.e., a suspension in which the disperse phase consists of nanoparticles (see the next section). Thus, the only classical disperse fluid, i.e., disperse fluid with macroscopic particles, in a microchannel is a coarse disperse suspension.

The single-fluid hydrodynamic description, i.e., description in which the disperse fluid is defined by the mean density, velocity, and temperature, can be used only if (i) the disperse phase distribution over the entire volume is sufficiently uniform and (ii) the physically infinitesimal hydrodynamic scales for the carrier phase $r_{fh} \sim \sqrt{\sigma d} \ll d$ and pseudo-gas of particles $r_{ph} \sim \sqrt{R_0 d} \ll d$ are sufficiently small, as compared to the characteristic size of the channel. In particular, the first condition implies that adsorption and absorption of particles on the channel walls and sedimentation of particles can be neglected. Otherwise, the particle distribution becomes nonuniform and has a maximum disperse phase density near the surface. According to the second condition, $r_{ph} \sim 10 \, \mu \text{m}$ in a microchannel with the characteristic size on the order of 100 µm and the particle size on the order of 1 µm (these are actually the Brownian particles; in Perrin's experiments, the particle size was $0.2 \div 1 \mu m$), which certainly does not satisfy the condition of existence of the hydrodynamic flow regime.⁴ Thus, in considering a disperse fluid in a microchannel, the single-fluid description is actually valid only for a granular medium with a characteristic particle size smaller than one micrometer, in which the second phase is represented by a certain gas whose contribution to the macroscopic characteristics can be neglected.⁵ The two-fluid description, in which each component is described by its own macroscopic variables (see, e.g., Soo 1990; Rudyak 2004, 2005) is impossible for the same reason.

⁴In experiments performed according to the method of Particle Image Velocimetry (PIV), the characteristic size of tracer particles is usually on the order of one micrometer. The estimates show that the single-fluid flow regime is violated in this case. For the fluctuations of the number of tracer particles N_{hp} in a physically infinitesimal hydrodynamic volume to be small, their density should satisfy the condition $1/\sqrt{N_{hp}} \sim 1/\sqrt{r_{ph}^3 n_p} \ll 1$. It can be easily seen that this condition is valid only if these particles are densely packed, which obviously contradicts the posed problem. In all other cases, the fluctuations of the number of tracer particles are so large that it is impossible to obtain reasonable data on the carrier fluid velocity field. Nanoparticles should be used as tracers in such microchannels, but it should be also done carefully (see the next section).

⁵Here, only suspensions are indicated; emulsions and gas-liquid media require a special analysis.

As was already noted, the Knudsen number for the pseudo-gas of particles in the suspension is $Kn_p \sim 1/(n_pR_0^2d)$. The Knudsen number for particles with the characteristic size on the order of 1 μ m in a channel 100 μ m in diameter is $Kn_p \sim 10^{10}/n_p$. On the other hand, the corresponding van der Waals parameter in a usually gas suspension with small volume concentrations of particles is $\varepsilon_p \sim n_pR_0^3 \sim 10^{-12}n_p \ll 1$. A comparison of these two estimates shows that $Kn_p \geq 1$, which means that the pseudo-gas consisting of particles should be described kinetically. The estimates become more rigorous as the particle size increases or the channel size decreases.

In situations when the carrier component can be described hydrodynamically and the disperse component cannot, a hybrid description should be used: the carrier component (gas or liquid) is described hydrodynamically, and the disperse component (particles) is described kinetically (Rudyak 1999). Let us consider a monodisperse two-phase medium with the carrier component being a liquid or a gas and the disperse component being solid particles. Let the carrier medium be a gas that is not strongly rarefied. Then, its dynamics is described by the following hydrodynamic equations for the density ρ_f , velocity \mathbf{u}_f , and energy E_f , which also include the forces of interaction between the phases \mathbf{F}_m , F_e :

$$\frac{\partial \rho_f}{\partial t} + \nabla \cdot \rho_f \mathbf{u}_f = 0, \quad \rho_f \frac{\partial \mathbf{u}_f}{\partial t} + \rho_f \mathbf{u}_f \cdot \nabla \mathbf{u}_f + \nabla \cdot \mathbf{J}_{2f} = \mathbf{F}_m,
\frac{\partial E_f}{\partial t} + \nabla \cdot E_f \mathbf{u}_f + \mathbf{J}_{2f} : \nabla \mathbf{u}_f + \nabla \cdot \mathbf{J}_{3f} = F_e.$$
(1.26)

The explicit form of the stress tensor, heat flux vector, and interphase interaction forces in these equations is determined by several factors. As previously, we assume that the carrier medium is a Newtonian fluid. Single-component Newtonian fluids are described by the Navier-Stokes equations, where the stress tensor and the heat flux vector are defined by linear local constitutive relations

$$\mathbf{J}_{2f} = p_f - \mu_f (\nabla \mathbf{u}_f)^s - \mu_{Vf} \nabla \cdot \mathbf{u}_f \mathbf{U}, \ \mathbf{J}_{3f} = -\lambda_f \nabla T_f.$$

In accordance with the usual phenomenological concepts, we use relations of the above-mentioned type, but involve the effective transport coefficients

$$\mathbf{J}_{2f} = p_f - \mu_{22}^{se} (\nabla \mathbf{u}_f)^s - \mu_{22}^{Ve} \nabla \cdot \mathbf{u}_f \mathbf{U}, \quad \mathbf{J}_{3f} = -\mu_{33}^e \nabla T_f, \tag{1.27a}$$

which can be chosen by using various available correlations. The thermal conductivity is related to the viscosity coefficient via the Prandtl number.

The interphase interaction forces can be presented for wide ranges of variation of the disperse fluid parameter as

$$\mathbf{F}_m = n_f K_m(\text{Re}_D, M_p)(\mathbf{u}_p - \mathbf{u}_f), \quad F_E = n_f K_E(\text{Re}_D, M_p)(T_p - T_f), \quad (1.27b)$$

where Re_D is the Reynolds number based on the disperse particle diameter D, M_p is the Mach number of particles, T_p , T_f are the temperatures of the carrier fluid and particles, n_f is the number density of the carrier phase, and \mathbf{u}_p is the macroscopic velocity of the pseudo-gas of particles. The friction coefficient K_m and heat transfer coefficient K_E are functions of the similarity parameters of the medium and can at least be determined experimentally.

Strictly speaking, the stress tensor, heat flux vector, and interphase interaction forces in Eq. (1.26) may contain some additional terms proportional to diffusion velocities and temperatures (see Rudyak 2005). They have to be taken into account when studying strongly nonhomogeneous transport processes, and this should be borne in mind in each particular case. Unfortunately, there is practically no experimental information about the coefficients at these terms.

Finally, one more comment should be made. In the general case, the stress tensor and heat flux vector include additional terms associated with allowance for dissipative fluxes of the disperse component for the carrier fluid. As a consequence, cross-coefficients of the form μ_{iifp} appear. However, it is difficult (practically impossible!) to measure these transport coefficients, though they can be calculated by constructing an appropriate solution to the Boltzmann equation (see Rudyak 2004) in the case of a rarefied carrier gas and by the molecular dynamics method for a dense gas or a liquid. Therefore, the constitutive equation (1.27a) should be considered as effective.

The disperse component dynamics is described in the general case by the kinetic equation⁶

$$\frac{\partial f_p}{\partial t} + \mathbf{V} \cdot \frac{\partial f_p}{\partial \mathbf{R}} = J_{pp}(f_p f_p) + J_{pg}(f_p f_g)$$
 (1.28a)

for the single-particle distribution function f_p . Here, J_{pp} , J_{pg} are the integrals of collisions of disperse particles with each other and with carrier medium molecules, f_g is the single-particle distribution function for gas molecules, and \mathbf{V} , \mathbf{R} are the velocity and coordinate of the center of mass of the disperse particle.

If the gas or liquid suspension is not too dense $(\varepsilon_p^{1/3} = n_p^{1/3} r_{0p} \ll 1$, where n_p is the density of the pseudo-gas consisting of disperse particles), then the integral of particle collisions J_{pp} can be modeled by the Boltzmann collision integral. For

⁶Strictly speaking, the disperse component is described by the kinetic equation for the single-particle distribution function only if the particles are not too coarse and the gas suspension is not too dense. Actually, such sufficiently rarefied gas suspensions are of interest for practice. Otherwise, the evolution of the disperse component is described by a system of kinetic equations, which, in addition to the equation for the single-particle distribution function, include equations for multiparticle distribution functions, in particular, the paired distribution function.

practical purposes, this integral can often be modeled by the relaxation collision integral

$$J_{pp}(f_p f_p) = -(f_p - f_{p0})\tau_p^{-1},$$

where f_{p0} is the local Maxwell function of the pseudo-gas of disperse particles and τ_p is their free flight time. If the disperse phase density is sufficiently high, the Enskog collision integral or other model collision integrals can be used as J_{pp} .

The pseudo-gas of particles behaves similarly to a non-ideal gas at sufficiently high densities, when the corresponding van der Waals parameter is $\varepsilon_p = n_p R_0^3 \ge 10^{-3}$. If $10^{-8} \ll \varepsilon_p < 10^{-3}$, the collision integral has the Boltzmann form. If the van der Waals parameter has even smaller values, particle collisions can be neglected, and the kinetic equation for the pseudo-gas becomes significantly simplified:

$$\frac{\partial f_p}{\partial t} + \mathbf{V} \cdot \frac{\partial f_p}{\partial \mathbf{R}} = J_{pg}(f_p f_g). \tag{1.28b}$$

In the collision of a molecule with a disperse particle, the velocity of the latter changes only slightly. By virtue of the adiabaticity of the change in the function f_p in the momentum space, the collision integral J_{pg} can be presented as the linear Fokker-Planck collision integral

$$J_{pg} = J_{FP} = K \frac{\partial}{\partial \mathbf{V}} \cdot \left(\mathbf{V} f_p + \frac{kT}{2M} \frac{\partial f_p}{\partial \mathbf{V}} \right), \tag{1.28c}$$

where K is a certain friction coefficient. If the drag force acting from the carrier fluid on the particle is defined by Eq. (1.27b), then $K = K_m$. Thus, the kinetic equation for the disperse component has the form

$$\frac{\partial f_p}{\partial t} + \mathbf{V} \cdot \frac{\partial f_p}{\partial \mathbf{R}} = J_{pp}(f_p f_p) + J_{FP}(f_p f_g). \tag{1.29}$$

System (1.26), (1.28a) of the hybrid kinetic-hydrodynamic description of disperse fluids was formulated phenomenologically. For rarefied fine disperse gas suspensions, it was formulated rigorously (Rudyak 2004), based on the system of kinetic equations that describe the evolution of the carrier and disperse components.

Formulating a boundary-value problem for the system of kinetic-hydrodynamic equations is a nontrivial task, because it is necessary to impose the boundary conditions on the solid surfaces for the hydrodynamic variables of the carrier gas, for the disperse particles, and for the distribution function of the latter. Concerning the boundary conditions for the hydrodynamic parameters of the carrier medium,

they are fairly obvious. They should be the no-slip condition or the velocity slip and temperature jump conditions (1.5).

Particles in medium and coarse disperse gas and liquid suspensions have sufficiently large sizes; therefore, their thermal velocities are very (or even negligibly) small: for particles of 10^{-7} m, the thermal velocity at room temperature is approximately $10^{-2} \div 10^{-1}$ m/s, which is smaller than the corresponding velocity of the carrier gas molecules by four or five orders of magnitude. As a result, the mechanisms of interaction of disperse particles and molecules with the wall are essentially different. At subsonic velocities, the velocity of the particles themselves is defined by the flow velocity. Interaction of disperse particles with the surface is determined by the laws of slipping and rolling along the solid wall, rather than by the law of particle scattering by the surface. The losses of energy and momentum on the surface depend on the corresponding slipping and rolling friction coefficients. The laws of such friction have not been adequately studied. Moreover, the process of particle motion along the surface is usually not continuous. Nevertheless, if particle slipping on the surface is assumed to follow the dry friction law, ${}^8F_f = k_f N$, then there is a certain region of particle velocity relaxation whose characteristic length in the simplest approximation is on the order of $x_r \sim M v_p^2(0)/k_f N(k_f)$ is the slipping friction coefficient, which can depend on velocity in the general case, and N is the force of the normal pressure of the particle onto the surface). The same effect is obtained by taking into account deceleration of disperse particles by the fluid. In this case, however, the relaxation region length is proportional to the particle velocity, and the boundary condition on the wall has the form (Soo 1990)

$$u_p^x(y=0) = U_p - cx,$$
 (1.30)

where c is the drag coefficient.

Particles become accumulated behind the relaxation region. As a result, the particle concentration near the solid surface appreciably increases, and a "boundary layer" consisting of disperse particles is formed. For this reason, a two-layer description (inside and outside the boundary layer) was proposed (Gorbachev 1981, 1982). In this case, however, the results can apparently depend both on the flow geometry and on the flow parameters. Nevertheless, the use of the no-slip condition in this region seems to be fairly reasonable in practical problems.

If the flow velocity has a non-zero component normal to the solid surface or the small (but not zero) thermal velocity of the particle is taken into account, an ensemble of reflected particles appears in the flow field. As the velocities of such

⁷It should be noted, however, that these velocities can be comparable to or even greater than the gas suspension flow velocity in a microchannel.

⁸For simplicity, a flat surface is considered here; otherwise, the friction force also depends on the particle velocity. However, the considered approximation is usually sufficient because the particle size is usually negligibly small as compared to surface curvature.

reflected particles themselves can noticeably differ⁹ from the velocities of particles in the bulk, the initially two-phase medium effectively transforms into a three-phase medium. An example of a description of such a medium can be found in the monograph (Nigmatulin 1987).

Formulation of boundary conditions for distribution functions satisfying kinetic equations has been well studied (see the monographs Cercignani 1975; Goodman and Wachman 1976). An additional difficulty in the considered problem is the possibility of particle slipping along the surface in addition to conventional scattering, and the dynamics of such slipping motion has not been studied. There is little information about the laws of interaction of disperse particles with surfaces of different physical nature, though the interest in this problem has been increasing over the last two decades, owing to several important applications: gas-dynamic spraying, interaction of spacecraft with their own atmosphere and microparticles of space origin, interaction of gas-powder jets with the rocket engine nozzle, and some others. Thus, before giving recipes for formulating boundary conditions for the distribution function of disperse particles, we have to consider how this problem was solved in the kinetic theory of rarefied gases. This is useful because the thus-obtained relations can at least be used for formulating boundary conditions for ultrafine gas suspensions.

As the kinetic equation for particles includes the derivative with respect to the coordinate, an appropriate boundary condition for the distribution function on the wetted surfaces S bounding the flow field should be imposed. In other words, the distribution function for molecules flying from the boundary toward the flow should be prescribed on these surfaces at each time instant. As the number of molecules incident onto the surface depends linearly on the distribution function of particles in the volume $f^-(\mathbf{v}) \cdot (\mathbf{n} \cdot \mathbf{v} < 0)$, the distribution function of molecules reflected from the surface $f^+(\mathbf{v}') \cdot (\mathbf{n} \cdot \mathbf{v}' > 0)$ is a certain linear functional of this function:

$$f^{+}(\mathbf{v}') = \mathsf{K}[f^{-}(\mathbf{v})] \text{ on } S \tag{1.31}$$

(**n** is the internal normal to the surface).

We can easily see that the functional K is an integral operator. Indeed, the number of molecules leaving from the surface element dS within a unit time with velocities in the interval $[\mathbf{v}, \mathbf{v} + d\mathbf{v}]$ near the point \mathbf{r} at $\mathbf{n} \cdot \mathbf{v}' > 0$ is $f^+(\mathbf{r}, \mathbf{v})(\mathbf{n} \cdot \mathbf{v})dSd\mathbf{v} > 0$. The number of molecules incident onto the same surface element within a unit time with velocities in the interval $[\mathbf{v}', \mathbf{v}' + d\mathbf{v}']$ is determined by a similar relation $-f^-(\mathbf{r}, \mathbf{v}')(\mathbf{n} \cdot \mathbf{v}')dSd\mathbf{v}' > 0$ at $\mathbf{n} \cdot \mathbf{v}' \leq 0$. We assume that all of these molecules become reflected from the surface, but the molecule moving with a velocity \mathbf{v}' in the interval $d\mathbf{v}'$ is reflected from the surface with a probability $\mathbf{R}(\mathbf{v}', \mathbf{v})$ with a velocity \mathbf{v} in the interval $d\mathbf{v}$. To obtain all molecules reflected within the considered velocity interval, the last relation should be integrated over all possible

⁹This depends on the surface properties, particle material, energy of interaction, and scattering laws.

velocities of incident molecules. As a result, the total number of reflected molecules is determined by the formula

$$f^{+}(\mathbf{r}, \mathbf{v})(\mathbf{n} \cdot \mathbf{v})dSd\mathbf{v} = -dSd\mathbf{v} \int_{\mathbf{n} \cdot \mathbf{v}' < 0} d\mathbf{v}'(\mathbf{n} \cdot \mathbf{v}')f(\mathbf{r}, \mathbf{v}')\mathsf{R}(\mathbf{v}', \mathbf{v})$$

or

$$f^{+}(\mathbf{r}, \mathbf{v}) = -\int_{\mathbf{r}, \mathbf{v}' \in \Omega} d\mathbf{v}' \frac{(\mathbf{n} \cdot \mathbf{v}')}{(\mathbf{n} \cdot \mathbf{v})} \mathsf{R}(\mathbf{v}', \mathbf{v}) f^{-}(\mathbf{r}, \mathbf{v}') \text{ Ha } S.$$
 (1.32a)

In deriving the last expression, it was assumed that molecule reflection from the surface occurs instantaneously. However, this is not so in the general case. Molecules can be adsorbed on the surface. Formally, this fact can be easily taken into account. If the time of adsorption of a molecule incident onto the surface with a velocity \mathbf{v}' is τ_a , then the distribution function of reflected molecules is

$$f^{+}(\mathbf{r}, \mathbf{v}, t) = -\int_{0}^{\tau} d\tau_{a} \int_{\mathbf{n} \cdot \mathbf{v}' < 0} d\mathbf{v}' \frac{(\mathbf{n} \cdot \mathbf{v}')}{(\mathbf{n} \cdot \mathbf{v})} \mathsf{R}(\mathbf{v}', \mathbf{v}, t, \tau_{a}) f^{-}(\mathbf{r}, \mathbf{v}', t - \tau_{a}). \quad (1.32b)$$

The number of molecules colliding in a unit time with the considered surface element is $n_g |\mathbf{n} \cdot \mathbf{v}| dS$. If $\bar{\tau}_a$ is the mean time of molecule adsorption, then the surface portion dS equal to $n_g |\mathbf{n} \cdot \mathbf{v}| \pi r_0^2 \bar{\tau}_a$ is occupied by adsorbed molecules. If all molecules incident onto the surface become reflected, we have

$$\int_{\mathbf{n},\mathbf{v}>0} d\mathbf{v}(\mathbf{n}\cdot\mathbf{v})f^{+}(\mathbf{r},\mathbf{v}) = -\int_{\mathbf{n},\mathbf{v}'<0} d\mathbf{v}'(\mathbf{n}\cdot\mathbf{v}')f^{-}(\mathbf{r},\mathbf{v}')$$

Therefore, the obvious condition of normalization of the scattering kernel is

$$\int_{\mathbf{n},\mathbf{v}'<0} d\mathbf{v} \mathsf{R}(\mathbf{v}',\mathbf{v}) = 1.$$

This relation is violated if some molecules incident onto the surface do not return to the volume.

In the general case, the scattering kernels R depend on the physical and chemical properties of the surface and on the energy, properties, and density of incident molecules. In principle, scattering kernels can be studied experimentally, but the number of parameters exerting a significant (often determining) effect on the final result is so large that there have yet been few successful investigations. Obviously, experiments should be combined with numerical simulations.

Certainly, one may try to calculate transport kernels. The formulation of the corresponding mathematical problem can be found in the monograph (Cercignani

1975). The difficulties of solving such a problem are clearly visible, and mathematical modeling is still the most universal method of solving practical problems despite significant success in understanding the phenomenon. Various issues of simulations were considered by many researchers. Below, we consider only two simple and popular models, which were formulated back in the 19th century.

Let the surface be absolutely elastic and smooth and let the molecule be modeled by an elastic hard sphere. When such a model collides with the surface, its tangential velocity \mathbf{v}_{τ}' (along the surface) remains unchanged, whereas the velocity directed normal to the surface \mathbf{v}_n' , changes into the opposite: $\mathbf{v}_{\tau}' = \mathbf{v}_{\tau}, \mathbf{v}_n' = -\mathbf{v}_n$ (the prime here denotes the velocities of the molecule incident onto the surface). This type of collision is called specular reflection, and the corresponding scattering kernel has the form

$$R(\mathbf{v}', \mathbf{v}) = \delta(\mathbf{v}' - \mathbf{v} + 2\mathbf{n}(\mathbf{n} \cdot \mathbf{v})). \tag{1.33}$$

As was mentioned above, another popular model is diffuse reflection, which implies that molecules are thermalized by the surface and leave the latter with the Maxwell distribution of velocities and with a temperature equal to the surface temperature. The corresponding scattering kernel is written as

$$\mathsf{R}_{d}(\mathbf{v}',\mathbf{v}) = \frac{1}{2\pi} \left(\frac{m}{kT_{\mathrm{w}}} \right)^{2} (\mathbf{n} \cdot \mathbf{v}) \, \exp\left(-\frac{m\mathsf{v}_{2}}{2kT_{\mathrm{w}}} \right). \tag{1.34}$$

In practice, a combination of the scattering kernels (1.33) and (1.34) is usually used:

$$\mathsf{R}(\mathbf{v}',\mathbf{v}) = (1 - \alpha_{\tau})\delta(\mathbf{v}' - \mathbf{v} + 2\mathbf{n}(\mathbf{n} \cdot \mathbf{v})) - \alpha_{\tau}\mathsf{R}_{d}(\mathbf{v}',\mathbf{v}), \tag{1.35}$$

where the tangential momentum accommodation coefficient α_{τ} is introduced.

The use of kinetic equations for the description of the disperse component dynamics is not only necessary for studying coarse disperse gas suspensions and liquid suspensions. The kinetic description of the disperse component evolution is required in all cases when the Knudsen number of the pseudo-gas of particles is not too small: $Kn_p > 10^{-2}$. For this reason, in discussing the boundary conditions in this section, we consider not only coarse disperse, but also fine disperse and ultrafine disperse gas and liquid suspensions.

For ultrafine and fine disperse particles, it is possible to use the method of boundary condition formulation developed in the kinetic theory of rarefied gases. In this case, it is also possible to use the specular-diffuse reflection law (1.35). It should be noted, however, that this model is rather rough and contradictory in some aspects. For instance, the accommodation coefficients depend, in the general case, on the distribution function of incident particles, material surface, and its temperature. One of the first models to take into account the dependence of the coefficient α_{τ} on velocity was proposed in Epstein (1967). It was assumed there that $[1 - \alpha_{\tau}(\mathbf{v}')]$ particles are reflected in a specula manner, and $\alpha_{\tau}(\mathbf{v}')$ particles are reflected diffusely, independent of \mathbf{v}' :

$$R(\mathbf{v}', \mathbf{v}) = [1 - \alpha_{\tau}(\mathbf{v}')]\delta(\mathbf{v}' - \mathbf{v} + 2\mathbf{n}(\mathbf{n} \cdot \mathbf{v})) - \alpha_{\tau}(\mathbf{v}')R_d(\mathbf{v}). \tag{1.36}$$

If the energies of particles incident onto the surface are sufficiently large, then the distribution of reflected particles has peaks at certain reflection angles. In this case, the scattering kernel can be simulated by a set of δ -functions with several values of the mean velocity \mathbf{v}_i of reflected particles:

$$R(\mathbf{v}', \mathbf{v}) = \sum_{i} \delta[\mathbf{v} - \mathbf{v}_{i}(\mathbf{v}')]. \tag{1.37}$$

More complicated models were also used (see, e.g., Cercignani 1983).

An important specific feature of interaction of disperse particles with the solid surface is its inelastic character caused by several factors: transfer of some part of energy and momentum to the crystal lattice of the surface, adsorption, presence of inhomogeneities on the surface, etc. Inhomogeneities on a treated surface, often called surface roughness, have the characteristic size from 10^{-8} to 10^{-4} m, which is comparable with the particle size. These inhomogeneities are randomly distributed; therefore, particle scattering laws depend on statistical properties of the surface. It is usually assumed that reflection from a surface element follows either a specular or a diffuse reflection model.

As was already noted, sufficiently coarse particles have small thermal velocities. When such particles interact with the surface, the probability of their sticking to the wall is fairly high. To characterize the particle impact onto the surface, we have to classify possible situations arising here.

- 1. Impact onto a smooth surface. In the case of particle incidence onto a smooth surface, the tangential component of the particle velocity remains unchanged, whereas the normal component is determined by the initial velocity \mathbf{v}_{n0} and surface properties: $\mathbf{v}_{\tau} = \mathbf{v}'_{\tau}$, $\mathbf{v}_n = f(\mathbf{v}'_{n0}, S)$. To describe the possibility of an inelastic impact, the recovery coefficient is introduced: $k_n = \mathbf{v}_n/\mathbf{v}'_n$. Thus, $k_n = 1$ for an absolutely elastic impact and $k_n = 0$ for an absolutely inelastic impact. If $0 < k_n < 1$, then the impact is not completely elastic. As $\mathbf{v}'_{\tau} = \mathbf{v}' \sin \alpha$, $\mathbf{v}_{\tau} = \mathbf{v} \sin \beta$, $\mathbf{v}'_n = \mathbf{v}' \cos \alpha$, and $\mathbf{v}_n = \mathbf{v} \cos \beta$, the recovery coefficient is equal to the ratio of the incidence angle tangent to the reflection angle tangent: $k_n = tg\alpha/tg\beta$.
- 2. Impact onto a rough surface. In an impact onto a rough surface, both the normal and tangential velocity components can change in the general case: $\mathbf{v}_{\tau} = k_{\tau} \mathbf{v}'_{\tau}$ and $\mathbf{v}_n = k_n \mathbf{v}'_n$; here, the recovery coefficient for the tangential velocity component is introduced: $k_{\tau} = \mathbf{v}'_{\tau}/\mathbf{v}_{\tau}$. Thus, $k_{\tau} = -1$ for an absolutely elastic rough surface and $k_{\tau} = 0$ for an absolutely inelastic rough surface.

The change in the particle momentum components $\mathbf{p} = \{p_n, p_\tau\}$ after its collision with the surface and the kinetic energy defect $\Delta E_k = E_k - E_k'$ are determined

by the relations $p_n = k_n p'_n$, $p_{\tau} = (k_{\tau} + 1)p'_{\tau}$, and $\Delta E_k = (1/2M)[p'^2_n(k_n^2 - 1) + p'^2_{\tau}k_{\tau}^2]$.

Thus, the simplest and most reasonable way (because of the lack of experimental information) to choose the scattering kernel of disperse particles by an arbitrary solid surface is to use the δ -shaped kernel

$$\mathsf{R}(\mathbf{v}',\mathbf{v}) = \delta[\mathbf{v}' - \mathbf{v} + (k_n + 1)\mathbf{n}(\mathbf{n} \cdot \mathbf{v}) + (k_\tau - 1)\tau(\tau \cdot \mathbf{v})].$$

The vector τ is directed along the surface and coincides with the direction of the corresponding component of the particle velocity \mathbf{v}' .

1.6 Modeling of Nanofluid Microflows

1.6.1 Methods of Modeling of Nanofluid Flows

Nanofluids¹⁰ are two-phase systems consisting of a carrier medium (liquid or gas) and nanoparticles. Nanoparticles are particles with characteristic sizes ranging from 1 to 100 nm, and they can be solid, liquid, or gaseous in the general case. Typical carrier liquids are water, organic liquids (ethylene glycol, oil, or biological fluids), and polymer solutions. Particles of chemically stable metals and their oxides are usually used as solid nanoparticles. Fullerene, whose diameter is about 1 nm, can be considered as the smallest nanoparticle. Viruses occupy an intermediate position (their size is around tens of nanometers). On the other hand, nanofluids based on carbon nanotubes have been intensely investigated. Such fluids differ considerably from the usual nanofluids and resemble various structured fluids (polymers, liquid crystals, etc.).

Studies of physical features of nanofluids and their transport properties were begun comparatively recently. They were initiated by using nano-disperse systems in various applications. The small size of nanoparticles is responsible for their specific properties. Nanofluids are characterized by particular transport properties, while nanoparticles experience practically no sedimentation in contrast to coarse particles, and they do not induce erosion in channels where they move. For these and some other reasons, nanofluids are already used or will be soon used in the following fields:

¹⁰The term "nanofluid" was first introduced by Choi (1995), who meant a suspension consisting of a carrier liquid and solid nanoparticles. It seems reasonable to extend this term to gas suspensions of nanoparticles for several reasons. First, gas suspensions of nanoparticles have many applications in practice, similar to liquid suspensions of nanoparticles. Second, many properties of nanofluids and nanosuspensions are very close to each other, especially if the carrier gas is sufficiently dense. Finally, the same methods or models can be used for modeling transport processes in gas and liquid suspensions of nanoparticles. For example, implementation of the molecular dynamics method is absolutely identical in both cases.

- Chemical processes including catalysis;
- Cooling of various devices;
- Creation of new systems for transportation and production of thermal energy;
- Biotechnologies, MEMS technologies, and nanotechnologies;
- Creation of new medicines and cosmetic formulations;
- Delivery of drugs, nanosensors, and nanoactuators;
- Creation of detection and recognition systems for various contaminants;
- Creation of air and water cleaning systems;
- Creation of new lubricants:
- Creation of new varnishes and paints.

This list can be expanded, but the key role in all of these processes belongs to the specific character of nanofluids and their transportation properties.

Of significant interest are magnetic nanofluids, which allow for controlling the behavior of carrier fluid. Magnetic nanoparticles are single-domain magnets. If a magnetic field is applied, such particles in the fluid are arranged in the field direction, and the fluid becomes magnetized. Strong magnetic fields can even induce macroscopic motion of the fluid. Magnetic nanofluids confined by a magnetic field are used as sealing materials in vacuum devices. These fluids are widely used for targeted drug delivery to damaged organs. They are already used for cancer treatment through the method of hyperthermia: reaching the tumor, magnetic nanoparticles kill cancerous cells by means of local heating of the damaged region in an alternating magnetic field. X-ray contrasting nanofluids based on yttrium tantalate allow for obtaining images of internal organs.

In addition to the applied aspect, investigations of transport processes in nanofluids have an important fundamental component, because there is no adequate qualitative understanding of their nature yet, leaving aside a comprehensive physical theory. At the same time, systematic applications of nanofluids will become possible only if their properties can be predicted in advance, which requires understanding of transport mechanisms in nanofluids. Despite a large amount of experimental and theoretical knowledge, there are still no systematic data, and experimental results are often contradictory. This is largely caused by objective factors that make experiments difficult. In particular, it is not easy to control the size and uniformity of the nanoparticle distribution; moreover, addition of nanoparticles can alter fluid rheology. 11 It is often impossible to determine how the transport properties will be changed owing to variations of certain parameters of the system: nanoparticle material, shape, size, volume concentration, etc. There is no physical understanding of the observed effects either. Thus, it is necessary, on the one hand, to develop an ab initio theory of transport processes by using, in particular, the kinetic theory and, on the other hand, to apply the molecular dynamics method, which has a predictive capability of an experiment and allows an "ideal" experiment to be performed.

¹¹This statement can be made even more severe: beginning from certain particle concentrations, all nanofluids composed on the basis of conventional Newtonian fluids become non-Newtonian.

Generally speaking, nanofluids (like disperse fluids, see Sect. 1.1) should be classified in terms of several attributes. The first one is the aggregate state. Here, we can distinguish gas nanosuspensions (gas+solid nanoparticles), nanosols (gas+liqnanosuspensions nanoparticles). liauid (liquid+solid nanoemulsions (liquid+liquid nanoparticles), and liquids with nanobubbles. The second attribute is the volume concentration of nanoparticles ϕ . Nanofluids can be classified as rarefied ($\phi \le 10^{-3}$), moderately dense $(10^{-3} \le \phi \le 10^{-1})$, and dense $(10^{-1} < \phi \le 4 \times 10^{-1})$. If the volume concentrations are even higher, we deal with nanopowders. Finally, as the nanoparticle sizes can vary by two orders of magnitude, nanofluids can also be classified in terms of the relationship of internal structural elements of the medium: nanoparticle and molecule sizes and mean free paths of fluid molecules and nanoparticles. This is particularly important for gas nano-suspensions, in which the degree of rarefaction of the carrier medium can vary noticeably. As a result, the mean free path of the carrier gas molecules l can be either greater or smaller than the particle radius R_0 . It was demonstrated (Rudyak 1992; Gladkov and Rudyak 1994a, b) that the dynamics of gas nano-suspensions with a sufficiently rarefied carrier gas is described by a system of the Boltzmann equations for the single-particle distribution functions of the carrier gas f_{1g} and pseudo-gas of nanoparticles f_{1n}

$$\frac{\partial f_{1g}}{\partial t} + \mathbf{v} \cdot \frac{\partial f_{1g}}{\partial \mathbf{r}} = J_B^{gg} + J_B^{gp}, \quad \frac{\partial f_{1p}}{\partial t} + \mathbf{V} \cdot \frac{\partial f_{1p}}{\partial \mathbf{R}} = J_B^{pg}, \quad (1.38)$$

where the collision integrals marked by the subscript "B" are the usual Boltzmann collision integrals, J_B^{gg} is the collision integral of carrier gas molecules, and J_B^{gg} and J_B^{pg} are the collision integrals of molecules with nanoparticles. If the carrier gas is sufficiently dense, the collision integrals in the kinetic equations contain additional terms whose structure was described in Gladkov and Rudyak (1994a, b).

The kinetic theory of nanofluids can be developed only if the carrier medium is a rarefied gas. Naturally, it cannot be constructed for liquid suspensions of nanoparticles. It may seem that nanofluids, in this case, could be treated with the usual methods of mechanics of continuous media. Indeed, a nanoparticle in the carrier fluid metric is a material point. Therefore, macroscopic flows of nanofluids and their microflows in channels with characteristic sizes of several micrometers can be modeled by using the conventional transport equations (1.3). However, there are several factors that should be taken into account.

First, in solving problems of isothermal nanofluid flows, it is almost always possible to use conventional single-fluid hydrodynamic equations with effective transport coefficients. At the same time, such problem formulation in a case with temperature gradients can lead to significant errors. The point is that, considering a nanofluid as a single homogeneous continuum, we imply that thermal diffusion of all its elements is identical. However, this is not so in the general case. It is impossible to introduce an effective coefficient of thermal diffusion of a nanofluid. Thermal diffusion of nanoparticles (see below) is essentially different from thermal diffusion of carrier fluid molecules. In the presence of temperature fields, the

nanoparticle distribution will be non-uniform. Thus, it is necessary to use a two-fluid description of the nanofluid flow, in which the carrier fluid and pseudo-gas of nanoparticles are described by a system of coupled hydrodynamic equations.

Second, at small concentrations of nanoparticles, the majority of nanofluids are conventional Newtonian fluids if the carrier fluid is a Newtonian fluid. In this case, the transport laws are described by the usual relations (1.4), for which effective transport coefficients are used.

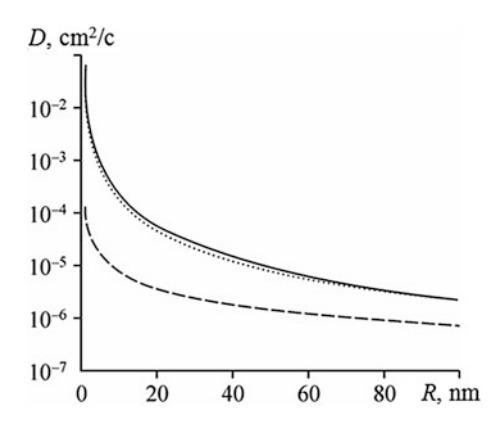
Third, even if the carrier medium is a Newtonian fluid, the nanofluid transforms into a non-Newtonian fluid beginning from a certain volume concentration of nanoparticles. The transition to the non-Newtonian rheology depends on the nanoparticle material and size. Changes in the rheological properties of nanofluids with increasing nanoparticle concentration have not been adequately studied yet; for this reason, no general recommendations can be formulated.

1.6.2 Diffusion of Nanoparticles in Gases and Liquids

Transport processes play a key role in the description of nanofluid flows. The development of a consistent theory of transport processes in nanofluids is complicated by many factors (both subjective and objective). Objectively, the theoretical description of transport processes, even in ordinary homogeneous fluids, is not yet sufficiently adequate. Therefore, there is little hope for constructing a theory of transport processes in nanofluids, which are significantly more complicated systems. The lack of experimental data can also be considered an objective factor, because investigations of nanofluids have only started comparatively recently. On the other hand, it has been commonly assumed for a long time that nanofluids are not principally different from the usual disperse fluids (with macroscopic particles). It is only now that researchers have gained the understanding that the situation in nanofluids is much more complicated. In the general case, nanofluids differ both from ordinary disperse fluids and from molecular solutions.

Probably, the only example of a consistent theory of transport processes in the present field is rarefied gas nano-suspensions. A kinetic theory was developed that made it possible to construct a regular theory of transport processes, which was then verified experimentally. In particular, diffusion of nanoparticles in gases at standard pressure (Rudyak 2004; Rudyak and Krasnolutskii 2001, 2002, 2003a; Rudyak et al. 2008a), thermal diffusion (Rudyak and Krasnolutskii 2010), and viscosity of gas nano-suspensions (Rudyak and Krasnolutskii 2003b, 2004) were studied. In all cases, it turned out that nanoparticle transport processes are essentially different from transport processes of ordinary disperse particles in gases, including Brownian particles, which are sufficiently small, but still macroscopic from the viewpoint of continuous media. The diffusion coefficient of Brownian particles of radius R ($R \gg l_f$) is determined by the Einstein formula (Einstein 1906)

Fig. 1.1 Diffusion coefficient (cm²/s) of Zn particles in Ne versus the nanoparticle radius (nm)



$$D_E = kT/(6\pi\mu R),\tag{1.39}$$

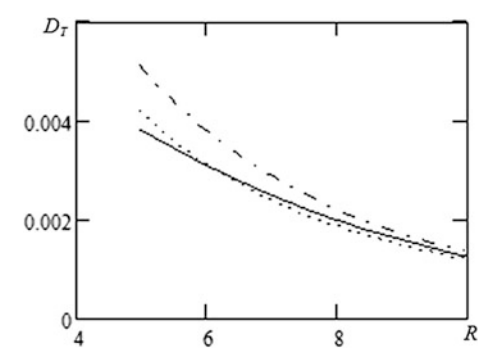
therefore, $D_E \sim R^{-1}$. The following estimate was obtained for nanoparticles (Rudyak and Krasnolutskii 2002; Rudyak 2004):

$$D \sim \frac{1}{R^2} \left(1 + \frac{a_1}{\sqrt{R}} + \frac{a_2}{R} \right) \tag{1.40}$$

Formulas (1.39) and (1.40) yield one asymptotic curve for sufficiently large particles, but the results are significantly different for small particles. The dependence of the diffusion coefficient on the particle radius at a fixed temperature (T =288 K) is illustrated in Fig. 1.1, which shows the diffusion coefficient of zinc particles in neon as a function of the particle radius at a fixed temperature T =300 K and atmospheric pressure as an example. The diffusion coefficient predicted by the kinetic theory is shown by the solid curve; the dashed curve is the dependence determined by the Einstein formula (1.39).The Cunningham-Millikan-Davies (CMD) correlation (Friedlander 2000) is plotted by the dotted curve. The last curve largely agrees with our data in the major part of the considered domain. In the range of small particle sizes (smaller than 10 nm), however, there is a significant difference between the CMD correlation and the kinetic theory. Moreover, diffusion of Brownian particles is determined only by the particle size and is independent of the particle material. At the same time, diffusion of sufficiently small nanoparticles depends on their material to a large extent (Rudyak et al. 2008a).

One of the most interesting and fine transport processes is thermal diffusion. Thermal diffusion of nanoparticles is often confused with thermophoresis typical for aerosol particles (see, e.g., the review Mädler and Friedlender 2007). However, there is a certain misunderstanding here. Strictly speaking, thermophoresis is the motion arising as a result of a non-uniformly heated particle surface. However, the nanoparticle size for a not-too-rarefied gas is on the order of the physically infinitesimal hydrodynamic scale, i.e., the nanoparticle in the carrier gas metric is a

Fig. 1.2 Thermal diffusion coefficient D_T (cm²/s) of Zn, Li, and U nanoparticles in Ne versus the nanoparticle radius R (nm)



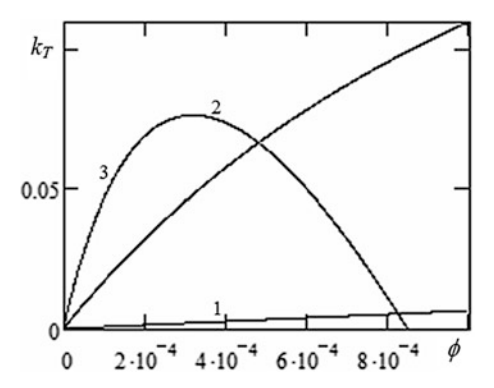
material point, so it makes no sense to talk about its non-uniform heating (even if it is non-uniformly heated!). For the same reason, this non-uniformity cannot arise at physically reasonable temperature gradients. Thus, the motion of nanoparticles in a non-uniform temperature field is nothing other than thermal diffusion.

Thermal diffusion of nanoparticles was studied on the basis of the kinetic theory in Rudyak and Krasnolutskii (2010). It was demonstrated, in particular, that thermal diffusion of nanoparticles, like their conventional diffusion, depends on the nanoparticle material. As an example, Fig. 1.2 shows the thermal diffusion coefficient D_T of Zn, Li, and U nanoparticles in Ne (dot-and-dashed, dotted, and solid curves, respectively). The volume concentration of nanoparticles is $\phi = 10^{-3}$, and the carrier gas temperature is T = 300 K. The values of the thermal diffusion coefficient are noticeably different for sufficiently small nanoparticles. However, they become almost material-independent for nanoparticles greater than 10 nm.

Another specific feature of thermal diffusion of nanoparticles (in contrast to thermal diffusion of molecules) is the absence of temperature inversion of the thermal diffusion factor. At low temperatures, it is monotonic and positive in all cases. Beginning from room temperature, the temperature dependence of the thermal diffusion factor becomes rather complicated and exhibits individual features for small nanoparticles. These differences become less noticeable as the particle size increases and are practically invisible for nanoparticles greater than 10 nm. Moreover, the absolute values of the thermal diffusion factor of nanoparticles are higher by more than an order of magnitude than the corresponding values for molecular systems. The thermal diffusion ratio for gas nano-suspensions at fixed volume concentrations of nanoparticles and pressure increases almost linearly with increasing temperature. This means that $D_T \sim DT$.

Finally, the dependence of the thermal diffusion characteristics on the volume concentration of nanoparticles should be noted. The thermal diffusion ratio k_T gives the quantitative characteristic of the ratio of the flux induced by thermal diffusion to the flux induced by diffusion at identical relative gradients of concentration and temperature. Therefore, an increase in this ratio with increasing nanoparticle concentration is a very important characteristic of nanoparticle diffusion and thermal diffusion. Figure 1.3 shows a typical dependence of the thermal diffusion ratio on

Fig. 1.3 Thermal diffusion ratio versus the volume concentration of the heavy component



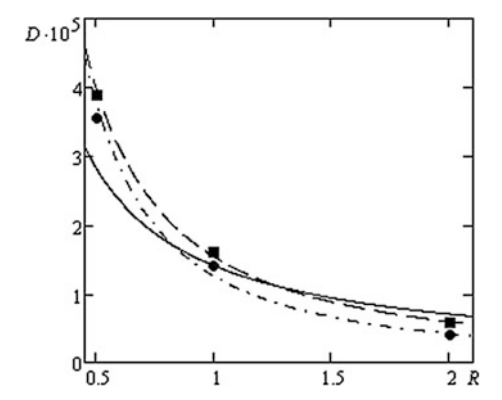
the concentration of nanoparticles (or heavy component molecules) ϕ at a fixed temperature $T=300~\rm K$ for suspensions of uranium nanoparticles in neon, $R=20~\rm nm$ (curve 1) and $R=1~\rm nm$ (curve 2) and for a mixture of Xe and Ne gases (curve 3). In the above-indicated range of concentrations, the thermal diffusion ratio monotonically increases (for large nanoparticles, almost linearly). As the particle size and mass increase, the relative influence of the thermal diffusion process becomes less pronounced. The values of the thermal diffusion factor for gas suspensions of nanoparticles can be higher, even significantly higher (small nanoparticles), and lower (large nanoparticles) than those of gas mixtures.

Diffusion of nanoparticles in liquids has not been adequately studied experimentally, partly because it is a popular opinion that it is described by the Einstein-Stokes law (1.39). Nevertheless, scarce experimental data testify that this law is invalid for nanoparticles (Evans et al. 1981; Haselmeyer et al. 1994; Kato et al. 1993; Wuelfing et al. 1999; Kowert et al. 2004). The reason for this discrepancy is often attributed to the necessity of using slip boundary conditions for the description of the force acting on the particle (Evans et al. 1981; Wuelfing et al. 1999). Certainly, this is a misunderstanding. The motion of nanoparticles in a fluid cannot be described hydrodynamically at all, because they are material points in the carrier fluid (continuous medium) metric. Is it possible to impose the slip condition on a material point? For this reason, there is no clear concept of the force acting on a nanoparticle. Therefore, many researchers (Evans et al. 1981; Nuevo et al. 1997) have proposed describing experimental data by a correlation of the form $D = A/\eta^p$, where the parameter A and p have to be chosen for a particular particle radius and medium temperature.

Attempts were made to verify the adequacy of the Einstein-Stokes law (1.39) by the molecular dynamics method (Nuevo et al. 1997; Ould-Caddour and Levesque 2000). The main conclusion that can be drawn is that this law does not describe nanoparticle diffusion in the general case. Simultaneously, a systematic study of diffusion of small nanoparticles 1–2 nm in diameter was performed (Rudyak et al. 2000). Nanoparticles and molecules were simulated by a system of solid spheres with different diameters. The carrier medium density was described by the

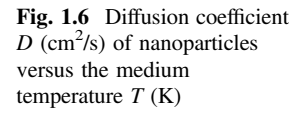
Fig. 1.4 Diffusion coefficient of nanoparticles versus the density. The solid curve is obtained in molecular dynamics simulations, and the dashed curve is predicted by the Einstein law (1.39)

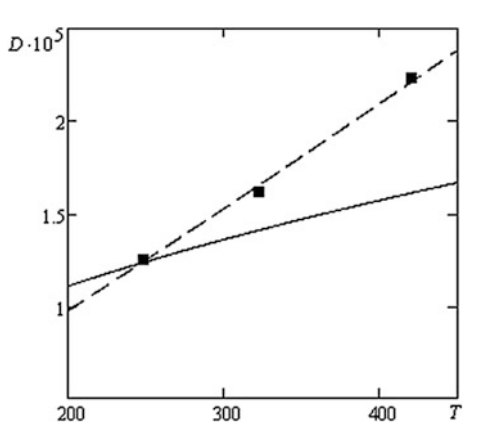
Fig. 1.5 Diffusion coefficient D (cm²/s) versus the radius R (nm). The dashed curve and squares show the results for Li nanoparticles, the dot-and-dashed curve shows the results for Al nanoparticles, and the solid curve is predicted by the Einstein formula



parameter $\alpha = (V - V_p)/V_0$ (V is the cell volume, $V_0 = Nr^3/8\sqrt{2}$ is the volume of a dense packing of molecules of radius r, and $V_p = 4\pi R^3/3$ is the nanoparticle volume), which varied from 2 to 75. The data obtained are plotted in Fig. 1.4. The dependence of the diffusion coefficient of nanoparticles on density is drastically different from the behavior predicted by Eq. (1.39).

As was already noted, diffusion of sufficiently small nanoparticles depends substantially on their material (Rudyak et al. 2008b). Figure 1.5 shows the diffusion coefficients of lithium and aluminum nanoparticles 1–4 nm in diameter in argon at a temperature of 322.5 K and argon density $\varepsilon_V = 0.707$ (Rudyak et al. 2011). The difference with Eq. (1.39) for small nanoparticles reaches 50%, and the difference in the diffusion coefficient of Al and Li nanoparticles can reach 20–30%. Moreover, in accordance with the Einstein theory, the diffusion coefficient of a particle is inversely proportional to the particle radius. In the general case, the diffusion coefficient as a function of the nanoparticle radius is described by a power-law





function, $D = aR^{-k}$, and the power-law exponent also depends on the nanoparticle material. The values are $k_{Li} = 1.37$ for Li particles and $k_{Al} = 1.59$ for Al particles.

The dependence of the diffusion coefficient on the fluid temperature is absolutely different. As for the Brownian particles, this dependence is described by a power-law function, $D \sim T^n$, where the power-law exponent n is not universal and depends on the nanoparticle material and size. As an example, Fig. 1.6 shows the temperature dependence of the diffusion coefficient of Li nanoparticles 2 nm in diameter in argon ($\varepsilon_V = 0.707$). The symbols here are the point predicted by molecular dynamics simulations, and the dashed curve is the approximation of these data by using the above-mentioned power-law dependence with the exponent value n = 1.1. The Einstein formula (solid curve) predicts a significantly smaller increase. This difference is aggravated as the temperature increases.

The entire set of experimental and numerical results shows that the commonly accepted theoretical models either are unable to describe diffusion of nanoparticles in gases and liquids, or are applicable within a rather narrow range of parameters. This is particularly important for sufficiently small nanoparticles. Large nanoparticles can certainly be described by relations derived for the Brownian particles.

1.6.3 Viscosity of Gas Suspensions of Nanoparticles

The viscosity coefficient of a nanofluid is one of the key parameters determining the nanofluid flow. It has been assumed for a long time that the effective viscosity coefficient of a nanofluid, similar to ordinary disperse fluids, depends only on the volume concentration of particles. However, the use of the kinetic theory for rarefied gas nano-suspensions has demonstrated that this is not so.

The effective viscosity coefficient of rarefied suspensions was calculated for the first time by Einstein (1906), who took into account the influence of particles on the hydrodynamic field of the carrier fluid velocity and, as a consequence, on the stress

tensor and viscosity coefficient. He demonstrated that the effective viscosity coefficient of the suspension

$$\eta = \eta_0 [1 + (5/2)\phi] \tag{1.41}$$

is always greater than the carrier fluid viscosity coefficient η_0 , where ϕ is again the volume concentration of disperse particles. There were many later publications in which the Einstein theory was extended to sufficiently dense suspensions and appropriate formulas were derived. With accuracy of terms on the order of ϕ^2 , these formulas have the form

$$\eta = \eta_0 [1 + (5/2)\phi + b\phi^2], \tag{1.42}$$

where the coefficient b usually varies from 5.9 to 7.2.

The situation in rarefied gas suspensions of nanoparticles, however, is more complicated. The viscosity coefficient of the considered rarefied gas suspension of nanoparticles is described by the formula (Rudyak and Krasnolutskii, 2003b, 2004)

$$\eta = (1+Z)/(X+Y), \tag{1.43}$$

where

$$\begin{split} X &= \frac{x_1^2}{\eta_1} + 2\frac{x_1x_2}{\eta_{12}} + \frac{x_2^2}{\eta_2}, \quad Y &= 0.6A_{12}^* \left\{ \mu \frac{x_1^2}{\eta_1} + 0.5x_1x_2 \frac{(1+\mu)^2}{\mu} \frac{\eta_{12}}{\eta_1\eta_2} + \frac{1}{\mu} \frac{x_2^2}{\eta_2} \right\}, \\ Z &= 0.6A_{12}^* \left\{ \mu x_1^2 + 2x_1x_2 \left[\frac{(1+\mu)^2}{4\mu} \left(\frac{\eta_{12}}{\eta_1} + \frac{\eta_{12}}{\eta_2} \right) - 1 \right] + \frac{1}{\mu} x_2^2 \right\}, \\ \eta_i &= \frac{5}{16} \frac{(\pi m_i kT)^{1/2}}{\pi \sigma_{il}^2 \Omega_i^{(2,2)*}}, \quad \eta_{12} &= \frac{5}{16} \frac{(\pi m_{12} kT)^{1/2}}{\pi \sigma_{12}^2 \Omega_{12}^{(2,2)*}}. \end{split}$$

Here, x_1 and x_2 are the molar fractions of components 1 and 2, and $\mu = m_1/m_2$, m_1 and m_2 are the mass of the carrier gas molecule and particle, respectively (the subscript 2 refers to nanoparticles everywhere, if not stated otherwise). T is the temperature, $A_{12}^* = \Omega_{12}^{(2,2)*}/\Omega_{12}^{(1,1)*}, \Omega_{12}^{(l,m)*}$ are the reduced Ω -integrals (Chapman and Cowling 1990), and $\sigma_2 = 2R$. Thus, similar to molecular mixtures of gases, the calculation of the transport coefficient for gas nano-suspensions reduces to the calculation of the corresponding Ω -integrals for the molecule-nanoparticle interaction potential (Rudyak and Krasnolutskii 1999). The viscosity coefficient of a gas nano-suspension (1.43) is a multiparameter function and varies considerably due to changes in the nanoparticle size, nanoparticle concentration, and gas suspension temperature. For small molar fractions of the disperse phase, $x_2 \ll 1$, coefficient (1.43) takes the form

$$\eta = \eta_1 \left\{ 1 + \frac{x_2}{1 + 0.6A_{12}^* \mu} \left[0.3A_{12}^* \frac{(1+\mu)^2}{\mu} \frac{\eta_{12}}{\eta_1} + 2 - 1.2A_{12}^* - 2\frac{\eta_1}{\eta_{12}} \right] \right\}. \quad (1.44a)$$

Function (1.44a) essentially depends on the relationship between the mass ratio μ , nanoparticle radius, nanoparticle temperature, and interaction potential parameters. In particular, the expression in square brackets in formula (1.44a) can change its sign at certain values of these parameters. This means that the addition of small volume fractions of solid nanoparticles to the gas can lead either to an increase or to a decrease in the effective viscosity of the medium. Specially aimed calculations have shown that this is indeed so; particular examples can be found in Rudyak and Krasnolutskii (2003b, 2004). Thus, the behavior of the effective viscosity of a gas suspension is determined by its composition and by the parameters of its components. Knowing these parameters, one can predict the behavior of the effective viscosity. At small volume fractions of particles, formula (1.44a) can be used. For gas suspensions, this formula also includes small parameters, because, usually, $\mu=m_1/m_2\ll 1$ and $s=\sigma_1/\sigma_2\ll 1$. In the general case, these parameters are related to each other and $\mu\alpha = s^3$, where α is the ratio of the particle material density to the carrier gas molecule density. As these parameters have small values, formula (1.44a) yields one more useful estimate:

$$\eta = \eta_1 \left\{ 1 + x_2 \left[1.2\sqrt{2} \frac{\alpha}{s} \frac{\Omega_1^{(2,2)*}}{\Omega_{12}^{(1,1)*}} + 2 - 1.2A_{12}^* - \frac{\sqrt{2}}{4} \frac{1}{s^2} \frac{\Omega_{12}^{(2,2)*}}{\Omega_1^{(2,2)*}} \right] \right\}.$$
 (1.44b)

If the sizes of carrier gas molecules and nanoparticles are significantly different, the last term in Eq. (1.44b) may become dominant, and the effective viscosity is expected to become smaller than the gas viscosity. Certainly, it is necessary to take into account the value of the parameter α and the values of the Ω -integrals, which can vary by a factor of 2–3.

Finally, it should be noted that, usually, $\sigma_1 \sim \sigma_2$ for gas mixtures; correspondingly, at $\mu \ll 1$, Eq. (1.44a) yields

$$\eta = \eta_1 \left[1 + 1.2\sqrt{2}x_2 \frac{s^2}{\mu} \frac{\Omega_{12}^{(2,2)*}}{\Omega_{12}^{(1,1)*}} + O(1) \right].$$

The addition of a small amount of a heavier gas to a light gas always leads to an increase in the mixture viscosity, as compared to the light component viscosity. However, this increase in the general case does not depend monotonically on the heavy component concentration and varies significantly as the temperature increases.

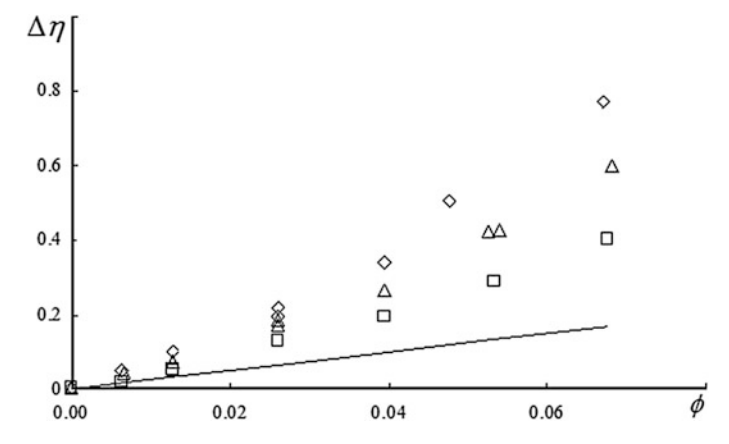


Fig. 1.7 Viscosity of a nanofluid consisting of ethylene glycol with SiO₂ nanoparticles on their volume

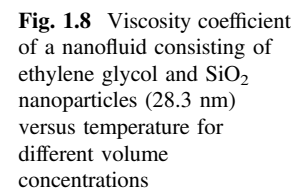
1.6.4 Viscosity of Nanosuspensions

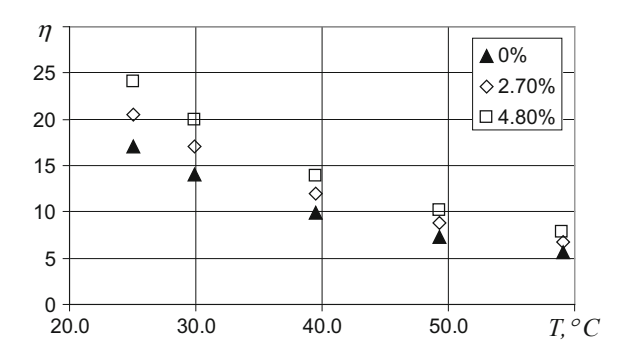
Viscosity of nanofluids has been intensely studied for the last two decades (see Hosseini et al. 2011; Mahbubul et al. 2012; Rudyak 2013). The following facts have been reliably established. First of all, nanofluids exhibit a Newtonian behavior only if the carrier fluid is Newtonian and the nanoparticle concentration is not very high. Apparently, the volume concentrations of nanoparticles are within 10-15% in this case. A typical dependence of the viscosity coefficient $\Delta \eta = \eta/\eta_0 - 1$ of a nanofluid consisting of ethylene glycol with SiO₂ particles on the volume concentration of nanoparticles is shown in Fig. 1.7 (Rudyak et al. 2013b). These measurements were performed at a temperature of 25 °C. The mean particle sizes are 18.1 nm (diamonds), 28.3 nm (triangles), and 45.6 nm (squares). The line is the viscosity coefficient predicted by the Einstein formula: $\Delta \eta = 2.5 \varphi$. The viscosity coefficients for three considered fluids are different and increase with decreasing nanoparticle size. The viscosity coefficient appreciably increases with increasing particle concentration; for the mass concentration of nanoparticles equal to 7%, the viscosity of the nanofluid with the largest particles increases by 40%, and that of the nanofluid with the smallest particles increases by almost 80%. These results agree with the data obtained by other researchers.

The effective viscosity coefficient for moderate concentrations of nanoparticles can always be presented as

$$\eta = \eta_0 [1 + k_1(D)\varphi + k_2(D)\varphi^2],$$
(1.45)

and the coefficients in this formula should be functions of the nanoparticle size D. The Einstein theory does not describe the nanofluid viscosity, even at small volume concentrations of nanoparticles. The experimentally measured value of the





coefficient k_1 for particles of various diameters varies from 4.3 to 22, which is several times greater than the value predicted by the Einstein formula [to obtain it, one has to set $k_1 = 2.5$ and $k_2 = 0$ in Eq. (1.45)]. It should again be emphasized that the values of the coefficients k_1 and k_2 are not universal. In the general case, they depend on the nanoparticle size: the nanofluid viscosity increases as the nanoparticle size decreases. Moreover, it turned out that the viscosity coefficient of nanofluids depends on the nanoparticle material. This dependence was first found through the molecular dynamics method (Rudyak and Krasnolutskii 2014), and was then confirmed experimentally (Rudyak et al. 2016).

The temperature dependence of the viscosity coefficient of a nanofluid is a very important thermophysical characteristic. In contrast to gases, the viscosity coefficient in liquids decreases with increasing temperature. Based on physical considerations, the same behavior should be expected for nanofluids. In fact, nanofluid viscosity does decrease with increasing temperature in almost all studies in which this dependence was determined. There are about 50 papers in which the temperature dependence of nanofluid viscosity was investigated; some of them were cited in the reviews (Hosseini et al. 2011; Mahbubul et al. 2012). These dependences are fairly similar in all of those studies. Naturally, the viscosity coefficient depends on the volume concentration of nanoparticles. As an example, Fig. 1.8 shows the viscosity coefficient as a function of temperature, which was obtained for a nanofluid consisting of ethylene glycol with silicon dioxide particles (Rudyak et al. 2013a). Indeed, the viscosity coefficient decreases with increasing temperature. Moreover, this decrease is fairly significant: as the temperature increases from 25 to 60 °C, the viscosity coefficient decreases by a factor of more than 4.

Many correlations were proposed to describe the viscosity coefficient of a nanofluid as a function of temperature. However, none of them are universal, and they all substantially depend on the concentration, material, and size of nanoparticles and on the carrier fluid viscosity. For this reason, it seems useful to understand the temperature dependence of the normalized nanofluid viscosity $\eta_r = \eta/\eta_0$. For the nanofluid in Fig. 1.7, the dependences of η_r on temperature are shown for different nanoparticle concentrations given in Fig. 1.9 (Rudyak et al. 2013a). At low and moderate concentrations of nanoparticles, the normalized viscosity

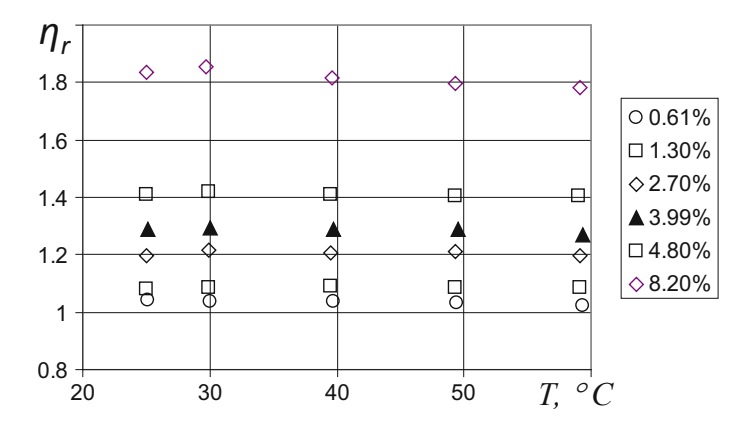


Fig. 1.9 Normalized viscosity coefficient of a nanofluid consisting of ethylene glycol and SiO_2 nanoparticles (28.3 nm) versus temperature for different volume

Table 1.1 Thermal conductivity of various solid and liquid substances at room temperature (Grigoriev and Moilikhova 1991)

Substance	Shape	Thermal conductivity, W/(m K)
Carbon	Nanotubes	1800-6600
	Diamond	900-2300
	Graphite	110–190
Metals	Silver	429
	Copper	401
	Nickel	91
	Aluminum	237
	Gold	317
	Zinc	116
Non-metals	Silicon	148
	Al ₂ O ₃	40
Liquids	Water	0.613
	Ethylene glycol	0.254
	Machine oil	0.145
	Freon-21	0.1005

coefficient remains unchanged with increasing temperature and slightly decreases (approximately by 3%) at the highest nanoparticle concentration (8.2%). Similar dependences were also obtained in Chen et al. (2007), Namburu et al. (2007), Nguyen et al. (2008) for nanofluids consisting of ethylene glycol and TiO_2 particles, aqueous solution of ethylene and SiO_2 particles, and water and Al_2O_3 and CuO particles, respectively.

1.6.5 Thermal Conductivity of Nanofluids

The use of elevated thermal conductivity of nanofluids in various applications is one of the main challenges in the field. It is well known (see Table 1.1) that the thermal conductivity of solids, in particular, metals, their oxides, graphite, and its derivatives, is several orders higher than that of commonly used liquid heat carriers (water, ethylene glycol, various freons, etc.). The idea of using disperse fluids as heat carriers and coolants was put forward long ago, but traditional disperse fluids could not be used for this purpose, because of sedimentation of disperse particles and their abrasive effect. Fortunately, nanofluids are devoid of these drawbacks. The very first experiments with measurements of the thermal conductivity of nanofluids (Masuda et al. 1993; Eastman et al. 1998; Wang et al. 1999) provided excellent results; the addition of even small amounts (on the order of fractions of a percent) of solid nanoparticles increased the thermal conductivity of the carrier fluid by several percent or even tens of percent. It should be noted that the classical theories predicted an increase proportional to the volume concentration of nanoparticles. The theory of the thermal conductivity of disperse fluids was developed by Maxwell (1881), who derived the following relationship between the thermal conductivities of the suspension λ and carrier fluid λ_0 :

$$\lambda = \lambda_0 \left[1 + \frac{3(1-\varpi)\phi}{1+2\varpi-\phi(1-\varpi)} \right],\tag{1.46}$$

where $\varpi=\lambda_0/\lambda_p,\lambda_p$ is the thermal conductivity of the particle material and ϕ is the volume concentration of nanoparticles. Formula (1.46) was obtained for spherical particles that do not interact with each other. The model proposed later by Bruggeman (1935) takes into account interaction of randomly distributed particles. The thermal conductivities of the suspension and carrier fluid are related as

$$\phi\left(\frac{\lambda_p - \lambda}{\lambda_p + 2\lambda}\right) + (1 - \phi)\left(\frac{\lambda_0 - \lambda}{\lambda_0 + 2\lambda}\right) = 0. \tag{1.47}$$

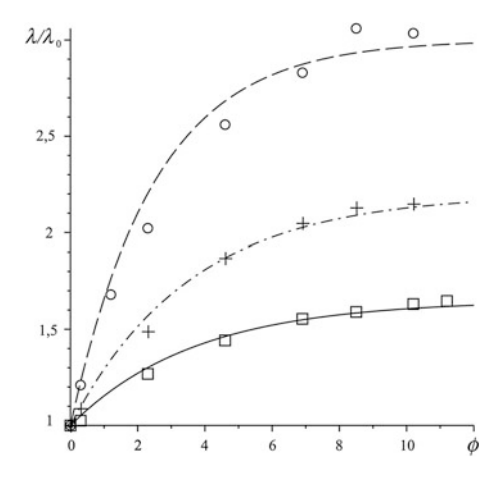
This model, in contrast to Eq. (1.46), has no constraints in terms of the particle concentration; however, within the limit of small concentrations, it yields the same results as the Maxwell model.

Hamilton and Crosser (1962) extended model (1.46) to non-spherical particles:

$$\lambda = \lambda_0 \frac{1 + (n-1)\varpi - (n-1)(\varpi - 1)\phi}{1 + (n-1)\varpi + (\varpi - 1)\phi},$$
(1.48)

where n is the particle surface factor determined via the spherical shape factor $\psi : n = 3/\psi$. The latter is defined as the ratio of the surface area of a sphere whose volume coincides with the particle volume to the particle surface area. If the

Fig. 1.10 Thermal conductivity versus the volume concentration of nanoparticles (in percent) for D/d = 4 and different mass ratios: M/m = 130 (Circles), M/m = 100 (Plus), and M/m = 80 (Squares). The carrier fluid density is $\xi = \pi d^3/6 = 0.37$

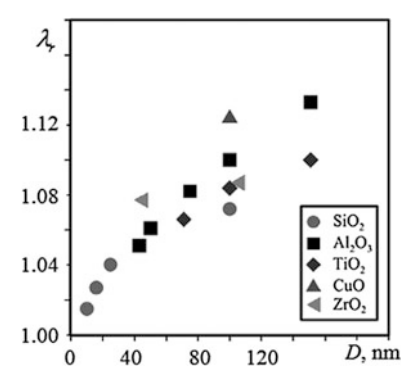


spherical shape factor is equal to unity, then the equation transforms into the Maxwell model.

The experimental data obtained for thermal conductivities of various nanofluids are usually greater than the values predicted by the classical theories (1.46)–(1.48). However, these data are rather contradictory (see the reviews Wang and Mujumdar 2007, 2008; Ding et al. 2007; Yu et al. 2007; Kleinstreuer and Feng 2011). The reasons are the same as those in studying nanofluid viscosity. Thermal conductivity coefficients of nanofluids with different nanoparticle sizes and materials were compared in many cases.

Molecular dynamics modeling of thermal conductivity was performed in Rudyak et al. (2010, 2012) for the hard sphere model and the particle sizes smaller than 2 nm. The normalized thermal conductivity is plotted in Fig. 1.10 as a function of the volume concentration of nanoparticles. In all cases, there is a certain limiting value of nanoparticle concentration above which thermal conductivity no longer increases. This behavior is also predicted by many experiments (see, e.g., Zhu et al. 2007). Moreover, for a fixed nanoparticle size, the thermal conductivity depends

Fig. 1.11 Normalized thermal conductivity coefficient of water-based nanofluids versus the particle size at room temperature and volume concentration of 2%



not only on the volume concentration ϕ , but also on the particle material density. It should be noted that many researchers have tried to represent thermal conductivity at moderate densities by a quadratic dependence of the form of Eq. (1.45) (see, e.g., Lu and Lin 1996). Nevertheless, such dependence is qualitatively incorrect.

It was clearly demonstrated in experiments that the thermal conductivity of nanofluids is not only a function of nanoparticle concentration, but also of nanoparticle size. Typical dependences of the relative thermal conductivity $\lambda_r = \lambda/\lambda_0$ of several nanofluids are plotted in Fig. 1.11 (Pryazhnikov et al. 2017). For a fixed particle concentration, the thermal conductivity increases with growth of the particle size.

The thermal conductivity of the disperse fluid in Eq. (1.46) depends on the thermal conductivity of the particle material. It has been definitively established that the increase in the thermal conductivity of the nanofluid as compared to the base fluid is independent of the thermal conductivity of the nanoparticle material. As the analysis of experimental data shows, however, the greater the nanoparticle density, the greater the thermal conductivity of the nanofluid. It was experimentally demonstrated that this dependence is close to linear (Pryazhnikov et al. 2017). Processing and analysis of experimental data made it possible to derive the following formula (Ceotto and Rudyak 2016; Pryazhnikov et al. 2017)

$$k_r = 1 + (0.0193 + 0.00383\tilde{\rho})\sqrt{\varphi\tilde{D}},$$
 (1.49)

which ensures an adequate description of the thermal conductivity coefficient of the nanofluid. Here, $\tilde{\rho} = \rho_p/\rho_f$, where ρ_p and ρ_f are the densities of the nanoparticle and carrier liquid materials, respectively.

1.7 Molecular Dynamics Method

In analyzing various methods of modeling micro- and nanoflows in the previous sections, it was demonstrated that methods of continuous mechanics have severe constraints. Beginning from certain characteristic channel sizes, it is necessary to use the molecular dynamics method. In this case, ab initio simulations of the system are performed on the basis of the set of particles (atoms or molecules) composing this system. This direct numerical molecular modeling of phenomena and processes is the most advanced and powerful tool for studying them. This technique is called the molecular dynamics (MD) method. This method is often preferred over experiments, because experimental investigations are usually much more expensive and sometimes impossible, e.g., in studying some properties of nanoparticles or flows in nanochannels.

At the moment, there are many MD algorithms, which were used as a basis for the development of dozens of standard software packages, including on-line available and free programs. There are also specialized packages, for example, for solving quantum chemistry problems, and universal packages, which can solve various problems of physics, mechanics, chemistry, and biology. The most popular universal packages are AMBER, CHARMM, NAMD, LAMMPS, DL-PLOY, GROMACS, and others.

The idea of the MD method is natural and simultaneously trivial: the system is presented as a set of interacting molecules (atoms) and their dynamics is considered. As the system dynamics is described by the Newton equations ¹²

$$m\frac{d^2\mathbf{r}_i}{dt^2} = \mathbf{F}_i, \quad i = 1, 2, ..., N,$$
 (1.50)

the initial problem reduces to solving this system of equations on a computer. This method was applied for the first time for solving physical problems more than 50 years ago by Alder and Wainwright (1959, 1960) and has been used since then for solving versatile problems of physics, chemistry, mechanics, and biology. Despite the apparent simplicity of the idea of the MD method, the situation is far from trivial. Indeed, the number of molecules in a real system is tremendous. For example, the number of molecules in one cubic centimeter of air at standard pressure is about 10¹⁹. The number of molecules in a liquid is greater by approximately three orders of magnitude. A modern computer with good performance allows one to study the dynamics of 10⁴ molecules (the greatest number of molecules used in MD simulations was 10¹¹). Can such a comparatively small number of molecules represent real properties of large systems? Numerous comparisons of MD data with various experimental observations show that this comparatively moderate number of molecules still makes it possible to obtain reasonable qualitative and quantitative results. It turned out that a system of several thousands of molecules is already sufficiently representative, though certain care should be applied in some cases. For example, many authors have indicated that several tens of particles are sufficient for modeling transport coefficients (see, e.g., Alder and Wainwright 1970). It was demonstrated, however, that this is not so (Rudyak et al. 2008a). Accuracy within 1% in modeling self-diffusion can be reached only by using several tens of thousands of molecules.

The main element of the MD method is setting interparticle forces. In the general case, the potential energy Φ of a system consisting of N particles can be presented in a series form as

$$\Phi = \sum_{i} \Phi_1(\mathbf{r}_i) + \sum_{i} \sum_{j>i} \Phi_2(\mathbf{r}_i, \mathbf{r}_i) + \sum_{i} \sum_{j>i} \sum_{k>j>i} \Phi_3(\mathbf{r}_i, \mathbf{r}_j, \mathbf{r}_k) + \ldots,$$

where \mathbf{r}_i is the radius-vector of the particle i, Φ_1 is the potential energy of external fields applied onto the system, and Φ_l with l > 1 is a two-particle, three-particle, etc., potential of particle interaction. Typical MD simulations, however, are usually

¹²Only the classical systems are considered in that which follows.

limited to only two-particle interaction potentials.¹³ This is usually fairly sufficient, especially in view of the fact that interaction potentials used in practice are actually effective potentials and take multiparticle interactions to a greater or smaller extent. The true two-particle potential is the hard sphere potential

$$\Phi(r) = \begin{cases}
\infty & \text{for } r \le d \\
0 & \text{for } r > d
\end{cases}$$
(1.51)

and as the time of interaction of hard spheres is equal to zero, only paired collisions are possible. Here, d is the effective diameter of the sphere used to represent a molecule. Using potential (1.51), one can model transport processes and obtain good quantitative results if an appropriately effective particle diameter is chosen. Nevertheless, this model has an obvious drawback: it ignores forces of intermolecular attraction. There are many models of real potential. The most popular one is the Lennard-Jones potential

$$\Phi(r) = 4\varepsilon \left[\left(\frac{\sigma}{r} \right)^{12} - \left(\frac{\sigma}{r} \right)^{6} \right], \tag{1.52}$$

where σ and ε are the parameters of the potential. This is the potential most frequently used in MD simulations.

After an appropriate choice of parameters with the help of potentials (1.51) and (1.52), it is possible to describe various properties of systems, from the laws of particle scattering after collisions to thermodynamic and transport properties of the system, including, e.g., pressure, temperature, density, viscosity and thermal conductivity coefficients, diffusion coefficient, etc. Implementation of the method is different in these two cases. The principal schemes of constructing the algorithms for both situations are considered below.

1.7.1 Continuous Potentials

If continuous potentials of the form (1.52) are used, the system dynamics is described by the Newton equations (1.50), and the task is to solve this system of equations on a computer. For this purpose, a cell is chosen, most often a cubic cell, and any amount of particles from several thousands to several tens or hundreds of thousands are placed into this cell. Each particle is assigned some initial velocity in accordance with a certain law. Then, the Cauchy problem should be solved for system (1.50) in order to determine the coordinates and momentums of all particles

¹³This assumption appreciably simplifies computations, though is not of principal importance. Moreover, the MD method is actually the only reliable tool for studying the effect of non-additive forces on transport processes.

at a certain time instant if the corresponding values at the previous time instant are known. For this purpose, Eq. (1.50) are replaced with finite-difference equations. From known dynamic variables for the *i*th molecule at the time t_n , it is possible to determine the values of these variables at the time $t_{n+1} = t_n + \delta t : \mathbf{r}_i^{(n+1)}, \mathbf{v}_i^{(n+1)}$. Many various algorithms were developed for calculating these dynamic variables. The simplest discretization of Eq. (1.50) has the form

$$\mathbf{r}_{i}^{(n+1)} = \mathbf{r}_{i}^{(n)} + \mathbf{v}_{i}^{(n)} \delta t, \ \mathbf{v}_{i}^{(n+1)} = \mathbf{v}_{i}^{(n)} + m^{-1} \delta t \sum_{j \neq i}^{N} \mathbf{F}_{ij}(\mathbf{r}_{i}^{(n)}, \mathbf{r}_{j}^{(n)}).$$

This is an explicit scheme with the first order of accuracy in terms of δt , and it is called the Euler scheme. There are also more complicated approximations. In the method of central differences, it is assumed that the increments of coordinates are determined by the velocities in the middle of the time step:

$$\mathbf{r}_i(t+\delta t) = \mathbf{r}_i(t) + \delta t \mathbf{v}_i(t+\delta t/2), \quad \mathbf{v}_i(t+\delta t/2) = \mathbf{v}_i(t-\delta t/2) + m^{-1}\delta t \sum_{j\neq i}^N \mathbf{F}_{ij}(t).$$

Many algorithms include an expansion of the function $\mathbf{r}_i(t\pm\delta t)$ into a series: $\mathbf{r}_i(t\pm\delta t)=\mathbf{r}_i(t)\pm\dot{\mathbf{r}}_i(t)\delta t+\ddot{\mathbf{r}}_i(t)(\delta t^2/2)+\ldots$ Summation of these two equations yields $\mathbf{r}_i(t+\delta t)+\mathbf{r}_i(t-\delta t)=2\mathbf{r}_i(t)+\ddot{\mathbf{r}}_i(t)\delta t^2$, with accuracy to the third-order terms. In turn, the velocity is obtained by subtracting one of these equations from the other. With the same accuracy, we have $\dot{\mathbf{r}}_i(t)=[\mathbf{r}_i(t+\delta t)-\mathbf{r}_i(t-\delta t)]/2\delta t$. As a result, we obtain

$$\mathbf{r}_i(t+\delta t) = -\mathbf{r}_i(t-\delta t) + 2\dot{\mathbf{r}}_i(t) + \ddot{\mathbf{r}}_i(t)\delta t^2.$$

The above-described algorithm was proposed by Verlet (1967). There are many other schemes, e.g., the predictor-corrector scheme, the Runge-Kutta methods of various orders of accuracy, etc. The most popular schemes used at the moment are the above-described Verlet scheme, the Schofield scheme (Schofield 1973), and the predictor-corrector scheme. The choice of the numerical approximation is actually determined by the problem to be solved and has to be discussed in each particular case. Different schemes have been compared in many papers (see, e.g., Allen and Tildesley 1989; Haile 1992; Rapaport 2005). The interval δt should be chosen in such a way as to ensure stability of integration of system (1.50) and obtain a solution with the deviation from the exact solution that grows as slowly as possible with time. Solution stability is usually verified on the basis of the satisfaction of conservation laws.

All coordinates, velocities, and accelerations of particles calculated at different time instants are stored in the computer memory and can be used later for computing various system properties. Computations are repeated many times, thus providing an ensemble of different variants of evolution of the considered system in the phase space.

An appropriate choice of the time step is also important. It should be greater than the inverse maximum frequency in the system.

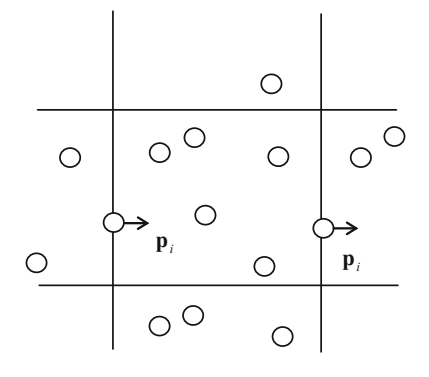
1.7.2 Smooth Hard Spheres

For a system whose molecules are simulated by elastic hard spheres (1.51), application of the MD method is appreciably simpler. There is no need to solve the Newton equations at all. The entire procedure reduces to finding the sequence of times between molecular collisions and determining the minimum value of this series at each step, which actually determines the pair of molecules colliding in reality. Then, all particles are shifted along their trajectories by this minimum time, and the velocities of two colliding particles are recalculated, after which the computation procedure is repeated. It is this technique that was proposed by Alder and Wainwright (1959, 1960) and now has many modifications (Rapaport 2005).

1.7.3 Boundary and Initial Conditions

As computer resources are limited, the number of molecules that can be used in computations is not very large; it ranges from several hundreds and thousands to hundreds of thousands. For such a comparatively "small" system to possess the properties of a system with a large number of particles modeling a liquid or a gas, the so-called periodic boundary conditions are most often used. For this purpose, the considered volume V is divided into cells, e.g., cubic cells with a rib length L and number of particles N. It is assumed that the cells form a periodic grid. Therefore, if some molecule with a momentum \mathbf{p}_i crosses the cell boundary and

Fig. 1.12 Periodic boundary conditions used in the MD method



leaves the cell, then a molecule with the same momentum enters this cell through the opposite face. This procedure is illustrated in Fig. 1.12 for a plane system.

If periodic boundary conditions are imposed, then the computations actually involve not only the main computational cell shown in Fig. 1.12, but all the cells around the main cell. These cells contain molecules with which molecules from the main cell interact, and molecules from these cells center the main cell when one molecule leaves the main cell. Thus, simulations are performed in the main cell and some of its copies: 8 cells for two-dimensional simulations and 26 cells for three-dimensional simulations. It should be borne in mind, however, that periodic boundary conditions can be used only for systems of particles with short-range interaction potentials, such as the Lennard-Jones potential. This approach is inapplicable for particle systems with long-range interaction, e.g., plasmas.

The molecular interaction potential is assumed to be truncated, and the effective radius of action of molecular forces should be much smaller than L. To reduce the computation time, periodic conditions can be modified by considering the motion of molecules at the cell boundaries in an explicit manner.

In the case of periodic boundary conditions, it is clear that the number of particles in each cell remains unchanged, as well as the energy and momentum (the angular momentum is certainly not unchanged). An ensemble corresponding to such a system is a microcanonical ensemble. As there are no fluctuations of the number of particles in the system, statistical errors associated with a finite number of particles and molecular correlations that are not typical for real systems will appear. These statistical errors can be reduced, first, by increasing the statistical information drawn from computations and, second, by assuming a possibility of fluctuations of the number of particles in the cell. Stochastic boundary conditions are used for this purpose. In this case, the particle intersecting the cell boundary leaves the system. However, new molecules with a random momentum are randomly inserted into the system (at random points in space and at random time instants). Obviously, the law of generation of new particles should prevent changes in the mean density, momentum, and energy in the system. An advantage of this system is the possibility of simulating the dynamics of a large canonical ensemble. It is only necessary to verify that the laws of conservation of the average values of the number of particles, momentum, and energy are satisfied, whereas fluctuations of these variables are allowed.

Both periodic and stochastic boundary conditions are only suitable for modeling unbounded systems. In flows bounded by solid surfaces, it is necessary to take into account interaction of gas or liquid molecules with the walls. In this case, periodic or stochastic conditions should be combined with boundary conditions of reflection of molecules from the solid surface or their interaction with molecules of the walls.

A complete formulation of the problem for system (1.50) also requires initial conditions to be imposed, i.e., coordinates and velocities of all molecules in the cell. The initial conditions are determined by the physical aspect of the problem. In high-density systems (solids or liquids), particles are arranged in an ordered or quasi-ordered manner. For example, as argon forms a face-centered cubic lattice after its crystallization, it is simulated with the use of a cubic cell. The molecules in

this cell form a face-centered cubic lattice and are located at the nodes of this lattice. Conversely, in studying gases, the molecule coordinates are defined in a pseudo-random manner, with an additional condition that there are no overlapping configurations of molecules. There are also many ways to define the initial values of molecule velocities. In problems aimed at studying equilibrium states, particle velocity should be subjected to conditions of a zero total momentum of the system and correspondence of the total energy of the system to its temperature. The temperature of the system is determined by its mean kinetic energy. This arbitrariness in initial conditions is caused by the fact that it is impossible to determine the correspondence between the microscopic and macroscopic states of the system.

1.7.4 Reaching Equilibrium in Molecular Systems

Despite the simplicity of the basic idea of the MD method, its implementation has turned out to be very fruitful. The reason is that the MD method ensures the evidential effect of experiments and allows one to perform "ideal" experiments to elucidate the mechanisms of various physical processes in nature and engineering facilities. Therefore, the MD method is successfully used for verification of various fluid theories, derivation of equations of state for liquids and non-ideal gases, calculation of transport coefficients, investigation of interaction of molecules with solid surfaces, simulation of epitaxy and crystal growth processes, condensation, crystallization, and formation of clusters, investigation of the molecular structure, creation of materials with prescribed properties, inspection of damages of walls of nuclear reactors, thermonuclear devices, and plasma reactors, in microelectronics, material science, chemistry, biology, and some other fields. It is impossible to make a comprehensive review of the results obtained owing to the sheer volume of them. There are dozens of topical reviews dealing with investigations of molecular systems using the MD method. The theory of the MD method was recently reviewed by Norman and Stegailov (2013), who discussed various principally important issues of the method; in particular, much attention was paid to studying phase trajectories of the system, the necessity of obtaining an ensemble of MD data, averaging of these data, etc.

MD simulations provide information about the dynamic variables of the system: the coordinates and velocities of particles composing this system. Based on these data, one can use the methods of statistical mechanics (Zubarev 1974; Rudyak 1987, 2004, 2005) to calculate all macroscopic characteristics of the system: pressure, density, velocity field, stress, transport coefficients, etc. The MD method

allows one to model both equilibrium and nonequilibrium properties of multiparticle systems. The correctness of simulations of equilibrium properties of the system depends, to a large extent, on whether or not the considered system reached the equilibrium state. To monitor the degree to which a homogeneous system has approached the equilibrium state, the following variables are usually calculated:

1. Mean particle energy per each degree of freedom:

$$\langle E_k \rangle = \frac{1}{N} \sum_{i=1}^{N} \frac{m v_{ik}^2}{2}, \quad k = x, y, z.$$

2. Root-mean-square fluctuations of the velocity of one particle:

$$<(\mathbf{v}-<\mathbf{v}>)^2> = \frac{1}{N}\sum_{i=1}^N <(\mathbf{v}_i-<\mathbf{v}>)^2>, \ <\mathbf{v}> = \frac{1}{N}\sum_{i=1}^N \mathbf{v}_i.$$

3. Mean distance between two particles in the cell:

$$R_a = \frac{2}{N(N-1)} \sum_{i \neq j}^{N} r_{ij}.$$

After the initial relaxation process, these variables reach their equilibrium values and fluctuate around them. The distribution of particle velocities in the equilibrium state is the Maxwell distribution. In particular, the distributions of the velocity v_x and the absolute value of the velocity v_x are described by the formulas

$$f_{10}(\mathbf{v}_x) = \sqrt{\frac{m}{2\pi kT}} \exp\left(-\frac{m\mathbf{v}_x^2}{2kT}\right),\tag{1.53}$$

$$f_{10}(v) = 4\pi \left(\frac{m}{2\pi kT}\right)^{3/2} v^2 \exp\left(-\frac{mv^2}{2kT}\right).$$
 (1.54)

1.7.5 Statistical Ensemble

It is usually assumed in MD simulations that interparticle forces are independent of time. As the system is closed, it moves over a constant-energy hypersurface. Such a

system corresponds to a microcanonical ensemble. Other types of ensemble are also used in simulations, in particular, canonical and isothermal-isobaric ensembles. Naturally, the corresponding macroscopic variables in the system should be monitored. In the two ensembles specified, it is necessary to control the temperature. The kinetic energy in the system is not conserved in the general case, even if the total energy is unchanged; hence, the temperature of the system also changes. A constant temperature can be ensured by several methods. For example, this can be done by using the so-called thermostats. A typical procedure is the use of the Berendsen thermostat (see, e.g., Berendsen 1986). This algorithm implies that the deviation of the system temperature T from the prescribed temperature T_0 is described by the relaxation equation

$$\frac{dT}{dt} = \frac{T_0 - T}{\tau},\tag{1.55}$$

where τ is the corresponding relaxation time. To introduce a required correction, a thermostat weakly coupled with the system is used, and the velocities of all molecules of the system are multiplied at each time step δt by the coefficient

$$\lambda = \left[1 + \frac{\delta t}{\tau} \left(\frac{T_0}{T} - 1\right)\right]^{1/2}.\tag{1.56}$$

In principle, the relaxation times in Eqs. (1.55) and (1.56) do not necessarily coincide.

Though the Berendsen thermostat is very effective in maintaining a prescribed temperature in the system, it does not generate states corresponding to the canonical ensemble. Thermostats that can be used to describe the canonical ensemble were developed by Nose (1984) and Hoover (1985). In Hoover's formulation, the equation of motion of each particle is supplemented with a certain drag force

$$m_i \frac{d^2 \mathbf{r}_i}{dt^2} = \mathbf{F}_i - \gamma \frac{d \mathbf{r}_i}{dt}, \quad i = 1, 2, \dots, N,$$
 (1.57)

where the drag coefficient is found by solving the equation

$$\frac{d\gamma}{dt} = \frac{(T - T_0)}{\tau^*}.$$

The relaxation time in this equation is a function of temperature and determines the degree of coupling of the system with the thermostat. There is a principal difference between two above-described thermostats: in the first case, temperature fluctuations decay exponentially; in the second case, relaxation is an oscillating function. References 53

References

Alder BJ, Wainwright TE (1959) Studies in molecular dynamics. I. General method. J Chem Phys 31(2):459–466

- Alder BJ, Wainwright TE (1960) Studies in molecular dynamics. II. Behavior of a small number of elastic spheres. J Chem Phys 32(3):459–463
- Alder BJ, Wainwright TE (1970) Studies in molecular dynamics. III. Transport coefficients for a hard-spheres fluid. J Chem Phys 53(10):3813–3826
- Allen MP, Tildesley DJ (1989) Computer simulation of liquids. Oxford University Press, Oxford Aristov VV et al (2007) Simulations of low speed flows with unified flow solver. In: Proceedings of 25th international symposium on rarefied gas dynamics, Publishing House of SB RAS, Novosibirsk, pp 1128–1133
- Berendsen HJC (1986) Biological molecules and membranes. In: Cicotti G, Hoover WG (eds) Molecular dynamics simulation of statistical mechanical systems. North-Holland Publishing Company, Amsterdam
- Bhatnagar PL, Gross EP, Krook M (1954) A model for collision processes in gases. Phys Rev 94(3):511–525
- Bird GA (1976) Molecular gas dynamics. Clarendon Press, Oxford
- Bruggeman DAG (1935) Berechnung verschiedener physikalischer Konstanten von heterogenen Substanzen. I. Dielektrizitatskonstanten undleitfahigkeiten der Mischkorper aus isotropen Substanzen. Ann Phys 24:636–679
- Ceotto D, Rudyak VY (2016) Phenomenological formula for thermal conductivity coefficient of water-based nanofluids. Colloid J 78(4):509–514
- Cercignani C (1975) Theory and application of the Boltzmann equation. Scottish Academic Press, Edinburg&London
- Cercignani C (1983) About methods of the Boltzman equation solution. In: Montroll VXEW, Lebowitz JL (eds) Nonequilibrium phenomena. I. The Boltzmann equation. Studies in statistical mechanics. North-Holland Publishing Company, Amsterdam
- Cercignani C, Pagani CD (1967) Variational approach to rarefied flows in cylindrical and spherical geometry. In: Proceedings of 5th international symposium on rarefied gas dynamics, vol 1. Academic Press, New York, pp 555–573
- Chapman S, Cowling TG (1990) The mathematical theory of non-uniform gases. Cambridge University Press, Cambridge
- Chen H, Ding Y, Tan C (2007) Rheological behavior of nanofluids. New J Phys 9(10), paper 367:1–24
- Choi S (1995) Enhancing thermal conductivity of fluids with nanoparticles. In: Siginer DA, Wang HP (eds) Developments applications of non-Newtonian flows, vol 231/MD. ASME, New York, pp 99–105
- Ding Y, Chen H, Wang L, Yang C-Y, He Y, Yang W, Lee WP, Zhang L, Huo R (2007) Heat transfer intensification using nanofluids. KONA 25:23–38
- Eastman JA, Choi US, Li S, Soyez G, Thompson LJ, DiMelfi RJ (1998) Novel thermal properties of nanostructured materials. Paper presented at the international symposium on metastable mechanically alloyed and nanocrystalline materials, Wollongong, Australia, 7–12 Dec 1998
- Einstein AA (1906) A new determination of molecular sizes. Ann Phys 19:289-306
- Epstein M (1967) A model of the wall boundary condition in kinetic theory. AIAA J 5(10): 1797–1800
- Evans DF, Tominaga T, Davis HT (1981) Tracer diffusion in polyatomic liquids. J Chem Phys 74:1298–1306
- Ferziger JH, Kaper HG (1972) Mathematical theory of transport processes in gases. North-Holland Publishing Company, Amsterdam
- Friedlander SK (2000) Smoke, dust, haze. Fundamentals of aerosol dynamics. Oxford University Press, Oxford

Gimelshtein SF, Rudyak VY (1991) Simulation of rarefied gas by the small number particles system. Tech Phys Lett 17(19):74–77

Gladkov MY, Rudyak VY (1994a) Kinetic equations for a finely dispersed rarefied gas suspensions. Fluid Dyn 29(2):285–290

Gladkov MY, Rudyak VY (1994b) Kinetic equations for a highly dispersed gas suspension. Tech Phys 39(4):441–443

Goodman FO, Wachman HY (1976) Dynamics of gas-surface scattering. Academic Press, New York

Gorbachev YE (1981) Boundary layer with pressure. Sov Phys Tech Phys 26(5):544-547

Gorbachev YE (1982) Boundary layer of finite thickness. Sov Phys Tech Phys 27(5):539-541

Graur I, Sharipov F (2008a) Non-isothermal flow of rarefied gas through a long pipe with elliptic cross section. Microfluid Nanofluid 6(2):267–275

Graur I, Sharipov F (2008b) Gas flow through an elliptical tube over the whole range of the gas rarefaction. Eur J Mech B/Fluids 27(3):335–345

Haile JM (1992) Molecular dynamics simulation: elementary methods. Wiley, New York

Hamilton RL, Crosser OK (1962) Thermal conductivity of heterogeneous two-component systems. I&EC Fundam 1:182–191

Haselmeyer R et al (1994) Translational diffusion in C_{60} and C_{70} fullerene solutions. Ber Bunsenger Phys Chem 98:878–881

Hoover WG (1985) Canonical dynamics: equilibrium phase-space distributions. Phys Rev A 31:1695–1697

Hosseini SS, Shahrjerdi A, Vazifeshenas Y (2011) A review of relations for physical properties of nanofluids. Aust J Basic Appl Sci 5(10):417–435

Kato T, Kikuchi K, Achiba YJ (1993) Measurement of the self-diffusion coefficient of C₆₀ in benzene-D₆ using ¹³C pulsed-gradient spin echo. J Chem Phys 97:10251–10253

Kharlamov GV, Rudyak VY (2004) The equilibrium fluctuations in small open systems. Phys A 340:257-264

Kleinstreuer K, Feng Y (2011) Experimental and theoretical studies of nanofluid thermal conductivity enhancement: a review. Nanoscale Res Lett 6(229):1–13

Klimontovich YL (1974) Kinetic equations for nonideal gas and nonideal plasma. Phys Usp 16:512–528

Kowert RW, Jones JB, Zahm JA, Turneret RM (2004) Size-dependent diffusion in cycloalkanes. Mol Phys 102(13):1489–1497

Lu SY, Lin HC (1996) Effective conductivity of composites containing aligned spheroidal inclusions of finite conductivity. J Appl Phys 79(9):6761–6769

Mädler L, Friedlender SK (2007) Transport of nanoparticles in gases: overview and recent advances. Aerosol Qual Res 7:304–342

Mahbubul IM, Saidur R, Amalina MA (2012) Latest developments on the viscosity of nanofluids. Int J Heat Mass Transf 55:874–885

Masuda H, Ebata A, Teramae K, Hishinuma N (1993) Alteration of thermal conductivity and viscosity of liquid by dispersing ultra-fine particles (dispersions of γ -Al₂O₃, SiO₂, and TiO₂ ultra-fine particles). Netsu Bussei (Japan) 7(4):227–239

Maxwell JC (1879) On stresses in rarefied gases arising from inequalities of temperature. Philos Trans Roy Soc Lond 70(6):231–256

Maxwell JC (1881) A treatise on electricity and magnetism. Clarendon Press, Oxford

Namburu PK, Kulkarni DP, Dandekar A, Das DK (2007) Experimental investigation of viscosity and specific heat and silicon dioxide nanofluids. Micro Nano Lett 2:67–71

Nguyen CT, Desgranges F, Galanis N, Roy G, Maré T, Boucher S, Mintsa AH (2008) Viscosity data for Al₂O₃-water nanofluid–hysteresis: is heat transfer enhancement using nanofluids reliable. Int J Therm Sci 47:103–111

Nigmatulin RI (1987) Dynamics of multi-phase media, Part 1. Nauka, Moscow

Norman GE, Stegailov VV (2013) Stochastic theory of the classical molecular dynamics method. Math Models Comput Simul 5(4):305–333

References 55

Nose S (1984) A molecular dynamics method for simulations in the canonical ensemble. Mol Phys 52:255–268

- Nuevo MJ, Morales JJ, Heyes DM (1997) Hydrodynamic behavior of a solute particle by molecular dynamics. Mol Phys 91:769–774
- Ould-Caddour F, Levesque D (2000) Molecular-dynamics investigation of tracer diffusion in a simple liquid: test of the Stokes-Einstein law. Phys Rev E 63:011205
- Grigoriev IS, Moilikhova EZ (eds) (1991) Physical values. Energoatomizdat, Moscow
- Pryazhnikov MI, Minakov AV, Rudyak VY, Guzei DV (2017) Thermal conductivity measurements of nanofluids. Int J Heat Mass Transf 104:1275–1282
- Rapaport DC (2005) The art of molecular dynamics simulation. Cambridge University Press, Cambridge
- Rudyak VY (1985) Derivation of a kinetic equation of the Enskog type for a dense gas. High Temp 23(2):215–219
- Rudyak VY (1987) Statistical theory of dissipative processes in gases and liquids. Nauka, Novosibirsk
- Rudyak VY (1989a) Basic kinetic equation of a rarefied gas. Fluid Dyn 24(6):954-959
- Rudyak VY (1989b) Transport coefficients for a nonideal gas. High Temp 27(4):548-553
- Rudyak VY (1991) Correlations in a finite number of particles system simulating a rarefied gas. Fluid Dyn 26(6):909–914
- Rudyak VY (1992) Kinetics of finely dispersed gas suspension. Sov Tech Phys Lett 18(10): 681-682
- Rudyak VY (1995) Nonlocality solution of the Boltzmann equation. Sov Phys Tech Phys 40:29–40
- Rudyak VY (1996) Classification principles of dispersed media. J Aerosol Sci 27(Suppl 1): 271–272
- Rudyak VY (1999) The mixing kinetic-hydrodynamical level of description of the dispersed fluids. Sov Tech Phys Lett 25(22):42–45
- Rudyak VY (2004) Statistical aerohydromechanics of homogeneous and heterogeneous media. Vol 1. Kinetic theory. Novosibirsk State University of Architecture and Civil Engineering, Novosibirsk
- Rudyak VY (2005) Statistical aerohydromechanics of homogeneous and heterogeneous media.
 Vol. 2: Hydromechanics. Novosibirsk State University of Architecture and Civil Engineering, Novosibirsk
- Rudyak VY (2013) Viscosity of nanofluids. Why it is not described by the classical theories. Adv Nanoparticles 2:266–279
- Rudyak VY, Kharlamov GV (2003) The theory of equilibrium fluctuations of the thermodynamic quantities in open systems with a small number of particles. High Temp 41(2):201–209
- Rudyak VY, Krasnolutskii SL (1999) The interaction potential of carrier gas molecules with dispersed particles. In: Proceedings of 21st international symposium on rarefied gas dynamics, vol 1. Gépadués-Éditions, Toulouse, pp 263–270
- Rudyak VY, Krasnolutskii SL (2001) Kinetic description of nanoparticle diffusion in rarefied gas. Dokl Phys 46(12):897–899
- Rudyak VY, Krasnolutskii SL (2002) Diffusion of nanoparticles in a rarefied gas. Tech Phys 47(7):807–813
- Rudyak VY, Krasnolutskii SL (2003a) On kinetic theory of diffusion of nanoparticles in a rarefied gas. Atmos Oceanic Opt 16(5–6):468–471
- Rudyak VY, Krasnolutskii SL (2003b) About viscosity of rarefied gas suspensions with nanoparticles. Dokl Phys 48(10):583–586
- Rudyak VY, Krasnolutskii SL (2004) Effective viscosity coefficient for rarefied nano gas suspensions. Atmos Oceanic Opt 17(5):468–475
- Rudyak VY, Krasnolutskii SL (2010) On thermal diffusion of nanoparticles in gases. Tech Phys 55(8):1124-1127
- Rudyak VY, Krasnolutskii SL (2014) Dependence of the viscosity of nanofluids on nanoparticle size and material. Phys Lett A 378:1845–1849

- Rudyak VY, Kharlamov GV, Belkin AA (2000) Direct numerical modeling of the transport processes in heterogeneous media. II. Nanoparticles and macro-molecules in dense gases and liquids. Preprint of Novosibirsk State University of Architecture and Civil Engineering No. 1(13)-2000
- Rudyak VY, Belkin AA, Ivanov DA, Egorov VV (2008a) The simulation of transport processes using the method of molecular dynamics. Self-diffusion coefficient. High Temp 46(1):30–39
- Rudyak VY, Krasnolutskii SL, Ivashchenko EN (2008b). Influence of the physical properties of the material of nanoparticles on their diffusion in rarefied gases. J Eng Phys Thermophys 81:520–524
- Rudyak VY, Belkin AA, Tomilina EA (2010) On the thermal conductivity of nanofluids. Tech Phys Lett 36(7):660-662
- Rudyak VY, Krasnolutskii SL, Ivanov DA (2011) Molecular dynamics simulation of nanoparticle diffusion in dense fluids. Microfluid Nanofluid 11(4):501–506
- Rudyak V, Belkin A, Tomilina E (2012) Molecular dynamics simulation of the thermal conductivity of nanofluids. In: Proceedings of 3rd European conference on microfluidics, European Molecular Biology Laboratory, Heidelberg, 3–5 Dec 2012, p 152
- Rudyak VY, Dimov SV, Kuznetsov VV (2013a) On the dependence of the viscosity coefficient of nanofluids on particle size and temperature. Tech Phys Lett 39(9):779–782
- Rudyak VY, Dimov SV, Kuznetsov VV, Bardakhanov SP (2013b) Measurement of the viscosity coefficient of an ethylene glycol-based nanofluid with silicon dioxide particles. Dokl Phys 58(5): 173–176
- Rudyak VY, Minakov AV, Smetanina MS, Pryazhnikov MI (2016) Experimental data on the dependence of the viscosity of water and ethylene glycol-based nanofluids on the size and material of particles. Dokl Phys 61(3):152–154
- Schofield P (1973) Computer simulation studies of the liquid state. Comput Phys Commun 5:17–23
- Shakhov EM (1968) Generalization of the Krook kinetic relaxation equation. Fluid Dyn 3(5): 95–96
- Smoluchowski M (1898) Uber Wärmeleitung in verdünten Gasen. Ann Phys Chem 64:101–130 Soo SL (1990) Multiphase fluid dynamics. Butterworth-Heinemann, Oxford
- Verlet L (1967) Computer experiments on classical fluids. I. Thermodynamical properties of Lennard-Jones molecules. Phys Rev 159(1):98–103
- Wang X-Q, Mujumdar AS (2007) Heat transfer characteristics of nanofluids: a review. Int J Thermal Sci 46:1–19
- Wang X-Q, Mujumdar AS (2008) A review on nanofluids—Part II: experiments and applications. Braz J Chem Eng 25(4):631–648
- Wang X, Xu X, Choi SUS (1999) Thermal conductivity of nanoparticle–fluid mixture. J Thermophys Heat Trans 13(4):474–480
- Wuelfing WP, Templeton AC, Hicks JF, Murray RW (1999) Taylor dispersion measurements of monolayer protected clusters: a physicochemical determination of nanoparticle size. Anal Chem 71(18):4069–4074
- Yu W, France DM, Choi SUS, Routbort JL (2007) Review and assessment of nanofluid technology for transportation and other applications. Reports Argonne National Laboratory ANL/ESD 07: 9
- Zhu HT, Zhang CY, Tang YM, Wang JX (2007) Novel synthesis and thermal conductivity of CuO nanofluid. J Phys Chem C 111:1646–1650
- Zubarev DN (1974) Nonequilibrium statistical thermodynamics. Consultants Bureau, New York

Chapter 2 Gas-Dynamic Structure and Stability of Gas Microjets



Abstract Microjets are widely used for the mixing of gases and the protection of surfaces from chemically aggressive and high-temperature media. The basic technological characteristics of jets in this case are their penetration capability and the intensity of mixing processes. The goal of the present chapter is to study the structure and stability of microjets. The overview of the works on the study of the gas dynamics of subsonic and supersonic mini- and microjets is given in Sect. 2.1. As tools used in experimental investigations are also very important, they are described in much detail. Diagnostic methods and the results of studying subsonic plane jet stability are described in Sect. 2.2. Experiments aimed at studying the structure and stability of supersonic axisymmetric microjets and the results obtained therein are discussed in Sect. 2.3. Much attention is paid to the techniques used to obtain experimental data. Finally, the problem of microjet modeling with the use of commonly used similarity parameters is discussed in Sect. 2.4.

2.1 Investigation and Application of Microjets

At the moment, gas microjets have found numerous applications in advanced technological processes, aviation, and space engineering (Tabeling 2005). In aviation, supersonic microjets are used to suppress the noise generated by jet engines (Alvi et al. 2003; Lou et al. 2006; Choi et al. 2006) and in amplifiers of automated pneumatic devices (Tanney 1970). Synthetic jets (with a zero integral flow rate) first proposed in Kosinov et al. (1990) are used for modeling unsteady wave processes to study the stability and receptivity of shear flows (Maslov et al. 2001; Fedorov et al. 2003) and for suppression of oscillations in laminar and turbulent flows (Zhuang et al. 2006; Zhang and Zhong 2010).

Supersonic microjets offer significant prospects for aviation and space engineering for the protection of surfaces in high-temperature flows and the suppression of plasma formation around aircraft and reentry vehicles (Parmentier et al. 1970; Akey 1970). Supersonic microjets are actively used in thrusters of orientation systems of so-called microsatellites with masses smaller than 10 kg (Bayt and

Breuer 2001; Zilic et al. 2007). The main advantage of microjets over macrojets is the possibility of creating ensembles of microjets with a high density per unit area at a fixed total flow rate of the gas. The supersonic core length of the jet plays a key role in estimating the efficiency of the jet action on the flow.

Practical needs are responsible for the academic interest in studying subsonic and supersonic microjets. Nevertheless, there is also a fundamental aspect of studying these jets, because it is not clear whether there are principal differences in the characteristics of macroscopic and microscopic jets. Another important issue arising here can be formulated as follows. Is it possible to simulate microjet characteristics by using similarity parameters involved in modeling macroscopic flows: Mach number, Reynolds number, Strouhal number, etc.?

The characteristics of supersonic microjets were studied in great detail in Scroggs and Settles (1996), Phalnicar et al. (2008) for nozzles with diameters ranging from 100 to 1200 μm , and no significant differences in the properties of micro- and macrojets were found. In particular, the measured supersonic core length of the jet was in good agreement with generalized data obtained for macrojets (Shirie and Siebold 1967; Pogorelov 1977). The flow structure in the first barrel of the wave structure of a plane supersonic underexpanded microjet of nitrogen that escaped from a slot sonic nozzle $17\times1875~\mu m$ was investigated in Fomin et al. (2010) with the use of a Pitot microtube. Total pressure measurements revealed the existence of streamwise structures whose amplitude increases in the downstream direction, whereas the number of these structures decreases. These structures are associated with micronozzle edge roughness and are identified with the Gortler vortices, which almost inevitably arise in the case of exhaustion of underexpanded macrojets.

It was only in Aniskin et al. (2011, 2013) that a drastic increase in the supersonic core length of microjets being exhausted out of sonic nozzles smaller than 60 μm in diameter was discovered for the first time. A previously unknown phenomenon of recovery of the supersonic core length after its reduction due to the laminar-turbulent transition in the jet for nozzles smaller than 20 μm in diameter was detected.

As was already noted, investigations of the characteristics of subsonic microjets are traditionally inspired by the necessity to organize gas flow mixing in various engineering processes. These characteristics largely depend on jet flow stability and the formation of certain structures during the transition to turbulence. Stability of subsonic macroscopic jets was intensely studied, both experimentally and numerically. A comprehensive review of the research on stability, noise generation, and acoustic influence on subsonic turbulent (mostly round) jets can be found in Ginevskiy et al. (2001). It was demonstrated that the rate of instability development and, hence, jet penetration depth and mixing intensity can be controlled by inserting artificial periodic perturbations into the jet. Various methods of periodic forcing of jet flows were reviewed in Brown (2005).

There are many recent numerical and experimental studies of the flow characteristics in subsonic low-velocity round and plane air jets from nozzles within the millimeter and submillimeter range. The nozzle diameter (or the smaller linear size

for plane nozzles) in those studies varied from 40 mm to 200 µm, and the maximum velocity of air exhaustion was smaller than 15 m/s. In particular, the effects of nozzle roughness (Kozlov et al. 2002; Litvinenko et al. 2004), velocity profile at the nozzle exit (Kozlov et al. 2008), and periodic acoustic action on the jet (Kozlov et al. 2010; Litvinenko et al. 2011) were considered. The results of those activities were summarized in the monograph (Grek et al. 2012).

The experiments (Kozlov et al. 2002, 2008, 2010; Litvinenko et al. 2004, 2011; Grek et al. 2012) were mainly performed through methods of smoke visualization, supplemented with stroboscopic illumination and hot wire anemometry. The experimental results were compared with predictions of the linear stability theory and direct numerical solution of Navier-Stokes equations at moderate Reynolds numbers. It was shown that surface roughness and the acoustic forcing of round jets lead to the emergence of the Kelvin-Helmholtz instability, which is well known in shear layer and boundary layers. At the nonlinear stage of instability development in a round jet, annular vortices are formed and united in pairs further downstream. In plane jets, instability has a sinusoidal character, and the jet becomes curved in its plane. At the nonlinear stage, vortices also appear in the form of staggered "rolls" entrained by the flow.

The presence of artificial roughness at the nozzle edge gives rise to the emergence of streamwise structures in the jet, which transform in the downstream direction into Ω -shaped vortices for round jets or into hairpin vortices for plane jets, after which the jet becomes turbulent. Acoustic forcing appreciably accelerates the process. The velocity profile at the nozzle exit was also found to affect the development of instability in subsonic jets. If the velocity profile is uniform over the radius and the boundary layer is small, instability development and jet turbulization occur rapidly. On the other hand, the laminar flow is appreciably longer for a parabolic velocity profile. A high-intensity transverse acoustic action on a round or plane jet leads to almost instantaneous development of sinusoidal instability with the formation of vortex streets separated in space. It is interesting that preliminary turbulization of the flow produces a minor effect on these phenomena.

Almost all of the above-described phenomena have already been discussed in publications dealing with stability and laminar-turbulent transition in boundary and shear flows at the macroscopic scale. Therefore, based on the data obtained in those studies, it was concluded that there is no essential difference between subsonic macrojets and subsonic microjets up to characteristic scales on the order of 200 µm.

Experiments with subsonic microjets escaping from nozzles 50, 100, and 200 μ m in diameter were described in Gau et al. (2009). For nozzles 50 μ m in diameter, a significant difference in instability development in microjets and macrojets was found for the first time. In particular, the absence of vortices at the mixing layer boundary and an increase in the penetration capability of the microjet were noted.

Experimental data for plane subsonic helium jets being exhausted out of a slot nozzle $17 \times 1875~\mu\text{m}^2$ into the atmosphere were reported in Fomin et al. (2010), Aniskin et al. (2012). The main results were obtained for the interaction of acoustic waves incident onto the microjet on the side of the greater linear scale of the nozzle.

The influence of the amplitude and frequency of acoustic waves and the helium jet velocity on the process of turbulization and breakup of the jet flow was studied, and the corresponding characteristics were reported.

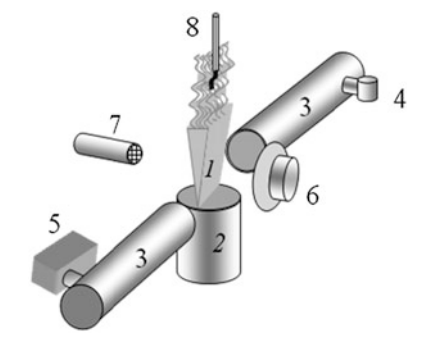
As was demonstrated by means of stroboscopic schlieren visualization and micro-PIV (Particle Image Velocimetry) measurements, when the flow transforms into the turbulent mode, the microjet becomes divided into several (up to four) vortex streets propagating at an angle to the initial microjet direction. The number of these vortex streets and the angle of their propagation depend on the frequency and amplitude of acoustic forcing and on the helium jet velocity. The drawback is the use of helium, because the density and mean velocity of the helium jet behave in a complex manner.

2.2 Stability of a Subsonic Plane Gas Microjet

The experiment with a subsonic plane microjet is schematically illustrated in Fig. 2.1. The helium jet exhausts vertically upward from a slot micronozzle into the atmosphere. The flow field is visualized in the direction of the greater linear scale of the slot micronozzle by a schlieren device. The schlieren device includes a stroboscopic light source, which can be synchronized with the source of acoustic forcing of the microjet for obtaining instantaneous averaged flow fields at given time instants. The visualization patterns are recorded by a digital video camera. The source of acoustic forcing is a loudspeaker with a power of 1 W. The direction of propagation of acoustic waves is normal to the jet plane. The amplitude and frequency of acoustic waves are registered by a microphone.

In the experiments described in this chapter, the stagnation temperature of the helium microjet was equal to room temperature (the temperature of the jet and atmosphere could vary from 293 to 298 K). A photograph of the slot nozzle and its sizes (in micrometers) is shown in Fig. 2.2. It is seen that the aspect ratio of the linear scales of the nozzle is more than 100, and the helium flow can be considered as a microjet only in one direction. The nozzle edge was not absolutely smooth

Fig. 2.1 Scheme of the experiment. 1—a helium jet, 2—slot micronozzle, 3—schlieren device, 4—stroboscopic light source, 5—digital video camera, 6—loudspeaker, 7—microphone, 8—sensor of hot-wire anemometer



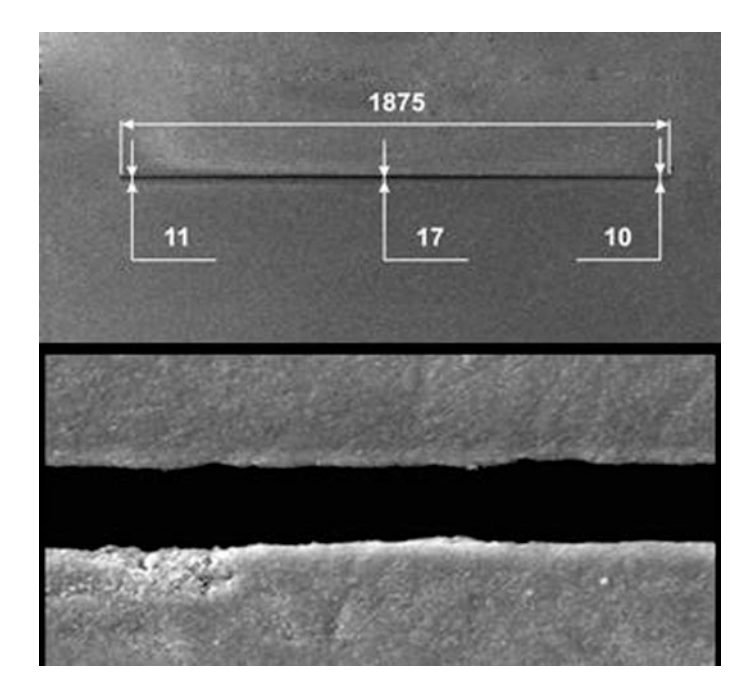


Fig. 2.2 SEM images of a slot nozzle and its increased central part. Size in microns

(the roughness level was about 1 μ m). The use of helium made it possible to apply the schlieren technique to visualize the microjet flow, owing to a significant difference in the refractive indices of helium and air. The ratio of the stagnation pressure of helium to the atmospheric pressure p_0/p_a varied from 1.016 to 1.12, which corresponded to exhaustion of a subsonic helium jet with an initial velocity in the interval $u_0 = 140 \div 370 \,\text{m/s}$. The Reynolds number of the jet based on the nozzle width h and velocity of gas exhaustion at the nozzle exit u_0 was in the interval $Re_h = 23 \div 62$, which corresponds to exhaustion of an initially laminar jet.

Despite the use of helium, the contrast of the schlieren image of the jet was insufficient for direct identification of the flow structure. Therefore, the image contrasting procedure was applied, i.e., the background image was subtracted during digital processing of visualization patterns.

The mass flow rate perturbations generated by the source of acoustic waves in the microjet were measured by an A.A. Lab Ltd constant-resistance hot-wire anemometer with a wire sensor (see Fig. 2.1) 5 μ m in diameter and 2 mm wide within the frequency range from 500 to 50 kHz. The hot wire was aligned normal to the direction of jet exhaustion from the nozzle. The wire sensor could be moved along the jet and across the greater side of the nozzle. For determining the spectral composition and characteristics of nonlinear interaction of disturbances in the jet, the hot-wire signals were processed by means of harmonic and bispectral (Shiplyuk et al. 2003) analysis.

The instantaneous and averaged velocity fields were measured by particle image velocimetry with a DANTEC laser microdiagnostic system. Glycerin tracer particles were simultaneously inserted into the system of helium injection to the micronozzle and to the ambient atmosphere surrounding the jet. The size of the tracer particles was determined in special experiments aimed at studying the velocity of particle deceleration in the shock wave in a supersonic flow. The estimates showed that the mean particle size was 0.25 um. To introduce controlled periodic perturbations, the helium microjet was subjected to the action of monochromatic acoustic waves with intensity L up to 125 dB in the frequency range $f_A = 4 \div 20$ kHz. These acoustic waves were generated by a loudspeaker located near the jet. The measurements of the mean velocity field in the jet flow showed that the flow velocity is already 10 m/s at a distance of 5 mm from the nozzle exit for the initial velocity of helium equal to 140 m/s, which is consistent with calculations of laminar helium jet exhaustion into the atmosphere performed in accordance with Vulis and Kashkarov (1965). Such a drastic decrease in velocity is caused by rapid mixing of the helium jet with ambient air and by the emergence of a dominant air jet flow. The action of intense acoustic waves shifts the beginning of the low-velocity section in the upstream direction to a distance approximately equal to 3 mm from the nozzle exit.

Figure 2.3 shows the stroboscopic patterns of the schlieren visualization of a plane microjet under acoustic forcing for some fixed parameters of jet exhaustion and acoustic forcing. The stroboscopic schlieren visualization was performed for the following constant parameters of the microjet flow: $f_A = 4.25$ kHz and $u_0 = 200$ m/s (Fig. 2.3a), u_0 is the velocity at the nozzle exit; $f_A = 4.25$ kHz and L = 125 dB (Fig. 2.3b); $u_0 = 200$ m/s and L = 120 dB (Fig. 2.3c). Flow field visualization has shown that the helium microjet is not intensely expanded without acoustic forcing or with weak acoustic forcing (less than 40 dB) and propagates in the form of a single-jet flow (see the left-hand photograph in Fig. 2.3a).

Intense acoustic forcing gives rise to rapidly growing sinusoidal disturbances of the jet flow field and breakup of the single-jet flow (see Fig. 2.4). After breakup of the original jet, a flow consisting of several jets with a large angle of expansion is formed (Fig. 2.3a–c). Depending on the acoustic forcing amplitude (Fig. 2.3a), gas velocity at the nozzle exit (Fig. 2.3b), and frequency of acoustic waves (Fig. 2.3c), there may be two, three, or even four individual jets. The process of breakup of the initial jet depends, in a complicated manner, on flow conditions and acoustic forcing intensity and is not yet adequately understood. The maximum expansion of the jet is reached at the acoustic forcing frequency $f_A = 4.25$ kHz for the helium exhaustion velocity $u_0 \cong 200$ m/s (see Fig. 2.3). Within the range of forcing amplitudes L = 110-125 dB, the splitting point location and the jet expansion angle depend weakly on the sound intensity. It should be noted that propagation of acoustic waves along the greater side of the nozzle reduces the efficiency of acoustic forcing of the microjet by an order of magnitude.

The use of PIV and the calculation of the instantaneous vorticity field for the example illustrated in Fig. 2.5 showed that individual plane jets visible in the stroboscopic pictures (see Fig. 2.3) are actually chains of vortices propagating at an

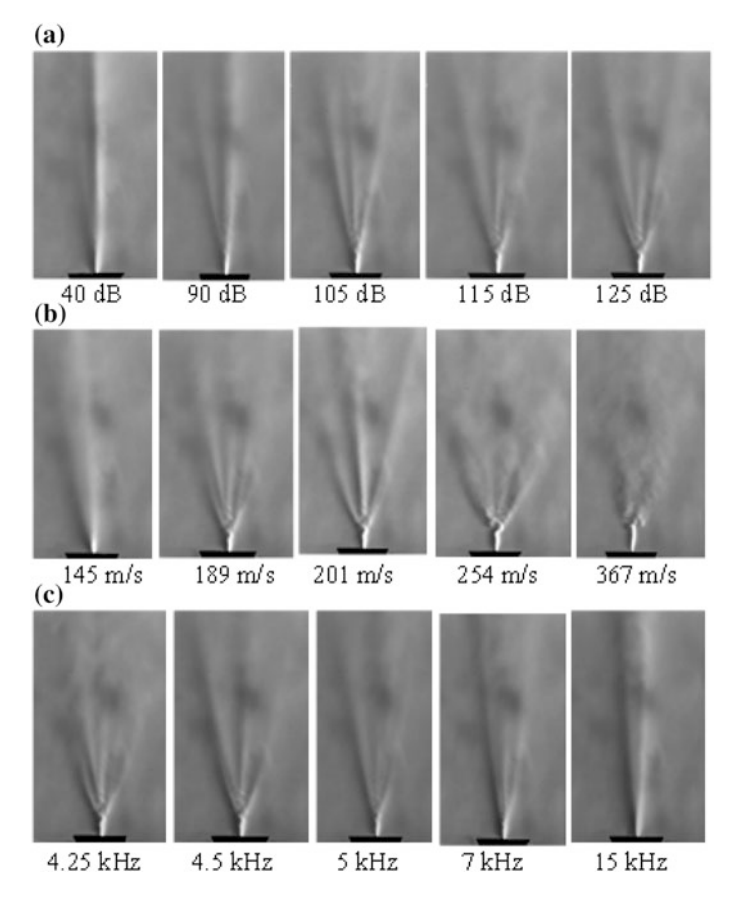


Fig. 2.3 Stroboscopic schlieren-visualization of the flow. $\bf a$ acoustic amplitude is changed, $\bf b$ the velocity is changed, $\bf c$ the frequency is changed

angle to the initial direction of the microjet flow. These vortices arise in the region of the maximum bending and breakup of the microjet and move upward or downward in the plane of the figure (see Fig. 2.5), depending on the direction of rotation.

An effect similar to the Magnus effect in translational motion of a vortex structure is observed here. Vortex structures of this kind were also observed in the case of exhaustion of a colored fluid jet into a transparent fluid (Reynolds et al. 2003). The formation of several pseudo-jets was numerically demonstrated in Danalia and van Boersma (2000) by averaging of the field of an unsteady single-jet flow with vortex structures. As additional (more than two) jets appear under high-intensity forcing, it may be assumed that their origin is caused by generation of new vortex streets by intense paired primary vortices. This process is illustrated in Fig. 2.5, where at least five vortex streets are clearly visible.

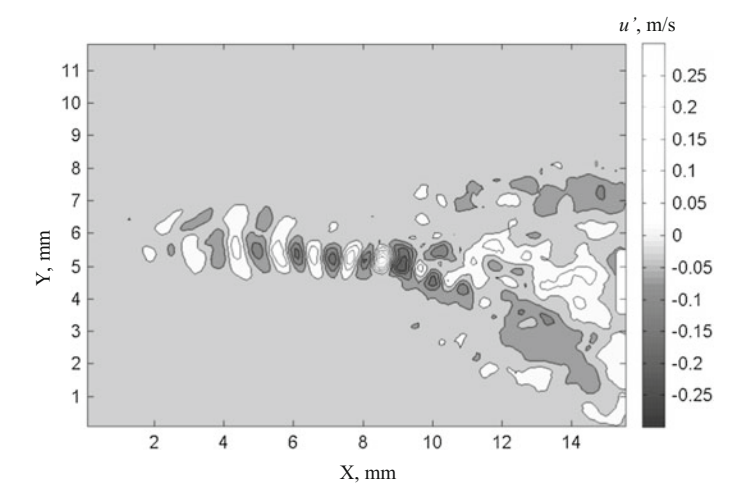
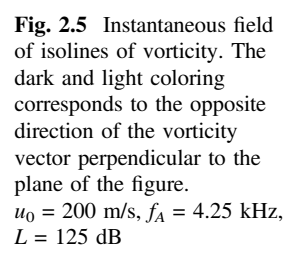
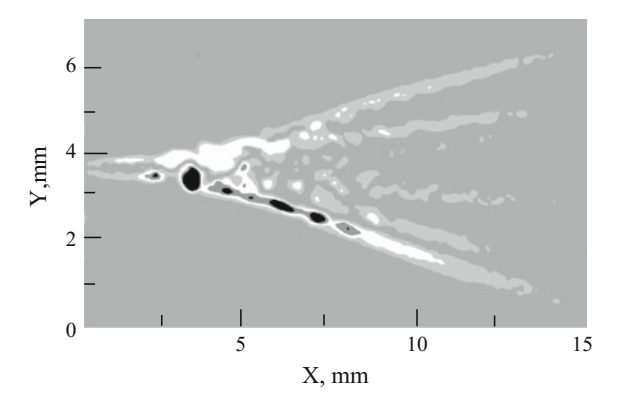


Fig. 2.4 The isolines of instantaneous pulsations of the jet velocity in the acoustic wave vector direction (in the direction of the coordinate Y)





The characteristics of mass flow rate perturbations in the low-velocity part of the jet were measured by a hot-wire anemometer in the range of distances $k = 60 \div 1072$ from the nozzle exit. Here, k = x/h is the dimensionless distance in calibers of the slot nozzle width h. The characteristics of both natural and controlled disturbances were studied. The latter were generated due to acoustic forcing of the jet. If an external acoustic field is applied, intense disturbances at the ground frequency and superharmonic frequency are observed near the nozzle, whereas the flow pattern far from the nozzle includes broadband turbulent oscillations combined with imposed oscillations at the ground frequency.

The dynamics of the spectra of the mass flow rate fluctuations as a function of the dimensionless distance from the nozzle k with different intensities of acoustic forcing of the plane microjet is presented in Fig. 2.6. The amplitudes of the power of oscillations are shown in the form of darkened isolines with the corresponding scales.

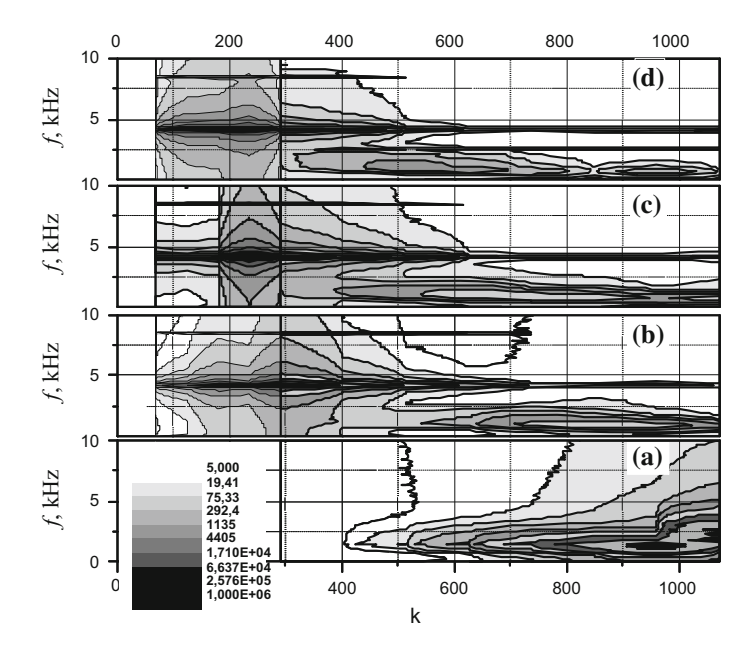


Fig. 2.6 Spectra of the mass flow rate fluctuations with different intensities of acoustic forcing on the jet: $\mathbf{a}\ L = 0$ dB, $\mathbf{b}\ L = 20$ dB, $\mathbf{c}\ L = 90$ dB, $\mathbf{d}\ L = 120$ dB, $u_0 = 220$ m/s, $f_A = 4.25$ kHz

If there is no acoustic forcing, the disturbances start to increase at a distance of about k = 500. They grow within a rather narrow range bounded by the frequencies 0.8-2.9 kHz (Fig. 2.6a). As the distance from the nozzle increases, the range of growing frequencies is enhanced; the spectrum of oscillations gradually covers the entire frequency range available for measurements and acquires the shape typical for turbulent flows with increasing amplitude of oscillations at low frequencies. The amplitude of broadband oscillations continuously increases up to the last measurement section. As the disturbance amplitude increases, nonlinear processes occur, beginning from the distance k = 610 in the frequency range bounded by the peak of natural fluctuations. Further downstream, the amplitude of disturbances and nonlinear interaction are enhanced.

If an acoustic field is applied onto the microjet, a sharp peak corresponding to the ground frequency of acoustic forcing $f_A = 4.2$ kHz, and also peaks of the superharmonics at f = 8.4, 12.6, and 16.8 kHz (the last two harmonics are not shown in the figure), appear in the spectra of the power of the mass flow rate fluctuations. The maximum amplitude of artificial disturbances is reached at a distance $k \approx 290$ (Fig. 2.6b). The superharmonics of artificial perturbations gradually decay in the downstream direction, and the spectra at a distance $k \approx 620$ have only the ground frequency of excitation left. The growth of natural low-frequency oscillations begins approximately in the same cross-section as in the case without

acoustic forcing. As the distance from the nozzle exit increases, however, disturbances are also enhanced, but then start to decay (at $k\approx 900$). Moreover, disturbances at this distance do not grow along the entire measured frequency range. Amplification of disturbances is limited by the frequency of 2.5 kHz. The center of the spectral peak has a lower frequency, which varies from 1.3 to 1 kHz, depending on the distance from the nozzle.

With a further increase in the amplitude of acoustic forcing (Fig. 2.5c), the low-frequency natural oscillations in the jet start to grow noticeably earlier. The low-frequency peak in the spectrum of oscillations can already be detected at a distance $k \approx 400$. Natural disturbances start to decay at distances of about $k \approx 930$, but then these disturbances are moderately enhanced again, beginning from distances $k \approx 1000$. The reason for the repeated growth of disturbances is not clear. As in the previous case, the growth of oscillations is limited by the frequency approximately equal to 2.5 kHz. The center of the spectral peak roughly corresponds to the same frequencies: f = 1.3-0.8 kHz. The maximum of artificial disturbances is shifted closer to the nozzle exit, and the amplitude of artificial perturbations decays faster.

A further increase in the amplitude of the external acoustic field practically does not affect the place where the maximum value of artificial perturbations is observed (k \approx 438, Fig. 2.5d). The harmonics of artificial perturbations already decay at k \approx 510. Enhancement of natural disturbances is shifted even closer to the nozzle exit (k \approx 350). The overall decay of artificial perturbations in the jet also occurs earlier, already at a distance k \approx 820. At k = 870, one can again see the growth of natural oscillations, which decay at k \approx 1040. However, the amplitude of natural disturbances is lower than that in the previous cases.

To identify specific features of nonlinear processes in the microjet, we applied the method of the bispectral analysis of the hot-wire signal, which has become very popular in investigations of boundary layer stability (Shiplyuk et al. 2003). The method ensures quantification of the degree of correlation between flow oscillations at two different frequencies in the spectrum and flow oscillations at a frequency equal to the sum of these two frequencies. This correlation is not equal to zero only if the oscillations at the summed frequency are generated by nonlinear interaction of two above-mentioned oscillations. Normalization of the desired correlation to autocorrelations of each wave in the triad yields the value of bicoherence, which varies in the interval from zero to unity. If the bicoherence value is close to unity, then the third wave is the result of nonlinear interaction of the first two waves. If the bicoherence value is equal to zero, these three waves are absolutely independent of each other. Figures 2.7, 2.8, 2.9, 2.10, 2.11 and 2.12 show the bicoherence spectra for mass flow rate oscillations in some cross-sections of the microjet in the form of darkened isolines corresponding to the bicoherence scale. The spectral on the left and on the right were obtained for the microjet without acoustic forcing and under the action of acoustic waves with the amplitude L = 90 dB, respectively. For convenience, the graphs also show (along the frequency axes) the spectra of the power of oscillations A_f (arbitrary units), which are checked in terms of nonlinear interaction between them. Projections of points in domains with nonzero bicoherence onto the abscissa and ordinate axes yield the values of nonlinearly interacting frequencies of oscillations in the microjet.

The analysis of these spectra shows that the domain of interacting waves expands and fills the entire range of the peak of natural oscillations (500 Hz < f_1 < 4.4 kHz, 500 Hz < f_2 < 2.2 kHz). The bicoherence spectrum displays the center of nonlinear processes at the frequencies f_1 = 1.5 kHz and f_1 = 2 kHz, which yields the third interacting wave with the frequency f_3 = f_1 + f_2 = 3.5 kHz. It is of interest to note that the frequency of the peak of nonlinear interaction (maximum bicoherence) differs from the frequency of the peak of natural oscillations f = 1.3 kHz.

A further analysis of the bicoherence spectra shows that there are already intense nonlinear processes induced by the imposed acoustic field in the first measurement section; these disturbances reach the highest intensity at a distance $k \approx 120-160$. All nonlinear processes are associated with the generation of superharmonics of the wave with the ground frequency $f_A = 4.2$ kHz (Figs. 2.7, 2.8 and 2.9): $f_1 = f_2 = f_A = 4.2$ kHz, $f_3 = f_1 + f_2 = 8.4$ kHz = $2f_A$ —generation of the first superharmonic; $f_1 = 8.4$ kHz = $2f_A$, $f_2 = f_A = 4.2$ kHz, $f_3 = f_1 + f_2 = 12.6$ kHz = $3f_A$ —generation of the second superharmonic, etc.

Beginning from the distance $k \approx 225$, one more type of nonlinear interaction appears at the frequency of the subharmonic of the wave with the ground frequency in bicoherence spectra: $f_1 = f_2 = 2.1$ kHz = $f_A/2$, $f_3 = f_1 + f_2 = 4.2$ kHz = f_A (see Fig. 2.10). Now we have three waves participating in nonlinear interaction: the wave with the ground frequency and its two subharmonics, similar to the situation in the boundary layer. Such interaction suggests that there is a subharmonic resonance. Apparently, it is the subharmonic resonance that is responsible for the earlier growth of natural low-frequency oscillations, which was mentioned above.

Thus, the energy of high-frequency disturbances is pumped via nonlinear interaction to low-frequency perturbations, thereby initiating the growth of the latter.

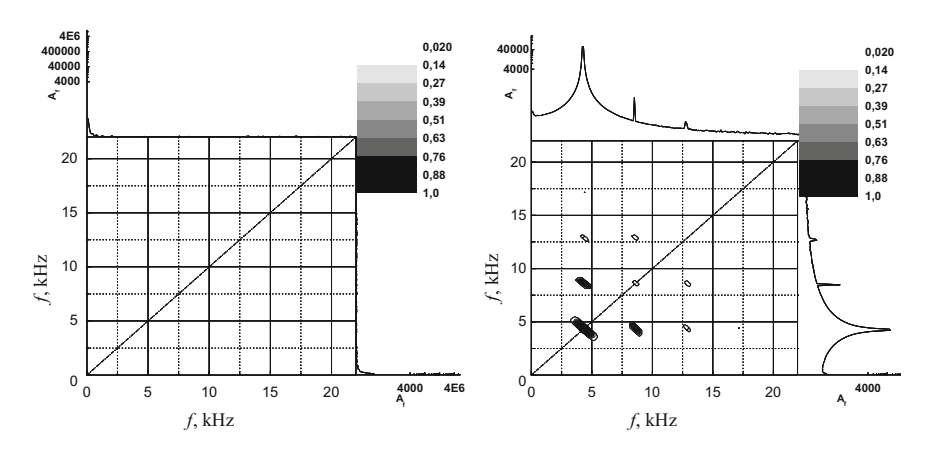


Fig. 2.7 Bicoherence spectra for mass flow rate oscillations, k = 95

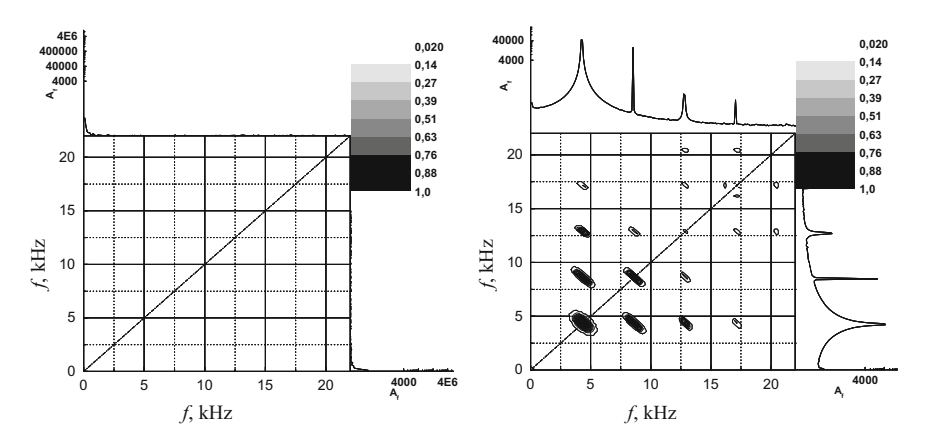


Fig. 2.8 Bicoherence spectra for mass flow rate oscillations, k = 127

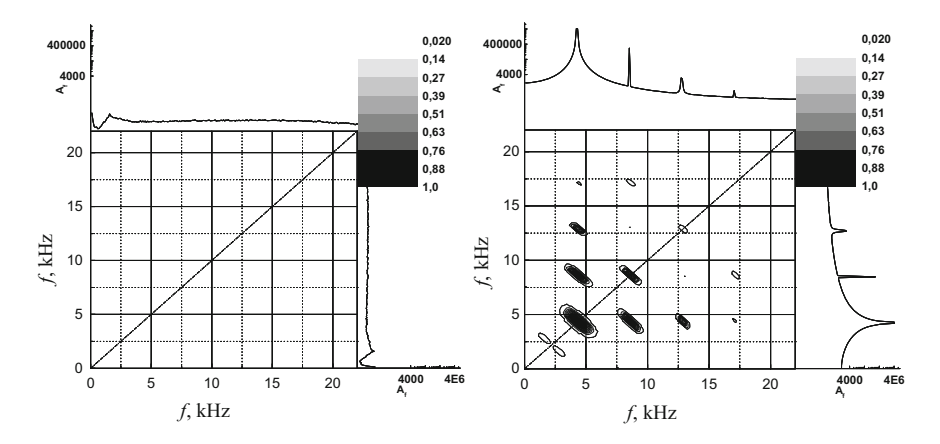


Fig. 2.9 Bicoherence spectra for mass flow rate oscillations, k = 195

As was already noted, similar processes occur in the boundary layer as well. As the distance from the nozzle increases, nonlinear processes associated with the imposed acoustic field gradually decay (see Figs. 2.11 and 2.12). The degree of this decay depends on the amplitude of artificial perturbations. Thus, nonlinear interaction ceases at $k \approx 720$ if the perturbation intensity is 60 dB, $k \approx 610$ at 90 dB, and $k \approx 510$ at 120 dB.

Nonlinear processes associated with natural disturbances in the jet, which correspond to the bicoherence spectra in the left parts of Figs. 2.7, 2.8, 2.9, 2.10, 2.11 and 2.12, slowly increase and reach the maximum intensity at distances where the nonlinear processes induced by the acoustic field are already finished (see the right-hand parts of Figs. 2.10 and 2.11); they are clearly visible even in the last measurement section. It follows from here that the development of natural

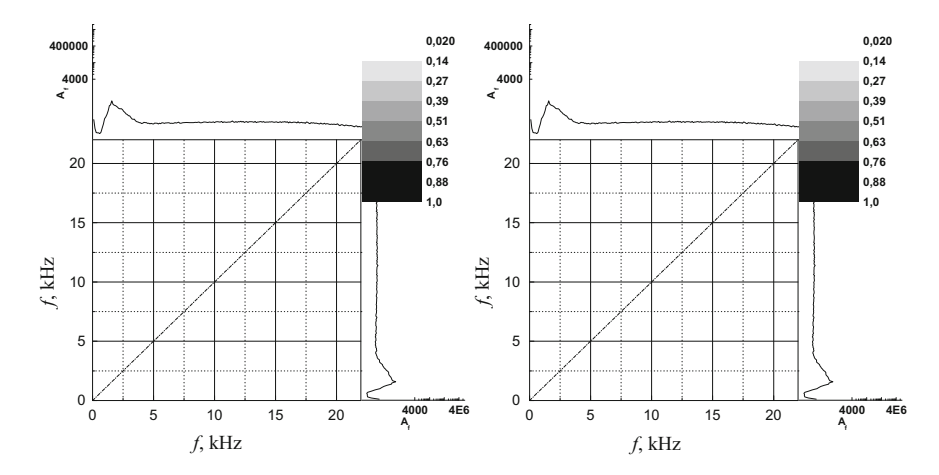


Fig. 2.10 Bicoherence spectra for mass flow rate oscillations, k = 345

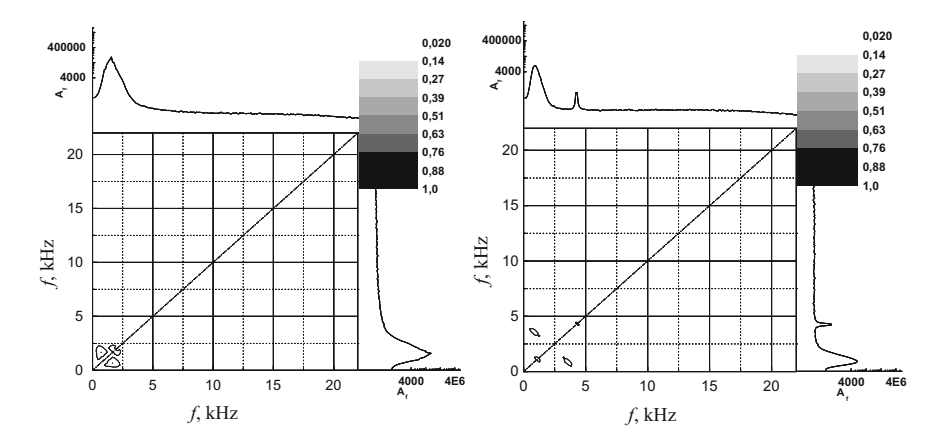


Fig. 2.11 Bicoherence spectra for mass flow rate oscillations, k = 690

disturbances in the microjet passes through the same stages that are typical for macroscopic shear flows.

The maximum receptivity of the microjet to acoustic forcing is observed at characteristic Strouhal numbers based on the helium flow velocity at the nozzle exit u_0 and the minimum micronozzle width h, $Sh = hf/u_0$, smaller than 10^{-3} . A comparison of the values of Sh and the level of acoustic forcing pressure oscillations obtained for the helium microjet with the corresponding data for air macrojets (Ginevskiy et al. 2001) shows that the greatest receptivity of air macrojets is reached at Strouhal numbers $Sh = 0.2 \div 0.3$. The small Strouhal number of the helium microjet can be explained by the fact that it is not absolutely appropriate to use the helium flow velocity at the nozzle exit and nozzle width for calculating the

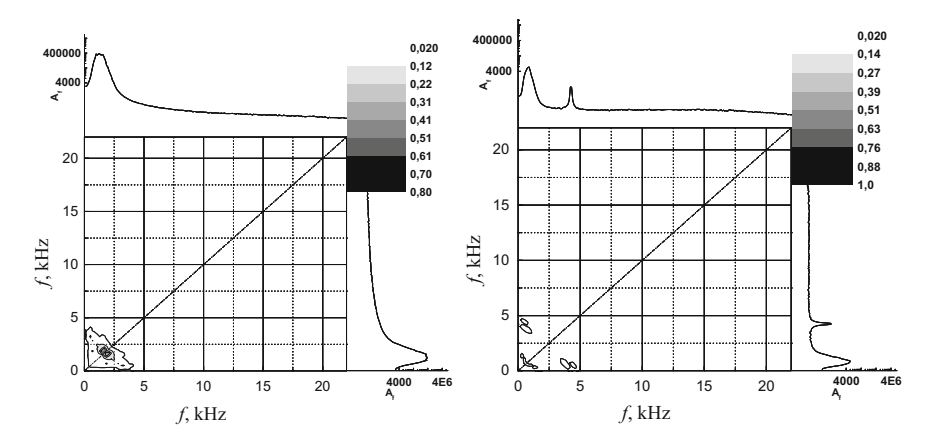


Fig. 2.12 Bicoherence spectra for mass flow rate oscillations, k = 885

Strouhal number. Helium has a comparatively high coefficient of diffusion in air, high frequency of collisions with nitrogen and oxygen molecules, and small relative atomic weight. Therefore, the helium microjet becomes rapidly mixed with ambient air, the flow velocity decreases, and the effective jet width increases. In fact, instability is developed in a low-velocity jet consisting almost completely of air.

The helium jet's receptivity to acoustic forcing is found to be higher than that of macrojets (Ginevskiy et al. 2001). The amplitude of acoustic forcing of the air macrojet needed for excitation is 20–40 dB higher than the amplitude of acoustic forcing necessary for microjet excitation. Thus, nonlinear processes in a subsonic microjet already start near the nozzle at the forcing amplitude of 60 dB, which can be attributed to an extremely thin shear layer near the nozzle and a comparatively small fraction of the potential flow, which is typical for plane microjets.

2.3 Structure and Characteristics of Stability of Supersonic Axisymmetric Microjets

2.3.1 Experimental Equipment

The experimental equipment, techniques, and results of studying the structure and characteristics of stability of supersonic underexpanded nitrogen microjets briefly outlined in Aniskin et al. (2011) are described in detail below.

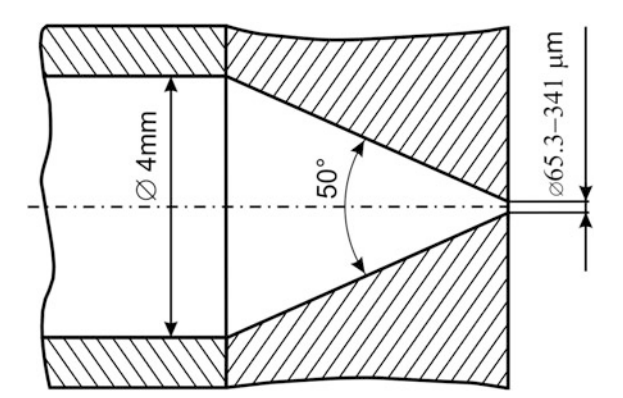
The micronozzle was a connecting pipe for pneumatic pipelines with bayonet fastening, which allowed for easy replacement of the nozzles. A hole was drilled in the connecting pipe, and a tube for measuring the pressure in the settling chamber was welded to this hole. The pressure was measured by a Honeywell sensor with a measurement range from 0 to 10 atm.

The connecting pipe was fixed onto a special table with a Plexiglas base and an arrester plate made of the same material attached normal to the base. The pipe axis was parallel to the table foundation and simultaneously perpendicular to the arrester. After that, a brass cylinder was tightly inserted into the pipe; one end of the cylinder was conically sharpened. The cone angle was 50° . The roughness of the conical cylinder was determined by a ZYGO 6200 microscope; its level was within $1-2~\mu m$. The tip of the conical part of the cylinder protruded from the pipe end by 3.5 mm and rested on the arrester plate on the table. After that, the conical part of the cylinder (i.e., the space between the arrester and the pipe end face) was filled with a photopolymer. After some time necessary for photopolymer solidification, the arrester was removed and the cylinder was withdrawn. Thus, nozzles with diameters of 341, 215, 149, and 65.3 μ m were fabricated. The geometry of these nozzles is shown in Fig. 2.13. Each time before nozzle fabrication, the cone was ground off to a needed diameter.

Nozzles with diameters smaller than 65 μ m were fabricated in two stages. The first stage is described above and consisted in fabricating a nozzle with a diameter of about 300 μ m. At the second stage (see Fig. 2.14), a cylindrical needle with double conical sharpening was fabricated. The needle was first ground off at an angle of 5.5°, and then at an angle of 22°. After that, the needle was inserted into the connecting pipe (with the already fabricated nozzle approximately 300 μ m in diameter) and was fixed there. The sharpened tip of the needle protruded from the nozzle fabricated at the first stage and rested on the arrester plate. After that, the photopolymer was poured (with subsequent polymerization), the arrester plate was separated, and the needle was removed. In this way, nozzles with diameters smaller than 5 μ m were fabricated. First, the nozzle with the smallest diameter was fabricated, then the needle was sharpened to a needled diameter and the nozzle with a greater diameter was fabricated, etc. The geometry of the thus-fabricated micronozzles is shown in Fig. 2.14. All nozzles were sonic, i.e., they had no expanding portion.

Figure 2.15 shows the nozzle exit images taken by the electron microscope (the ratio of the scales of different images is not retained). There are dust particles at the

Fig. 2.13 Sketch of nozzles with a diameter of $341-65 \mu m$



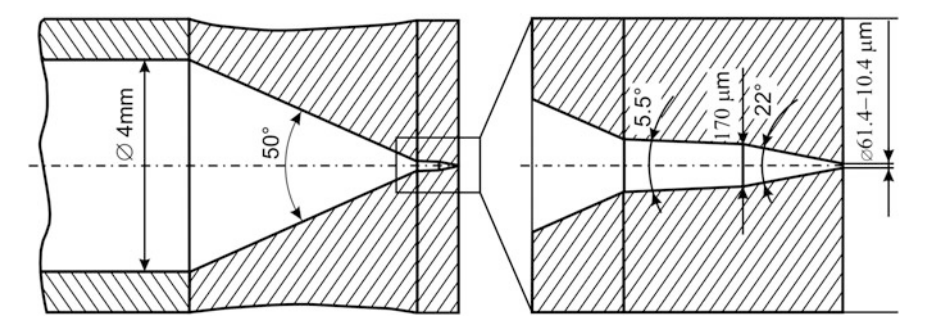


Fig. 2.14 Sketch of nozzles with a diameter less than 65 μm

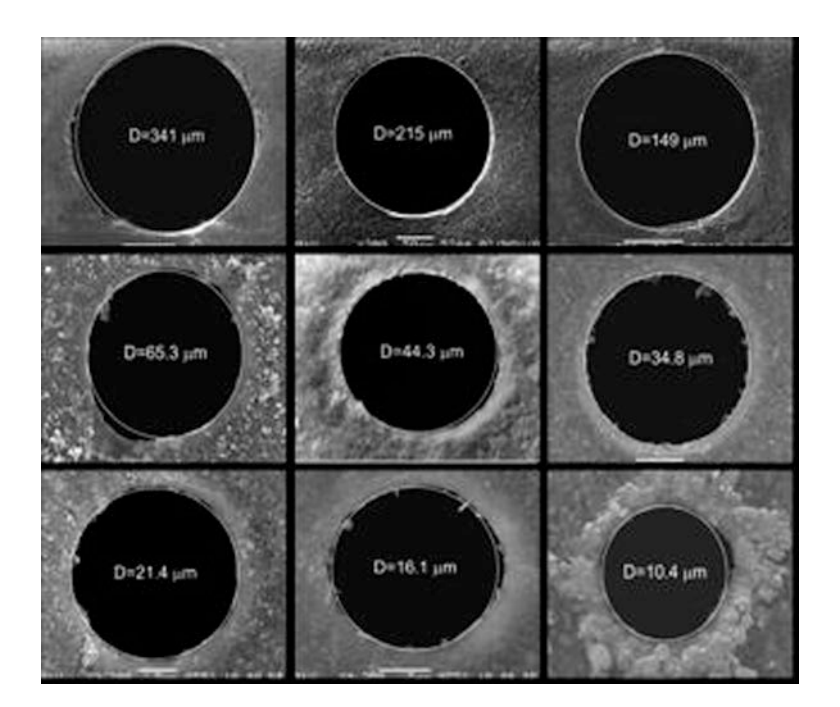


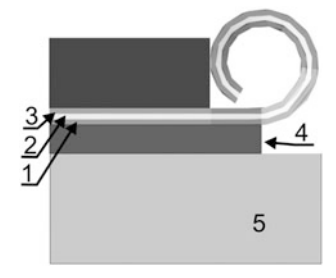
Fig. 2.15 Scanned electron microscope images of the micronozzle outlets

edges of some nozzles, which are shed away during the first test performed in them. Some nozzles have deviations from the inscribed circle shape, e.g., nozzles 341 or 149 μ m in diameter. Moreover, it cannot be definitively argued that the nozzle edges are absolutely smooth. The data on the maximum deviations of the nozzle exit shape from a circumference, the absolute roughness levels, and the estimates of the relative roughness level from above based on the absolute level are summarized in Table 2.1. Here, D is the nozzle diameter and Δ is the maximum deviation of the nozzle exit shape.

D (μm)	341	215	149	65.3	61.4	54.5	44.3	36
Δ (μ m)	5	1	1	1.5	1.8	1.1	1.1	1
δ	0.015	0.0057	0.007	0.023	0.029	0.02	0.025	0.028
D (μm)	34.8	26	24.3	21.4	18.4	16.1	10.4	
Δ (μ m)	1	0.9	1	1.1	0.9	0.5	0.4	
δ	0.029	0.035	0.04	0.05	0.049	0.028	0.034	

Table 2.1 The roughness of the micronozzles

Fig. 2.16 Cross-sectional view of the microtube; 1 compressed layer; 2 stretched layer; 3 conducting layer; 4 sacrificial layer; 5 substrate



Several methods are usually used for studying the structure of supersonic jets: schlieren visualization, hot-wire anemometry, PIV, and Pitot tube measurements. Some of these methods are principally inapplicable for studying microjet characteristics, while others can be used to a limited extent. Among the above-mentioned techniques, the best tool for studying the structure of sufficiently small supersonic microjets is the Pitot tube. In this case, microtubes can be used as the Pitot tube taps; the fabrication technology of these microtubes was described in Prinz et al. (2000, 2001), Golod et al. (2001), Vorob'ev and Prinz (2002). The microtube is formed from a stressed heterofilm, which is rolled due to internal stresses when it is peeled off from the substrate. The cross-sectional view of the microtube is illustrated in Fig. 2.16 (Seleznev et al. 2009). The tube diameter is determined by the thickness of the rolling heterofilm and by the values of elastic stresses in the film; in the molecular beam epitaxy process, it is defined with extremely high accuracy within the range from hundreds of micrometers to several nanometers.

These microtubes were used as a basis for fabrication of a miniature Pitot tube (Fig. 2.17). The tube consisted of three elements: pressure tap, pipeline, and receiver tube. The pressure tap was a Honeywell sensor with a pressure range from 0 to 7 atm.

The pipeline was made of a glass tube bent at an angle of 90° – 120° . The glass tube length was 15–20 mm, and its external diameter was 0.3–0.4 mm. One end of the glass tube was tightly attached directly to the pressure tap. The other end of the tube was constricted and contained the receiver microtube. The tube constriction was provided by pulling the glass tube in the air above the alcohol burner flame, with the tube then being broken in the narrowest place. The space between the

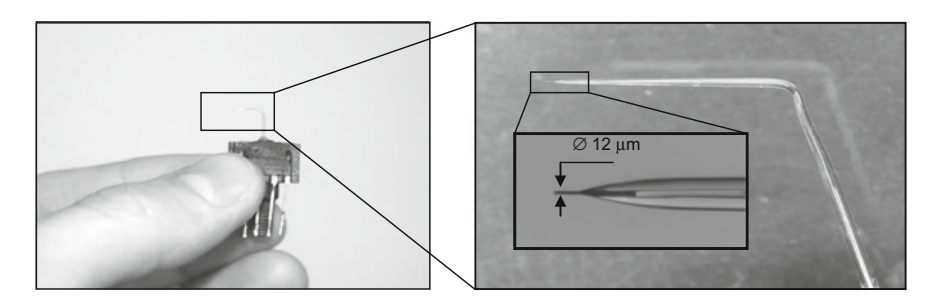


Fig. 2.17 Pitot microtube (the inserts are made with ever increasing magnification)

internal surface of the glass tube and the microtube was filled with the epoxy compound.

The receiver microtube had an outer diameter of 12 μ m, and the thickness of the tube wall was about 0.1 μ m. The design of the Pitot microtube structure ensured the minimum volume. A typical time of pressure stabilization in the microtube was determined experimentally, based on the time needed for the pressure to reach a constant value, and was found to be smaller than a second.

It should be noted that a sufficiently large outer diameter of the glass tube is required by the strength condition (at the end, the glass tube has a diameter on the order of 100 μm). The point is that the glass tube starts to vibrate if its diameter is too small, e.g., 50 μm , as was observed experimentally, especially near the nozzle. The amplitude of these vibrations can reach 200 μm . It should also be noted that the end face was specially sharpened to have a streamlined shape before the microtube was inserted into the tube.

2.3.2 Experimental Arrangement and Measurement Conditions

All experiments were performed with nitrogen as a test gas. The nitrogen was at room temperature and escaped into the atmosphere. The experimental arrangement is shown in Fig. 2.18. A pressurized gas was injected into the settling chamber after passing through three filters: 10, 1.4, and 0.45 μ m. Such severe requirements for gas purity are caused by the small diameter of the microtube and the submicrometer thickness of the tube wall. Without triple cleaning of the gas, fine particles either break the microtube or become deposited on the internal surface and plug the tube, thus making the latter unsuitable for measurements.

The microtube was fixed onto a holder, which was moved in space by a Narishige NT-88E micromanipulator with accuracy of $\pm 1~\mu m$ in three mutually perpendicular directions. The Pitot microtube's position was monitored by a Nikon SMZ1500 stereoscopic microscope. The data from the pressure sensors were reflected by a microvoltmeter and recorded on a computer.

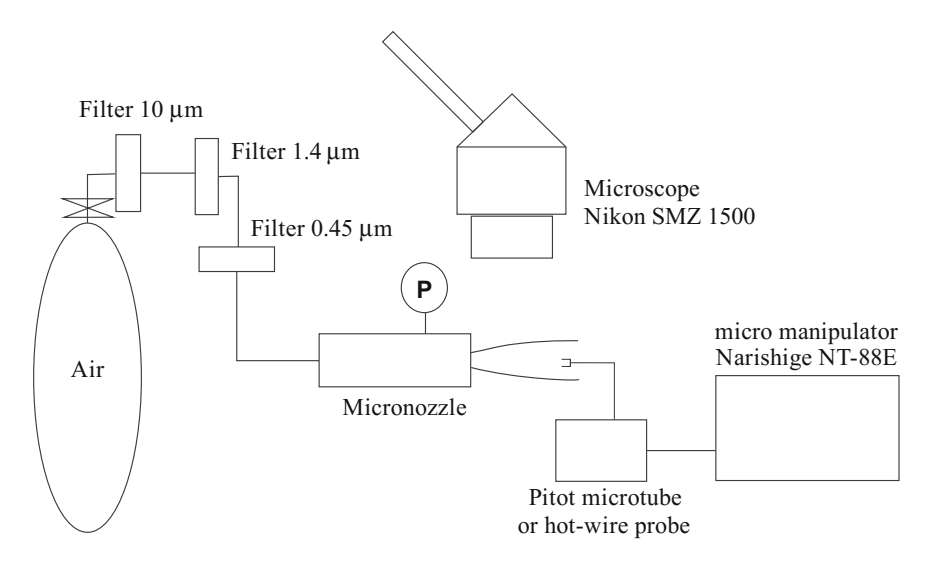


Fig. 2.18 Sketch of the experiment

A problematic aspect of the experiments was the lack of coincidence of the jet axis and the line of Pitot microtube motion. The maximum misalignment was about one degree, which corresponds to a deviation of 9 μ m from the jet axis at a distance of 500 μ m.

Three domains are usually identified in a supersonic jet: the basic part of the jet (with a self-similar velocity profile), the initial part, and the transitional region. In the basic part of the jet, the pressure profile measured by the Pitot tube has a bell-shaped form. In this region, the Pitot tube was tuned to the maximum readings of the microvoltmeter. This served as a criterion verifying that the Pitot microtube is located at the jet axis. In the initial section of the jet, the criterion that confirmed the Pitot microtube location at the jet axis was the maximum or minimum readings of the microvoltmeter. In the transitional region, the hat-shaped profile ultimately transforms into the bell-shaped profile, and this reconstruction is sometimes asymmetric. As a result, the clear criterion (extreme readings of the microvoltmeter exactly at the jet axis) is no longer valid, and data scatter is most often observed in this region.

First, the Pitot microtube was placed at the nozzle exit and was then moved along the jet. The step of Pitot microtube motion along the jet axis was varied from 2 to 20 μm depending on the nozzle diameter. After one, two, or three steps (depending on the position at the axis), the Pitot microtube's position with respect to the jet axis was checked.

The test conditions are listed in Table 2.2. The pressure in the settling chamber was varied from 2 to 8 atm. The maximum pressure in the settling chamber was determined, on the one hand, by the strength of the connection of the gas supply system fittings and, on the other hand, by the microtube's strength. Here, NPR is the

D (μm)	NPR	JPR	M	Re_D	Kn
341	$2.2 \div 5.7$	1.2 ÷ 3	$1.1 \div 1.8$	$10857 \div 27875$	0.0001
215	$2.3 \div 7.4$	1.2 ÷ 4	1.1 ÷ 2	6938 ÷ 22817	0.00016
150	$2.1 \div 7.3$	$1.1 \div 3.9$	$1.1 \div 2$	4560 ÷ 15682	0.00023
65.3	2.2 ÷ 7.2	1.2 ÷ 3.8	1.1 ÷ 2	2098 ÷ 6771	0.00052
61.4	$2.1 \div 6.9$	$1.1 \div 3.7$	1.1 ÷ 1.9	1805 ÷ 6102	0.00058
44.3	$1.9 \div 5.8$	1 ÷ 3.1	$1.1 \div 1.8$	1233 ÷ 3710	0.00082
34.8	$2.1 \div 7.2$	$1.1 \div 3.8$	1.1 ÷ 1.9	1068 ÷ 3568	0.001
21.4	2.2 ÷ 6.3	1.2 ÷ 3.4	1.1 ÷ 1.9	669 ÷ 1946	0.0016
16.1	2.3 ÷ 7.6	1.2 ÷ 4	1.2 ÷ 2	529 ÷ 1759	0.002
10.4	2.1 ÷ 7.8	$1.1 \div 4.1$	$1.1 \div 2$	312 ÷ 1163	0.0033

Table 2.2 Flow parameters in experiments

nozzle pressure ratio, i.e., the ratio of the pressure in the settling chamber to atmospheric pressure. The jet pressure ratio (JPR) is the ratio of the pressure at the nozzle exit to atmospheric pressure. The value of JPR is smaller than NPR by a factor of $[1+(\gamma-1)/2]^{\gamma/(\gamma-1)}$. The jet is underexpanded at JPR > 1 and overexpanded at JPR < 1.

The number M in the table is the Mach number of the so-called design (completely expanded) jet. The Reynolds number Re_D was calculated on the basis of the nozzle diameter and flow parameters at the nozzle exit. The value of Re_D was linearly related to n. The Knudsen number Kn was determined as the ratio of the Mach number M to $\sqrt{JPR} \cdot Re_D$, and Table 2.2 shows the maximum values of this ratio for the examined ranges of M, JPR, and Re_D . In fact, the Knudsen number was determined on the basis of the length and flow parameters in the first cell (barrel) of the wave structure of the jet. It can be seen from the table that jet flows correspond to a continuous medium. The accuracy of pressure assignment in the settling chamber of the micronozzle was 3% within the pressure range from 2 to 4 atm and 1% for pressures higher than 4 atm. The accuracy of Pitot microtube mounting at the nozzle exit was 0–5 μ m. The nominal error of the pressure sensors was $\pm 0.25\%$. In all cases, the size of the symbols in the graphs presented below is greater than or equal to the measurement error.

2.3.3 Measurement Results

Figures 2.19, 2.20, 2.21 and 2.22 show the total pressure distributions along the microjet axis measured by the Pitot microtube and normalized to the total pressure at the nozzle exit p'/p_0 as functions of the normalized distance from the nozzle exit X/D. Different curves in the graphs show the results for different jet pressure ratios. [AU: I didn't see an 'n's in any of the graphs, so I assumed this was a typo.] It is seen that the total pressure displays periodic oscillations along the jet axis. They are

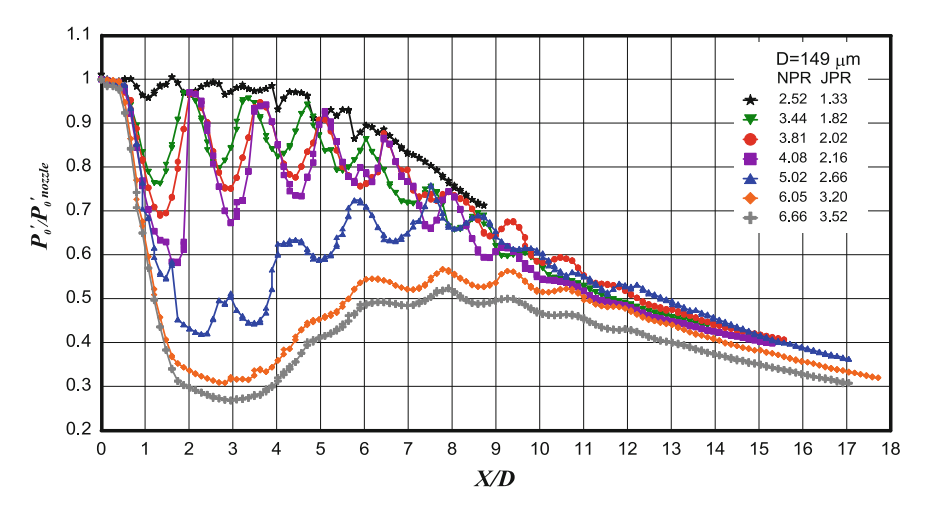


Fig. 2.19 Axial distribution of the total pressure. The nozzle diameter is $149 \mu m$

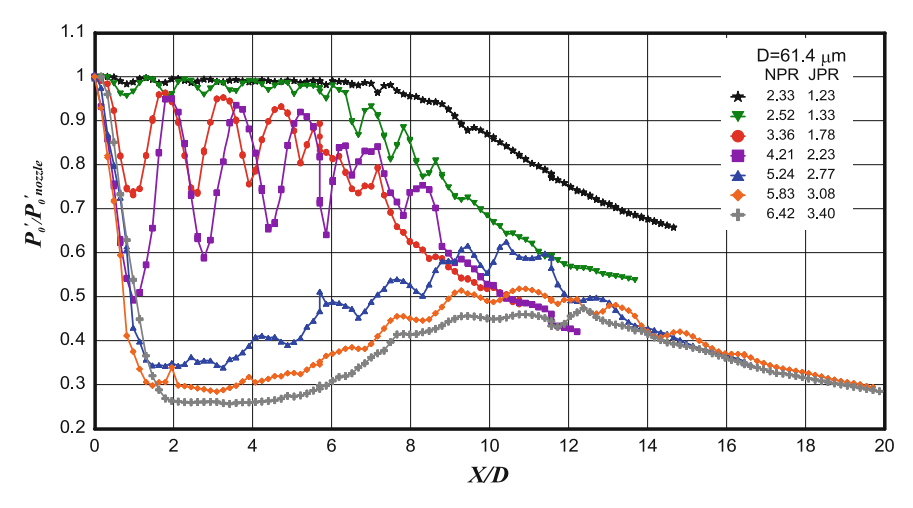


Fig. 2.20 Axial distribution of the total pressure. The nozzle diameter is $61.4 \mu m$

caused by the existence of the shock wave structure (cells of the wave structure) in the underexpanded jet. It can be noted that the first and even the second cell is hard to identify at JPR > 3, and it is next to impossible to determine their positions, which is typical for jets of all diameters. Moreover, it was found that a large number of cells of the wave structure are formed in jets escaping from the nozzles with the diameters 34.8, 21.4, and 16.1 μ m within a very narrow range of pressures.

Thus, for example, 28 cells of the wave structure were observed in the jet being exhausted from the 21.4- μ m nozzle and 35 cells were detected in the jet escaping from the 16.1- μ m nozzle, which was not observed in macroscopic,

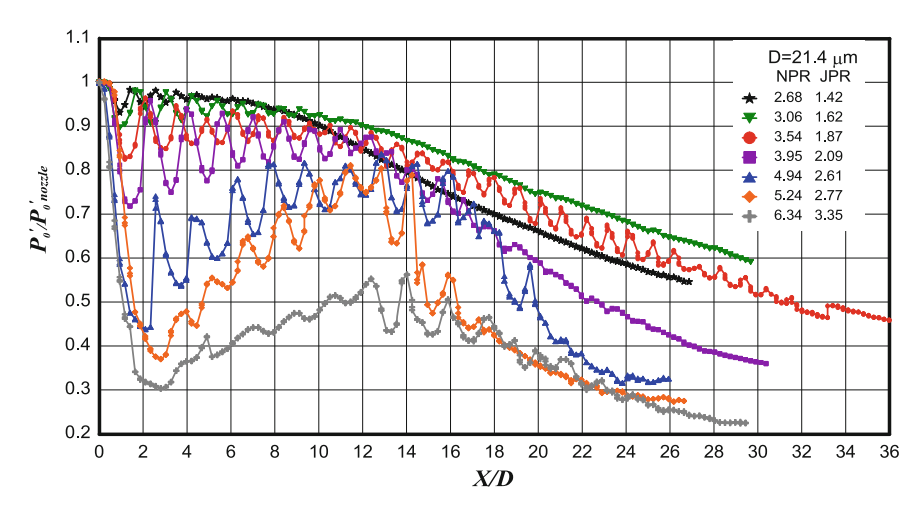


Fig. 2.21 Axial distribution of the total pressure. The nozzle diameter is $21.4 \mu m$

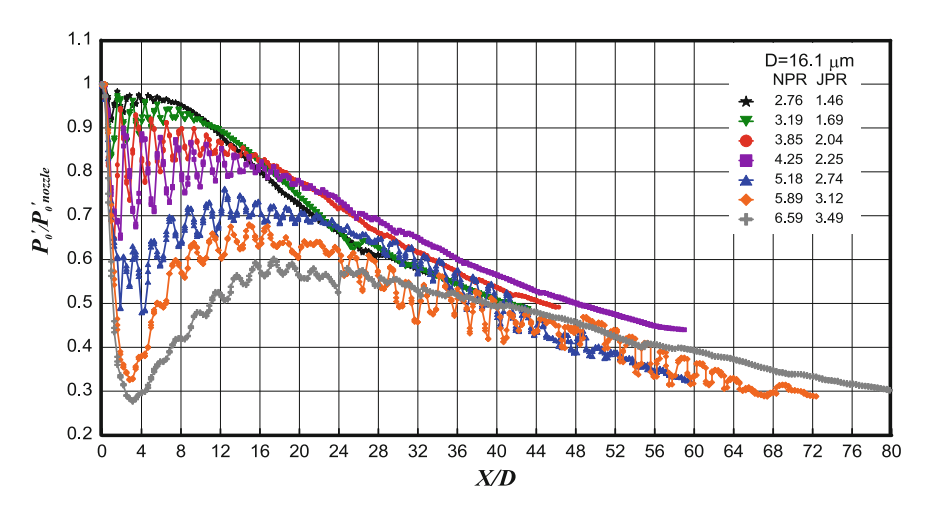


Fig. 2.22 Axial distribution of the total pressure. The nozzle diameter is 16.1 μm

underexpanded jets. At pressures in the settling chamber higher or lower than this range, the number of cells is not that large. The smaller the nozzle diameter, the greater the range of existence of the "multi-cellular" flow regime. For the jet being exhausted from the 34.8- μ m nozzle, this regime was observed only at one value of the jet pressure ratio JPR = 1.6. For the jet escaping from the 21.4- μ m nozzle, this flow regime existed within a certain range of the jet pressure ratios JPR = 1.82 \div 1.89. The greatest interval of existence of the multi-cellular regime was found in the microjet being exhausted from the 16.1- μ m nozzle: JPR = 2.74 \div 3.12.

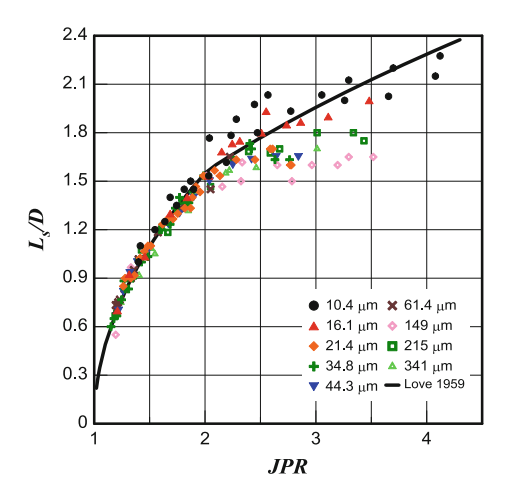
Such regimes were not observed in jets escaping from the 44.3 and 10.4-µm nozzles. Strictly speaking, it does not mean that they do not exist. Possibly, the interval of existence of the multi-cellular regime for the jet escaping from the 44.3-µm nozzle is so small that it could not be detected in the present experiments. For the jet being exhausted from the 10.4-µm nozzle, this regime may be located within the range of the jet pressure ratios that was not reached in these experiments.

It is known that the cell size of the wave structure in jets escaping into a submerged space permanently decreases with increasing distance from the nozzle because of mixing layer thickening and flow deceleration. The sizes of the second, third, and fourth cells were mainly used to determine the mean cell size l_a . At small jet pressure ratios, only the second cell size or, if the third cell could be detected by the Pitot microtube, the second and third cell sizes were taken for this purpose.

At JPR > 3, when it was impossible to determine the end of the first cell and the beginning of the second cell, the sizes of the third and fourth cells were used. The data obtained are shown in Fig. 2.23. The solid curve is the approximation of the experimental data for the air macrojet escaping from the 14-mm nozzle (filled circles) measured in the schlieren photographs. It is seen that the data for all microjets coincide with each other up to the jet pressure ratio JPR < 2 and lie slightly higher than the dependence for the macrojet, but the qualitative agreement is fairly good. The experimental data for JPR > 2 are considerably scattered, but they are still also consistent with the dependence for the macrojet. This good agreement shows that a decrease in the nozzle diameter does not exert any noticeable effect on the wave structure of the jets.

As is seen from Fig. 2.15, there is noticeable roughness on the micronozzle edges. For small-diameter nozzles, the relative roughness level is sufficiently high. Therefore, good agreement of the mean cell sizes for all microjets in Fig. 2.23 also suggests that the nozzle edge roughness produces a weak effect on the gas-dynamic structure of the jet flow. Nevertheless, the deformation of the jet flow boundary was measured in the first cell of the microjet being exhausted from the 23- μ m nozzle at

Fig. 2.23 The average shock cell size versus JPR



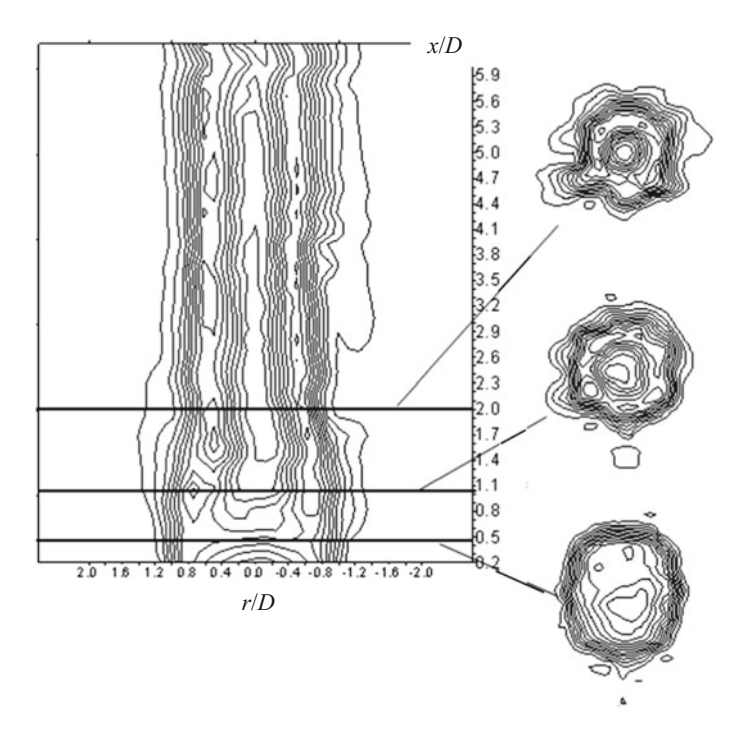


Fig. 2.24 Isolines of total pressure along a microjet and in three sections of the first shock cell

JPR = 3.8. Figure 2.24 shows the results of these measurements for three cross-sections. The jet boundary deformation is enhanced with distance from the nozzle, which was observed earlier for plane supersonic underexpanded microjets (Fomin et al. 2010). For macroscopic jets, this phenomenon has been known for a long time; it is attributed to the development of the streamwise Görtler vortices in underexpanded jets.

Using the total pressure distribution at the jet axis, we studied the supersonic core length of the jet. It was determined as the distance from the nozzle exit to the point where the gas velocity reaches the local velocity of sound and the pressure in the Pitot tube reaches 1.89 atm. The supersonic core length of the microjet normalized to the nozzle diameter L_c/D is plotted in Figs. 2.25, 2.26 and 2.27 as a function of the jet pressure ratio n. The solid and dotted curves are the generalized dependences of the normalized supersonic core length for macroscopic turbulent jets obtained in Shirie and Siebold (1967), Pogorelov (1977).

The data obtained for microjets escaping from the largest nozzles agree well with the generalized dependences for turbulent macrojets (Fig. 2.25). They are also consistent with the experimental data (Phalnicar et al. 2008) for nozzles 200 and 400 μ m in diameter.

Figure 2.26 shows the data for microjets being exhausted from intermediate-size nozzles (61.4 \div 21.4 μ m in diameter). In this case, the microjet's supersonic core

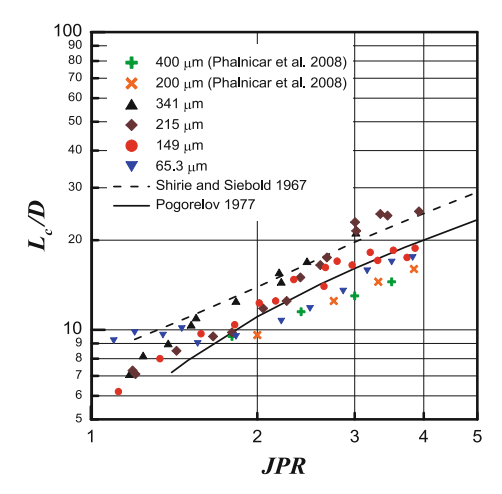


Fig. 2.25 The normalized supersonic core length versus the jet pressure ratio for the jets escaping from nozzles with a diameter from 400 to 65.3 μm

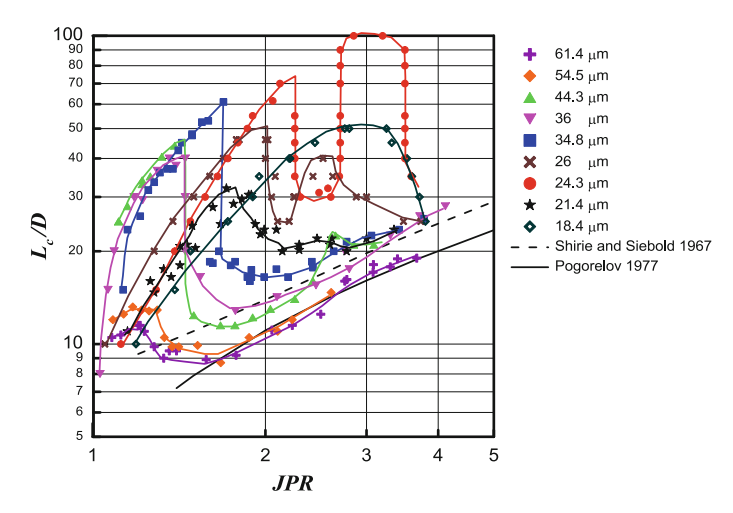
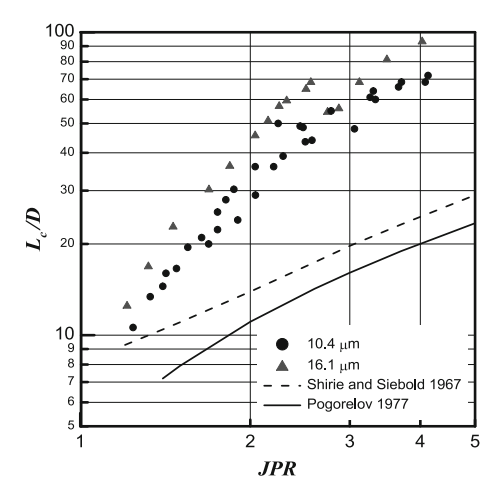


Fig. 2.26 The normalized supersonic core length versus the jet pressure ratio for the jets escaping from nozzles with a diameter from 61 to 21 μm

length appreciably (several-fold) increases and then drastically decreases to the supersonic core length of turbulent macrojets. Finally, the pattern for jets escaping from the smallest nozzles is essentially different (Fig. 2.27).

Here, the supersonic core length of the jet also significantly exceeds the corresponding values for macroscopic jets, and the supersonic core length of the jet does not decrease to the level of the generalized dependences for macrojets within the entire examined range of the jet pressure ratios. Drastic reduction of the supersonic

Fig. 2.27 The normalized supersonic core length versus the jet pressure ratio for the jets escaping from nozzles with a diameter from 16.1 to 10.4 μm



core length of the microjet with an increase in the jet pressure ratio is associated with the laminar-turbulent transition. This fact was demonstrated by means of measuring the intensity of the mass flow rate oscillations at the microjet axis performed by a hot-wire anemometer.

Figure 2.28 shows the isolines of the intensity of the mass flow rate oscillations in the plane of the frequency f versus the normalized distance along the jet axis X/D for three points of the dependence L_c/D (JPR). Brown regions in these plots correspond to higher intensities of oscillations. It is seen that the spectrum does not substantially contain oscillations before the supersonic core length decreases. However, the mass flow rate oscillations are drastically enhanced immediately after reduction of the supersonic core length. Further on, as the distance increases, the frequency spectrum of oscillations is expanded. This fact shows that instability in the microjet is convective rather than global. Otherwise, these oscillations would be detected over the entire length of the microjet.

An interesting phenomenon was detected in the range of nozzle diameters from 30 to 20 µm. The supersonic core length of the microjet decreased with increasing jet pressure ratio due to the laminar-turbulent transition and then started to increase again (see Fig. 2.29). The intensity of oscillations in the microjet decreased in this case. The repeated increase was observed only in a comparatively moderate interval of the jet pressure ratios; however, with a further increase in JPR, the supersonic core length of the jet decreased again to the corresponding values for turbulent macrojets. Intense oscillations of the mass flow rate at the microjet axis were observed in the entire region of supersonic core length. Moreover, the length of the second region in terms of the value of JPR, where the supersonic core length of the microjet increased, becomes greater as the nozzle diameter decreases (cf. the data in Fig. 2.29).

To illustrate the situation, let us combine hot-wire measurements for different jet pressure ratios and construct isolines of integral oscillations in the coordinates

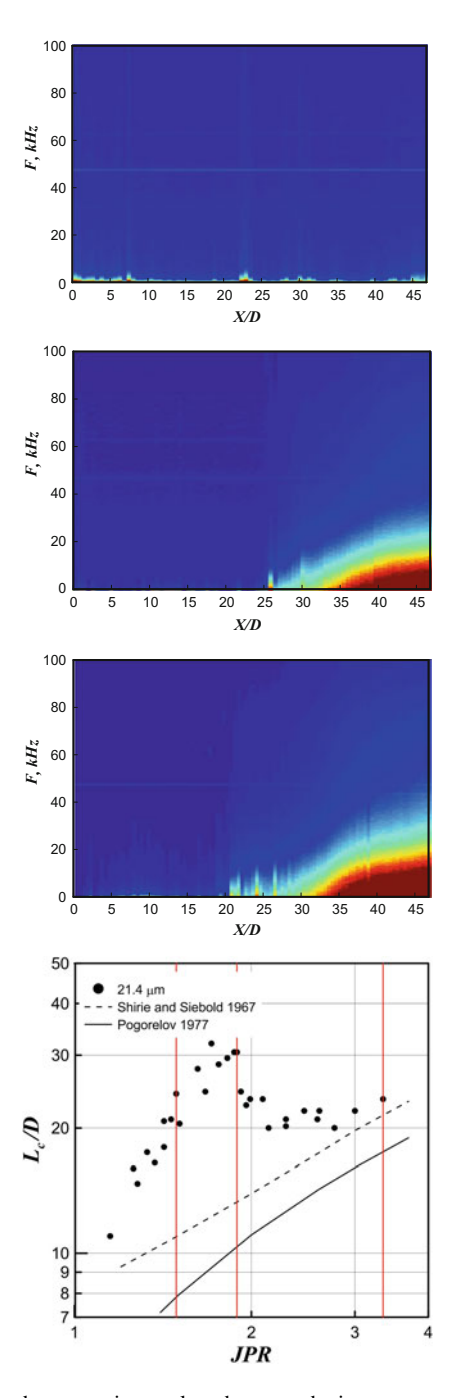
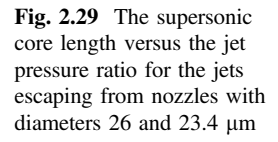
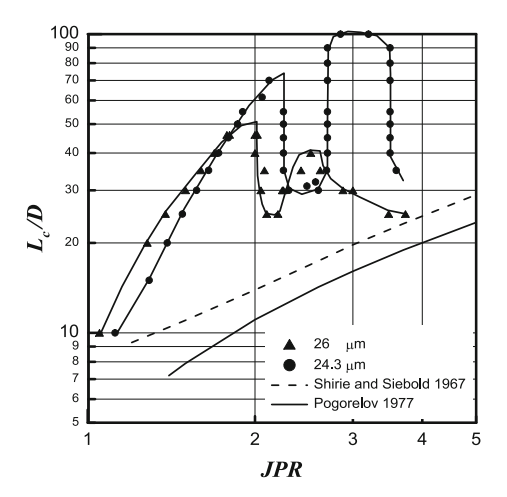


Fig. 2.28 The normalized supersonic core length versus the jet pressure ratio for the jets escaping from nozzles with a diameter 21.4 μ m and spectra of mass flow pulsations along the jet axis for three values of the jet pressure ratio: *I*—JPR = 1.49; 2—1.89; 3—3.35





JPR $-L_c/D$. We also construct the supersonic core length of the jet curves in the same coordinates and impose them onto the plots obtained from the hot-wire measurements. Let us compare the domains of drastic changes in the supersonic core length with regions where elevated oscillations were obtained by means of hot-wire anemometry (i.e., the laminar-turbulent transition).

Examples of such comparisons for jets escaping from the nozzles less than 60 μ m in diameter are given in Fig. 2.30. The red lines in these graphs show the value of the integral oscillations from which their growth begins. This curve actually indicates the position of the laminar- turbulent transition in the jet as a function of the jet pressure ratio. The solid and dotted curves are the generalized dependences of the supersonic core length for turbulent macrojets (Pogorelov 1977; Shirie and Siebold 1967). These dependences play a key role in the analysis of the plots in Fig. 2.30.

As is seen in these figures, the jet is turbulized almost instantaneously. If the supersonic core length is greater than that of turbulent macrojets, the jet turbulization point clearly correlates with the location of the laminar-turbulent transition in the jet. If the laminar-turbulent transition point is shifted closer to the nozzle, the supersonic core length becomes consistent with the generalized dependences for turbulent macrojets and independent of the position of the laminar-turbulent transition in the mixing layer of the jet.

Thus, the increase of the supersonic core length of microjets is associated with the laminar character of the flow in these jets. Vice versa, the decrease in this length is caused by jet flow turbulization and by enhancement of oscillations in microjets. The repeated increase in the microjet length is associated with flow relaminarization, which is observed, however, in a very narrow interval of the jet pressure ratios. For small microjet diameters, the laminar-turbulent transition is absent in the examined range of the jet pressure ratios (Fig. 2.27).

To determine the influence of the roughness of the micronozzle edge on the supersonic core length of the microjet, we performed measurements with micronozzles 44.3, 34.8, 21.4, 16.1, and 10.4 μm in diameter with rough edges at

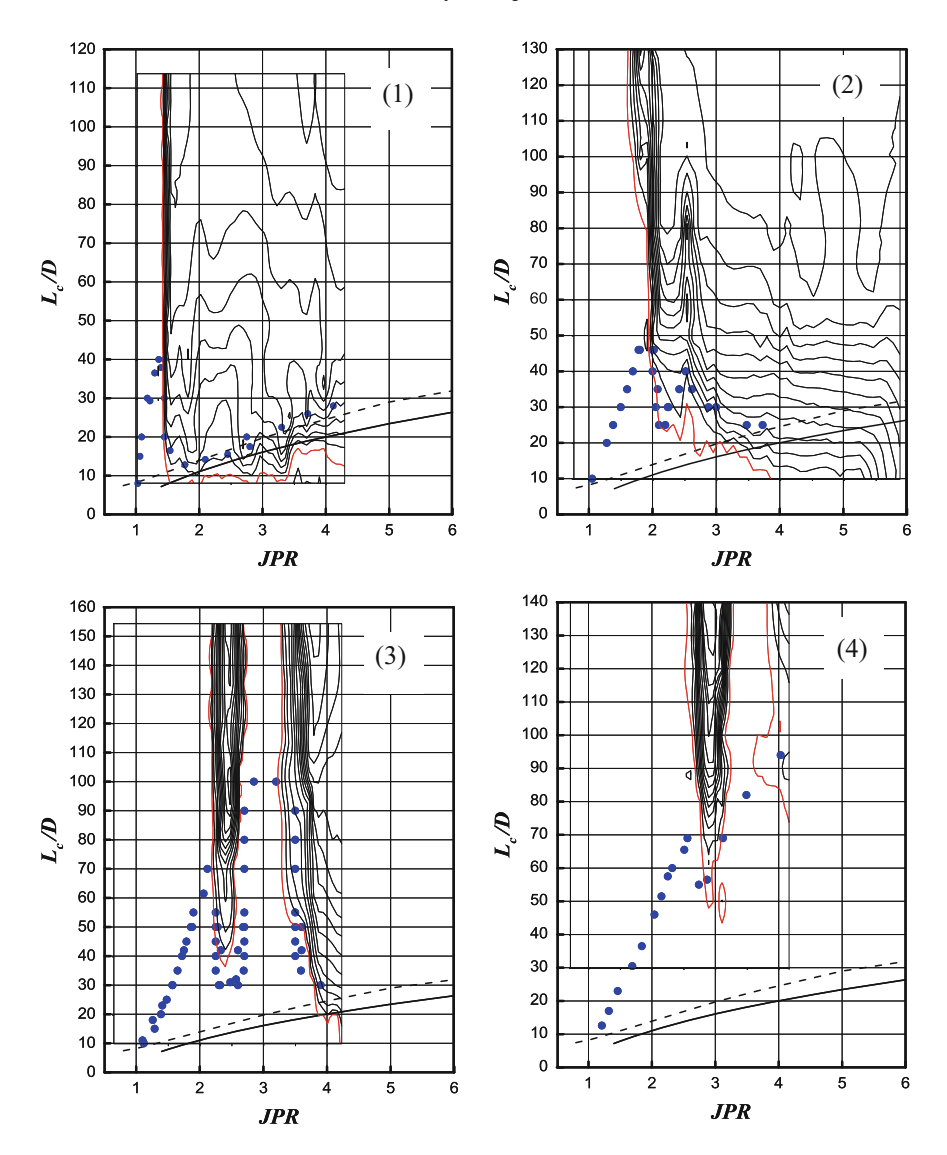


Fig. 2.30 Isolines of mass flow integral pulsations and the normalized supersonic core length versus the jet pressure ratio: $1-D=36~\mu m;~2-26~\mu m;~3-24.3~\mu m;~4-16.1~\mu m$

the nozzle exit. The rough edges were produced by means of repeated purging of the nozzles with nitrogen in the absence of filters in the gas supply system. Rust particles approximately 10 μ m in size partly destroyed the micronozzle edges. The absolute level of roughness determined from electron microphotographs was approximately 1 \div 1.5 μ m. As an example, Fig. 2.31 shows the SEM images of nominally "smooth" (left) and rough (right) micronozzles.

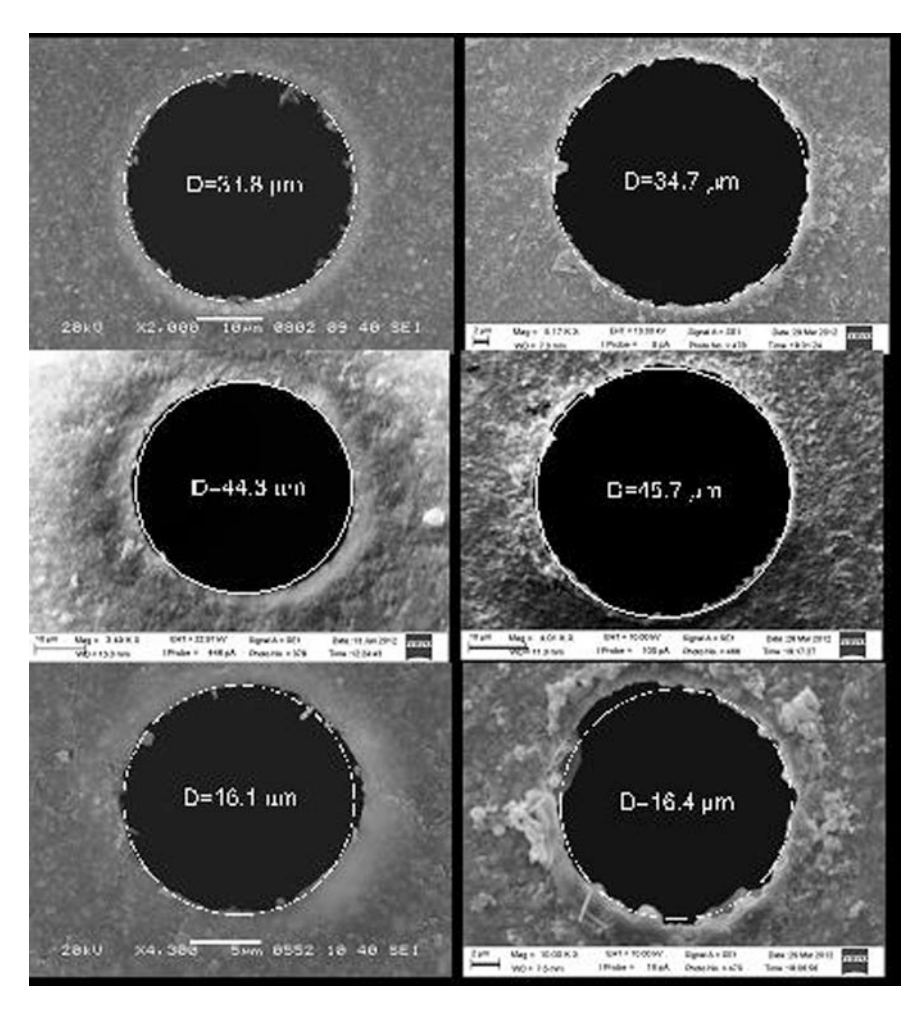


Fig. 2.31 Scanned electron microscope images of nominally "smooth" (left) and rough (right) micronozzles

Figures 2.32 and 2.33 show some dependences of the normalized supersonic core length of the microjet as a function of the jet pressure ratio for nominally "smooth" (circles) and rough (filled points) nozzles of similar diameters.

As is seen from the graphs, the roughness of the micronozzle edge exerts versatile effects on the length of the supersonic core. At small values of n, the data for smooth and rough nozzles are fairly close to each other. The major difference is observed in the region where the flow regime changes. It was found that the transition in flows generated by rough micronozzles may occur at both lower and higher values of JPR and, hence, of the flow Reynolds numbers.

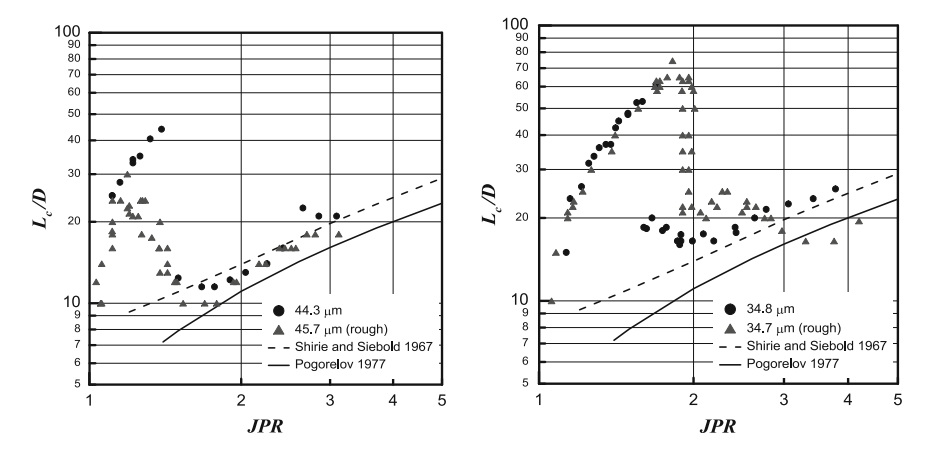
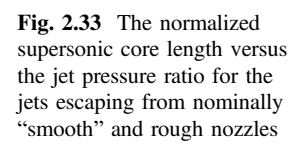
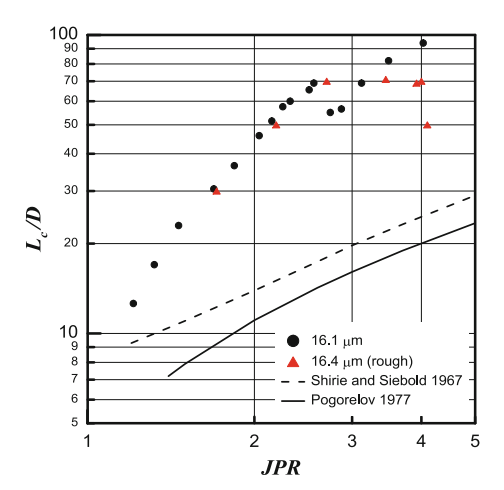


Fig. 2.32 The normalized supersonic core length versus the jet pressure ratio for the jets escaping from nominally "smooth" and rough nozzles





2.4 Microjet Simulation with the Use of Macrojets

To consider the possibility of modeling microjets with the help of parameters similar to those used in macroscopic flows (in particular, Reynolds number), we performed experiments aimed at measuring the supersonic core length of the jets escaping from a macroscopic sonic nozzle 1 mm in diameter. A medical needle with an inner diameter of $100~\mu m$ served as the Pitot tube. The experiments were performed in the low pressure chamber; the experimental layout and the photographs of the nozzle and Pitot tube are shown in Figs. $2.34~\mu m$

These experiments were performed with a smooth sonic nozzle. Exhaustion of microjets from nozzles with diameters ranging from 40 to 2 µm was considered.

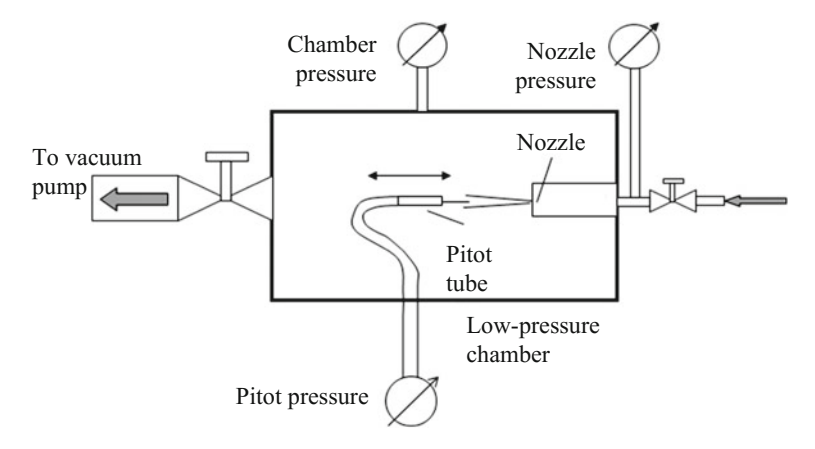
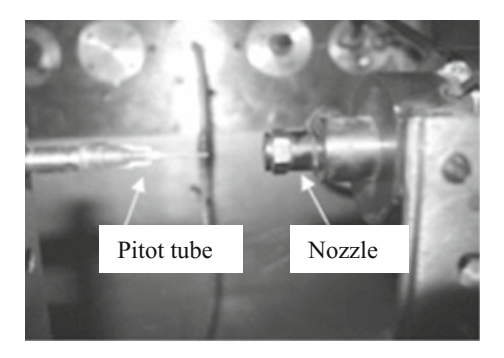


Fig. 2.34 The sketch of experiments in a low-pressure chamber

Fig. 2.35 Photograph of the nozzle and Pitot tubes in a low-pressure chamber



The Reynolds number at the sonic nozzle exit Re_D and the JPR were maintained approximately equal to their values in microjets. Low values of Re_D in the 1-mm nozzle were provided by reducing the pressure in the settling chamber. JPRs equal to or even higher than those in experiments with microjets were obtained by decreasing the pressure in the low-pressure chamber. Thus, for each value of Re_D , it is possible to introduce an effective nozzle diameter $D_{\rm eff}$ equivalent to the micronozzle diameter in experiments with jet exhaustion into the atmosphere.

The normalized mean length of the shock cells of model microjets L_s/D was measured in the low-pressure chamber. Figure 2.36 shows some examples of the dependence of L_s/D on the JPR for real (filled points) and model (open points) microjets escaping from real and effective nozzles of similar diameters. It is seen that these dependences coincide with each other within the measurement scatter, and the gas-dynamic structure of microjets and macrojets is adequately modeled.

Figure 2.37 shows the measured length of the supersonic core for the 1-mm nozzle. The effective nozzle diameters $D_{\rm eff}$ are also indicated in the figure. The main conclusion can be formulated as follows. The length of the supersonic core of

Fig. 2.36 The average shock cell size of the real (filled symbols) and model (light symbols) microjets versus jet pressure ratio

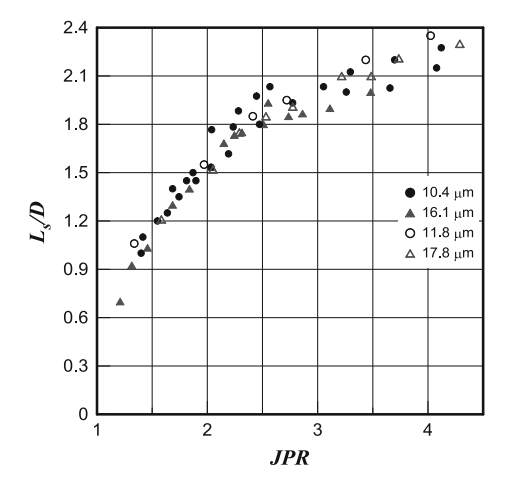
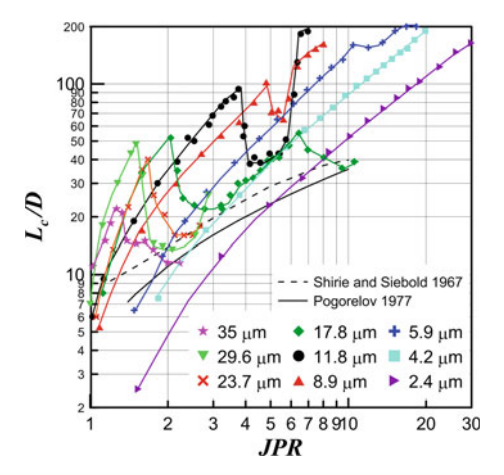


Fig. 2.37 The normalized supersonic core length of the model jets versus the jet pressure ratio



model microjets also increases rapidly at the beginning, and then it decreases to the turbulent limit. As $D_{\rm eff}$ decreases, the decrease in L_c/D is terminated beginning from the diameter of 15 μ m, and the supersonic core length starts to increase again with increasing jet pressure ratio n. This phenomenon is similar to the relaminarization of the microjet flow shown in Fig. 2.29. For $D_{\rm eff} < 5~\mu$ m, only the growth of the supersonic core length was observed in the examined interval of the jet pressure ratios. For $D_{\rm eff} < 10~\mu$ m, it was also found that the roughness of the nozzle edge does not produce any noticeable effect on the supersonic core length as a function of the jet pressure ratio. The most probable reason is rapid decay of streamwise structures generated by the notches on the nozzle edge.

The dependences L_c/D on JPR for four diameters of real and model microjets are compared in Fig. 2.38 (the filled and open points refer to the model and real microjets, respectively). It was impossible to make the effective nozzle diameters in

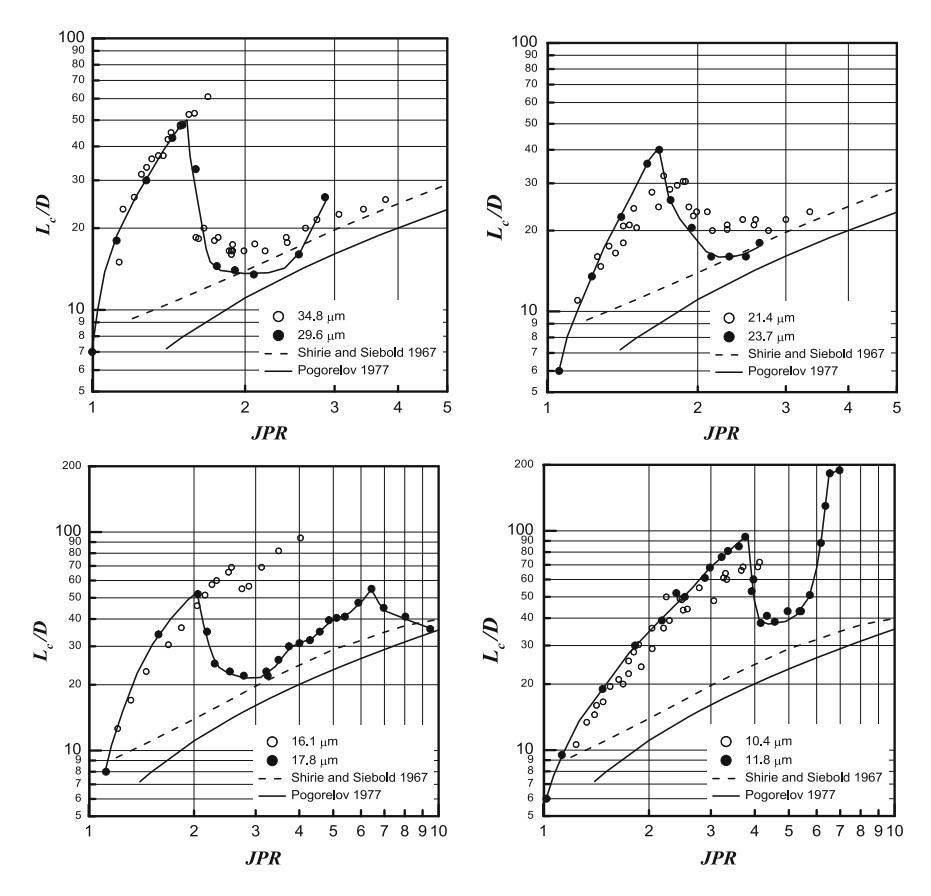


Fig. 2.38 Comparison of the supersonic core length versus JPR for real (circles) and model (filled points) microjets

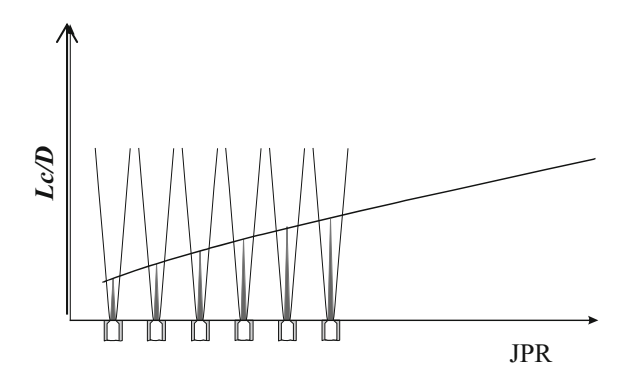
the low-pressure chamber exactly identical to those of real micronozzles, but they were fairly close to each other. It is seen that the dependences of the normalized length of the supersonic core of real and model microjets on the nozzle pressure ratio are in good quantitative agreement.

A detailed analysis of the supersonic core length's behavior and development of oscillations in the mixing layer in microjets allowed us to obtain flow fields for different values of the nozzle pressure ratio.

In terms of the mechanism of evolution of disturbances in the mixing layer, all jets can be conventionally classified into four groups.

The first group includes jets escaping from nozzles with diameters greater than 60 μ m (macrojets and minijets). The second group consists of jets being exhausted out of nozzles with diameters ranging from 60 to 35 μ m. Jets generated by nozzles with diameters between 35 and 10 μ m are included in the third group. Finally, the

Fig. 2.39 The jet flow pattern for the first group $(D > 60 \mu m)$



fourth group includes jets escaping from nozzles with diameters smaller than $10 \mu m$.

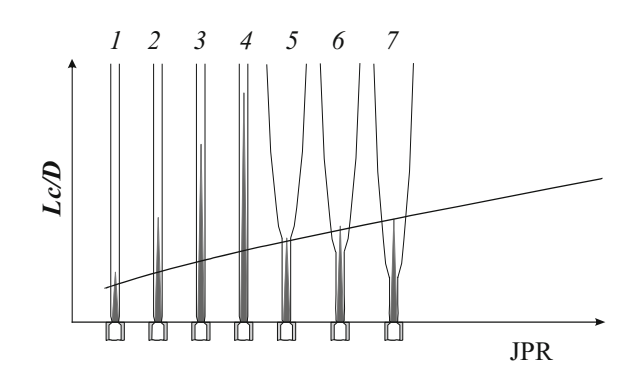
A jet of the first group is schematically shown in Fig. 2.39, with the axes being the jet pressure ratio and the normalized supersonic core length. The curve is the generalized dependence for the supersonic core length of turbulent macrojets. The central part is the supersonic core length of the jet.

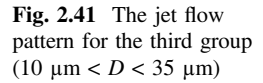
The jet boundaries and the nozzle are also shown. Different positions of the nozzle correspond to different jet pressure ratios.

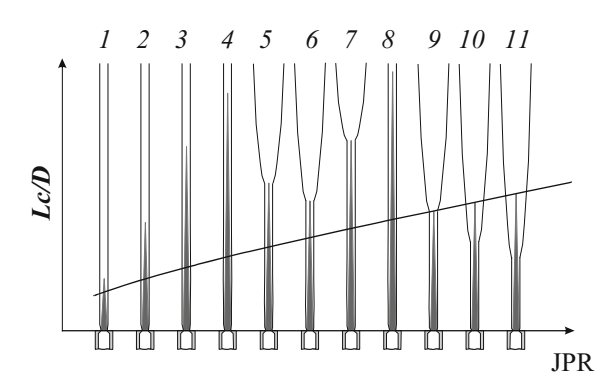
In turbulent macrojets, the mixing layer already becomes turbulent within the first cell (barrel) of the jet (Avduevskiy et al. 1971). As the jet pressure ratio increases, the mixing layer remains turbulent, while the supersonic core length increases, as predicted by the generalized dependences. The pattern in Fig. 2.39 can be conventionally called the turbulent macroscenario of supersonic core length changing.

Figure 2.40 shows the supersonic core length behavior for jets of the second group (35 μ m < D < 60 μ m). At moderate values of the jet pressure ratio, the mixing layer is laminar, and the supersonic core length increases without experiencing any effect produced by growing disturbances (Fig. 2.40, I–4). Then, sudden turbulization occurs (Fig. 2.40, I), and the point of the laminar-turbulent transition

Fig. 2.40 The jet flow pattern for the second (35 μ m $< D < 60 \mu$ m)







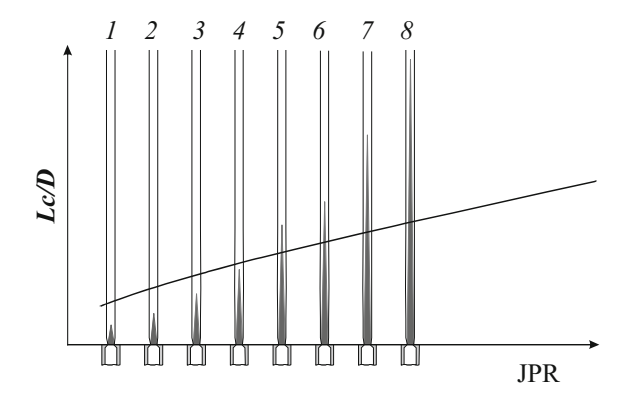
and the value of the supersonic core length approach the generalized dependence for turbulent macrojets. With a further increase in the jet pressure ratio (Fig. 2.40, 6, 7), the position of the laminar-turbulent transition in the mixing layer of the jet is shifted toward the nozzle, whereas the supersonic core length increases in accordance with the turbulent macroscenario.

The behavior of the supersonic core length for jets of the third group ($10 \ \mu m < D < 35 \ \mu m$) is schematically illustrated in Fig. 2.41. At the beginning, at small values of the jet pressure ratio, the mixing layer is laminar, and the supersonic core length increases (Fig. 2.41, I–4). As the jet pressure ratio increases, the laminar-turbulent transition occurs in the mixing layer, but the transition point lies higher than the generalized dependence for macrojets (Fig. 2.41, 5). A further increase in JPR shifts the transition point even closer to the nozzle, but it is still higher than the generalized dependence (Fig. 2.41, 6). As JPR is further increased to higher values, sometimes complete relaminarization of the flow may occur (Fig. 2.41, 8). With a further increase in n, the laminar-turbulent transition point is shifted back to the nozzle [to the generalized dependence for macrojets (Fig. 2.41, 9)], and the turbulent macroscenario is realized after that (Fig. 2.41, 10, 11).

For jets of the fourth group ($D < 10 \, \mu m$), the behavior of the supersonic core length is illustrated in Fig. 2.42. It should be noted here that the supersonic core length for these jets with the initial (small) values of the jet pressure ratio (Fig. 2.42, I-3) does not reach the level of the normalized supersonic core length of macroscopic jets, whereas it is from this level that the supersonic core length starts to increase for jets of the second and third groups (at JPR $\cong 1-1.05$). As the jet pressure ratio is increased (Fig. 2.42, 4), the supersonic core length reaches the corresponding level for macrojets and then exceeds the latter (Fig. 2.42, 5-8). The subsequent behavior of the supersonic core length is not clear, because there are no data for very large values of the jet pressure ratio (n > 30).

The generalized dependence of the Reynolds number at the place of the laminar-turbulent transition on the nozzle diameter is shown in Fig. 2.43. The red and blue points are the Reynolds number for the complete change in the flow regime (Fig. 2.40, 5–7) and the beginning of the development of turbulence in the mixing layer (see Fig. 2.41, 5). The triangles show the Reynolds numbers at which

Fig. 2.42 The jet flow pattern for the fourth group $(D < 10 \mu m)$



either partial (Fig. 2.41, 6) or complete (Fig. 2.41, 8) relaminarization of the flow occurs. The Reynolds numbers of repeated shifting of the laminar-turbulent transition point are marked by green diamonds (Fig. 2.41, 9).

The diagram of regimes of jet exhaustion from the micronozzle can be conventionally divided into four basic domains. The first domain (blue color in Fig. 2.43) corresponds to subsonic exhaustion of the jet.

The second domain (green color in Fig. 2.43) is the regime of a large supersonic core length and laminar mixing layer. The left boundary of the second domain is bounded by the Reynolds number reached in experiments.

The third domain (pink color in Fig. 2.43) corresponds to the regime typical for turbulent macrojets. There are no differences between macrojets and microjets in this domain.

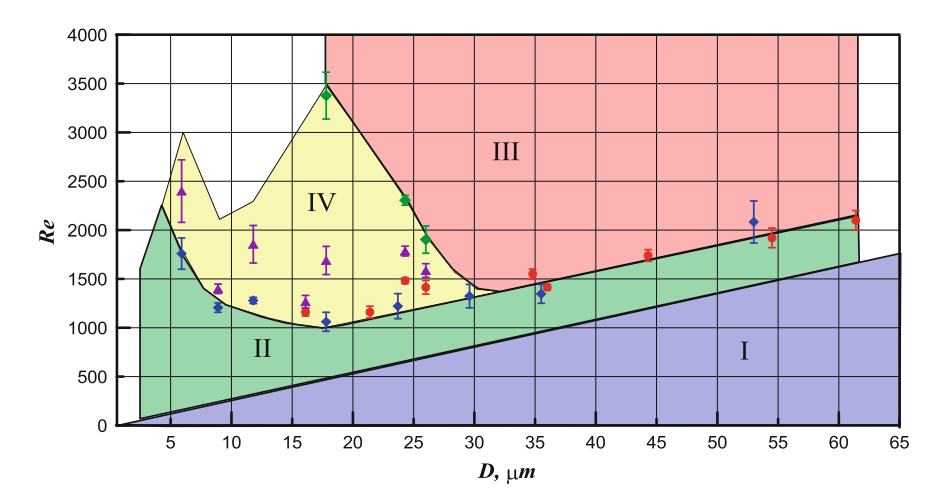


Fig. 2.43 Reynolds number of the jet flow regime change depending on the nozzle diameter

Finally, the fourth domain (yellow color in Fig. 2.43) is the region where the supersonic core length can decrease because of the laminar-turbulent transition, but is still greater than the supersonic core length of macrojets. The fourth domain can be divided into two subdomains, one where the jet range decreases and one where the supersonic core length increases again.

Based on comparisons of the data for real and model microjets in Figs. 2.36 and 2.38, we can argue that it is possible to model the domains with changes in the microjet flow regimes in terms of the Reynolds number. On the other hand, it seems that the jet flow in the third domain is not absolutely stable and again becomes turbulent as Re_D increases. It should be noted that the repeated laminar-turbulent transition obtained in real microjets was not observed in model microjets (see Fig. 2.37). Possibly, it can be detected at higher values of JPR (higher Reynolds numbers).

The transition of the flow from domain 1 to domain 2 in supersonic macrojets has been well studied. The transition from domain 2 to domain 3 was observed only for microjets. The laminar domain 3 is not formed for all nozzle sizes. It is observed only for nozzle diameters of about 25 μ m. This value can be considered as a boundary between gas microjets and macrojets. However, the dimension value of the nozzle diameter responsible for this boundary cannot yet be considered as definitely established.

References

Akey ND (1970) Overview of RAM reentry measurements program. In: Proceedings of the reentry plasma sheath and its effect on space vehicle electromagnetic systems, vol 1. NASA Langley Research Center SP-252, pp 25–26

Alvi FS, Shih C, Elavarasan R, Garg G, Krothapalli A (2003) Controll of supersonic impinging jet flows using supersonic microjets. AIAA J 41(7):1347–1355

Aniskin VM, Maslov AA, Mironov SG (2011) Effect of nozzle size on supersonic microjet length. Tech Phys Lett 37(11):1046–1048

Aniskin VM, Bountin DA, Maslov AA, Mironov SG, Tsyryul'nikov IS (2012) Stability of a subsonic gas microjets. Tech Phys 57(2):174–180

Aniskin V, Mironov S, Maslov A (2013) Investigation of the structure of supersonic nitrogen microjets. Microfluid Nanofluid 14(3):605–614

Avduevskiy VS, Ivanov AV, Karpman IM, Traskovskiy VD, Yudelovich MY (1971) Effect of viscosity on movement in the initial section of a highly underexpanded jet. Dokl Phys 197 (1):46–49

Bayt R, Breuer K (2001) Systems design and performance of hot and cold supersonic microjets. AIAA Paper 2001-0721

Brown CA (2005) Acoustics of excited jets—a historical perspective. NASA TM. 2005-213889 Choi JJ, Annaswamy AM, Lou H, Alvi FS (2006) Active control of supersonic impingement tones using steady and pulsed microjets. Exp Fluids 41:841–855

Danalia I, van Boersma B (2000) Direct numerical simulation of bi-furcating jets. Phys Fluids 12 (5):1255–1257

Fedorov A, Shiplyuk A, Maslov A et al (2003) Stabilization of a hypersonic boundary layer using an ultrasonically absorptive coating. J Fluid Mech 479:99–124

References 95

Fomin VM, Aniskin VM, Maslov AA, Mironov SG, Tsyryul'nikov IS (2010) Gas-dynamic flow structure and development of perturbations in microjets. Dokl Phys 55(8):419–422

- Gau C, Shen CH, Wang ZB (2009) Peculiar phenomenon of micro-free-jet flow. Phys Fluids 21:092001 (1-13)
- Ginevskiy AS, Vlasov EV, Karavosov RK (2001) Acoustic control of turbulent jets. Fizmatlit, Moskow
- Golod SV, Prinz VY, Mashanov VI, Gutakovsky AK (2001) Fabrication of conducting GeSi/Si micro-and nanotubes and helical microcoils. Semicond Sci Technol 16:181–185
- Grek GR, Kozlov VV, Litninenko YA (2012) Stability of subsonic jet streams. Tutorial. Editorial Publishing Center NSU, Novosibirsk
- Kosinov AD, Maslov AA, Shevelkov SG (1990) Experiments on the stability of supersonic laminar boundary-layers. J Fluid Mech 219:621–633
- Kozlov VV, Grek GR, Lofdahl LL, Chernoray VG, Litvinenko MV (2002) Role of localized streamwise structures in the process of transition to turbulence in boundary layers and jets (review). J Appl Mech Tech Phys 43(2):224–236
- Kozlov GV, Grek GR, Sorokin AM, Litvinenko YuV (2008) Influence of initial at nozzle section on flow structure and instability of plane jet. Vestn NSU Phys Ser 3(3):25–37
- Kozlov VV, Grek GR, Litvinenko YV, Kozlov GV, Litvinenko MV (2010) Subsonic round and plane jets in the transversal acoustic field. Vestn NSU Phys Ser 5(2):28–43
- Litvinenko MV, Kozlov VV, Kozlov GV, Grek GR (2004) Effect of streamwise streaky structure on turbulization of a circular jet. Appl Mech Tech Phys 45(3):349–357
- Litvinenko YA, Grek GR, Kozlov VV, Kozlov GV (2011) Subsonic round and plane jets in a transverse acoustic field. Dokl Phys 56(1):26–31
- Lou H, Alvi FS, Shih C (2006) Active and passive control of supersonic impinging jets. AIAA J 44(1):58–66
- Maslov AA, Shiplyuk AN, Sidorenko AA et al (2001) Leading-edge receptivity of a hypersonic boundary layer on a flat plate. J Fluid Mech 426:73–94
- Parmentier EM, Wray KL, Weiss RF (1970) Aerophysical plasma alleviation. In: Proceedings of the reentry plasma sheath and its effect on space vehicle electromagnetic systems, vol 1. NASA Langley Research Center SP-252, pp 579–616
- Phalnicar KA, Kumar R, Alvi FS (2008) Experiments on free and impinging microjets. Exp Fluids 44:819–830
- Pogorelov VI (1977) Parameters determining the range of a supersonic gas jet. Sov Tech Phys 47(2):444–445
- Prinz VY, Seleznev VA, Gutakovsky AK, Chehovskiy AV, Preobrazhenskii VV, Putyato MA, Gavrilova TA (2000) Free-standing and overgrown InGaAs/GaAs nanotubes, nanohelices and their arrays. Physica E 6:828–831
- Prinz VY, Grutzmacher D, Beyer A, David C, Ketterer B, Deckardt E (2001) A new technique for fabricating three-dimensional micro- and nanostructures of various shapes. Nanotechnology 12:399–402
- Reynolds WC, Parekh DE, Juvet PJD, Lee MJD (2003) Bifurcating and blooming jets. Annu Rev Fluid Mech 35:295–315
- Scroggs SD, Settles GS (1996) An experimental study of supersonic microjets. Exp Fluids 21:401–409
- Seleznev VA, Prinz VY, Aniskin VM, Maslov AA (2009) Generation and registration of disturbances in a gas flow. 1. Formation of arrays of tubular microheaters and microsensors. J Appl Mech Tech Phys 50(2):291–296
- Shiplyuk AN, Bountin DA, Maslov AA, Chokani N (2003) Nonlinear mechanisms of the initial stage of the laminar-turbulent transition at hypersonic velocities. J Appl Mech Tech Phys 44(5):654–659
- Shirie JW, Siebold JG (1967) Length of supersonic core of jets. AIAA J 5(11):2062-2064
- Tabeling P (2005) Introduction to microfluids. Oxford University Press, Oxford
- Tanney JW (1970) Fluidics. Prog Aerosp Sci 10:401-510

Vorob'ev AB, Prinz VY (2002) Directional rolling of strained heterofilms. Semicond Sci Technol 17:614–616

Vulis LA, Kashkarov VP (1965) Theory of viscous fluid jets. Nauka, Moskow

Zhang S, Zhong S (2010) Experimental investigation of flow separation control using an array of synthetic jets. AIAA J 48(3):611–623

Zhuang N, Alvi FS, Alkilsar M, Shih C (2006) Aeroacoustic properties of supersonic cavity flows and their control. AIAA J 44(9):2118–2128

Ziliĉ A, Hitt DL, Alexeenko AA (2007) Numerical simulations of supersonic flow in a linear aerospike micronozzle. AIAA Paper 2007-3984

Chapter 3 Fluid Flows in Microchannels



Abstract The chapter describes the results of measurements of friction factors in microchannels of various shapes and various diameters for laminar and turbulent flows, as well as the friction factor for input regions. Much attention is paid in this chapter to technologies of fabrication of test benches, methodical aspects of experiments, and evaluation of reliability of experimental data. The chapter is organized in such a way that all aspects of microflow experiments are consecutively considered: from the development of test benches through choosing measurement techniques to estimating the error of results obtained.

3.1 Methods of Determining the Friction Factor in Tubes

The development of advanced technologies required applications and, correspondingly, fabrication of miniature fluidic devices. The design of microfluidic devices raised the following question: are the known laws of fluid motion in macrochannels valid for fluid motion in channels of micron and submicron sizes? Many research teams have reported their results on measurements of the friction factor and pressure distribution for laminar and turbulent fluid flows in microchannels and also on heat transfer during the last 15–20 years. These results are scattered and often contradictory. Measurements by microscopic probes impose particular requirements on experiment arrangement, fabrication of test benches, and measurement techniques. Moreover, measurement errors should be carefully estimated. Methods developed for semiconductor instruments are now being increasingly used for the fabrication of microscopic devices. However, manual work is still widely used for test bench assembling. In addition, measured results should be accurately and carefully interpreted because these results are affected, e.g., by the roughness of even smoothly polished surfaces.

The following characteristics can be chosen to classify microchannels into several groups:

- Microchannel shape (straight or curved);
- Cross-sectional profile of the microchannel;

- Microchannel size:
- Material of the microchannel walls;
- Wall roughness;
- Presence or absence of holes in the microchannel walls.

In practice, various cross-sectional shapes are used (circular, square, rectangular, or tapered cross-sections). The channel walls can be made of versatile materials: silicon, glass, quartz, polytetrafluorethylene (PTFE), metals, photopolymers, polydimethylsiloxane, and polymethylmethacrylat (PMMA). The majority of experiments are performed with three types of fluid: gas, liquid, and nanofluid. Two flow regimes (laminar and turbulent) are formed in microchannels, similar to macrochannels.

Kandlikar (2003) proposed the following classification of microchannels in accordance with their size:

- Conventional channels: *D* > 3 mm;
- Minichannels: $3 \text{ mm} \ge D > 200 \mu\text{m}$;
- Microchannels: 200 μ m $\geq D > 10 \mu$ m;
- Transitional channels: 10 μ m $\geq D > 0.1 \mu$ m;
- Transitional microchannels: $10 \mu m > D > 1 \mu m$;
- Transitional nanochannels: $1 \mu m \ge D > 0.1 \mu m$;
- Molecular nanochannels: 0.1 μ m > D,

where D is the hydraulic diameter of the channel, D = 4S/P (S is the cross-sectional area and P is the channel perimeter).

As a whole, this classification is not very effective because of the dimensional parameter D used as a basis for the classification. Possibly, it is more correct to use specific features of physical processes in the fluid flow in the channel as a criterion. However, there are no sufficient systematic theoretical and experimental investigations to derive such a criterion. Therefore, this classification is applied to consideration of flows in microchannels and transitional microchannels in this chapter.

Investigations aimed at finding the law of fluid motion in tubes have occupied a key position in the history of hydrodynamics. One of the main problems solved by researchers was determining the friction factor in tubes. Let us consider various methods of determining the friction factor in a microchannel, based on commonly accepted approaches for large-diameter tubes.

The pressure decrease over the channel length is a sum of the pressure drops in different regions of the channel schematically shown in Fig. 3.1. The pressure decreases at the channel input ($\Delta P_{\rm in}$) and output ($\Delta P_{\rm out}$) owing to a drastic change in the cross-sectional area of the channel where the fluid flows. At the initial part of the channel, the pressure decrease $\Delta P_{\rm dev}$ occurs in the region of stabilization of the pressure profile from the uniformly distributed pressure at the channel input to the pressure profile corresponding to a developed flow. In the laminar flow, this is the Poiseuille parabola. The length of the developing flow region $L_{\rm dev}$ depends on the hydraulic diameter of the microchannel D and on the Reynolds number. Various researchers believe that it is determined as 0.029DRe (Idel'chik 1992; Shiller 1936)

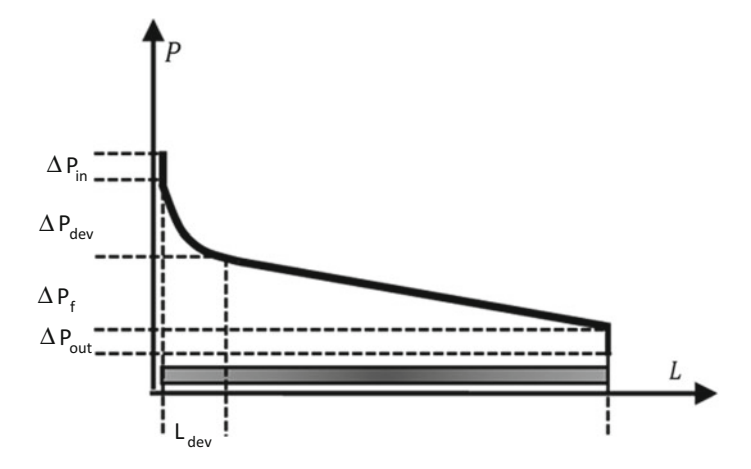


Fig. 3.1 Schematic distribution of fluid pressure inside the channel

or as 0.05*D*Re (Donsqing 2008). Thus, the total decrease in the liquid pressure along the microchannel is a sum of the pressure drops in the above-mentioned regions:

$$\Delta P = \Delta P_{in} + \Delta P_{dev} + \Delta P_f + \Delta P_{out}.$$

The change in pressure in the fully developed flow region is induced only by friction and is determined as

$$\Delta P = f \frac{\rho V^2}{2} \frac{L}{D},\tag{3.1}$$

where ρ is the fluid density, D is the channel diameter, V is the mean mass velocity of the fluid in the channel, L is the channel length, and f is the coefficient of proportionality between the pressure drop in the microchannel and dynamic pressure, which is called the friction factor and depends on the cross-sectional shape of the microchannel, wall roughness, and Reynolds number.

Determination of the friction factor on the basis of the pressure difference. Expressing the friction factor f from Eq. (3.1), we obtain

$$f = 2\frac{\Delta P}{\rho V^2} \frac{D}{L} \tag{3.2}$$

Thus, for determining the friction factor of the microchannel, it is necessary to measure the pressure difference in the developed flow region.

If the measurements are performed at several points of the developed flow, then Eq. (3.2) can be rewritten as

$$f_{ij} = \frac{\pi^2 D^5 \Delta P_{ij}}{8\rho Q^2 L_{ii}},\tag{3.3}$$

where $Q = V\pi D^2/4$ is the volume flow rate of the fluid, ΔP_{ij} are the pressure differences between the measurement points i and j, and ΔL_{ij} are the distances between these points.

In practice, however, it is not always possible to measure the pressure directly inside the microchannel. The pressures in manifolds at the channel input and output are usually measured. In this case, it should be borne in mind that the thus-measured pressure difference is a sum of the pressure losses in various parts of the microchannel. To eliminate edge effects, which are understood as the decrease in pressure at the microchannel input and output, as well as in the developing flow region, some researchers (Rands et al. 2006; Barlak et al. 2011) use reference values of local loss coefficients available for macrochannels.

Method of two channels. The friction factor is often determined, in practice, by the method of two channels (Mala and Li 1999; Celata et al. 2006). The main idea behind this method can be formulated as follows: the edge effects are independent of the channel length; they are determined only by the flow rate of the fluid. This means that the edge effects are identical in microchannels of identical diameter, but are of different lengths if the flow rates of the fluid in these channels are identical. If we consider two microchannels of the same diameter but different length, and ensure identical flow rates of the fluid in these channels, then the pressure drop at the microchannel input and output can be eliminated. The difference in the pressure drops in these microchannels corresponds to the difference in their linear sizes. This idea is illustrated in Fig. 3.2.

Equation (3.2) can be rewritten in accordance with the method of two channels as

$$f = 2\frac{\Delta P_1 - \Delta P_2}{L_1 - L_2} \frac{D}{\rho V^2},$$

where ΔP_1 is the pressure decrease in the longer microchannel, ΔP_2 is the pressure decrease in the shorter microchannel, and L_1 and L_2 are the lengths of the corresponding microchannels.

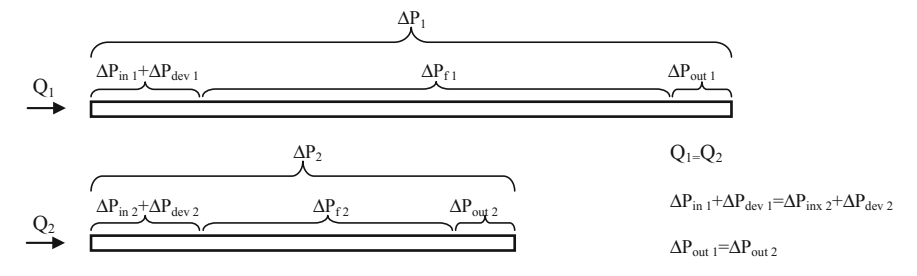


Fig. 3.2 Illustration of the method of two channels

Let us transform the resultant expression by using measurable quantities:

$$f = \frac{1}{8} \frac{\pi^2 D^5}{\rho Q^2} \frac{\Delta P_1 - \Delta P_2}{L_1 - L_2},\tag{3.4}$$

where Q is the volume flow rate of the fluid.

3.2 Fabrication Technology and Characteristics of Microchannels

For the fabrication of microfluidic systems, it is necessary to solve a number of problems associated with fabrication of the microchannel proper and its connection with channels providing fluid or gas inflow and outflow. Various methods are applied for microchannel fabrication. Selective etching of silicon is used most frequently (Wu and Cheng 2003; Chen et al. 2004). Microchannels are etched into the silicon substrate in a procedure consisting of several steps. In this case, microchannels can have tapered, triangular, or rectangular shapes (Wu and Cheng 2003; Tsai et al. 2004; Morini 2004).

Tubes used for studying the friction factor of microchannels and solving problems of heat transfer in microchannels usually have a circular cross-section and are made of glass (Li et al. 2003; Cui and Silber-Li 2004), quartz (Judy et al. 2002; Rands et al. 2006), or stainless steel (Lelea et al. 2004; Wook and Kim 2006). PTFE tubes are also used sometimes (Celata et al. 2006). Methods of fabrication of metallic microchannels with a rectangular cross-section are available (Costaschuk et al. 2007).

An interesting method of fabrication of micron- and submicron-size channels was proposed by Zhang et al. (2008). In that work, nano-sized quartz filaments obtained by the drawing of a heated quartz rod are used as a mold for the initial shape. These filaments are inserted into a polycarbonate substrate by means of hot stamping. Submicron channels and nanochannels are formed after the quartz filaments are removed by using hydrofluoric acid.

Fluid input/output in circular microchannels proceeds coaxially (Cui and Silber-Li 2004; Rands et al. 2006). In microchannels etched into a silicon plate and in other composite microchannels, fluid input/output occurs at an angle of 90° to the microchannel or a system of microchannels (Wu and Cheng 2003; Costaschuk et al. 2007).

To calculate microfluidic systems, one needs to know not only the microchannel resistance in the steady flow region, but also the hydraulic resistance of input/output regions where the flow turns by 90° (Costaschuk et al. 2007). It is also necessary to know the friction factor of elbow regions, bending and branching parts of the channel, and also the constricting and expanding regions of microchannel systems. Because of the complex geometry of the microchannel, reference values for

large-size channels cannot be used in many cases. Therefore, it is necessary to measure the static pressure inside microchannels to justify the applicability of reference values of local values of friction factor available for macrochannels.

There were some activities in which channels with holes were fabricated to measure the pressure along the microchannel. Thus, Kohl et al. (2005) used silicon microchannels with rectangular cross-sections and hydraulic diameters from 25 to 100 μ m. Water was used as a working fluid. The microchannel system consisted of three silicon chips containing microchannels, and also integrated outputs from the microchannels for pressure measurements, which were sensitive to the membrane pressure. Eight holes $7 \times 10~\mu m$ were made in the channel wall.

Costaschuk et al. (2007) performed experimental investigations of the fluid flow in an aluminum microchannel with a rectangular cross-section and a hydraulic diameter of 169 μ m within the range of Reynolds numbers from 230 to 4740. Eight holes 27 μ m in diameter were made in the channel wall; six of them were located near the microchannel entrance so as to study the developing flow region. The holes in the channel wall were made through microelectrodischarge machining.

Actually, investigations aimed at pressure measurements inside microchannels were only reported in those two publications. The lack of studies of this kind is caused by the complexity and labor intensity of fabrication of such microchannels. At the same time, it is clear that the possibility of pressure measurements inside microchannels would be a reliable basis for determining both the friction factor of microchannels proper and the local losses (i.e., resistances of the input and output regions). It is particularly important to determine the local losses for microchannels, because reference books (e.g., Idel'chik 1992) often do not provide information on geometric configurations of input and output regions of microchannels. As these measurements are extremely important, the technology of fabrication of microchannel systems is considered in detail in this section, following the publication of Aniskin et al. (2012).

Fabrication of test benches for studying flows in microfluidic systems starts from fabrication of microchannels themselves. In this section, we describe the basic stages of fabrication of glass, photopolymer, and silicon microchannels. Straight-line and U-shaped channels with circular and square cross-sections are considered. The fabrication technology of polymer microchannels implies the presence of holes in microchannel walls for static pressure measurements.

Glass microchannels. Microchannels are fabricated from glass capillaries by means of heating and drawing above open flame. Microchannels of needed length are consecutively cut off from the thus-obtained microcapillary workpieces of different diameters. The shapes and sizes of cross-sections of the resultant microchannels are measured by scanning electron microscopy.

Precise determination of the shape and size of the microchannel cross-section is an extremely important task, because even small errors in size determination may lead to large errors in determining the friction factor. Figure 3.3 shows the SEM photographs of the input cross-sections of microchannels fabricated according to the above-described method. The analysis of these photographs shows that a small difference in the sizes of the input and output cross-sections cannot be avoided in

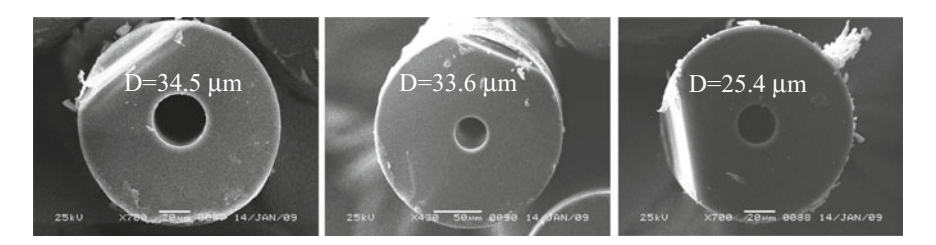


Fig. 3.3 SEM images of microchannel cross-sections

this technology. In addition, certain ellipticity of the cross-sections is observed in some cases, which is then taken into account in determining the hydraulic diameter.

The aspect ratio of glass microchannels varies from 80 to 600.

Conditions for pressure measurements along glass microchannels are not provided. The roughness of the inner surface of microchannels is determined by a Zygo NewView 6300 three-dimensional analyzer of the surface structure. For this purpose, the examined channel is cut along the axis. It is found that the inner surface roughness is within 5 nm, which allows these microchannels to be considered as smooth.

Polymer microchannel. Polymer microchannels are fabricated with outputs for static pressure measurements, which offer a possibility of measuring the pressure distribution along the microchannel. The technology allows for fabrication of both straight microchannels and microchannels of complex curved shapes. The technology is based on the molding principle and has the following stages. First, the shapes of the channel and outputs for pressure measurements are formed. Then, the mold is flooded with a liquid photopolymer, which is solidified due to exposure to light with a certain wavelength. When the photopolymer transforms into the solid state, the material used for molding is removed. As a result, a microchannel with holes in the walls is formed.

Let us consider the main stages of fabrication of the microchannel system for studying the flow in a cylindrical microchannel.

Definition of the channel shape. At the first stage, the shape of the examined channel is defined by using a fish line. A piece of the fish line of a required diameter shaped like the future channel is flooded with a photopolymer and exposed to light with a certain wavelength; after solidification, the fish line is removed. It is easy to remove the fish line, because its diameter slightly decreases due to tension, resulting in decoupling of the connection between the fish line's surface and the solidified photopolymer. A channel is left in the photopolymer. The channel's diameter, its surface roughness, and its shape correspond to the diameter, roughness, and shape of the fish line.

Formation of outputs for pressure measurements. Fish line pieces (or, e.g., synthetic hair lines of paint brushes) forming outputs for pressure measurements are superimposed at a right angle onto the basic fish line used to form the curved or straight microchannel. Tight contact with a very small area is provided at the points

of intersection of these lines. When the structure is flooded with a photopolymer, it does not penetrate to the places of this tight contact, and a hole connecting the examined microchannel and the outputs for pressure measurement is formed after photopolymer solidification. After photopolymer exposure and removal of all lines, the basis of the microchannel system, with a possibility of measuring the pressure distribution along the curved channel, is formed.

Formation of end plates. The next important step is the formation of end planes (microchannel entrance and exit). These are also fabricated on the basis of the molding principle. The photopolymer is poured into a narrow slot, and a fish line is again used to produce holes. Two plates approximately 500 μ m thick with through holes at the center are fabricated. One of the plate sides (which is further used as a working surface) is polished. After polishing, the plates are washed in an ultrasonic bath.

Fabrication of the microchannel system. The end plates are mounted on a Plexiglas plate normal to its plane at the distance required to form the channel shape. Their polished surfaces are turned toward each other. These plates are connected by a fish line, which forms the microchannel; the ends of this line pass through the holes in the end plates and are fixed outside. Then, outputs for pressure measurement are formed in accordance with the above-described technique.

The entire structure is flooded with a photopolymer and exposed to radiation; after removal of the end plates and fish lines, a microchannel system with a curved or straight microchannel and outputs for pressure measurement are formed. The prepared mold (a) and the resultant straight microchannel (b) are shown in Fig. 3.4.

Input-output of the fluid and connection of sensors. The final stage of the procedure is creating ducts for fluid input and for connection of various sensors. A copper plate 1 (Fig. 3.5) with c soldered tubes 2 is fixed on the Plexiglas plate. The microchannel system 3 is located at the center. The cylindrical manifold 4 made of the photopolymer is connected to the fluid input tube 5. The manifold is immediately adjacent to the end face of the c 6, and the junctions are thoroughly greased with epoxy resin 7.

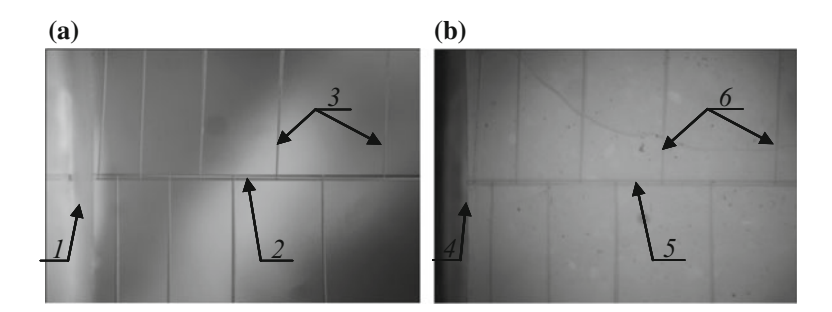


Fig. 3.4 Prepared mold **(a)** and fabricated microchannel **(b)**: *I*—plate for the formation of end cross-sections; 2—fish line forming the microchannel; 3—lines forming outputs for pressure measurements; 4—end face of the fabricated microchannel system; 5—microchannel; 6—outputs for pressure measurements

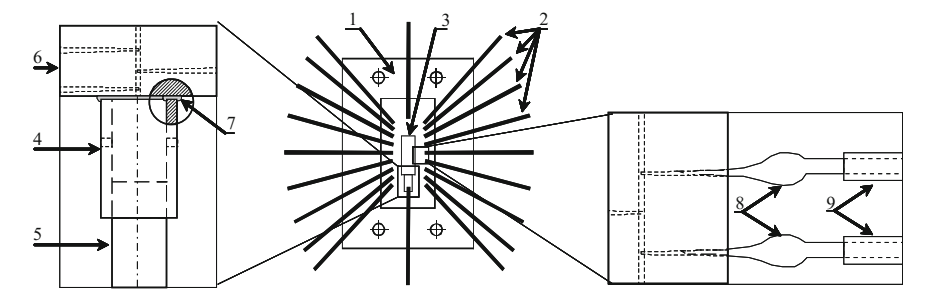
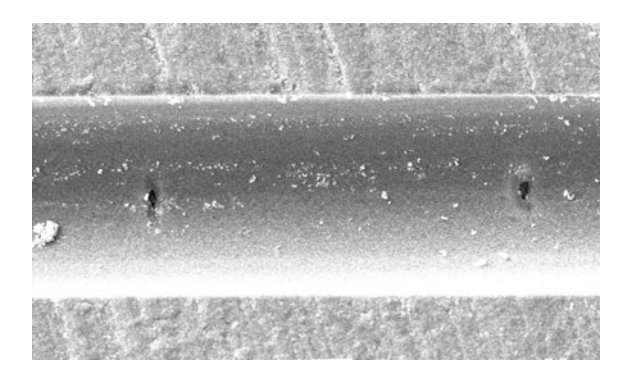


Fig. 3.5 Test bench and connection of manifolds

Fig. 3.6 SEM image of the longitudinal slice of the microchannel



Specially prepared fish lines 8 are used to ensure a fluid flow from small-diameter outputs to larger-diameter tubes to which pressure transducers are connected (Fig. 3.5). One end of the line has a diameter of about 1 μ m and is inserted into the output hole of the microchannel system. The other end of the line has a diameter of 0.2 mm and is inserted into the tube of the pressure sensor 9. After the manifolds and micro-outputs are connected, the entire structure is flooded with the photopolymer and exposed to radiation, followed by removal of the fish lines.

Figure 3.6 shows a SEM image of the longitudinal slice of the microchannel. The holes in the microchannel wall are clearly visible. They have an oval shape with a size of $5 \times 10~\mu m$. The SEM images of the end faces of the microchannel at various stations (Fig. 3.7) allow one to measure the microchannel diameter and also to determine its variation along the microchannel. For this purpose, a copy of the microchannel is fabricated, which is cut along the channel. It should be emphasized again that precise measurement of the microchannel diameter is extremely important for determining the friction factor.

This technology was applied to fabricate various straight and curved microchannels. A typical example of a curved microchannel is shown in Fig. 3.8.

Advantages and disadvantages of the technology. The above-described technology offers the following advantages:

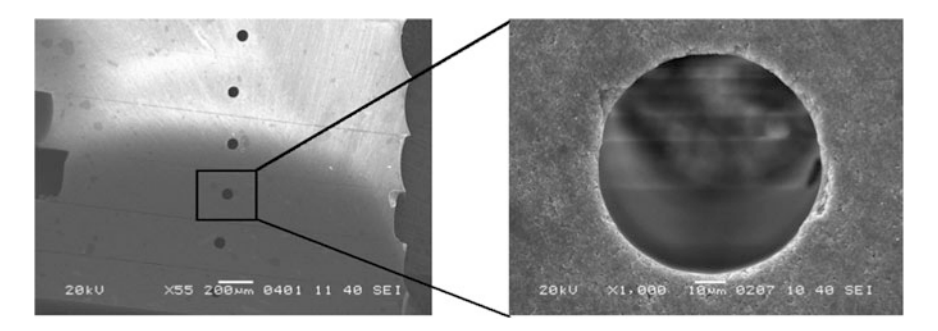
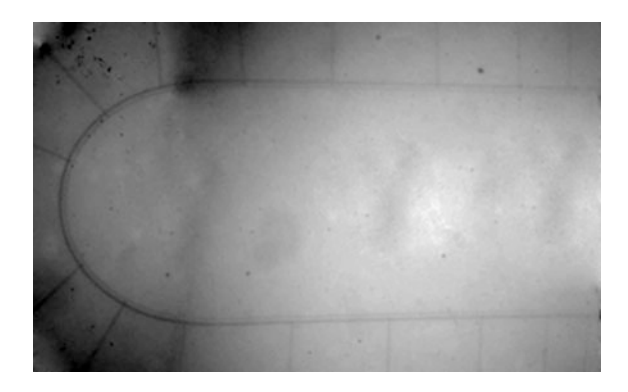


Fig. 3.7 SEM image of the transverse slice of the microchannel

Fig. 3.8 Photograph of a curved microchannel



- Fabrication of microchannels with a circular cross-section and holes in the channel walls;
- Fabrication of complex-shape microchannels: *U*-shaped and *S*-shaped channels with different bending radii, and also out-of-plane microchannels (e.g., coil pipes);
- Broad variations of manifold design;
- Fabrication of not only microchannels, but also other objects of versatile axisymmetric shapes: diffusers, nozzles, etc.;
- Fabrication of channels that cannot be produced by other methods.

The main drawback of this technology is its poor manufacturability: it is completely manual and rather complicated, because it requires special skills of working with microscopic objects.

Silicon microchannel structures. A silicon microchannel matrix is a regular system of microchannels with a square cross-section and vertical walls whose length reaches hundreds of micrometers, whereas the transverse size ranges from several to several tens of micrometers (Figs. 3.9 and 3.10). To obtain such matrices with different channel parameters, researchers at the Institute of Semiconductor Physics of the Siberian Branch of the Russian Academy of Sciences developed a

Fig. 3.9 SEM images of silicon microchannel matrices 4×4 µm: top view and side view (presented by Romanov)

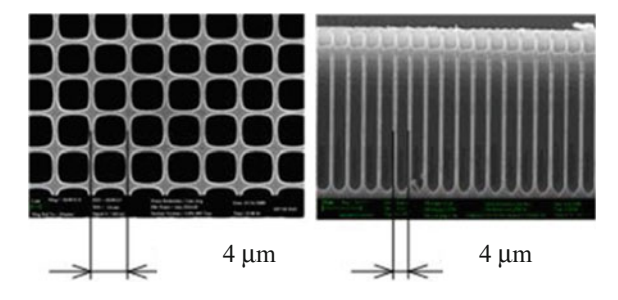
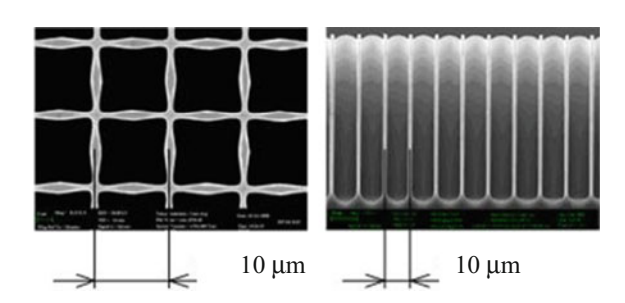


Fig. 3.10 SEM images of silicon microchannel matrices $10 \times 10 \mu m$: top view and side view (presented by Romanov)



special process of electrochemical anodic etching of hole-type monocrystalline silicon. The current density in this process changes during etching in accordance with a certain law described analytically within the framework of the patented phenomenological model of obtaining silicon microchannels with a prescribed profile (Romanov et al. 2011).

Microflow experiments were performed in microchannel matrices with lattice constants of 6×6 and $15\times 15~\mu m$. The transparency coefficient of silicon microchannel matrices was sufficiently high: 56 and 64% for matrices with the lattice constants of $6\times 6~\mu m$ and $15\times 15~\mu m$, respectively. As a result, a large flow rate of the fluid is reached with a moderate pressure difference on the plate. For this reason, such structures are fairly attractive for applications.

In experiments aimed at determining the friction factor, it is desirable to obtain as high as possible Reynolds numbers. For this purpose, the flow velocity in the microchannel is increased owing to reduction of the number of microchannels on the plate.

The number of channels in microchannel matrices is determined by considering the matrix photograph taken in transmitted light. The photograph is analyzed by the Image Pro software, which allows the number of channels to be counted with an error of 0.5–1%. Figure 3.11 shows photographs of microchannel matrices with lattice constants of 6 and 15 μ m. The thickness of the microchannel matrices (equal to microchannel length) is 190 μ m (for the lattice constant of 6 μ m) and 200 μ m (for the lattice constant of 15 μ m).

As was noted above, precise determination of the transverse size of microchannels is a key factor affecting the accuracy of calculating the friction

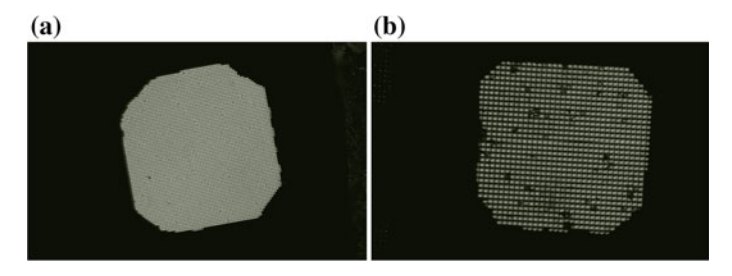
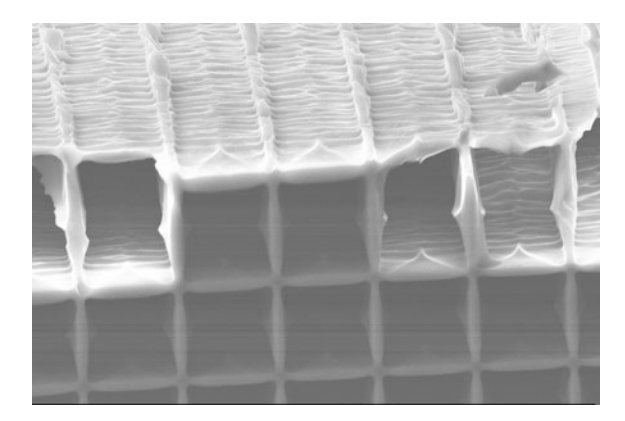


Fig. 3.11 Photographs of microchannel matrices with lattice constants of $6 \times 6 \mu m$ (a) and $15 \times 15 \mu m$ (b) (presented by Romanov)

Fig. 3.12 SEM image of the inner wall of the microchannel with lattice constant of $15 \times 15 \mu m$



factor. The area and perimeter of microchannels used for calculating the hydraulic diameter are determined by the Image Pro software. As an example, Fig. 3.12 shows a SEM image of the inner wall of the microchannel with the lattice constant of $15\times15~\mu m$. Based on the SEM images of the inner surface of microchannels, the absolute value of roughness is estimated as $1~\mu m$. The normalized roughness is 0.08. SEM images of the inner wall of microchannels with a smaller lattice constant do not reveal any wall roughness.

Test benches. A special test bench is made for each microchannel so as to perform experiments. Examples of test benches are shown in Fig. 3.13. The main problem in test bench fabrication is connecting the glass microcapillary and metallic tubes. Special fittings were developed and fabricated for this purpose. One of the fittings is schematically shown in Fig. 3.14. Fitting I is made of a photopolymer. Fluid input and output are provided through a cylindrical channel 2 with a diameter of 1400 μ m. In the side wall of the input channel 2, an additional channel 3 with a diameter of 300 μ m leading to pressure sensors is made. The microcapillary 4 is fixed in the fitting with epoxy resin 5. The accuracy of positioning of the end face of the microcapillary with respect to the end plane of channel 2 is ± 25 μ m, which is comparable with the internal diameter of the microcapillary.

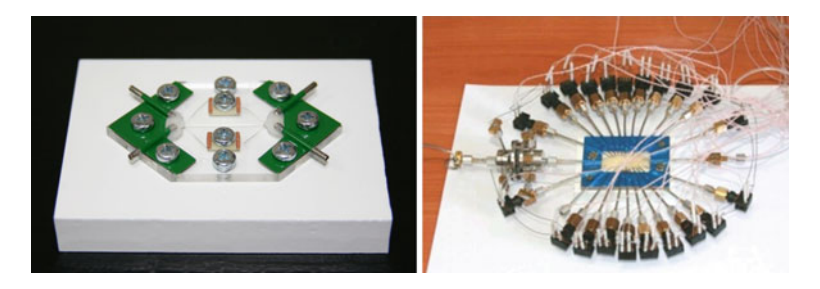


Fig. 3.13 Test benches

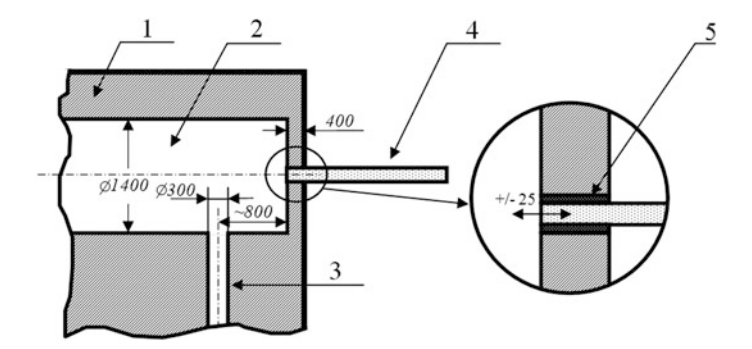
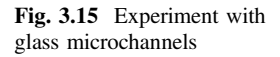


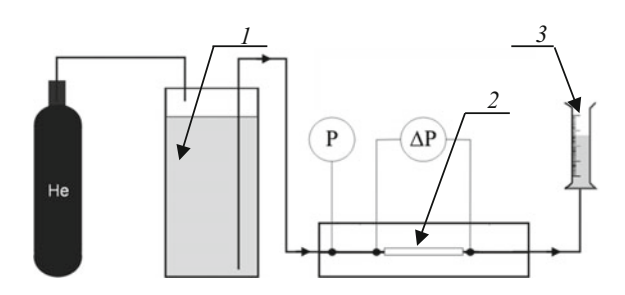
Fig. 3.14 Microchannel fitting. The sizes are given in micrometers

3.3 Experimental Arrangement

Distilled deionized water is used in all experiments described below. In addition, water is outgassed by means of purging a small amount of helium with a constant flow rate. Water outgasing is needed to prevent the effect of cavitation in the microchannel, which leads to the formation of microbubbles and to errors in fluid flow rate measurement. Let us consider some possible experimental arrangements.

Arrangement of experiments aimed at fluid flow rate measurements. This experimental arrangement is shown in Fig. 3.15. Under the influence of the helium





pressure, water moves from the reservoir I to the microchannel 2 located on the test bench, and then to the tube for fluid flow rate measurement 3. The parameters measured in experiments are the fluid flow rate, fluid pressure at the microchannel entrance, and pressure difference in the microchannel. The fluid motion in the tube for flow rate measurement is recorded by a video camera. The pressure is measured by pressure sensors, e.g., Honeywell sensors of the 26PC 100 psi series.

Arrangement of experiments aimed at pressure measurements. This experimental arrangement is shown in Fig. 3.16. The test fluid 2 is outgassed by helium 1 and is directed by the fluid pump 4 through the filter 3 to the microchannel 6 located on the test bench. The Gilson 305 fluid pump ensures a constant flow rate of the fluid up to 10 ml/min with a step of 0.1 ml/min. The channel provides the possibility of pressure measurement. The parameters measured in experiments are the fluid pressures at the microchannel entrance and exit, as well as at some points along the channel. If necessary, the scales 5 are used for monitoring the flow rate of the fluid. Depending on the test conditions, various pressure sensors with suitable ranges and measurement accuracy can be used, e.g., Honeywell 250 or 100 psi and Druck 250 bar.

Experimental arrangement with microchannel matrices. This experimental arrangement is shown in Fig. 3.17. The fluid 2 is driven by the fluid pump 4 through the filter 3 to devices 6, in which the experimental samples are fixed. The flow rate is monitored by the scales 5. The filter pore size is $0.45~\mu m$.

Some comments on specific features of experiments of this kind. The most important factor for obtaining reliable data is water purity. The filter is followed by threaded connections, which may serve as a source of contamination. Before the

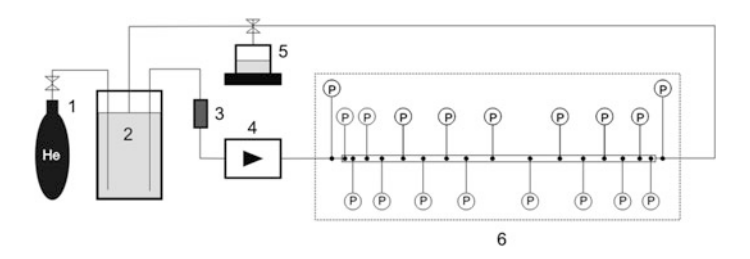
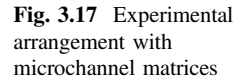
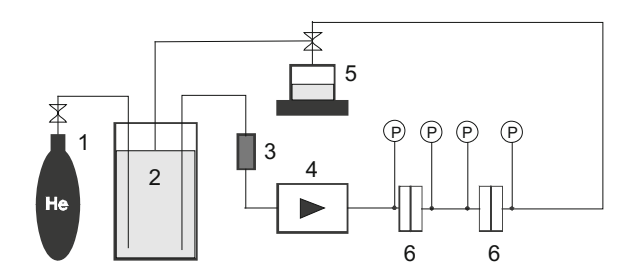


Fig. 3.16 Experimental arrangement for pressure measurements





system is assembled, all elements are carefully washed, first in an ultrasonic bath and then in running water. The entire experimental system is assembled (except for the microchannel matrix), and the fluid is purged through the system with the maximum flow rate that can be ensured by the pump. This is made to remove possible contaminants from the system behind the filter. It is only after this procedure that the microchannel matrices are connected.

3.4 Errors in Microchannel Measurement

The measurement accuracy is extremely important in studying fluid flows in microchannels. Let us consider possible sources of errors. Various types of errors and their contributions to determining the friction factor were analyzed by Lorenzini et al. (2009). They concluded that the most important contributions to the total error are made by errors in pressure and flow rate measurement at low Reynolds numbers and errors in microchannel diameter measurement at high Reynolds numbers. The accuracy of channel diameter measurement is limited by the capabilities of electron microscopy. However, the question concerning diameter homogeneity along the channel still remains open. Possible sources of measurement errors for glass and polymer microchannels and for microchannel matrices are analyzed below.

The measurement error is determined in a standard manner as

$$e_F = \pm \sqrt{\sum_{i=0}^n \left(\frac{\partial F}{\partial x_i} e_{x_i}\right)^2},$$

where F is the variable whose measurement error is estimated, x_i is the experimentally measured quantity used for determining F, e_{x_i} is the error of x_i measurement, and n is the number of experimentally measured quantities used for determining F.

Glass microchannels. To estimate the influence of the experimental parameters on the friction factor of microchannels with smooth walls and without outputs for pressure measurement, it is convenient to convert Eq. (3.2) into the form based on the measured quantities as

$$f = 2\frac{\pi D^5 \Delta P t^2}{\rho l^2 L d^4},$$

where D is the internal diameter of the microchannel, d is the diameter of the glass tube for fluid flow rate measurement, L is the microchannel length, l is the height of the fluid column in the tube for fluid flow rate measurement, and t is the time needed for the fluid to cover the distance l.

The normalized error in determining the friction factor in this case is determined as

$$\frac{e_f}{f} = \sqrt{\left(5\frac{e_D}{D}\right)^2 + \left(\frac{e_P}{P}\right)^2 + \left(2\frac{e_t}{t}\right)^2 + \left(\frac{e_L}{L}\right)^2 + \left(2\frac{e_l}{l}\right)^2 + \left(4\frac{e_d}{d}\right)^2}.$$

It is seen from this formula that the maximum contribution to the error in determining the friction factor can be made by an error in microchannel diameter measurement. The error in microchannel diameter determination is 1%. The error in fluid flow rate determination is 4% at low Reynolds numbers and 2% at high Reynolds numbers. The channel length is measured within $\pm 50~\mu m$. The nominal error in the pressure sensor specification is 0.25%. Thus, the error in friction factor measurement varies from 8 to 13%.

Polymer microchannels. To estimate the error in determining the friction factor in microchannels with holes for pressure measurement, we use Eq. 3.3. The normalized error of the friction factor as a function of the errors of independent variables is determined by the formula

$$\frac{e_f}{f} = \sqrt{\left(5\frac{e_D}{D}\right)^2 + \left(\frac{e_P}{P}\right)^2 + \left(\frac{e_L}{L}\right)^2 + \left(2\frac{e_Q}{Q}\right)^2}.$$
 (3.5)

The error in diameter measurement in a microchannel with a diameter of 68.9 μm is $\pm 0.56~\mu m$ for a straight microchannel and $\pm 2.26~\mu m$ for a curved microchannel. The error in microchannel length determination is $\pm 0.02~m m$ in both cases, and the error in fluid flow rate measurement is $\pm 0.06~m l/m in$ on average. The error in pressure measurement is determined by the sensors used; the nominal value is $\pm 0.25\%$ of the measured value. Thus, the friction factor measurement error is 7–10% for a straight microchannel and 10–18% for a curved microchannel.

Microchannel matrices. For microchannel matrices, the normalized error of the friction factor is determined by Eq. 3.5 as a function of the errors of independent variables.

The hydraulic diameters of the microchannel matrices with the lattice parameters of 6×6 and $15\times 15~\mu m$ are 4.5 and 12 μm , respectively. The error in determining the microchannel size is 0.1 and 0.3 μm , respectively. The thickness of the microchannel matrices is determined within 2 μm . The error in fluid flow rate determination is $\pm 0.06~m l/min$ on average. The error in pressure measurement is determined by the sensors used; the nominal value is $\pm 0.25\%$ of the measured value. Thus, the friction factor measurement error is 11–16% for the microchannel with hydraulic diameter of 4.5 μm and 13–14% for the microchannel with hydraulic diameter of 12 μm .

3.5 Fluid Flow in Straight Tubes

The study of flows in straight tubes is the classical problem of fluid dynamics. Beginning from the experiments of Hagen (1839) and Poiseuille (1841), various researchers have investigated this problem: Stokes (1845), Reynolds (1883), Lord Rayleigh (1892), Darcy (1858), and many others. At the beginning of the 20th century, Nikuradse (1933) performed comprehensive experiments aimed at studying the effect of roughness on laminar and turbulent flows in tubes. All of these investigations were performed for tubes with sufficiently large diameters.

Systematic investigations in microchannels were started at the end of the 20th century. Thus, based on modern concepts, Bontemps (2005) considered various effects arising in microchannel flows in great detail. However, the available experimental data are sometimes contradictory. In many investigations, experimentally measured friction factors coincide with theoretical predictions for macroscopic tubes. One such publication is that of Rands et al. (2006), who performed experiments in tubes 16.6-32.2 µm in diameter. Lelea et al. (2004) did not find any discrepancies between experimental results and theoretical estimates either (diameters of microchannels made of stainless steel in their studies were 100, 300, and 500 µm). The experimental data of (Judy et al. 2002) are also in good agreement with theoretical macroscopic values; those experiments were performed for different fluids (distilled water, isopropanol, and methanol) in microchannels made of stainless steel and quartz with different cross-sectional shapes (circular and square) and hydraulic diameters of 15-150 µm. The friction factor for smooth microchannels made of glass and quartz with diameters ranging from 80 to 205 µm (Li et al. 2003) and from 50 to 100 µm (Li et al. 2007) in the laminar case is also consistent with the classical theory. As a whole, the data of (Celata et al. 2006) for microtubes 31–326 µm also agree with theoretical macroscopic predictions, but the scatter of data is sometimes greater than 10%.

At the same time, some investigations reveal significant differences between experimental and theoretical macroscopic data. Thus, for instance, such differences were noted by Mala and Li (1999), who studied the flow of deionized water in quartz and stainless steel microtubes with circular cross-sections and diameters smaller than 150 μ m, and also by Cui and Silber-Li (2004), who performed experiments with tubes 3, 5, and 10 μ m in diameter. It was noted that the flow rate of the fluid is greater than that predicted by the classical theory, whereas the normalized Poiseuille number is smaller than unity.

In experiments with microtubes, special attention should be paid to their inner surface roughness. It is usually difficult to control the roughness level, glass and quartz surfaces are often considered smooth, and the differences in data obtained in stainless steel channels are often attributed to the roughness effect of the walls. As a whole, roughness increases the friction factor. For example, the Poiseuille number in experiments with stainless steel channels was 15% greater than the theoretical value for a laminar flow (Li et al. 2003). Kandlikar et al. (2003) considered the influence of roughness on the distilled water flow in tubes 0.62 and 1.067 mm in

diameter and proved that roughness increases the pressure drop in the microchannel and affects the friction factor for channels smaller than 1 mm.

The friction factors for smooth quartz microchannels and rough stainless steel microchannels were compared by Li et al. (2007). The diameter of quartz microchannels varied from 50 to 100 μ m, and the diameter of stainless steel microchannels varied from 373 to 1570 μ m. It was noted that the friction factor for rough channels is greater than that predicted by the theory and increases with increasing normalized roughness. The use of methanol as a test fluid also showed that the surface roughness, viscosity, and channel geometry exert significant effects on microchannel flow characteristics (Chen et al. 2004). The hydraulic diameter in that work varied in the interval of 57–267 μ m.

There are also discrepancies in determining the Reynolds number of the transition from a laminar to a turbulent flow. The transition location is affected by several factors: surface roughness, differences in the input regions, aspect ratio of the channel, accuracy of channel geometry, etc. It is not always possible to detect these factors at the microscopic level. Experimentally determined transition locations display significant scattering. Thus, it was demonstrated for silicon channels with a tapered cross-section (Wu and Cheng 2003) that the transition from a laminar to a turbulent flow in channels with large hydraulic diameters (103.4–291 μm) occurs within the range of Reynolds numbers from 1500 to 2000. Barlak et al. (2011) experimentally studied the fluid flow in steel microtubes with diameters ranging from 200 to 589 μm and found that the laminar-turbulent transition is observed at Reynolds numbers in the interval from 2000 to 2500. Morini et al. (2007) considered a nitrogen flow in circular microchannels 100–130 μm in diameter and found the transition Reynolds number to be 2100–3900.

Let us consider some new results obtained recently. Detailed measurements of the fluid flow rate in microchannels and the pressure distribution along the channel were performed by Aniskin et al. (2012) in microchannels fabricated in accordance with the technology described in this chapter.

Fluid flow rate through microchannels. Some measured data on the fluid flow rate through glass and silicon microchannels are shown in Fig. 3.18.

It is seen that the fluid flow rate in all experiments within the considered ranges of parameters is directly proportional to the pressure drop along the microchannel, which is consistent with the classical data.

Pressure distribution inside microchannels. A specific feature of the pressure distribution inside the microchannels is the experimental arrangement with the opposite directions of fluid motion, i.e., the fluid flow input and output were alternated. In what follows, they are mentioned as forward and backward flows. This experimental arrangement allowed the number of measurement points to be doubled, and the effect of the input conditions could be observed. Though the fittings were fabricated by the same technology, there might be some differences in the input conditions.

The pressure distributions along a straight microchannel with a diameter of $100~\mu m$ and length L=19.35~mm for four Reynolds numbers are plotted in Fig. 3.19. The abscissa axis shows the normalized length of the channel. The

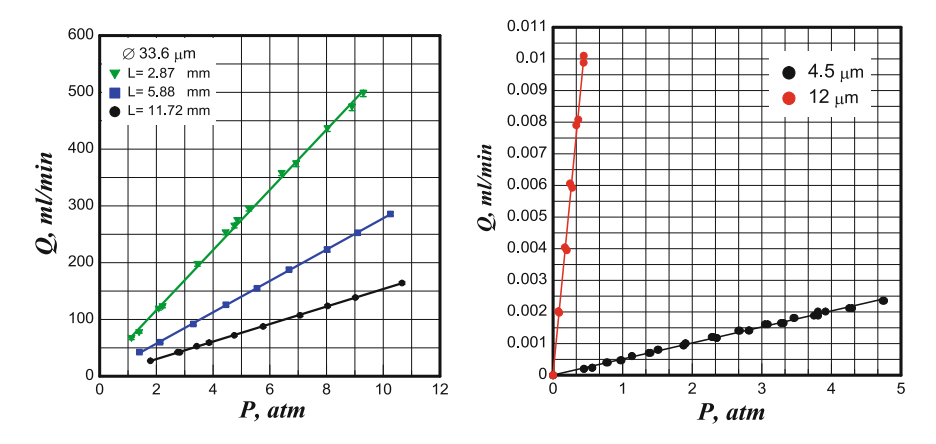
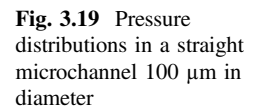
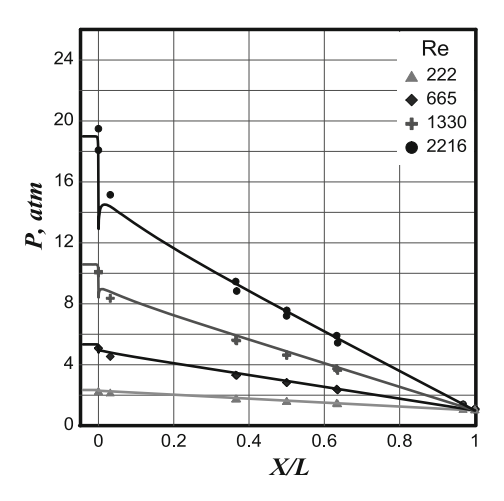


Fig. 3.18 Fluid flow rate versus the pressure drop in the microchannel





pressure distributions are computed by the ANSYS Fluent software package for the chosen Reynolds numbers. The computed results are indicated by the curves and agree well with the experimental points.

More detailed pressure distributions in a channel with a diameter of $68.9~\mu m$ and length of 11.33~mm for six Reynolds numbers ranging from 322 to 2895 are plotted in Fig. 3.20. The filled and open points show the pressure distributions for the forward and backward flows, respectively. At low Reynolds numbers, the pressure distributions for the forward and backward flows coincide with each other. However, the curves differ from each other for elevated Reynolds numbers from 1800 to 2574. The reason for these differences can be formulated as follows: the transition from a laminar to a turbulent flow already begins in the backward flow, whereas the forward flow is still laminar, as is demonstrated below. At the Reynolds

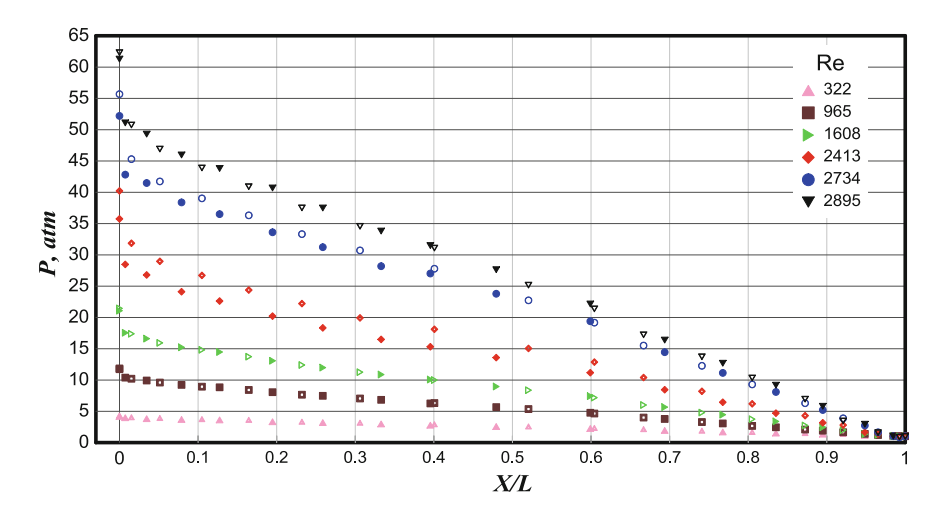


Fig. 3.20 Fluid pressure distributions in a straight microchannel 68.9 μm in diameter

number equal to 2895, the pressure distributions for both cases coincide again, which means that the laminar-turbulent transition has already occurred in both cases and the fluid flows are turbulent.

For Reynolds numbers higher than 600, there is some nonlinearity in the pressure distribution as a function of the streamwise coordinate (a "hump" in the middle of the curve). This deviation from linearity is observed in both forward and backward flow cases. Such situations were also observed in earlier investigations. Thus, nonlinearity is observed in the data of Kohl et al. (2005), but the authors ignored this nonlinearity and considered the dependence as linear. Costaschuk et al. (2007) observed a nonlinear pressure distribution inside the microchannel, which was attributed to a possible effect of the separation region in the initial part of the microchannel. In our opinion, the nonlinearity of the pressure distribution inside the microchannel is induced by different rates of the pressure decrease in the region of developing and fully developed flows. In further experiments, the friction factor was determined only in the fully developed flow region.

Friction factor of glass microchannels. The friction factors for glass microchannels calculated according to the method of two channels (Eq. 3.4) are shown in Fig. 3.21. For better presentation, the curves are given for the normalized Poiseuille number C^* as a function of the Reynolds number, where the normalized Poiseuille number is defined as the ratio of the experimentally determined Poiseuille number to the value theoretically predicted for a macroscopic laminar flow:

$$C^* = \frac{(f \operatorname{Re})_{\exp}}{(f \operatorname{Re})_{theor}}.$$

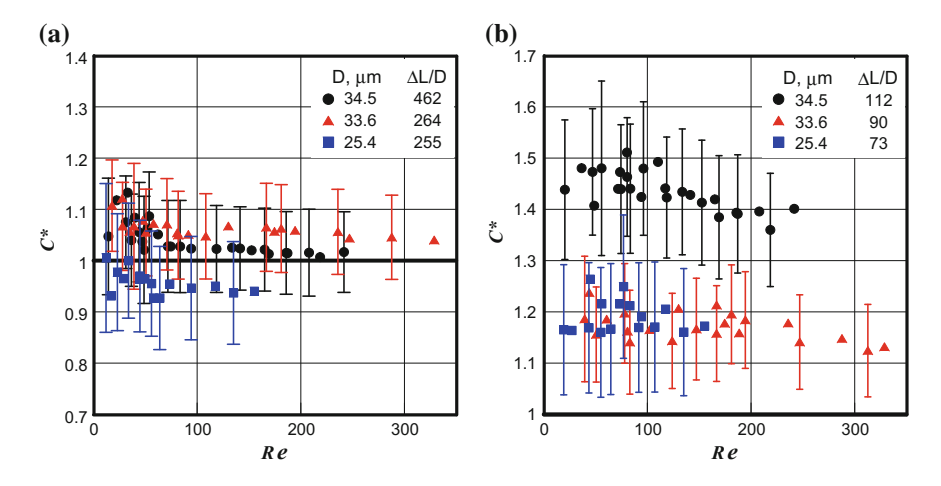


Fig. 3.21 Normalized Poiseuille number versus the Reynolds number for channels with different aspect ratios

Figure 3.21a shows the normalized Poiseuille number for microchannels 34.5, 33.6, and 25.4 μm in diameter. The difference in the length of these channels normalized to the microchannel diameter $\Delta L/D$ is 462, 264, and 255, respectively. In all measurements, the normalized Poiseuille number is close to unity within the experimental accuracy, i.e., the experimental data are adequately predicted by the macroscopic theory.

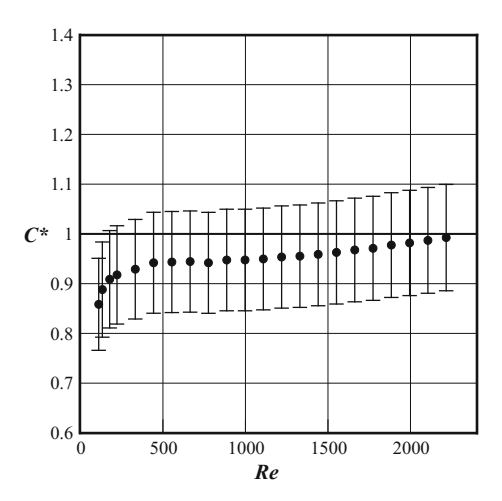
Figure 3.21b shows the data obtained for the same hydraulic diameters, but for the values of $\Delta L/D$ being 112 for the channel diameter of 34.5 μ m, 90 for the channel diameter of 33.6 μ m, and 73 for the channel diameter of 25.4 μ m. It is seen that the friction factors exceed the theoretical value by 15–50%. The normalized Poiseuille number, i.e., the ratio of the experimental to theoretical data, stays within the interval from 1.15 to 1.5.

The conducted experiments showed that the area of application of the method of two channels is limited. For this method to ensure correct results, the length of the short microchannel should be at least 150 calibers (diameters), and the difference in the lengths of two microchannels should be 150–170 calibers or more. The method of two channels is invalid for short microchannels (shorter than 100–120 calibers).

Friction factor of polymer microchannels. Figure 3.22 shows the friction factor for a straight microchannel $100~\mu m$ in diameter and 19.39~mm long as the normalized Poiseuille number versus the Reynolds number. The Reynolds numbers reached in the experiment varied from 150~to~2200. Within the experimental accuracy, the values of the normalized Poiseuille number are close to unity (except for very low Reynolds numbers), i.e., the friction factor of the microchannel is consistent with its theoretical value.

Figure 3.23a shows the friction factor for a straight channel 68.9 μ m in diameter (L=11.33 mm) for the forward and backward flow cases. In this case, the

Fig. 3.22 Normalized Poiseuille number versus the Reynolds number for a microchannel 100 μm in diameter



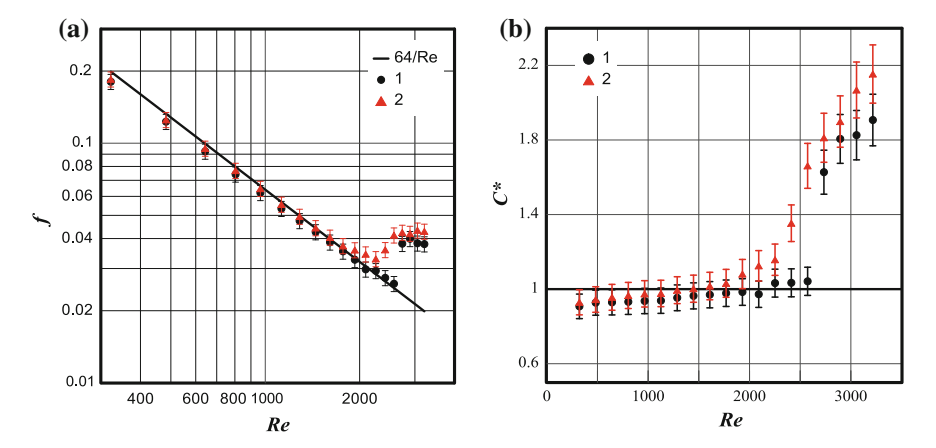


Fig. 3.23 Friction factor (**a**) and normalized Poiseuille number (**b**) for a microchannel 68.9 μ m in diameter; forward flow (1) and backward flow (2)

laminar-turbulent transition occurs at Reynolds numbers of 2300 for the backward flow and 2600 for the forward flow. The difference in the Reynolds numbers is apparently caused by the difference in the input conditions at the opposite ends of the microchannel. The corresponding normalized Poiseuille number C^* is plotted in Fig. 3.23b. In the transition region, C^* starts to grow, because normalization is performed to the theoretical value for a laminar flow.

Friction factor of silicon microchannels. The friction factor for a single channel in a microchannel matrix is determined by Eq. 3.2. The edge effects can be

neglected for low Reynolds numbers. As is seen from the pressure distribution along a straight microchannel (Fig. 3.20), there is no drastic decrease in pressure at the microchannel entrance at Reynolds numbers smaller than 200. In view of this fact, the friction factor can be calculated on the basis of the total pressure drop along the microchannel matrix and the microchannel length. The thus-treated experimental results are shown in Fig. 3.24 as the normalized Poiseuille number C^* versus the Reynolds number. The Poiseuille number for channels with a square cross-section is 56.9. The normalized Poiseuille number is close to unity, i.e., good agreement is observed between the experimental and theoretical data.

Friction factor of the input region of microchannels. The channel input region (more exactly, the friction factor of this region) is of significant interest from the viewpoint of microchannel design and determining its total friction factor. Problems of studying this important issue are aggravated by the extremely small size of this region, where a decrease in pressure occurs. Figure 3.25 shows the friction factors of input regions, which were determined for microchannels on the basis of pressure measurement. It should be noted that the reference book on friction factors contains

Fig. 3.24 Normalized Poiseuille number versus the Reynolds number for silicon microchannels

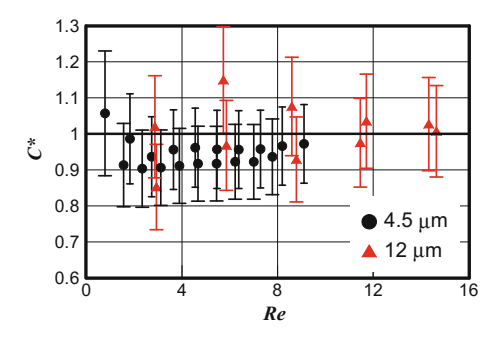
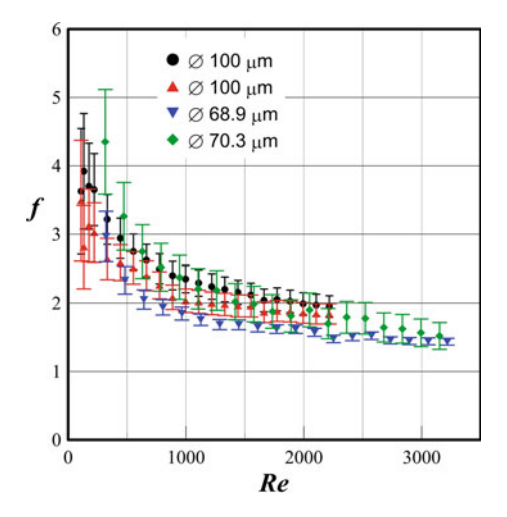
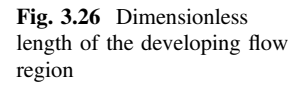
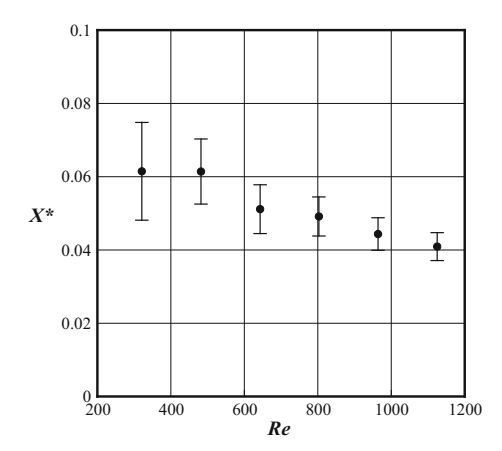


Fig. 3.25 Friction factor of microchannel input regions







no data for the configuration of manifolds and Reynolds numbers considered in the present study.

The length of the developing flow region in these experiments is calculated as $L_{dev} = X*D$ Re. It is determined from the pressure distribution in a straight microchannel 68.9 µm in diameter for Reynolds numbers ranging from 321 to 1125. For finding the developing flow region, the experimental pressure distribution is approximated by the fourth-power polynomial. The coordinate of the point of intersection of the approximation curve with the straight line drawn through the points of the fully developed flow region was taken as the length of the developing flow region. Figure 3.26 shows the dimensionless length of the developing flow region. The value of X* lies in the interval from 0.04 to 0.06, which is consistent with X* = 0.05 (Donsqing 2008) and is greater than X* = 0.029 (Idel'chik 1992; Shiller 1936). Thus, the value X* = 0.05 is preferable for estimating the length of the developing flow region in microchannels.

3.6 Fluid Flows in Curved Tubes

Elbow tubes are necessary and important elements of pipelines for flow turning. The fluid flow in curved tubes was studied by Dean (1927). A secondary transverse flow arises in curved tubes and channels owing to a change in the flow direction, i.e., a paired vortex is formed, which is superimposed onto the main flow; for this reason, the streamlines acquire a screw-like shape. The emergence of such a vortex is explained by the fact that the rapidly moving central portions of the fluid are displaced by centrifugal forces to the external walls; in turn, they displace slowly moving peripheral portions of the fluid, which finally form a paired vortex owing to flow symmetry. Motion of this type increases the friction factor of the channel.

In addition to the basic governing parameters, the motion in curved tubes is also characterized by the bending radius R_0 . A special dimensionless parameter (the Dean number) is introduced for such a flow:

$$Dn = Re \left(\frac{D}{2R_0}\right)^{0.5}.$$

It is commonly assumed (Idel'chik 1992) that tubes are smoothly curved if the ratio of the bending radius to the tube diameter is much greater than 1.5: $R_0 \gg 1.5D$.

The total friction factor of smoothly curved tubes and channels is not only a function of the Reynolds numbers, but also of the bending radius:

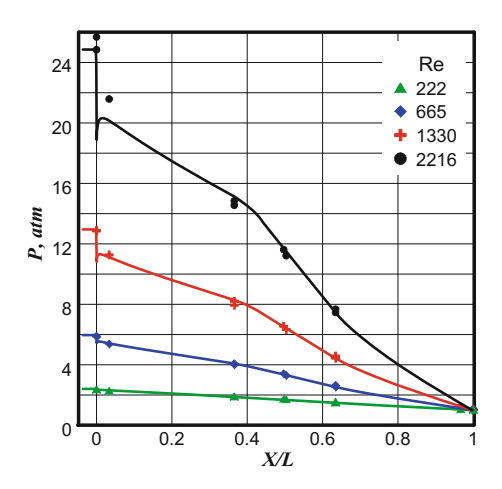
$$f = \frac{20}{\text{Re}^{0.65}} \left(\frac{D}{2R_0}\right)^{0.175}.$$

This formula is valid for the range of the Dean numbers from 50 to 600.

Pressure distribution inside curved microchannels. The pressure distributions inside a curved microchannel $100~\mu m$ in diameter obtained in experiments by Aniskin et al. (2012) are shown in Fig. 3.27. In addition, the corresponding computations were also performed with the use of the ANSYS Fluent software package for Reynolds numbers reached in these experiments. The computed results are shown by the curves, which are seen to be in good agreement with the experimental points. The fluid pressure distribution has a nonlinear character.

The calculations show that the Dean vortices are formed in the curved region; these vortices arise even at small flow rates and lead to a nonlinear pressure distribution. Figure 3.28 shows the transverse distributions of the fluid velocity at the beginning of the curved region (cross-section I), in the middle (cross-section I), and at its end (cross-section I). The flow direction is from cross-section I to

Fig. 3.27 Pressure distributions in a curved microchannel



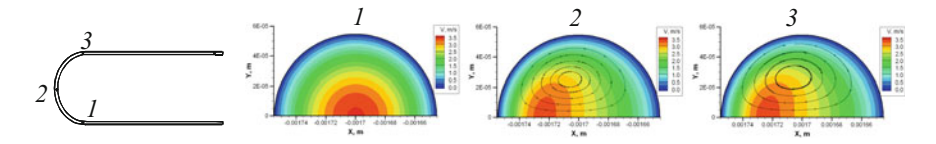


Fig. 3.28 Transverse distributions of the fluid velocity for Q = 1 ml/min

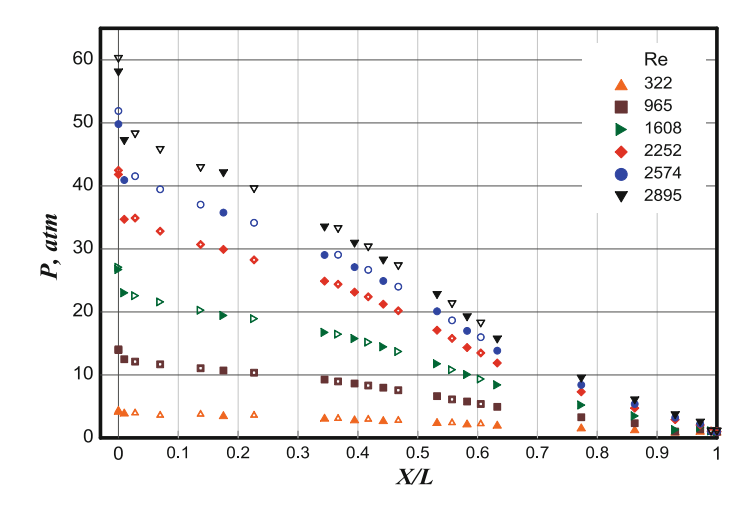


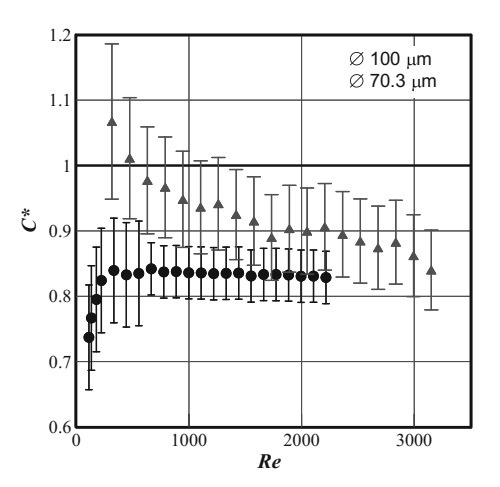
Fig. 3.29 Pressure distributions in a curved microchannel

cross-section 3. The results are given for the fluid flow rate Q = 1 ml/min. Vortex structures are visible in the elbow region and at the beginning of the straight-line part of the channel.

More detailed pressure distributions along a microchannel 70.3 μ m in diameter are shown in Fig. 3.29. In this case, the elbow region was studied in great detail. Here, the filled and open points show the pressure distributions for the forward and backward flow cases, respectively. For all Reynolds numbers, the pressure distributions in the forward and backward flow cases coincide with each other. The data in the figure confirm the nonlinear character of the pressure distributions in the fluid flow in a curved channel.

Friction factor of curved microchannels. The rounded (elbow) region is of major interest in curved microchannels. Yang et al. (2005) measured the friction factor of microchannels 100 μ m high and 0.5–1.0 mm wide, with banding radii ranging from 33 to 53 mm. The friction factor was found to decrease slightly as the bending radius was increased, and its value was smaller than that predicted by the classical Navier-Stokes equations for hydraulically smooth surfaces. The calculated results become consistent with the experiment if the surface roughness is taken into account. However, Yang et al. (2005) did not consider the flow in the input region, which may lead to significant distortion of the results.

Fig. 3.30 Normalized Poiseuille number for the bending region of curved microchannels



Chu et al. (2010) considered the flow in curved rectangular channels with different geometric parameters on a silicon plate in the interval Dn = 10-167. The results calculated by the classical Navier-Stokes equations were observed to agree well with experimental values. For the range of Reynolds numbers 80 < Re < 876, the mean differences between the predicted values of the friction factor and the experimental results are smaller than 10%. It was noted that the geometric ratio of the channel sides exerts an appreciable effect on the pressure decrease; moreover, the smaller the channel bending radius, the higher the pressure loss. The number Po = f Re for four bent configurations of microchannels varies almost linearly and increases with increasing Dn.

The friction factors in the bending region were determined by Aniskin et al. (2012); they are shown in Fig. 3.30 for curved microchannels with diameters of 100 and 70.3 μ m. The results obtained in this study were compared to the reference value for smoothly curved tubes (Idel'chik 1992).

For the 100 μ m microchannel, the friction factor of the bending region is smaller than the reference value by 17%. For the microchannel 70.3 μ m in diameter, the difference varies from 10–16% for Reynolds numbers higher than 1500.

As a whole, the reported results show that the friction factor of straight microchannels can be described by the classical formulas derived for large-diameter channels. Such data are available in the literature and can be used in applications with a 10% error in the range of fluid flow parameters discussed in this chapter. The friction factor of the bending region of curved channels is smaller than the reference values by 10–17%.

Experimentally determined friction factors of output regions are extremely important for the design of microfluidic devices. In the present work, however, only one input region configuration is considered. In practice, it is necessary to know friction factors for many other input geometries, which requires new experiments with microchannels.

A nonlinear pressure distribution along the length of the straight microchannel is detected. The friction factor of microchannel input for the given geometries and the Reynolds numbers of the input sections not represented in the reference literature are determined. For curved microchannel sections, the friction factors obtained in the present study are less than those indicated in the literature for the corresponding Reynolds numbers and curvatures of microchannels.

References

- Aniskin VM, Adamenko KB, Maslov AA (2012) Measurement of pressure inside microcanals of various form. Nanosystems Phys Chem Math 3(2):37–46
- Barlak S, Yapici S, Sara ON (2011) Experimental investigation of pressure drop and friction factor for water flow in microtubes. Int J Thermal Sci 50(3):361–368
- Bontemps A (2005) Measurements of single-phase pressure drop and heat transfer coefficient in micro and minichannels. Microscale heat transfer fundamentals and applications. Springer, Berlin
- Celata GP, Cumo M, McPhail S, Zummo G (2006) Characterization of fluid dynamic behaviour and channel wall effects in microtube. Int J Heat Fluid Flow 27(1):135–143
- Chen Y-T, Kang S-W, Tuh W-C, Hsiao T-H (2004) Experimental investigation of fluid flow and heat transfer in microchannels. Tamkang J Sci Eng 7(1):11–16
- Chu J-C, Teng J-T, Greif R (2010) Experimental and numerical study on the flow characteristics in curved rectangular microchannels. Appl Thermal Eng 30(13):1558–1566
- Costaschuk D, Elsnab J, Petersen S, Klewicki JC, Ameel T (2007) Axial static pressure measurements of water flow in a rectangular microchannel. Exp Fluids 43(6):907–916
- Cui H-H, Silber-Li Z-H (2004) Flow characteristics of liquids in microtubes driven by a high pressure. Phys Fluids 16(5):1803–1810
- Darcy H (1858) Recherches experimentales relatives au mouvement de l'eau dans les tuyax. Memoires a l'Academie d. Sciences de l'Institute imperial de France 15:141
- Dean WR, (2007) Note on the motion of fluid in a curved pipe. Phil. Mag. 4:208-223.
- Donsqing L (eds) (2008) Encyclopedia of microfluidics and nanofluidics. Springer, Berlin
- Hagen G (1839) Über die Bewegung des wassers in engen cylindrischen Röhren. Pogg Anna. d Phys u Chem (2) 16:423–442
- Idel'chik IE (1992) Reference book on hydraulic resistance. Mashinostroenie, Moskow
- Judy J, Maynes D, Webb BW (2002) Characterization of frictional pressure drop for liquid flows through microchannels. Int J Heat Mass Transf 45(17):3477–3489
- Kandlikar SG (2003) Microchannels and minichannels—history, terminology, classification and current research needs. In: Abstracts of first international conference on microchannels and minichannels, Rochester, New York, USA, 24–25 Apr 2003
- Kandlikar SG, Joshi S, Tian S (2003) Effect of surface roughness on heat transfer and fluid flow characteristics at low Reynolds numbers in small diameter tubes. Heat Transf Eng 24(3):4–16
- Kohl MJ, Abdel-Khalik SI, Jeter SM, Sadowski DL (2005) An experimental investigation of microchannel flow with internal pressure measurements. Int J Heat Mass Transf 48(8):1518– 1533
- Lelea D, Nishio S, Takano K (2004) The experimental research on microtube heat transfer and fluid flow of distilled water. Int J Heat Mass Transf 47(12–13):2817–2830
- Li Z-X, Du D-X, Guo Z-Y (2003) Experimental study on flow characteristics of liquid in circular microtubes. Microscale Thermophys Eng 7(3):253–265
- Li Z, He Y-L, Tang G-H, Tao W-Q (2007) Experimental and numerical studies of liquid flow and heat transfer in microtubes. Int J Heat Mass Transf 50(17):3447–3460

References 125

Lorenzini M, Morini GL, Henning T, Brandner J (2009) Uncertainty assessment in friction factor measurements as a tool to design experimental set-ups. Int J Thermal Sci 48(2):282–289

- Mala GM, Li D (1999) Flow characteristics of water in microtubes. Int J Heat Fluid Flow 20 (2):142-148
- Morini GL (2004) Laminar-to-turbulent flow transition in microchannels. Nanoscale Microscale Thermophys Eng 8(1):15–30
- Morini GL, Lorenzini M, Colin S, Geoffroy S (2007) Experimental analysis of pressure drop and laminar to turbulent transition for gas flows in smooth microtubes. Heat Transf Eng 28(8–9):670–679
- Nikuradse J (1933) Law of flow in rough pipes. Technical memorandum 1292, National Advisory Committee for Aeronautics; translation of "Stromungsgesetze in rauhen Rohren," VDIForschungsheft 361, 1950. Beilage zu "Forschung auf dem Gebiete des Ingenie urwesens" Ausgabe B Band 4
- Poiseuille JLM (1841) Recherches experimentales sur les movement des liquides dans les tubes de tres petits diameters. Comp Rend 11:961–1041
- Rands C, Webb BW, Maynes D (2006) Characterization of transition to turbulence in microchannels. Int J Heat Mass Transf 49:2924–2930
- Rayleigh L (1892) On the question of the stability of the flow of fluids. Philos Mag (5) 34 (206):59-70
- Reynolds O (1883) An experimental investigation of the circumstances which determine whether the motion of water shall be direct or sinuous, and of the law of resistance in parallel channels. Philos Trans Roy Soc Lond 174:935–982
- Romanov SI, Vandisheva NV, Semenova OI, Kosolobov SS (2011) Method for obtaining a channel matrix. RU Patent 2,428,763, 10 Sept 2011
- Shiller L (1936) Flowing of liquids in pipes. ONTI NKTP USSR, Moskow
- Stokes GG (1845) On the theories of the internal friction of fluids in motion, and of the equilibrium and motion of elastic solids. Trans Camb Philos Soc 8:287–305
- Tsai H-H, Lin C-Y, Huang C-F, Chien C-M, Hsieh S-S (2004) Gas flow in a long microchannel. Int J Heat Mass Transf 47(17–18):3877–3887
- Wook YH, Kim MS (2006) The pressure drop in microtubes and the correlation development. Int J Heat Mass Transf 49(11–12):1804–1812
- Wu HY, Cheng P (2003) Friction factors in smooth trapezoidal silicon microchannels with different aspect ratios. Int J Heat Mass Transf 46(14):2519–2525
- Yang W-H, Zhang J-Z, Cheng H-E (2005) The study of flow characteristics of curved microchannel. Appl Thermal Eng 25(13):1894–1907
- Zhang L, Gu F, Tong L, Yin X (2008) Simple and cost-effective fabrication of two-dimensional plastic nanochannels from silica nanowire templates. Microfluid Nanofluid 5(5):727–732

Chapter 4 Modeling of Micromixers



Abstract Mixing of fluids is an extremely important process, widely used in various microfluidic devices (chemical microreactors, chemical and biological analyzers, drug delivery systems, etc.). Mixing in macroscopic flows usually occurs in the turbulent regime. However, microflows are mainly laminar, and mixing under standard conditions is caused only by molecular diffusion. Because of the extremely low values of the molecular diffusion coefficient, this manner of mixing is very ineffective. To increase the mixing velocity, it is necessary to use special devices: micromixers. For this reason, such devices are key elements of many microelectromechanical systems (MEMS). This chapter describes the results of CFD simulations of the simplest micromixers. The method used to solve the Navier-Stokes equations is described in the first two sections. Sections 4.3 and 4.4 are devoted to the study of the flow and mixing regimes in Y-type micromixers at low and moderate Reynolds numbers. In the next section, the flow in T-type micromixers is studied experimentally and the obtained data is compared with those from modeling. Modeling of two-phase flow and heat transfer in micromixers is considered in the two subsequent sections. One simple active method for mixing is discussed in the last section.

4.1 Algorithm for Solving the Navier-Stokes Equations

There are passive and active methods of mixing velocity enhancement (see, e.g., Karnidakis et al. 2005; Tabeling 2005; Karnik 2008). In the first case, the channel geometry is varied, various inserts are used, etc. In the second group of methods, some external (acoustic, electrical, or magnetic) fields are applied or the flow rate of the fluid is varied.

Though the problem is urgent, the structure and properties of flows in such channels have not been adequately studied. Experimental investigations are difficult because of extremely small channel sizes. Only the integral properties of flows can be measured experimentally: flow rate of the fluid at a prescribed pressure gradient, velocity profile, pressure drop, etc. However, to optimize the mixing process, it is necessary to

understand the flow structure and the mixing mechanisms. Thus, mathematical modeling plays a key role in studying such flows. There are many publications in which micromixer design has been investigated through methods of computational fluid dynamics (CFD) (see, e.g., the reviews (Stroock et al. 2002; Karnidakis et al. 2005), the papers (Vanka et al. 2004; Hong et al. 2004; Jiménez 2005; Aubina et al. 2005; Lin et al. 2007; Cao et al. 2008), and the references cited therein). The general principles of micromixer operation were discussed in Tabeling (2005). At the same time, the number of already developed and possible new mixers is so large that, on the one hand, their simulations should be continued and, on the other hand, some optimization research is needed. The Reynolds numbers are usually not very high, especially in sufficiently small microchannels, and the flow is laminar. Therefore, the first challenge in studying micromixers is the investigation of the character of microflows in this range of Reynolds numbers. In practice, however, there are situations with sufficiently high Reynolds numbers (Re) in microflows (Hoffmann et al. 2006; Mansur et al. 2008). Moreover, if the Reynolds number in the microchannel flow is sufficiently high, some new interesting phenomena occur, which have to be considered both from the basic research viewpoint and for applications. These processes can be studied using the Navier-Stokes equations.

A considerable number of algorithms for solving the Navier-Stokes equations are available today. These are various modifications of the Galerkin method, including spectral methods, finite element and finite volume methods, various meshless methods, large eddy simulation, etc. Several commercial software packages have also been developed. In the present work, the flow and heat transfer in microchannels were simulated with the SigmaFlow package, which is suitable for solving a large class of problems of hydrodynamics, heat and mass transfer, and combustion. The package is based on the algorithm for solving the Navier-Stokes equations according to the finite volume method; the basic features of the algorithm were formulated in Rudyak et al. (2008), Minakov et al. (2008), Gavrilov et al. (2011). The algorithm is briefly described below, and only incompressible flows of Newtonian fluids are considered here. In this formulation, the flow is described by the Navier-Stokes equations (1.3). However, for the present purpose, it is more convenient to rewrite these equations in a different form. The continuity and momentum equations are transformed into

$$\frac{\partial \rho}{\partial t} = -\nabla \cdot \rho \mathbf{u}, \quad \frac{\partial \rho \mathbf{u}}{\partial t} + \nabla \cdot (\rho \mathbf{u} \mathbf{u}) = -\nabla p + \nabla \cdot \mathbf{\tau} + \rho \mathbf{g}, \tag{4.1}$$

where ρ is the fluid density, **u** is the velocity vector, p is the pressure, and the viscous stress tensor components are defined as $\tau = -\mu \mathbf{D}$.

Introducing the enthalpy of the system

$$h(T) = \int_{T_0}^{T} c_p dT, \tag{4.2}$$

we can write the energy conservation equation in the form

$$\frac{\partial \rho h}{\partial t} + \nabla \cdot (\rho \mathbf{u} h) = \nabla \cdot (\lambda \nabla T), \tag{4.3}$$

where λ is the thermal conductivity of the fluid and c_p is the specific heat. As the flows under consideration may be non-isothermal, both the specific heat of the fluid and the transport coefficients are functions of temperature. In the algorithm, this temperature dependence is represented by a fourth-power polynomial.

Thus, the fluid temperature T at each point is calculated from Eq. (4.2) with the enthalpy value found from Eq. (4.3). The fluid density as a function of temperature is described by the formula

$$\rho = \frac{\rho_0}{1 + \beta(T - T_0)}.$$

Here, ρ_0 is the fluid density at room temperature T_0 and β is the thermal expansion coefficient.

The CFD equations (4.1), (4.3) were discretized on the chosen grid according to a widely known control volume method for unstructured grids, which automatically ensures the conservativeness of the resultant scheme. A finite difference analog of these equations is obtained by integration over all control volumes (Ferziger and Peric 2006).

The convective terms are approximated by the QUICK second-order upwind scheme (Leonard 1979). The unsteady terms are discretized according to a first-order implicit scheme. The diffusion fluxes and the source terms are approximated with the second order of accuracy.

The input boundary of the computational domain is subjected to the Dirichlet condition, i.e., all three components of the velocity vector and the medium temperature are assumed to be known. At the output boundary of the computational domain, the Neumann conditions (the so-called "soft" conditions) are imposed for all scalar variables Φ considered in the study: $\partial \Phi/\partial \mathbf{n} = 0$, where \mathbf{n} is the vector of the external normal to the computational domain. The correct boundary conditions on the microchannel walls for the fluid velocity components in most cases are the no-slip or slip conditions. The last condition, in our case, can be rewritten in the form of the Neumann condition: $b\partial u/\partial \mathbf{n} = 0$, where b is the slip length.

As only incompressible flows are considered here and the equations of motion include only the pressure gradient, it is not necessary to calculate the absolute value of pressure. The relative pressure value is used here for flow modeling. Moreover, as the SIMPLEC algorithm is applied for solving the CFD equations, which implies solving the equation for the pressure correction, the boundary condition should be imposed only for correcting the pressure p'. The Neumann condition is used in this algorithm for the pressure correction on all boundaries of the computational domain (input, output, and walls).

Depending on the considered problem, the computational algorithm offers a possibility of setting all three kinds of boundary conditions for heat exchange with the solid wall. The boundary conditions of the first kind imply that the temperature dependence on the time t and coordinates \mathbf{r} on the boundary is known: $T_w = f(\mathbf{r}, t)$. If the amount of heat incoming from outside is known, then the boundary condition of the second kind is imposed; in this case, the specific heat flux through the body surface is specified:

$$\mathbf{q}_w = -\lambda(\partial T/\partial \mathbf{n});$$

moreover, the heat flux can be an arbitrary function of the coordinates and time.

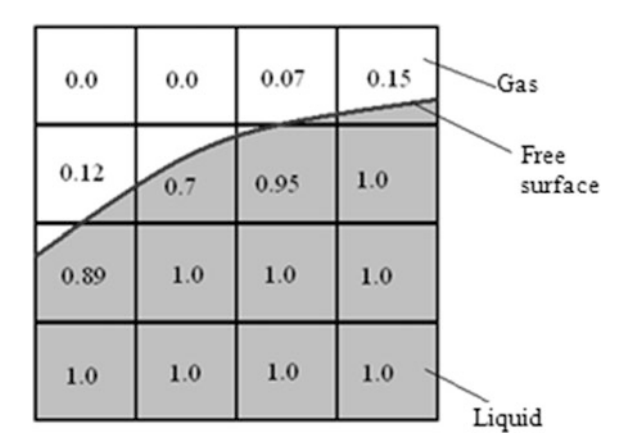
The boundary conditions of the third kind imply prescribing the ambient temperature and the coefficient of heat exchange between the surface and the ambient medium in accordance with the Newton-Richman law. Thus, the amount of heat released (or received) by a unit surface with a temperature T_w per unit time to (from) the ambient medium with a temperature T_m is directly proportional to the difference between the surface and ambient temperatures: $q_w = \alpha(T_w - T_m)$. The amount of heat released (or received) by the surface to (from) the ambient medium determined by this formula should be equal to the amount of heat transferred to this surface by means of heat conduction, which is determined by the Fourier law. The equality of these fluxes yields the boundary condition of the third kind

$$\left. \frac{\partial T}{\partial n} \right|_{w} = -\frac{\alpha}{\lambda} (T_w - T_m).$$

Multiphase flows in microchannels are fairly typical. The calculation of two-phase flows is a challenging task, because fluid-wall interaction in microchannels is very important. In this work, two-phase flows are simulated by a numerical technique based on the volume of fluid (VOF) method (Hirt and Nichols 1981), which was well approved in calculations of various macroscopic flows, including those with a free surface (Gavrilov et al. 2011; Podryabinkin and Rudyak 2011). The main idea of the method is to consider the fluid and the gas as a unified two-species medium, with the spatial distributions of the phases within the computational domain being determined by a special marker function F(x, y, z, t), whose value defines the volume fraction of the fluid phase in the computational cell in the following manner: F(x, y, z, t) = 0 if the cell is empty, F(x, y, z, t) = 1 if the cell is completely filled with the liquid, and 0 < F(x, y, z, t) < 1 if the cell contains the interface between the phases. Figure 4.1 shows an example of the representation of the free surface of the fluid with the use of the function F(x, y, z, t) on a rectangular computational grid.

As the free surface moves together with the fluid, its motion is traced by solving the transport equation for the volume fraction of the fluid phase in the cell:

Fig. 4.1 Representation of the free surface of the fluid by the function F(x, y, z, t)



$$\frac{\partial F}{\partial t} + \mathbf{u} \cdot \nabla F = 0. \tag{4.3}$$

Here, \mathbf{u} is the velocity vector of the two-phase medium found through CFD equations.

The density and molecular viscosity of the considered two-component medium are found by using the volume fraction of the fluid in the cell: $\rho = \rho_1 F + (1-F)\rho_2$ and $\mu = \mu_1 F + (1-F)\mu_2$, where ρ_1 and μ_1 are the density and viscosity coefficient of the liquid, whereas ρ_2 and μ_2 are the density and viscosity coefficient of the gas. The thus-obtained values of the densities and viscosity coefficients are included in the equations of motion and determine the physical properties of the two-phase medium.

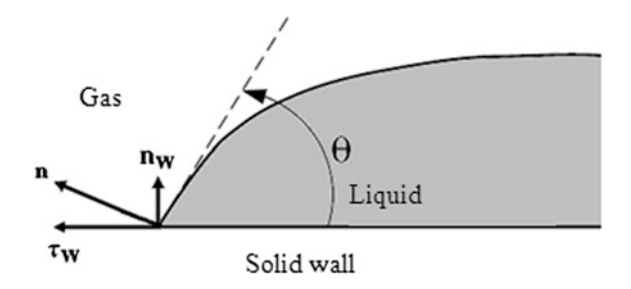
In considering fluid flows with an interface, one encounters surface tension, which cannot be neglected for microchannel flows, because it plays a key role in some cases. It is not a simple task to study flows controlled by surface tension forces. Nevertheless, this method allows for the influence of surface tension forces to be taken into account comparatively easily.

The algorithm most often used for surface tension simulation within the framework of the VOF method is the so-called continuum surface force (CSF) algorithm (Brackbill et al. 1992). It implies insertion of an additional volume force \mathbf{F}_s into the equations of motion; the magnitude of this force is determined by the relation $\mathbf{F}_s = \sigma k \nabla F$, where σ is the surface tension coefficient and k is the free surface curvature determined by the divergence of the normal vector $k = \nabla \cdot (\mathbf{n} | \mathbf{n} |)$. In turn, the normal to the free surface is calculated as the gradient of the volume fraction of the liquid phase in the cell: $\mathbf{n} = \nabla F$. On the solid wall, the magnitude of the normal vector is determined on the basis of the wetting angle θ as

$$\mathbf{n} = \mathbf{n}_w \cos \theta + \mathbf{\tau}_w \sin \theta$$
,

where \mathbf{n}_w and $\mathbf{\tau}_w$ are the normal and tangential vectors to the wall (see Fig. 4.2).

Fig. 4.2 Conditions on the contact line



The accuracy of this numerical technique depends, to a large extent, on the quality of solving Eq. (4.3). Therefore, particular attention was paid to testing and choosing the method for solving this equation. In particular, three different methods of integration of Eq. (4.3) were considered. The first one was the explicit TVD scheme

$$F^{n+1} = F^{n} - \frac{\tau}{h_{x}} (u_{R}F_{R} - u_{L}F_{L})^{n} - \frac{\tau}{h_{y}} (v_{D}F_{D} - v_{F}F_{F})^{n} - \frac{\tau}{h_{z}} (w_{T}F_{T} - w_{B}F_{B})^{n} + \tau F^{n}\nabla \cdot \mathbf{v}_{s},$$

where u_K , v_K , and w_K are the velocity vector components at the K-th face of the control volume, h is the computational grid step, τ is the time step found from the Courant condition, n is the number of the time layer, and F_K is the fraction of the liquid phase at the corresponding face of the control volume. The following example illustrates how this fraction is found. For instance, this fraction for the right face is found as $F_R = F_{i,j,k} + \partial F_R^+$ if $u_R > 0$ and $F_R = F_{i,j,k} + \partial F_R^-$ if $u_R < 0$. The first term of this expression corresponds to the first-order UDS scheme, which ensures computation stability, and the second one is a correction, which increases the order of approximation. The value of this correction is found by the formula

$$F_R = F_{i,j,k} + \partial F_R^+ = \frac{1}{2} \Psi \left(\frac{F_{i+1,j,k} - F_{i,j,k}}{F_{i,j,k} - F_{i-1,j,k}} \right) (F_{i,j,k} - F_{i-1,j,k}),$$

where $\Psi(r)$ is a limiter, which ensures solution monotonicity in high-gradient regions. In this work, we use the Superbee limiter (Ferziger and Peric 2006)

$$\Psi(r) = \max(0, \min(2r,1), \min(r,2)).$$

Then, we considered an explicit TDV scheme with local one-dimensional splitting in space (Marchuk 1990)

$$\begin{split} \hat{F} &= F^n - \frac{\tau}{h_x} (u_R F_R^n - u_L F_L^n), \quad \tilde{F} &= \hat{F} - \frac{\tau}{h_y} (v_D \hat{F}_B - v_F \hat{F}_F), \\ F^{n+1} &= \tilde{F} - \frac{\tau}{h_z} (w_T \tilde{F}_T - w_B \tilde{F}_B) + \tau F^n \nabla \cdot \mathbf{v}_s, \end{split}$$

where the convective fluxes through the control volume faces are determined in the same manner as described above.

In addition, we also used the first-order implicit scheme

$$\frac{F^{n+1} - F^n}{\tau} + \mathbf{v}_s^n \cdot \nabla F^{n+1} = 0$$

and the second-order implicit scheme

$$\frac{3F^{n+1} - 4F^n + F^{n-1}}{2\tau} + \mathbf{v}_s^n \cdot \nabla F^{n+1} = 0.$$

These equations were solved according to an iterative method of incomplete factorization. The convective fluxes on the faces were approximated by various upwind schemes, including some TDV schemes. The results of testing will be discussed in the next section.

Though turbulent regimes are not typical for microchannel flows, they may occur, which is of significant interest from both fundamental and practical viewpoints. Turbulent flows are calculated by an algorithm based on semi-empirical turbulence models formulated with the use of the Reynolds approach. Normally, this is the standard k- ε model or the so-called k- ω SST model of turbulence (Menter 1993).

In the case of turbulent flows, it is necessary to specify the turbulence characteristics in addition to the usual boundary conditions at the computational domain input. The kinetic energy of turbulent fluctuations k and the turbulence dissipation rate ε at the input are defined by the relations $k_{in} = (3/2)I^2\bar{\mathbf{v}}^2$ and $\varepsilon_{in} = C_{\mu}^{3/4}k_{in}^{3/2}/l$. Here, $\bar{\mathbf{v}}$ is the mean input velocity, l is the characteristic size of vortices, and l is the level of turbulent fluctuations at the input. It is rather difficult to determine the exact values of the last two variables; for this reason, they are usually defined by the formulas $l = 0.16(\mathrm{Re})^{1/8}$ and $l = (0/07 \div 0.1)L$. Here, l is the reference input number and Re is the Reynolds number determined on the basis of l and $\bar{\mathbf{v}}$.

The turbulent characteristics in close vicinity to the wall are determined by using the wall functions (Menter 1993). In this method, the flow parameters are related to the distance from the wall, and a simplified analytical solution is found. With the use of the wall functions, it is possible to avoid extreme refining of the computational grid and, correspondingly, significant computer expenses, while reasonable accuracy sufficient for solving engineering problems is still provided.

4.2 Testing of the Algorithm

Let us start by testing the algorithm through verification of the solution of Eq. (4.3). A two-dimensional convective problem (convective transfer of a square) is considered. The initial distribution for this problem is shown in Fig. 4.3 (left). The function F in the entire computational domain is equal to zero, except for the square located in the bottom left corner of the computational domain, where it is equal to unity. This square is transferred by a uniform flow directed along the diagonal of the computational domain. The flow velocity is $\mathbf{v} = 1.41 \,\mathrm{m/s}$. Naturally, the exact solution of the problem in this formulation is the shift of the initial distribution upward along the diagonal of the computational domain to a distance proportional to the computation time (Fig. 4.3, right). The computational domain size is 1 m \times 1 m. The square rib size is 0.25 m.

The computation was performed on a uniform orthogonal grid consisting of 61×61 nodes. The Courant number was set equal to 0.8 for the TVD schemes and to 0.25 for other schemes. The computational time was 0.6 s. The problem was solved through many methods in which not only different schemes of approximation of the convective fluxes were used, but different techniques of discretization of the time derivative as well. The results calculated with the use of several schemes are presented in Fig. 4.4, which shows the isolines of the function F. The blue and red colors correspond to F = 0 and F = 1, respectively. The letters indicate the implicit first-order (a) and second-order (b) schemes with respect to time, the explicit first-order scheme with respect to time (c), and the explicit scheme with local one-dimensional splitting (d). The analysis of data in Fig. 4.4 allows one to draw the following conclusions. The use of first-order schemes leads to significant smearing of the numerical solution. The solution amplitude is approximately halved after the first 50 time steps. Naturally, it is not reasonable to use schemes of this kind for solving problems of the class under discussion.

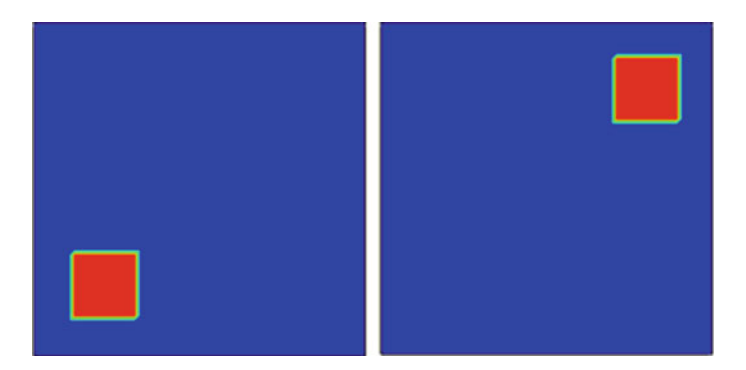


Fig. 4.3 Problem of convective transfer of a square: initial distribution (left) and exact solution (right)

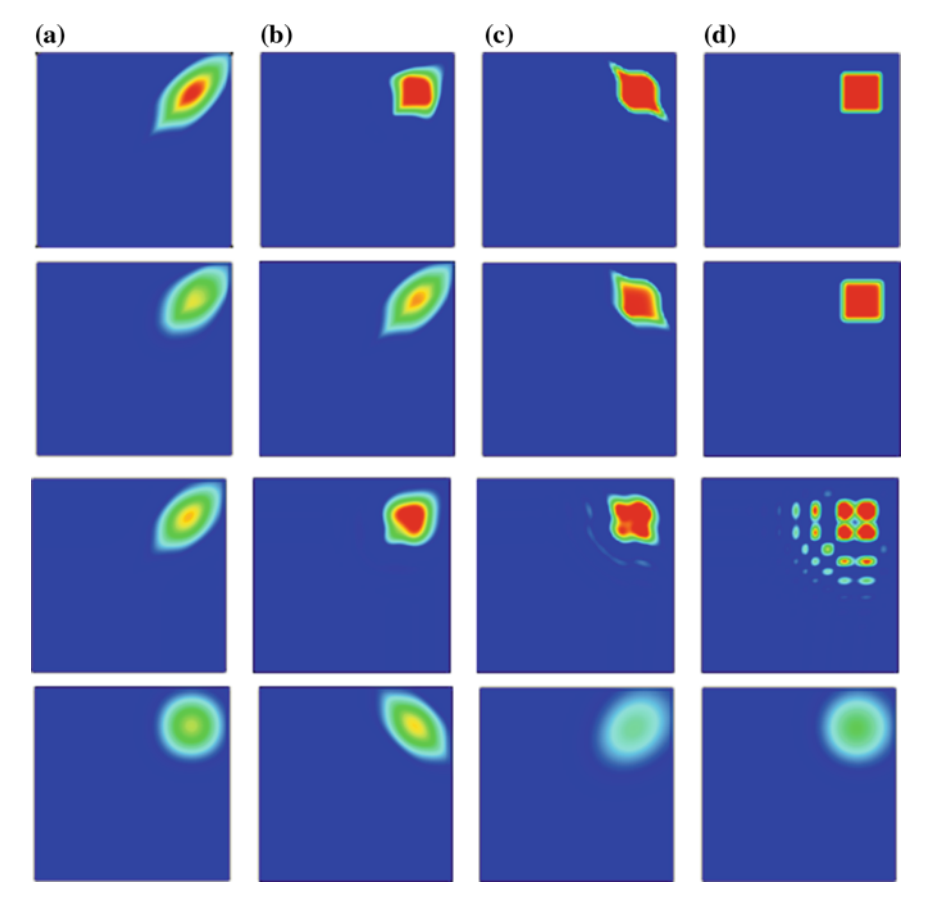


Fig. 4.4 Numerical solution of the problem of square transfer. The following numerical schemes are used: Superbee TVD scheme (first row), UMIST TVD scheme (second row), QUICK scheme (third row), and first-order scheme (fourth row)

The use of high-order upwind schemes, such as QUICK, gives rise to solution oscillations, which can be damped only by decreasing the time step or by grid refining. Therefore, it is undesirable to use such schemes for solving Eq. (4.3). Local one-dimensional splitting of the spatial operator ensures appreciable improvement of the quality of solving the multidimensional problem posed. An interesting difference was found in the behavior of solutions obtained by using the implicit and explicit schemes. When the transfer equation is solved, the implicit and explicit schemes "stretch" the solution in the velocity vector direction and the perpendicular direction, respectively. Moreover, the implicit scheme turned out to be more dissipative than the explicit scheme; therefore, the explicit scheme is preferable for solving Eq. (4.3), though the time step should be limited by the Courant condition in this case. Thus, the best option for solving Eq. (4.3) turned out to be the Superbee explicit TVD scheme with local one-dimensional splitting.

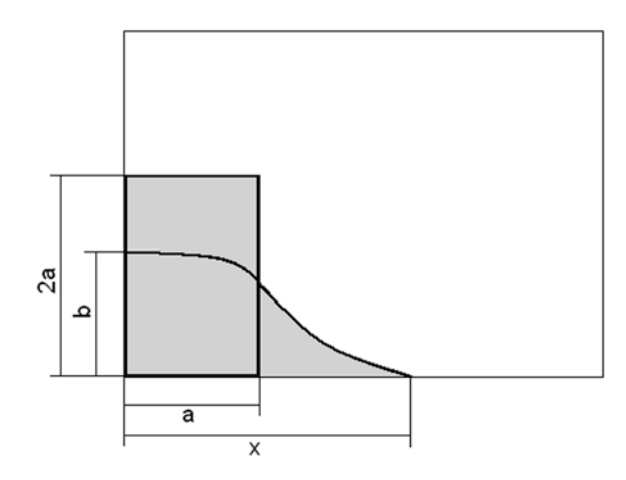
The evolution of a collapsing water column is one of the most popular tests for algorithms developed for solving problems with free surfaces. Numerical solutions of such problems through various methods have been reported in many publications (Wang and Su 1993; Monaghan 1994, 2005; Zaleski et al. 1995; Morris 1997; Koshizuka et al. 1998; Liu and Liu 2003). The problem formulation is illustrated in Fig. 4.5. A water column of width a is bounded by a wall of height 2a. At the initial time instant, the wall is instantaneously removed, and the fluid spreads under the action of the gravity force. In fact, this is the problem of dam breakdown, and numerical predictions are usually compared with the experimental data (Martin and Moyce 1952). These comparisons are performed in terms of two parameters: distance x covered by water during the time t from the beginning of the dam opening and water level b at the left wall of the reservoir containing the fluid (Fig. 4.5).

The results of water column collapsing reported below were obtained for the following parameters: computational domain size 1.25×0.7 m, initial width of the water column a = 0.2 m, and its height 0.4 m. A uniform grid consisting of 80×142 nodes was used in these computations. The computational domain boundaries were subjected to slip and no-slip conditions.

The QUICK scheme was used for approximating the convective terms of the hydrodynamic equations. The transfer equation for the volume fraction of the fluid phase in the computational cell was solved by the Superbee explicit TVD scheme with local one-dimensional splitting. The time step for solving the hydrodynamic equations was set to 0.0025 s. The time step for solving the transfer equation for the fluid phase concentration was determined from the Courant condition, CFL = 0.7.

The numerical and experimental (Martin and Moyce 1952) data are compared in Fig. 4.6, which shows that the results agree with each other well. The qualitative behavior of the fluid after dam breakdown is illustrated in Fig. 4.7. Here, the first and third pictures are the photographs of the laboratory experiment (Martin and Moyce 1952), whereas the second and fourth pictures are the numerical predictions. It can be seen that the numerical results provide an adequate description of the experimentally observed fluid evolution.

Fig. 4.5 Formulation of the problem of water column collapsing



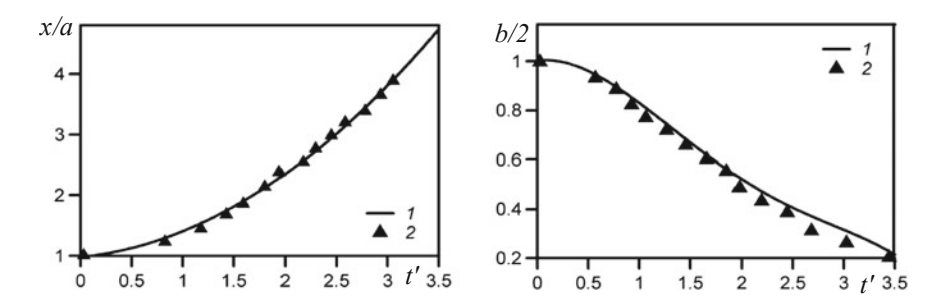
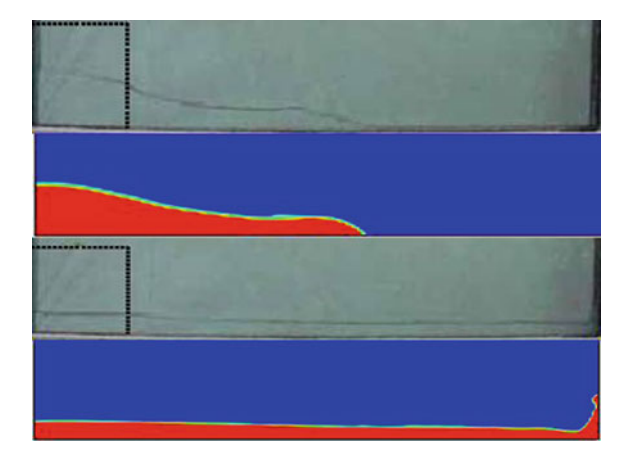


Fig. 4.6 Distance x/a covered by water during the time $t' = \sqrt{ga}$ (left) and dynamics of the water level at the left wall of the reservoir (right). 1—computation, 2—experimental data (Martin and Moyce 1952)

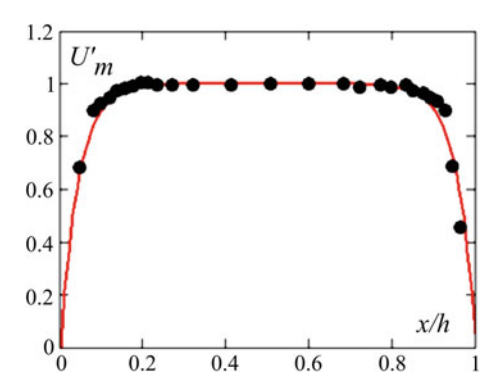
Fig. 4.7 Comparison of the predicted and experimental (Martin and Moyce 1952) shapes of the water surface at t = 0.3 s (two upper pictures) and t = 0.6 s (two lower pictures)



As was already noted, the developed algorithm was used for solving a broad range of problems of external and internal flows. However, its applicability for microflows had to be specially tested. Three examples of such testing are described in the present section for flows with low Reynolds numbers (see also Rudyak et al. 2010).

Let us consider the flow of a Newtonian fluid in a microdiffuser (Wing and Rajan 2004). The channel height is $h = 100 \, \mu m$, and the channel width is $w = 150 \, \mu m$ at its narrow part and $W = 750 \, \mu m$ at its broad part. The fluid moves from the narrow part of the channel to the broad part. The solid walls are subjected to the no-slip condition. The flow rate of the fluid corresponding to the Reynolds number Re = 1 is fixed at the input boundary. The dimensionless velocity profile $U' = U/U_m$ (U_m is the maximum value of the flow velocity in this section) calculated according to the algorithm described in the previous section is compared in Fig. 4.8 with the experimental data (Wing and Rajan 2004) obtained by micro-PIV in the broad part of the diffuser. It is seen that the numerical data (solid curve) are in good agreement with the experimental (filled points).

Fig. 4.8 Comparison of the numerical (solid curve) and experimental (Wing and Rajan 2004) results (filled points) for the velocity profile in a microdiffuser. The input Reynolds number is Re = 1



The next test example is also taken from Wing and Rajan (2004). A micro-wave consisting of an input channel with a symmetric rectangular branching is considered. The height and width of all three channels are identical and equal to 100 μ m. The solid walls are subjected to the no-slip conditions. The Reynolds number based on the flow rate at the channel input is Re = 1. Figure 4.9 shows the calculated (solid curves) and measured (filled points) dimensionless velocity profiles. The dimensionless velocity profiles are obtained by means of normalization to the velocity U_Q determined by the flow rate Q at the input: $U_Q = Q/\rho S$, where ρ is the fluid density and S is the cross-sectional area of the microchannel. The measurements and calculations were performed in two cross-sections: in the middle of the input channel (curve 1) and in the middle of the symmetric part of the channel (curve 2). The calculated and measured data are again seen to be in good agreement.

Fig. 4.9 Comparison of the predicted (solid curves) and experimental (Wing and Rajan 2004) (filled points) normalized values of the streamwise velocity of the flow in a micro-wye. Re = 1. Curves 1 and 2 show the data in the middle of the input channel and in the middle of the symmetric part of the micro-wye, respectively

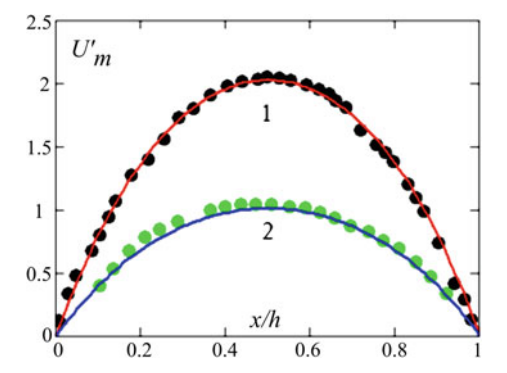


Fig. 4.10 Y-type micromixer

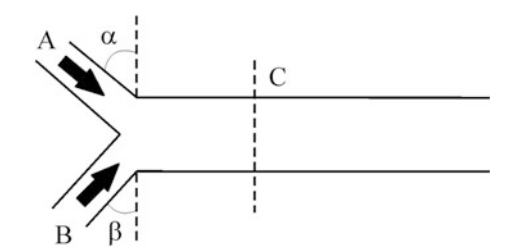
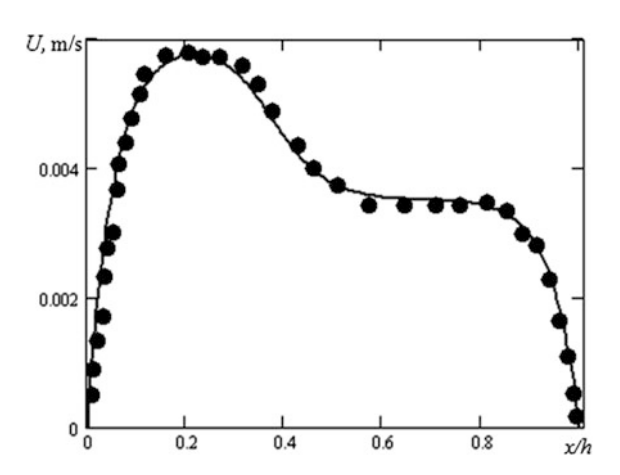


Fig. 4.11 Comparison of the calculated (solid curve) and experimental (filled points) values (Kim et al. 2004) of the streamwise velocity in a Y-type micromixer in cross-section C (see Fig. 4.10) in the case of water mixing with a 20% glycerol solution



Finally, let us give one more test example in which the flow in a Y-type micromixer was studied (Fig. 4.10). Mixing of glycerol solution (input A) with water (input B) was studied in Kim et al. (2004). The width of the input channels A and B was 150 μ m, and the mixer width was 300 μ m. The height of all channels was identical and equal to 50 μ m. The angles α and β were identical in the experiment. Water was mixed with 20, 50, and 60% glycerol solutions, with consecutively increasing density and viscosity coefficient. In all cases, the calculations provide an adequate description of the experimental data. Figure 4.11 shows the streamwise velocity profile in cross-section C for the 20% glycerol solution. As previously, the solid curve and the filled points show the calculated and experimental data, respectively.

4.3 Mixing of Fluids in a Y-Type Mixer at Low Reynolds Numbers

A Y-type micromixer is one of the simplest configurations. Mixing in such a micromixer has been intensely studied in the last decade. Nevertheless, there are practically no systematic data on the effect of some flow parameters on the mixing

process. For this reason, we begin studying micromixers from consideration of devices of this kind. In this section, we follow the papers of Rudyak et al. (2010), Minakov et al. (2010). Let us consider the mixing of two identical fluids, black and gray, in the micromixer shown in Fig. 4.10. For certainty, let the black fluid enter the micromixer through input A and the gray fluid enter the micromixer through input B. The mixing process is affected, to a large extent, by equalization of the velocity profile in the mixing channel. As the Reynolds number in microchannels considered in this section is very low, the velocity profile becomes equalized close to the channel entrance (approximately at a distance 0.06H, where H is the mixing channel width, see Fig. 4.10). If the flow rates in both input channels are identical, then the Reynolds numbers of the flows in channels A and B are also identical and equal to Re = $\rho U_O w / \mu$. The mixing time is determined only by the fluid diffusion coefficient D (it is on the order of $\tau_m \sim w^2/D$). If the mixer channel has a length L, then the time needed for the fluid particle to pass through this channel is on the order of $\tau_L \sim L/U_Q \sim (\rho L w h)/Q$. In this case, the mixing efficiency in the channel is determined by the ratio of these two times:

$$\frac{\tau_m}{\tau_L} \sim \frac{w^2 U_Q}{DL} \sim \frac{w}{L} \operatorname{Re} \frac{v}{D},\tag{4.4}$$

where $v=\mu/\rho$ is the kinematic coefficient of viscosity. Therefore, for a given channel and given fluids, the mixing time increases with the increasing Reynolds number. If water is taken as a mixing fluid, then Eq. (4.4) predicts that mixing in a channel of length L=1 cm will be effective if $\tau_m\ll 10{\rm Re}\tau_L$, which is valid only for very low Reynolds numbers. In particular, it follows from here that the mixing efficiency will remain almost unchanged beginning from certain values of the Reynolds number. This prediction is also confirmed by direct numerical simulations. Indeed, the mixing efficiency at Reynolds numbers from 10 to 0.01 is almost constant.

Equation (4.4) readily yields one more estimate

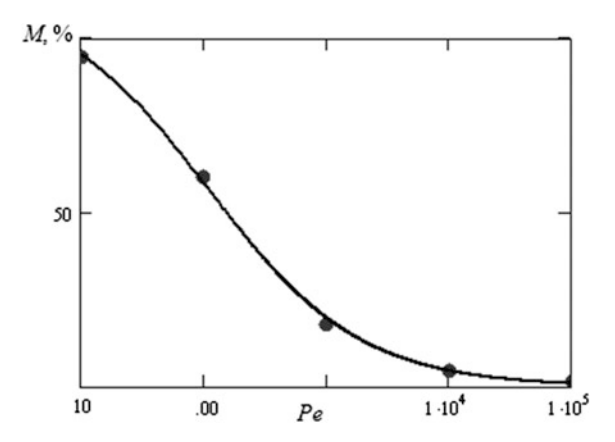
$$\frac{\tau_m}{\tau_L} \sim \frac{w}{L} Pe, \tag{4.5}$$

which includes the diffusion Peclet number $Pe = wU_Q/D$. For a given Peclet number, the smaller the channel width, the smaller the mixing length $L_m \sim U_Q \tau_m \sim wPe$. Moreover, this length increases with the Peclet number.

However, it should be emphasized that the mixing efficiency is a nonlinear function of the Peclet number. It is shown in Fig. 4.12. Here, the mixing efficiency M is determined by the formula

$$M = \left[1 - \frac{2}{W} \int_{0}^{H} (C - 0.5) dy\right] \cdot 100\%, \tag{4.6}$$

Fig. 4.12 Mixing efficiency in a Y-type mixer versus the Peclet number



where $H=300~\mu m$ is the width of the channel where the mixing process occurs (see Fig. 4.10) and C is the dye concentration in the cross-section located at a distance of 4000 μm from the point where the flows merge together. This dependence is adequately described by the formula

$$M = \frac{113.2}{1 + 0.037 Pe^{0.7}},$$

shown by the solid curve in Fig. 4.12, whereas the calculation is presented by the filled points. Certainly, this dependence is rather conventional, because it is related, in particular, to determination of the mixing efficiency.

Let us now consider the influence of the angles α and β on the mixing efficiency. Each of the angles was varied from 0° to 90° (see Fig. 4.10). It was found that the angle between channels A and B has a minor effect on the mixing efficiency. The difference for the mixer where two identical fluids were mixed was approximately 7%. In the case of identical angles (symmetric mixer), the maximum efficiency was reached at $\alpha = \beta = 90^\circ$. Thus, the efficiency of the T-type mixer turned out to be slightly lower than the efficiency of the Y-type mixer. As the angles were increased up to 90° , the mixing efficiency monotonically decreased from 18.2 to 17.6%. The mixing efficiency of the asymmetric mixer is lower than that of the symmetric mixer. Thus, the mixing efficiency of the mixer with $\alpha = 60^\circ$, $\beta = 10^\circ$ was 17.4%, which is lower than the minimum value of the mixing efficiency for the symmetric mixer. These differences are slightly higher if two different fluids are mixed. In all situations, however, the symmetric mixer is more effective at the minimum angles between the input channels. These results are fairly predictable and are related to changes in the local values of the Peclet number.

As the most important factor of the mixing process in microchannels is diffusion, the channel length should be sufficiently large so as to ensure mixing. A natural result is a significant pressure drop because of friction on the channel walls. On the other hand, this decrease is smaller if flow slipping on the channel walls is provided

17.9

18.4

rather than the no-slip condition. At the macroscopic level of the flow analysis, the no-slip boundary condition is always imposed. The slip boundary condition is used only for sufficiently rarefied gas flows. The reason is that the characteristic slip length b on the walls is on the order of the Knudsen number, $b \sim Kn$, which can be rather large in gases (here, the slip length on the wall is determined by the condition $v = b(\partial v/\partial y)$, where the flow is directed along the x axis, v is the flow velocity in this direction, and the y axis is normal to the channel wall). In macroscopic fluid flows under standard conditions, the slip length varies from several nanometers to several tens of nanometers. In this case, slipping can be neglected. In microflows, however, this slipping can be fairly significant. Moreover, the slip length in microflows can reach hundreds of nanometers because of changes in the near order of the fluid near the surface, possibility of gas release on the channel walls, etc. Slipping leads to considerable reduction of the friction drag on the channel walls and, hence, to a smaller decrease in pressure. The slip length can be increased by various hydrophobic or even ultrahydrophobic coatings (see, e.g., Ou et al. 2004; Lauga et al. 2005). In this case, the slip length can reach tens of micrometers.

Systematic calculations of the flow in a Y-type micromixer were performed in Minakov et al. (2010) for studying the influence of slipping. The slip length was varied from 10 nm to 20 um; the corresponding data are listed in Table 4.1. An increase in the slip length up to 5 µm reduces the pressure decrease by a factor of almost 2. It should be emphasized that the mixing efficiency in the case of slipping on the channel walls remains unchanged at small slip lengths, and even somewhat increases at large slip lengths.

Up to now, we have discussed the mixing of identical fluids. In practice, however, it is of interest to consider the mixing of different fluids. Naturally, the developed algorithm allows one to analyze such situations as well. As an example, the data on mixing water with another fluid in a Y-type micromixer are given below (Table 4.2). Water enters the channel through input A. As the physical characteristics of these fluids are considerably different, the efficiencies of their mixing with water are also different. In particular, the parameter M for acetone, glycerin, ethyl alcohol, and isopropyl alcohol is 36.8, 3.1, 18.2, and 9.4%, respectively. In this

Table 4.1 Effect of slipping on the channel walls on the pressure difference and mixing efficiency									
b	0	0.01	0.05	0.1	1	5	20		
<i>∆p</i> (Pa)	293.3	293.1	291.7	290.1	263.0	184.5	87.6		

17.6

17.7

Table 4.2 Parameters of mixing fluids (Physical Values 1991; Reid et al. 1977)

17.6

17.6

17.6

M(%)

	ρ (kg/m ³)	μ (Pa s)	$D \times 10^{-9} \text{ (m}^2\text{/s)}$
Acetone	800	0.00029	4.56
Glycerol	1260	1.48	0.0083
Ethanol	790	0.0012	1.24
Isopropyl alcohol	786	0.0029	0.38

case, the pressure drop in inputs A and B are different and vary from 239.5 kPa for glycerin to 165 Pa for acetone.

Relations (4.4) and (4.5) yield estimates of the mixing time and mixing length, thus providing an estimate of the micromixer's efficiency. It is clear from the general considerations that the mixing time can be appreciably reduced through multiple splitting of the mixing flow. This is the principle on which operation of lamination mixers is based. A similar idea is to insert a number of obstacles into the flow that change the flow's structure, thus accelerating the mixing process. Obviously, symmetrically located obstacles are ineffective in a laminar flow. In addition, the characteristic size of these obstacles should be comparable with the channel width. The mixer can be easily optimized in terms of this parameter. The results of such calculations for mixers of various types are presented below.

As the first example, Fig. 4.13 illustrates the mixing of two fluids in a T-type mixer with asymmetrically arranged three, five and seven rectangular inserts [a T-type mixer is actually a symmetric Y-type mixer with the angle between the input channels equal to $\pi/2$ (see Fig. 4.10)]. The width of the mixing channel is 100 μ m, the width of the input channels is 50 μ m, and the mixer height is 50 μ m. The Reynolds number is Re = 2, and the Peclet number is $Pe = 5 \times 10^3$. As the channel length increases with an increasing number of inserts, it is reasonable to analyze the mixing characteristics and the pressure drop normalized to the channel length (Table 4.3). The first column in Table 4.3 shows the number of inserts, the size of all inserts is identical except for the last row, the cross-sectional size of the inserts was 50 μ m × 20 μ m, and the insert height was 50 μ m.

The mixing efficiency increases with the number of inserts, but the pressure drop also increases. The latter can be reduced by using hydrophobic coatings. For instance, for the slip length $b=1~\mu m$, the pressure drop can be reduced by 10%. The inserts in the second and third pictures are arranged in a staggered order at a certain distance from the channel walls. The mixing efficiency can be appreciably

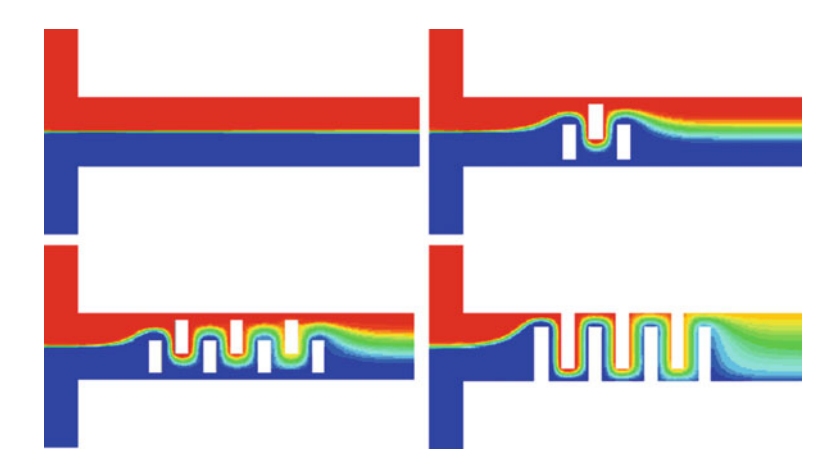


Fig. 4.13 Mixing of two fluids in a T-type mixer with rectangular inserts

Table 4.3 Specific (per unit)
length) mixing efficiency and
specific decrease in pressure
in the mixer with rectangular
inserts

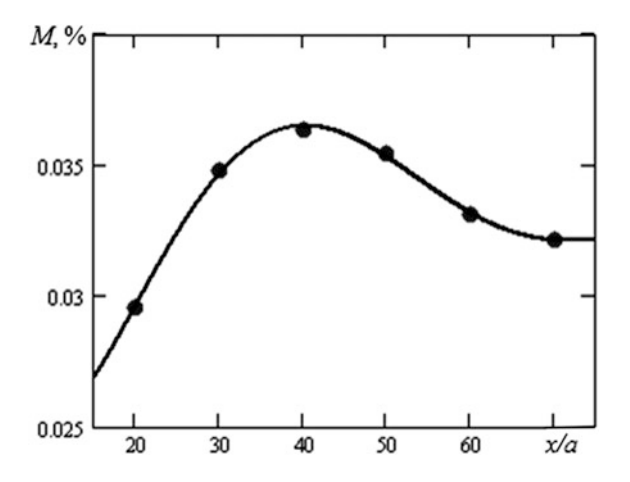
N	M (%/μm)	Δp (Pa/μm)
0	0.0094	0.37
3	0.026	0.92
5	0.035	1.44
7 ₁	0.045	1.92
7 ₂	0.085	7.38

increased by extending the inserts and connecting them with the channel walls. The last picture in Fig. 4.13 shows the mixing process in such a mixer with seven inserts $70~\mu m \times 20~\mu m$. The mixing efficiency in this mixer is given in the last row of Table 4.3.

Certainly, the flow topology depends, to a large extent, on the channel geometry, in particular, on the distance between the inserts. By varying this distance, it is possible to increase the mixing efficiency. As an example, Fig. 4.14 shows the mixing efficiency in a channel with five rectangular inserts as a function of the dimensionless width of the insert a, which is equal to 20 μ m. The cross-sectional size of the inserts is again $50~\mu\text{m} \times 20~\mu\text{m}$, and the flow characteristics are the same as those in Fig. 4.13. This mixer ensures optimal operation if the distance between the inserts is approximately 2a. By increasing the distance between the inserts, we monotonically reduce the pressure drop. Thus, as the distance between the inserts is increased from a to 2a, the pressure drop can be reduced by 25%. On the other hand, slipping on the mixer walls has a smaller effect on the decrease in pressure than it would in a smooth channel.

Finally, it should be noted that optimization of micromixer parameters in the general case also depends on the Reynolds and Peclet numbers. As was already noted, however, the mixing efficiency is almost independent of the Reynolds number within a wide range of this parameter ($Re \le 1$) and starts to increase only at Re > 1. The mixing efficiency weakly depends on the Peclet number beginning

Fig. 4.14 Normalized mixing efficiency in a mixer with five rectangular inserts versus the dimensionless distance between them



from $Pe \sim 10^3$. On the other hand, the mixing efficiency changes approximately by an order of magnitude as the Peclet number increases from 10 to 10^3 .

4.4 Mixing of Fluids in a T-Type Micromixer at Moderate Reynolds Numbers

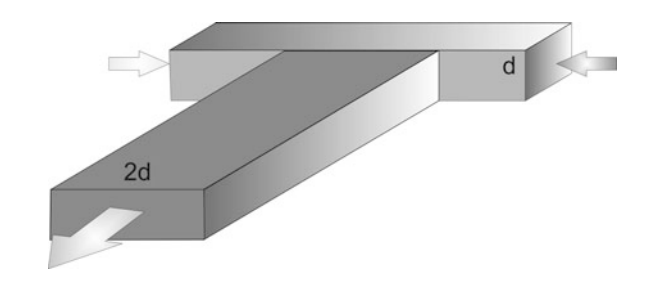
Flow regimes in micromixers arising at elevated Reynolds numbers have been intensely studied for the last decade. The most attention was paid to studying flows in T-type micromixers. In this case, a complex vortex flow characterized by the formation of the so-called Dean vortices occurs in the microchannel. The existence of a critical Reynolds number at which the Dean vortices become asymmetric was experimentally demonstrated in Engler et al. (2004). It was found that the critical Reynolds number for a $600 \times 300 \times 300$ µm channel is about 150. It was shown that the critical Reynolds number depends on the channel size. Numerical simulations were performed in Telib et al. (2004) to study transitional flow regimes (at Reynolds numbers in the interval Re = 300-700), but mixing processes were not considered. Mixing of two fluids within the range of the Reynolds numbers from 50 to 1400 was studied experimentally and numerically in Wong et al. (2004). Gobert et al. (2006) were the first researchers to numerically demonstrate the existence of an unsteady periodic flow regime at some values of the Reynolds number. A comprehensive experimental study of mixing in a T-type microchannel at moderate Reynolds numbers (100–400) was performed in Hoffmann et al. (2006), in which the velocity and concentration fields in various cross-sections of the mixer were studied with the use of μ-LIF and μ-PIV. The mixing efficiency was measured for the first time.

Finally, some numerical and experimental investigations (Bothe et al. 2004; 2006; Dreher et al. 2009) should be noted, in which some flow regimes in T-type microchannels were calculated. Some characteristic flow regimes were identified, and the flow structure in these regimes was studied. The mixing efficiency was then calculated. The calculated and experimental mixing patterns were then qualitatively compared, and the distribution of the mixing efficiency along the channel was calculated.

Despite a comparatively large number of papers dealing with the flow and mixing in T-type micromixers at moderate Reynolds numbers, the data have not been systematized for a long time. This gap was filled by Minakov et al. (2012), who performed systematic simulations of the flow and mixing of incompressible fluids in a T-type micromixer at Reynolds numbers ranging from 1 to 1000. Below, we follow this work, as well as (Minakov et al. 2013a, b, c).

The geometry of the modeled micromixer is schematically shown in Fig. 4.15. Below, we present the results of CFD simulations of various flow regimes in a T-type micromixer at Reynolds numbers Re = $(\rho U h/\mu)$ from unity to one thousand. Here, $U = Q/(2\rho dh^2)$, $d = 100 \mu m$ is the channel height and $h = 133 \mu m$ is

Fig. 4.15 Geometry of a modeled T-type mixer



the hydraulic diameter. The mixing channel has a cross-section of $100 \times 200~\mu m$ and a length of $1500~\mu m$. The input channels are symmetric with respect to the mixing channel and perpendicular to the latter; their cross-sectional size is $100 \times 100~\mu m$, and their total length is $800~\mu m$. Pure water is fed through the left input, and water colored with rhodamine is fed through the right input. The flow rates of these fluids are identical and equal to Q. The densities and viscosity coefficients of both fluids are identical and equal to $1000~kg/m^3$ and $1000~m^2/s$. Thus, the Schmidt number for the considered flow $1000~kg/m^3$ and $1000~m^2/s$. Thus, the Schmidt number for the considered flow $1000~kg/m^3$ is $1000~m^2/s$. Thus, the thickness of the hydrodynamic boundary layer is much greater than the thickness of the diffusion boundary layer. Therefore, obtaining high-quality numerical results requires the use of sufficiently fine computational grids, which can resolve the mixing layer. The computations were performed on a two-block grid consisting of $1000~m^2$. The mixing channel width, $1000~m^2$ 0 over its height, and $1000~m^2$ 0 nodes along the channel).

As a result, five different flow regimes were detected; each of them is formed at certain Reynolds numbers. At low Reynolds numbers (Re < 5), a steady flow without vortices is formed in the mixer. In this case, mixing is induced by the usual molecular diffusion, and the mixing efficiency is rather low (see the previous section). The flow structure in the streamwise and transverse sections of the mixer can be illustrated by trajectories of tracer particles. At low Reynolds numbers, it has the form shown in Fig. 4.16a.

As the Reynolds number increases, a pair of steady symmetric horseshoe vortices are formed at the mixing channel entrance (see Fig. 4.16b), which are usually called the Dean vortices. The resultant vortex structure can be seen especially clearly in three projections in terms of the isosurface of the variable λ_2 , which is the second eigenvalue of the tensor $(S:S + \Omega:\Omega)$, where

$$\mathbf{S} \equiv \mathbf{S}_{ik} = \frac{1}{2} \left(\frac{\partial \mathbf{v}_i}{\partial x_i} + \frac{\partial \mathbf{v}_j}{\partial x_i} \right)$$

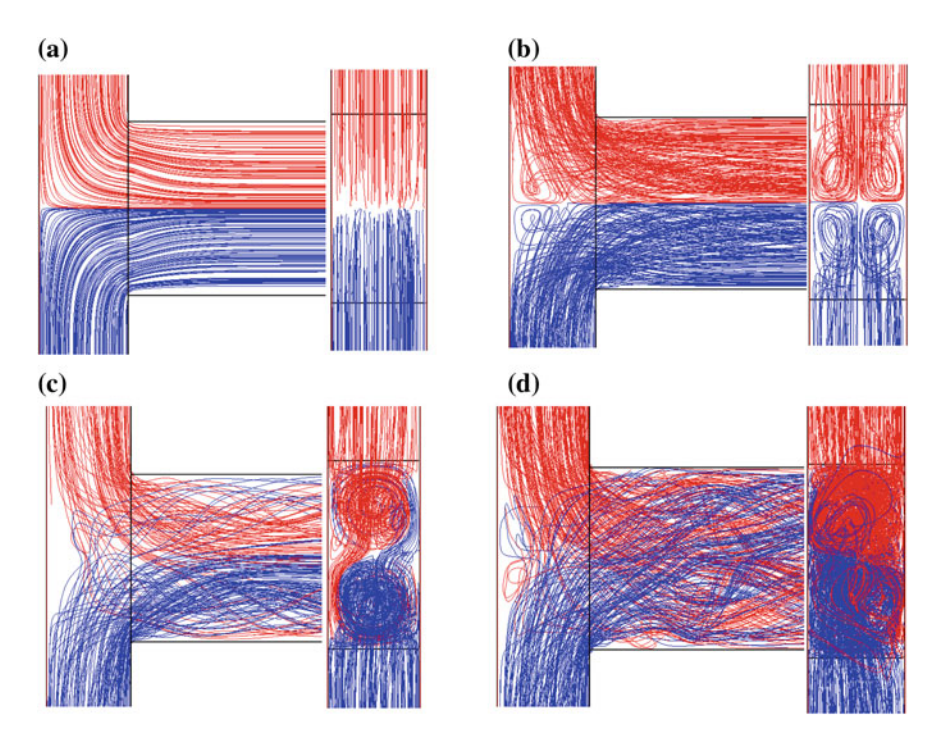


Fig. 4.16 Trajectories of tracer particles in a T-type micromixer for different Reynolds numbers. **a** Re = 1, **b** Re = 120, **c** Re = 186, **d** Re = 600

is the strain rate tensor and

$$\mathbf{\Omega} \equiv \mathbf{\Omega}_{ik} = \frac{1}{2} \left(\frac{\partial \mathbf{v}_i}{\partial x_j} - \frac{\partial \mathbf{v}_j}{\partial x_i} \right)$$

is the vorticity tensor. The corresponding structure of vortices for the flow with the Reynolds number Re = 120 is shown in Fig. 4.17.

Horseshoe vortices appear owing to the development of secondary flows caused by the action of the centrifugal force induced by flow turning. The structure of the velocity field evolution with an increase in the Reynolds number is shown in Fig. 4.18. Figure 4.18a, b correspond to the Reynolds numbers of 20 and 120. The vortices formed at the channel entrance dissipate and move further along the channel. Vortex dissipation is caused by fluid viscosity; therefore, the dissipation rate decreases with increasing Reynolds number. For the flow with the Reynolds number Re = 120 (see Fig. 4.18b), the horseshoe vortices decay in the mixing channel at distances on the order of 400 μ m from the entrance cross-section, whereas the corresponding distance for Re = 20 (Fig. 4.18a) is about 70 μ m. This means that the intensity of the Dean vortices increases with increasing Reynolds number. Moreover, their configuration becomes different (cf. Fig. 4.18a, b).

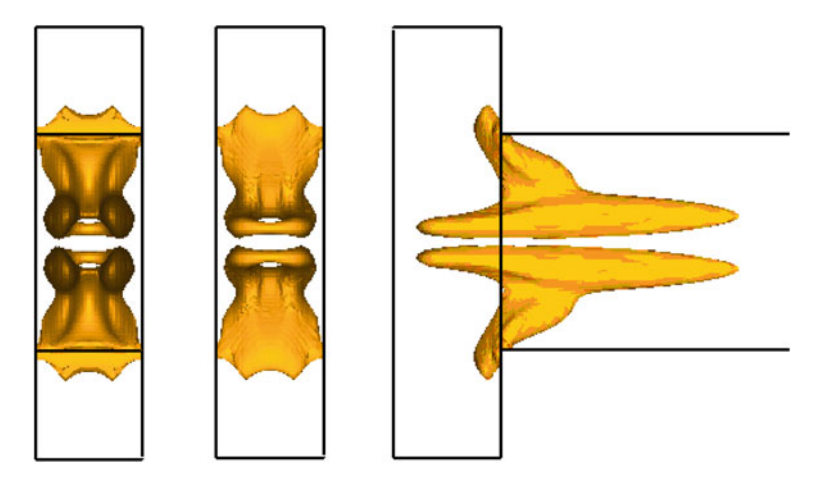


Fig. 4.17 Vortices formed at the mixing channel entrance. Re = 120. Front view (left), back view (center), and side view in the vertical section of the channel (right)

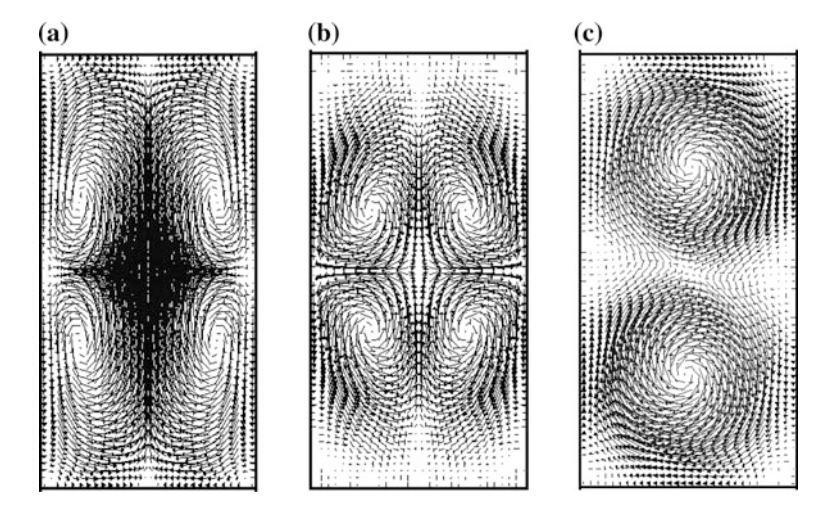


Fig. 4.18 Velocity field in the mixing channel cross-section at a distance of $100 \mu m$ from the channel entrance for different Reynolds numbers. **a** Re = 20, **b** Re = 120, **c** Re = 186

The emergence of the Dean vortices is a threshold phenomenon. The corresponding Reynolds number, generally speaking, is determined by the channel size and can be characterized by the critical Dean number $\mathrm{Dn} = \mathrm{Re}\sqrt{d/R}$ (Kelleher et al. 1980), where R is the radius of curvature of flow turning. In the channel considered in the present work, the Dean vortices were detected at $\mathrm{Re} \approx 20$. If the radius of flow turning in this microchannel is assumed to be R = d/2, this corresponds to the critical value of the Dean number $\mathrm{Dn} = 28$.

With a further increase in the Reynolds number, an interesting reconstruction of the flow can be observed. Beginning from the Reynolds number approximately equal to 150, the pair of horseshoe vortices turns in a jump-like manner by 45° toward the central streamwise plane of the mixer, owing to the development of the Kelvin-Helmholtz instability. This reconstruction of the flow is clearly visible in Fig. 4.19, where the flow is presented in terms of the isosurface λ_2 . The upper and lower pictures correspond to Re = 120 and Re = 186 (which is higher than the critical value at which flow reconstruction occurs). This flow reconstruction can also be clearly seen in Figs. 4.17 and 4.18 (see also Fig. 4.16c).

The Kelvin-Helmholtz instability leads to the formation of a diagonal shear flow in the channel cross-section. The center of symmetry of the flow is shifted to the central streamwise line passing over the mixing channel. As a result, already at a distance on the order of 400 µm from the mixing channel entrance, instead of four vortices (Fig. 4.18b) as in the case of a symmetric flow (Re < 150), we can see two intense vortices with an identical direction of vorticity (Fig. 4.18c). The flow has an S-shaped vortex structure, which can be seen particularly clearly in Fig. 4.20 (left picture). Here, mixing is illustrated as dye concentration isolines in four cross-sections of the mixer. From left to right, the first cross-section is the mixing channel entrance, the second one is located at a distance of 100 um from the entrance, the third is located at a distance of 200 µm from the entrance, and the fourth is located at a distance of 400 µm from the entrance. The blue and red colors in the first correspond to pure water and to water with rhodamine added, respectively. This flow regime is also steady and is observed up to the Reynolds number of 240. The flow structure is illustrated in Fig. 4.21, where the flow in the mixing channel formed at Re = 186 is shown in terms of the isosurface λ_2 .

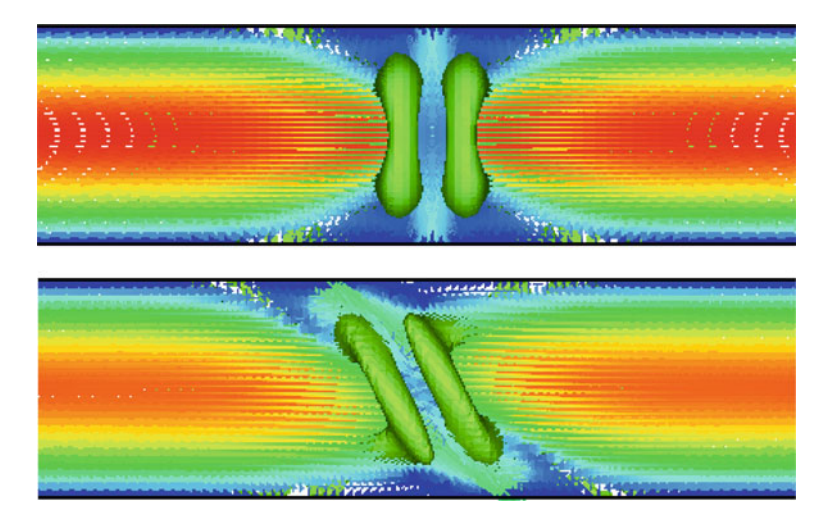


Fig. 4.19 Velocity field in the mixer cross-section (view from the end face) and isosurface λ_2 , Re = 120 (upper picture) and Re = 186 (lower picture)

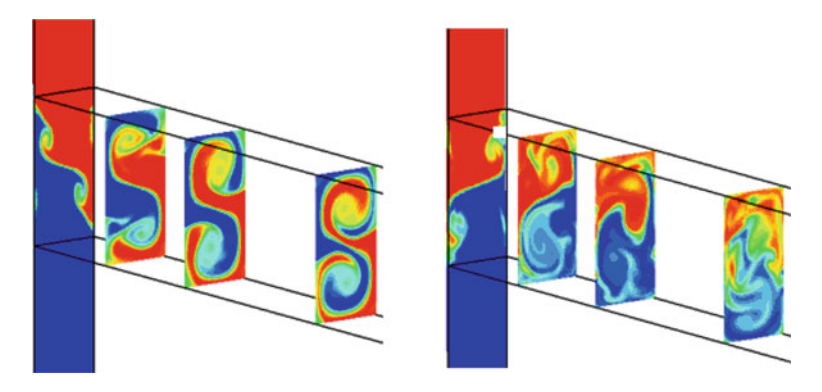


Fig. 4.20 Mixing process in the micromixer for different Reynolds numbers. Re = 186 (left) and Re = 600 (right)

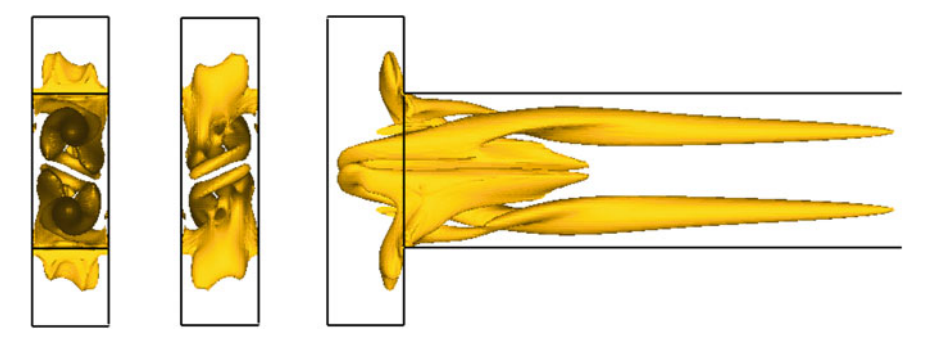


Fig. 4.21 Vortices formed at the mixing channel entrance. Re = 186. Front view (left), back view (center), and side view in the vertical section of the channel (right)

In a symmetric flow (Re < 150), the vortices compensate for each other, and the total hydrodynamic moment is equal to zero. In an asymmetric unsteady flow, the hydrodynamic moment of the flow differs from zero, because the vortices in the S-shaped structure rotate in the same direction. Naturally, the total mechanical moment in the system is preserved in both cases, because the compensating moment in the asymmetric regime is formed on the channel walls. Finally, it should be noted that the intensity of the vortices in the asymmetric mode is appreciably higher than that in the symmetric flow. Therefore, these vortices are visible over the entire length of the mixer despite dissipation.

The emergence of S-shaped vortices was already observed in experiments. The results of experimental visualization (Hoffmann et al. 2006) and computations (Minakov et al. 2012) for Re = 186 in three cross-sections of the micromixer are compared in Fig. 4.22. The experiment was performed for the same micromixer with the use of laser-induced fluorescence (μ -LIF). The upper, middle and lower pictures show the distributions of the concentrations of the mixing species in the

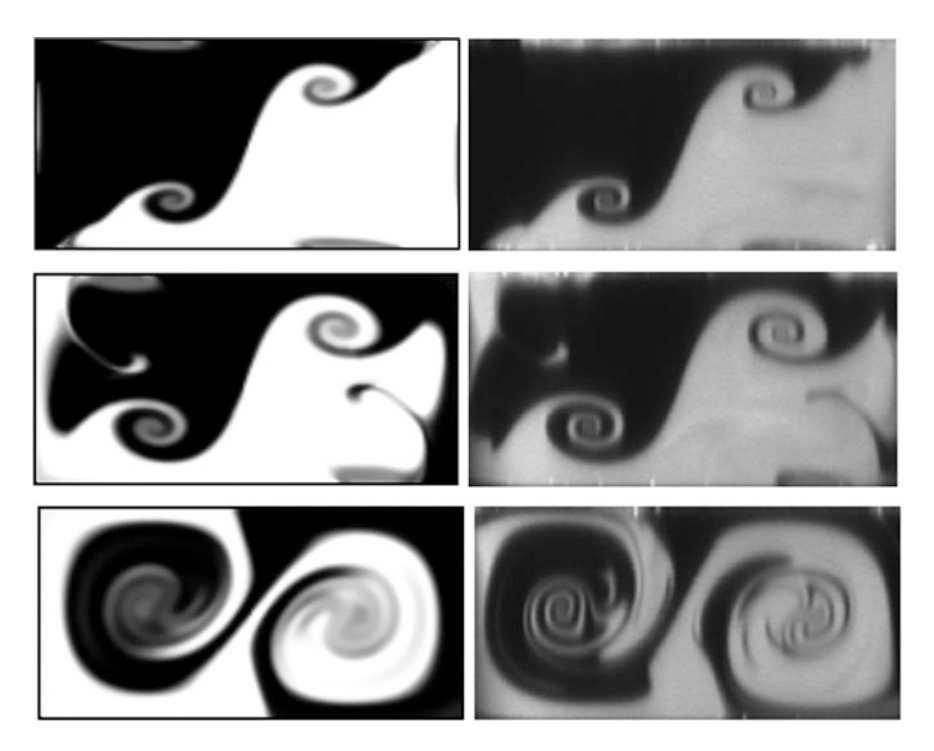


Fig. 4.22 Isolines of the dye concentration in different cross-sections of the mixer at Re = 186. Results of computations (left) and μ -LIF measurements (right) (Hoffmann et al. 2006)

cross-section at the mixing channel entrance, at a distance of $1000~\mu m$ from the entrance, and at the exit from the mixer, respectively. It can be seen that the shapes of the interface between the fluid in the calculations and experiments are in good agreement.

The above-described steady asymmetric flow regime is observed in the interval of the Reynolds numbers from 140 to 240. Beginning from the Reynolds number approximately equal to 240, the flow is no longer steady. A periodic flow regime is observed in the interval of the Reynolds numbers 240 < Re < 400. In particular, this means that the flow velocity is also a periodic function of time. This flow regime is described by the lower curve in Fig. 4.23.

The frequency of flow oscillations f is determined by many factors: channel geometry, fluid viscosity, and Reynolds number. This dependence can be characterized by the Strouhal number $St = (fd^2)/(v\text{Re})$, which is actually the dimensionless frequency of flow oscillations normalized to the Reynolds number (v is the kinematic viscosity coefficient). The Strouhal number as a function of the Reynolds number is plotted in Fig. 4.24 (square symbols). The frequency of oscillations monotonically increases up to Re = 300, and then slightly decreases. The data of our calculations agree well with the experimental results (Dreher et al. 2009), which are represented by the filled points in Fig. 4.24. The maximum differences are

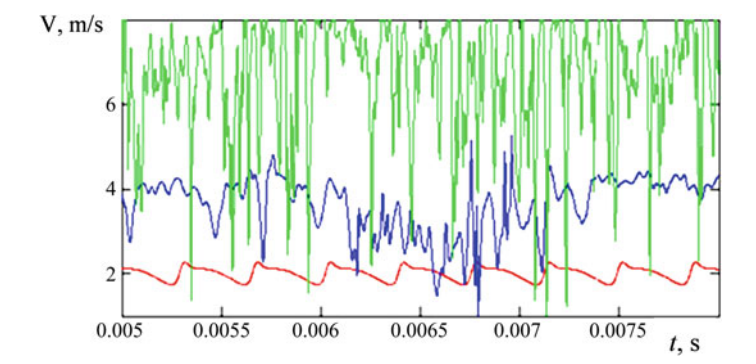
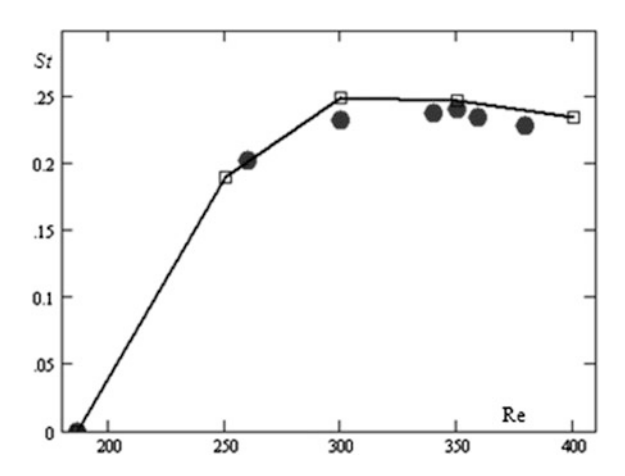


Fig. 4.23 Flow velocity at the exit of the mixing channel versus time. The lower, middle, and upper curves show the results for Re = 300, 600, and 1000, respectively

Fig. 4.24 Strouhal number versus the Reynolds number in steady periodic flow regimes in the mixing channel

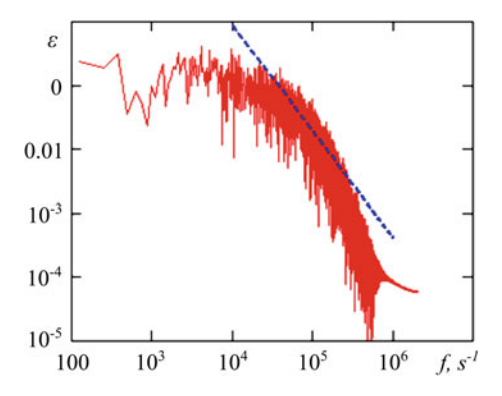


observed at high Reynolds numbers, but it should be borne in mind that the experimental data were obtained in a channel with a cross-sectional size of $600 \times 300~\mu m$.

Beginning from the Reynolds number of about 450, the flow oscillations are no longer rigorously periodic. First, the flow becomes quasi-periodic (450 < Re < 600), and then chaotic (Re > 600). The frequency spectrum of the velocity field becomes further filled. This is clearly seen in Fig. 4.23, where the middle and upper curves correspond to the Reynolds numbers Re = 600 (see also Fig. 4.20) and Re = 1000, respectively.

The distribution of the kinetic energy of the flow oscillations ε in terms of frequencies for Re = 600 is shown in Fig. 4.25. This spectrum was obtained for a point lying at the center of the mixing channel at a distance of 400 μ m from the channel entrance. The dotted straight line corresponds to the universal

Fig. 4.25 Spectrum of the kinetic energy of velocity oscillations for Re = 600



Kolmogorov-Obukhov law. Though the spectrum for Re = 600 cannot be considered as a complete continuum, as in the case of a developed turbulent flow, it still has a large number of frequencies and an inertial interval, which allows us to say that the flow regime is at least transitional. This early beginning of the development of turbulence for channel flows is caused by the Kelvin-Helmholtz instability at the initial portion of the mixing channel. At the same time, the calculations show that the flow oscillations decay with distance from the place of flow merging if the channel is sufficiently long, the flow is relaminarized, and a steady velocity profile is formed.

Naturally, the distance needed for the velocity profile to become stabilized depends on the Reynolds number. To prove it, we solved a problem for a channel 7000 μ m long. The results are illustrated in Fig. 4.26, where the velocity profiles for two Reynolds numbers are compared: Re = 186 (Fig. 4.26a, b) and Re = 600 (Fig. 4.26c–e). Laminar velocity profiles are formed in both cases, but the length needed for velocity profile equalization is close to 3500 μ m for Re = 186 and to 700 μ m for Re = 600.

The friction coefficient λ of the mixing channel as a function of the Reynolds number for this mixer is plotted in Fig. 4.27. This coefficient is determined by the formula $\lambda = (2\Delta Pd)/(\rho U^2L)$, where ΔP is the pressure difference in the channel and L is the channel length. The calculated data are represented by the filled point and the line connecting them. For comparison with the calculated data, the dashed line in the figure shows the friction coefficient for a steady laminar flow in a rectangular channel with a height-to-width aspect ratio of 0.5. In this case, the friction coefficient is close to 64/Re (green dotted line). Nevertheless, the analysis shows that the friction coefficient in the micromixer at low Reynolds numbers is greater (on average, by 20–30%) than the friction coefficient in a steady flow.

Then, the friction coefficient abruptly deviates from the dependence $\lambda = 64/\text{Re}$, which testifies to the laminar-turbulent transition. The calculated values of the

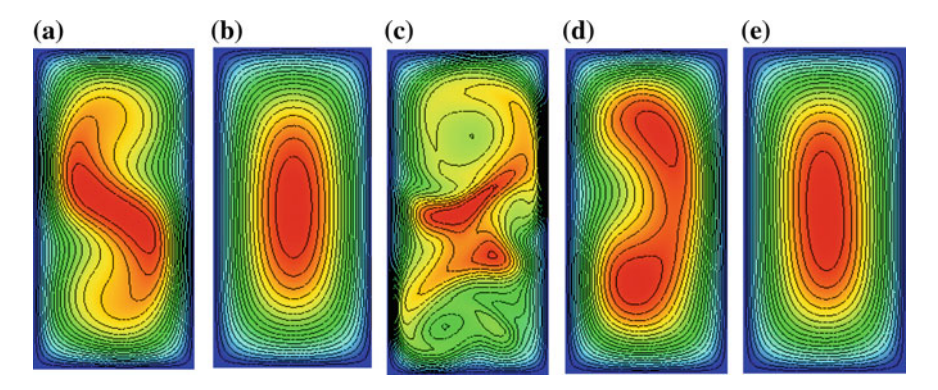
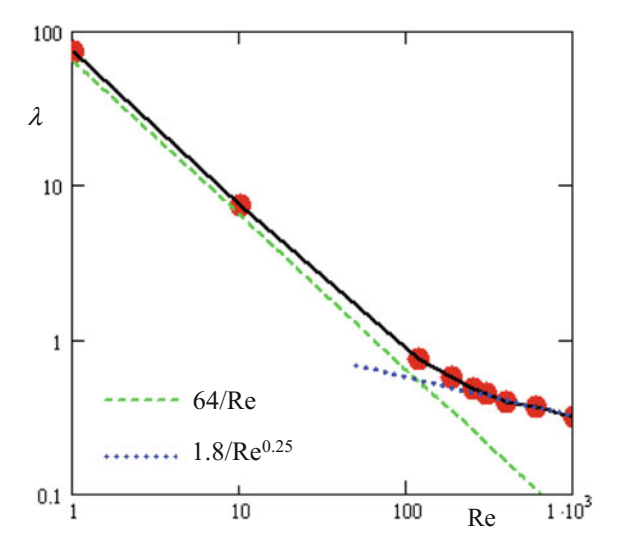


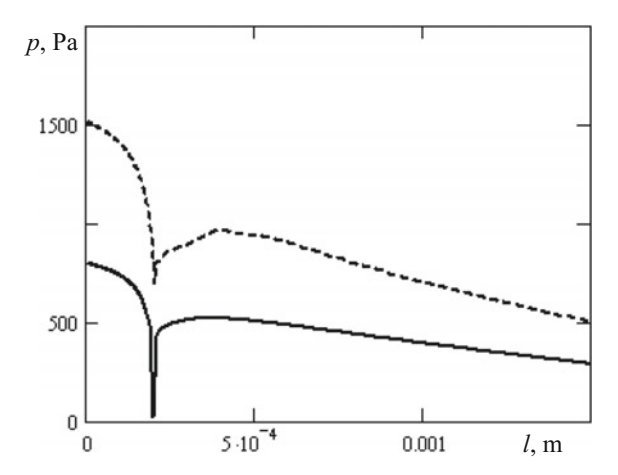
Fig. 4.26 Velocity profiles in different cross-sections of the mixing channel. **a** Re = 186, L = 500 μ m, **b** Re = 186, L = 3500 μ m, **c** Re = 600, L = 500 μ m, **d** Re = 600, L = 3500 μ m, **e** Re = 600, L = 700 μ m

Fig. 4.27 Friction coefficient in the mixing channel versus the Reynolds number



friction coefficient in the micromixer at moderate Reynolds numbers are adequately described by the dependence $\lambda=1.8/{\rm Re^{0.25}}$. The corresponding value of the friction coefficient is higher almost by a factor of 6 than the classical Blasius dependence ($\lambda=0.316/{\rm Re^{0.25}}$) for a developed turbulent flow in a straight channel. Such a large difference is caused both by turning of the flows entering the channel and by the flow swirling in the mixing channel. In particular, the pressure behavior is not monotonic along the channel. The pressure evolution for two Reynolds numbers is illustrated in Fig. 4.28 (the lower and upper curves correspond to the Reynolds number values of 120 and 186, respectively).

Fig. 4.28 Pressure distribution on the mixer walls



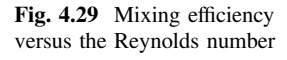
At high Reynolds numbers, the flow and the mixing process are essentially three-dimensional. In this case, it is convenient to describe the mixing efficiency by using the parameter $M = 1 - \sqrt{\sigma^2/\sigma_0^2}$, where

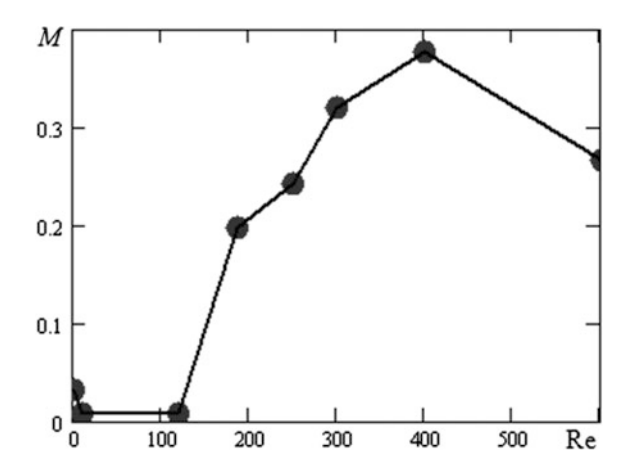
$$\sigma^2 = \frac{1}{V} \int_{V} (f - \bar{f})^2 dV$$

is the concentration dispersion over the mixer volume V[f] is the species concentration, \bar{f} is the corresponding average value, and $\sigma_0^2 = \bar{f}(1-\bar{f})$].

As was already noted, a steady flow without vortices is formed in the mixer at low Reynolds numbers (Re < 5). In this case, mixing is caused by the usual molecular diffusion, and its efficiency is rather low (about 3%, see Fig. 4.29). As the Reynolds number increases, steady Dean vortices are formed. These horseshoe vortices are symmetric with respect to the central streamwise plane of the mixer. Each horseshoe vortex is located within one fluid and actually does not cross the interface between the mixing media; for this reason, this interface remains almost plane. As the diffusion Peclet number increases with increasing Reynolds number, the mixing efficiency becomes even smaller than that in a vortex-free flow (see Fig. 4.29) and stays at this low level up to Reynolds numbers on the order of 150. When the Dean vortices lose their symmetry and an S-shaped vortex structure is formed, the mixing character becomes qualitatively different. The contact surface of the mixing fluids appreciably increases; as a consequence, the mixing efficiency drastically increases. For instance, as the flow transforms from symmetric (Re < 150) to asymmetric (Re > 150), the mixing efficiency increases by a factor of 25 (see Fig. 4.29).

After the transition to turbulence, the S-shaped structure, which was formed in the mixing channel at Re > 150 and existed in the unsteady flow regime, is destroyed (see Fig. 4.20, which shows the evolution of the S-shaped vortex





structure for Re = 600). The flow disintegrates into a large number of sufficiently large vortices. As a result, the contact area of the mixing fluids becomes smaller and the mixing efficiency drastically decreases (M = 26% for Re = 600). Naturally, with a further increase in the Reynolds number, large-scale vortex structures disintegrate into a large number of small vortices, which ensure very good mixing of the flow. Therefore, the mixing efficiency in a developed turbulent flow is significantly higher than the corresponding laminar value.

To ensure effective mixing, the mixer length should usually be sufficiently large. In this case, naturally, there are significant pressure losses induced by friction on the walls. On the other hand, these losses can be reduced by using hydrophobic or even ultrahydrophobic coatings. As was shown in the previous section, the mixing efficiency remains almost unchanged if the flow's Reynolds number is sufficiently low. However, the situation is different at moderate Reynolds numbers.

Slipping on the channel walls leads to significant changes in the flow regime. Figure 4.30 shows the flow structure for the Reynolds number Re = 186 and different values of the slip length b. As was noted above, a two-vortex structure is formed if the no-slip condition is applied (Fig. 4.30a). However, this structure transforms into a configuration with one vortex if the slip length is sufficiently large (see Fig. 4.30b, c).

The change in the flow structure with increasing slip length is also illustrated in Fig. 4.31, which shows the dye concentration isolines in the mixer cross-section at a distance $x = 1000 \,\mu m$ for different slip lengths. If there is no slipping (Fig. 4.31, left), the S-shaped structure is clearly expressed. As the slip length increases, the S-shaped structure becomes smeared and transforms into a single vortex. Naturally, the mixing efficiency increases in this case (for the mixer considered here, by approximately 30%). On the other hand, the pressure drop monotonically decreases with increasing slip length (for the mixer considered here, by approximately 30–40%). Therefore, hydrophobic coatings can be used for flow control.

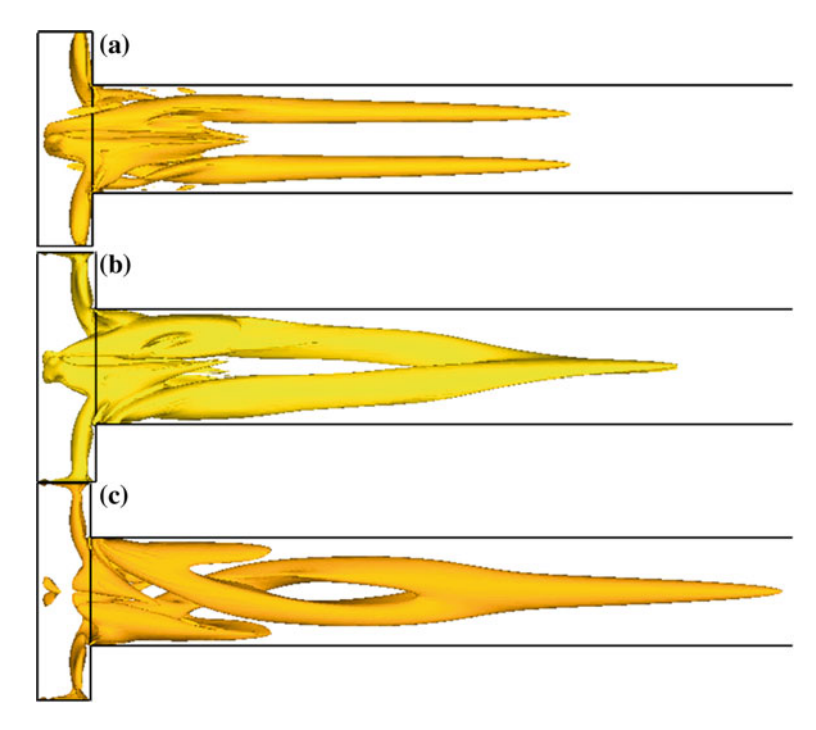


Fig. 4.30 Vortex structure of the flow in the micromixer for different slip lengths b. Re = 186. **a** b = 0; **b** b = 10 μ m; **c** b = 30 μ m

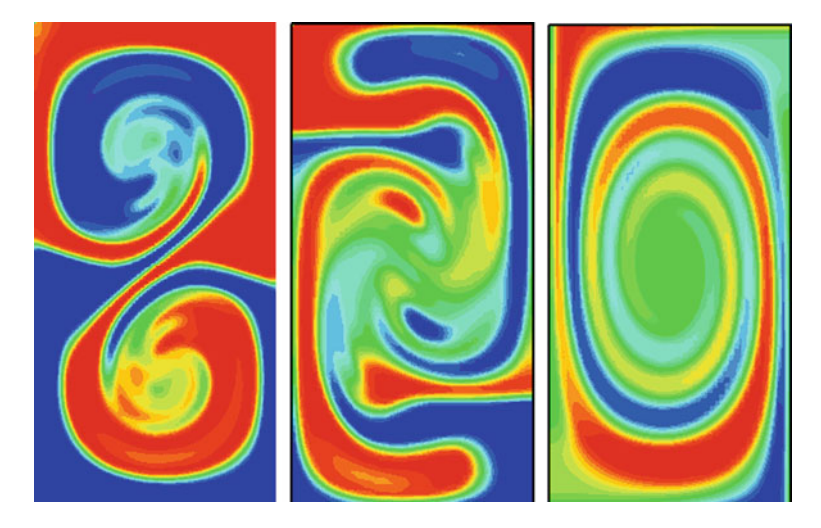


Fig. 4.31 Dye concentration isolines for flows with different slip lengths b for Re = 186 and b = 0 (left), b = 10 μ m (center), and b = 30 μ m (right)

In practice, the roughness of the wall can significantly alter the character of microflows. To study the influence of roughness, several series of computations were performed. Periodic roughness elements in the form of protruding rectangular obstacles were prescribed on the side (upper and lower) walls. Two types of roughness element were considered. In the first case, they were regularly arranged. The roughness height was 4 μ m, the width of the roughness elements was 2 μ m, and the distance between them was 10 μ m. In the other series of computations, the width of the roughness elements was prescribed randomly within the interval from 1 to 5 μ m. The presence of the roughness elements appreciably changed the hydraulic resistance of the mixing channel. Figure 4.32 shows the pressure difference as a function of the Reynolds number. The upper and lower curves correspond to rough and smooth channels, respectively. The hydraulic resistance remains almost unchanged at low Reynolds numbers, because the flow regime is laminar in both cases. Then, the hydraulic resistance in the rough channel rapidly increases.

On the other hand, the mixing efficiency behaves in a different manner. At low Reynolds numbers, it is almost identical in both mixers (see Fig. 4.33). As the Reynolds number increases, however, the mixing efficiency in the smooth channel is higher than that in the rough channel approximately up to Re \sim 350. At higher Reynolds numbers, the mixing efficiency in the rough channel exceeds that in the smooth channel, because the turbulence in the rough channel develops faster than in the smooth channel. The spectra of the kinetic energy of velocity oscillations E are compared in Fig. 4.34 (the red and green curves are the spectra obtained in the rough and smooth channels, respectively). The blue line corresponds to the universal Kolmogorov–Obukhov law.

Fig. 4.32 Pressure difference in the channel versus the Reynolds number

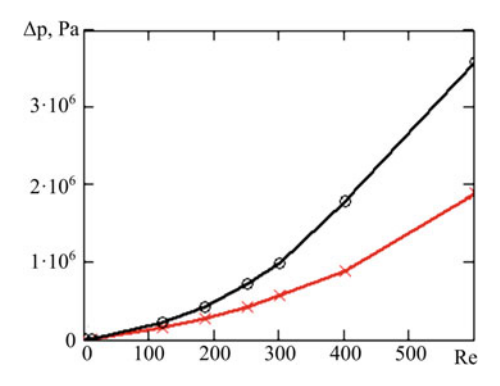


Fig. 4.33 Mixing efficiency versus the Reynolds number

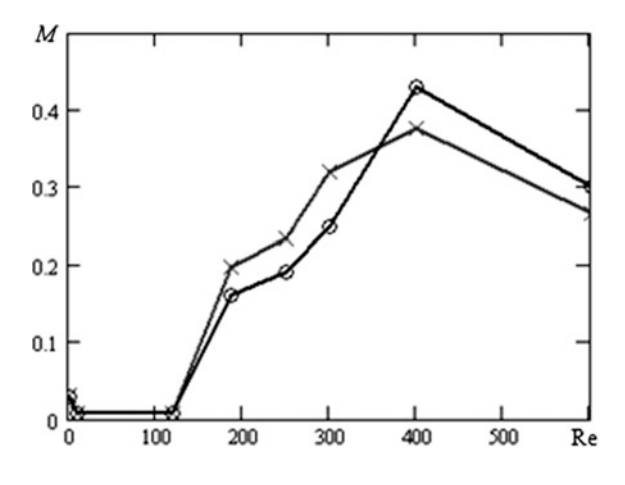
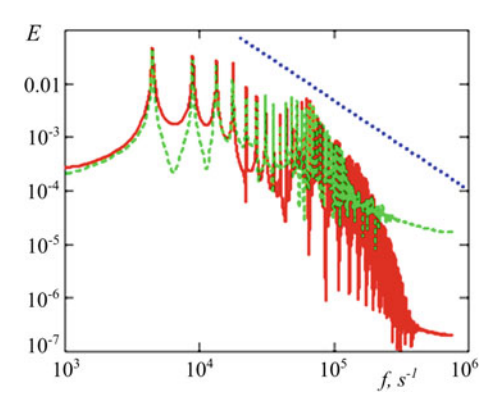


Fig. 4.34 Spectrum of the kinetic energy of velocity oscillations for Re = 300



4.5 Experimental Study of Flow Regimes in a T-Type Micromixer

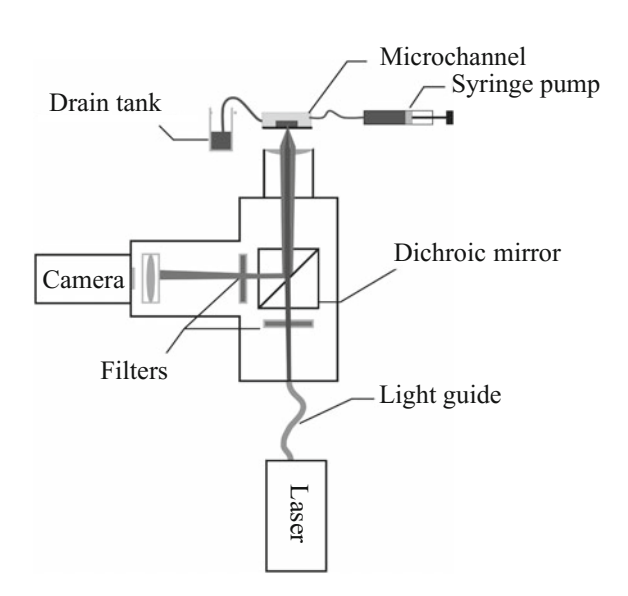
Experimental investigations of microflows involve certain difficulties discussed in the previous sections. In practice, two methods are widely used for this purpose: digital tracer visualization (or microscopic particle image velocimetry, micro-PIV) and microscopic laser-induced fluorescence (micro-LIF). The main idea of micro-PIV is the recording of consecutive tracer patterns in certain time intervals and subsequent cross-correlation processing of these images. Knowing the time between the light flashes and the displacements of the tracer particles, one can calculate the instantaneous and average velocity fields in the micromixer. Micro-LIF is a method for measuring the concentration and temperature fields with a micron-level resolution. It is based on the fact that the fluorescence intensity is

proportional to the concentration of the fluorescent dye and decreases with increasing temperature. In the case of micro-LIF measurements, a fluorophore is added to the examined flow, which is illuminated by exciting light. By virtue of proportionality of the intensity of the fluorescence to the dye concentration (which have to be small), the fluorescence patterns allow one to reconstruct the instantaneous velocity field. The experiments described below were performed in Minakov et al. (2013a, b, c).

The experimental setup is schematically shown in Fig. 4.35. The image formation system consists of a Carl Zeiss AxioObserver.Z1 epi-fluorescent inverted microscope with 20x/NA = 0.3 and 5x/NA = 0.12 objectives for micro-PIV and micro-LIF experiments, respectively. Flow illumination and recording of images by a digital camera are provided by a PILIS measurement system, which consists of the following basic elements: double pulsed Nd:YAG laser with a pulse energy of 50 mJ, wavelength of 532 nm, and pulse repetition frequency of 8 Hz, which illuminates the flow through the microscope objective, liquid light guide used to direct the beam to the microscope, system of fiber alignment with the optical path of the microscope, mercury lamp used to illuminate the microchannel during the micro-LIF experiments, cross-correlation digital camera used for image recording, personal computer used to process the data obtained in the experiment, and programmable processor, that ensures synchronization of the operation of the entire system. Experiment control and data processing were performed with the use of the ActualFlow software package.

The experiments were performed within the range of the Reynolds numbers from 10 to 300. The fluid motion was controlled by an infusion syringe pump with a controlled flow rate of the fluid. The fluid flow was seeded with fluorescent tracer particles produced by DukeScientific. The particles consisted of a melamine

Fig. 4.35 Experimental setup for micro-PIV and micro-LIF experiments



polymer marked with a rhodamine B fluorescent dye. The particle density was $1.05~\text{g/cm}^3$, and the mean particle diameter was $2~\mu\text{m}$. For detection of light emitted by the particles and suppression of light reflected from the channel, we used a light splitter consisting of a dichroic mirror and two filters for excitation and detection of rhodamine B.

The T-type micromixer is schematically shown in Fig. 4.15; the experiments were performed with a mixer produced by MicroLiquid (Spain). The cross-sectional sizes of the input and mixing channels of the micromixer were $200 \times 200 \,\mu m$ and $200 \times 400 \mu m$, respectively. The lengths of the input and mixing channels were identical and equal to 5 mm. Distilled water was used as a test fluid. Micro-PIV measurements were performed in three regions of the T-type mixer; therefore, the velocity field was calculated up to seven calibers from the mixing channel entrance. The measurements were performed in the central plane of the channel at the Reynolds numbers from 10 to 300 with a step of 30. As the entire depth of the microchannel is illuminated in micro-PIV experiments, the thickness of the cross-section of velocity measurements is determined by the depth of focus of the objective. Micro-PIV measurements usually involve a notion of the "correlation depth" defined as a double distance from the focal plane to the nearest plane where the particles become sufficiently defocused and do not make any significant contribution to the cross-correlation function. In Hoffmann et al. (2006), the correlation depth is defined by the relation

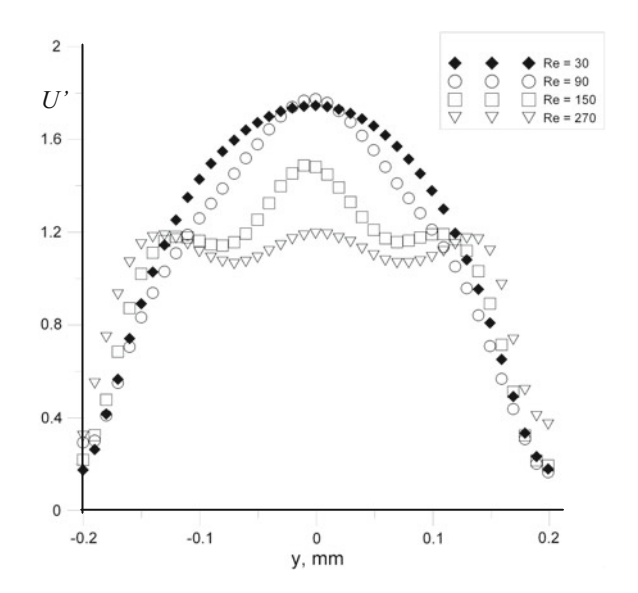
$$\delta z = \frac{3n\lambda_0}{NA^2} + \frac{2.16d_p}{\tan\theta} + d_p,\tag{4.7}$$

where n is the refractive index of the immersion fluid, λ_0 is the wavelength of light emitted by the fluorescent particles, NA is the numerical aperture of the microscope objective, θ is the aperture angle of the objective lenses, and d_p is the diameter of the tracer particles. Thus, according to Eq. (4.7), the correlation depth in the present experiment was 34 μ m.

Figure 4.36 shows the normalized velocity profiles U' in the central section of the mixing channel at a distance of 2.5 calibers from the mixing channel entrance. Normalization was performed to the velocity U_Q determined by the flow rate Q at the entrance: $U_Q = Q/\rho S$. The average velocity fields in the central section of the micromixer for different Reynolds numbers are shown in Fig. 4.37. The analysis of the velocity profiles and fields shows that the velocity profiles change at Reynolds numbers of 150 and higher, and inflections appear in the velocity profiles (see Fig. 4.36). This behavior is caused by the formation of an S-shaped structure in the mixing channel; a systematic description of this regime can be found in the previous section. The transition to this regime occurs at 120 < Re < 150.

For correct interpretation of the experimental data obtained through the micro-LIF method and comparisons with results of numerical simulations, we have to estimate the spatial resolution of the method. It can be demonstrated that the intensity of radiation of a point source at a distance *z* from the object plane is

Fig. 4.36 Normalized velocity profiles in the central section of the mixing channel



$$J(z) = \frac{J_0 D_a^2 (s_0 + z)^4}{4\pi (d_s^2 + M^2 D_a^2 z^2)^2 s_o^2},$$
(4.8)

where s_0 is the working distance of the microscope objective, M is the objective magnification, D_a is the lens aperture diameter, J_0 is the light flux emitted by the point source, λ_0 is the wavelength of fluorophore emission, N_A is the numerical aperture, and $d_s = 1.22(M+1)\lambda_0/N_A$. It was further found that the mean diameter of spatial averaging of the method is equal to the mean diameter of the point spread function. For instance, for the 5x/NA = 0.12 objective and the channel depth of $200 \ \mu m$, the mean diameter of spatial averaging is $55 \ \mu m$.

A mercury lamp was used for illumination in micro-LIF measurements. The above-described objective was used for flow visualization. With the use of a green light filter, the green wavelength was cut out of the mercury lamp radiation spectrum. A light filter was used to detect the light emitted by the rhodamine 6G fluorophore and suppress the reflected light. The fluorophore radiation was recorded by a Videoscan digital camera with a resolution of 2048×2048 pixels and dynamic range of 12 bit.

First, we determined the range of concentrations in which the fluorophore radiation intensity is a linear function of its concentration. For this purpose, aqueous solutions of rhodamine 6G with concentrations of 0, 10, 25, 40, 50, 62.5, and 75 mg/liter were fed into the T-type channel. The channel image was recorded for each fluorophore concentration. After that, a special calibration series of measurements was performed, which made it possible to eliminate spatial inhomogeneity of light in the channel.

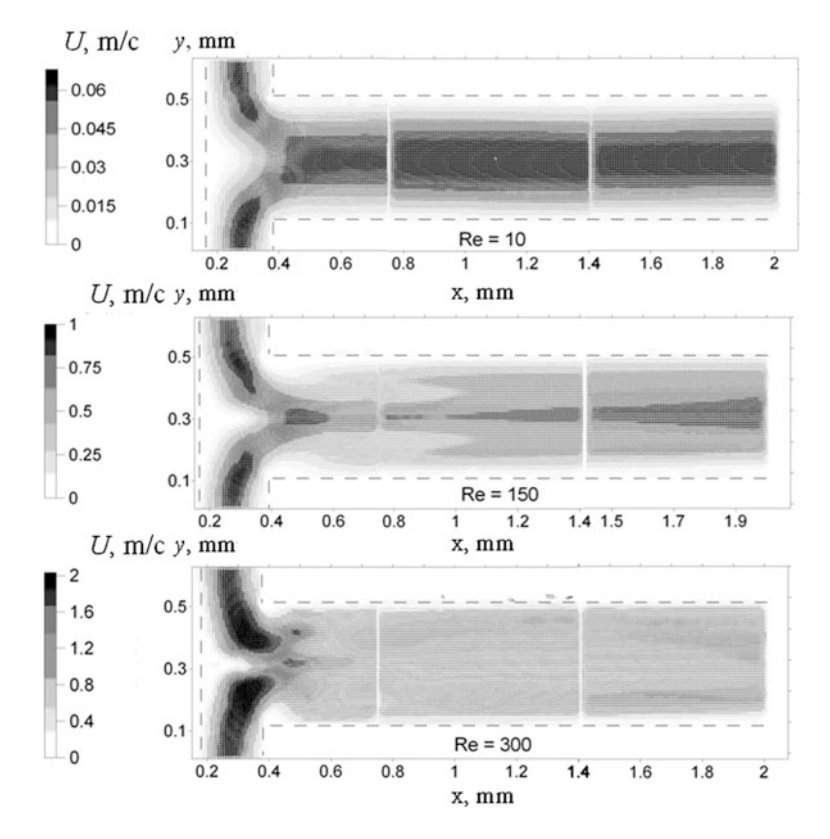


Fig. 4.37 Average velocity fields in the central section of the T-type micromixer for different Reynolds numbers

In concentration field measurements, distilled water was fed into one of the input channels of the T-type mixer and an aqueous solution of rhodamine 6G with a concentration of 60 mg/l was fed into the other input channel. Five hundred images were recorded for each flow regime corresponding to a prescribed Reynolds number. Then, the images were averaged, and the background noise was subtracted from the averaged image. Figure 4.38 shows the fields of the concentration C normalized to the maximum concentration $C_{\rm max}$ in the mixing channel for the Reynolds numbers of 30, 150, and 300. Visualization of the concentration fields shows that intense mixing of the fluids begins when an S-shaped structure is formed (at the Reynolds number of 150).

Spatial averaging of data over the depth of the T-type mixer was performed for comparisons of the concentration fields obtained through numerical simulations and experiments. This procedure was applied to the concentration fields in the XY plane in eleven cross-sections over the depth symmetrically with respect to the center of the T-type mixer. The concentration fields for each section were spatially averaged by using a "moving average" filter with a circular window whose diameter was

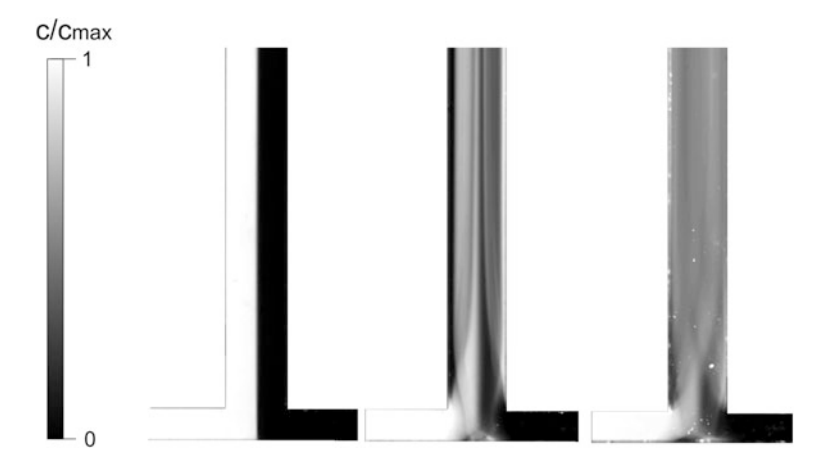
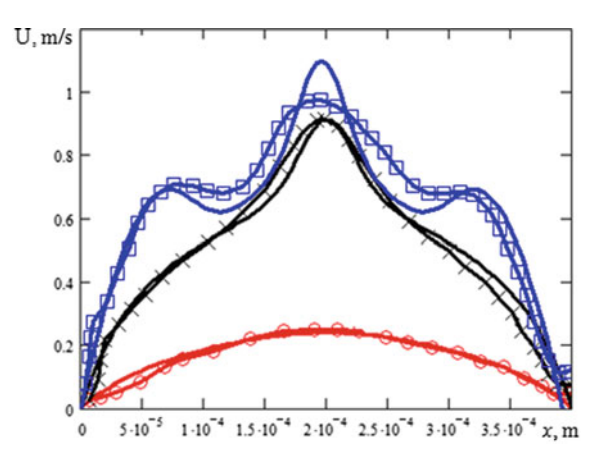


Fig. 4.38 Average concentration fields in the T-type mixer for different Reynolds numbers. From left to right: Re = 30, Re = 150, and Re = 300

equal to the point spread function diameter in this section. The resultant concentration field was calculated as the arithmetic mean for these eleven sections. The computed velocity fields and the averaged experimental values for different Reynolds numbers are shown in Fig. 4.39. The velocity profiles were obtained in the central section at a distance of 2.5 calibers from the mixing channel entrance. Here, the points connected by the curves are the experimental data, whereas the curves that are not marked by the points are the results of numerical simulations. The data for the Reynolds numbers of 30, 120, and 150 are marked by the circles, crosses, and squares, respectively. In all cases, the experimental data are seen to be in good agreement with the numerical predictions, but the resolution of the experimental data interpretation (determined by the correlation depth) at the highest Reynolds numbers is insufficient to provide an adequate description of the complex

Fig. 4.39 Velocity profiles in the central streamwise section of the mixing channel



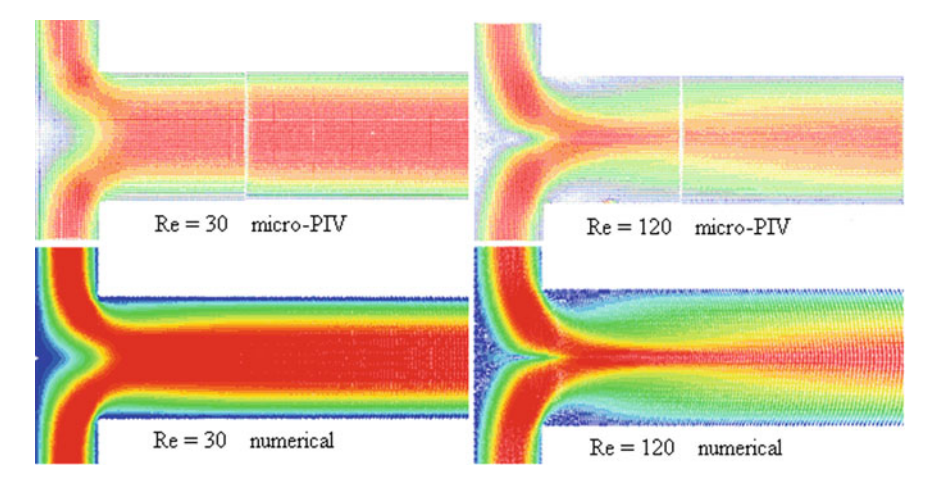


Fig. 4.40 Averaged experimental and computed velocity fields in the central streamwise section of the mixer

behavior of the velocity profile caused by the formation of S-shaped structures. Numerical simulations ensure better accuracy.

The numerical and experimental data are qualitatively compared in Figs. 4.40 and 4.41, which show the velocity isolines at the input part of the mixer (Fig. 4.40) and in the mixing channel (Fig. 4.41) for several Reynolds numbers. Here, the data are in fairly good agreement as well. Concerning the dye concentration, the predicted and experimental profiles are in excellent agreement (see Fig. 4.42). Here, the Reynolds number is Re = 30, the points show the experimental data, and the solid curve is the numerical prediction.

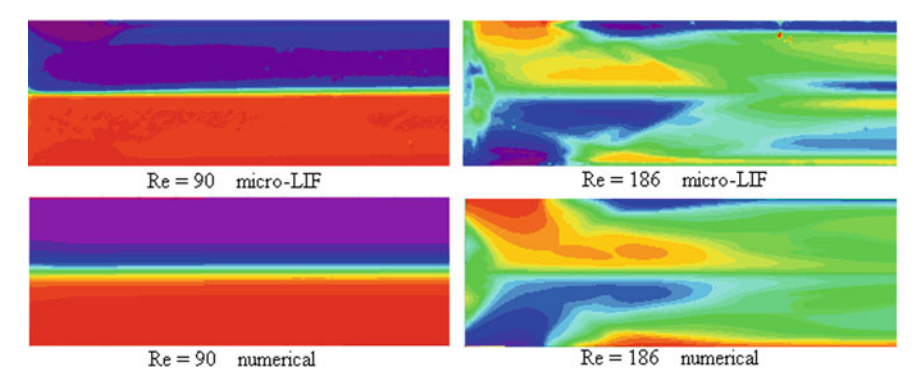
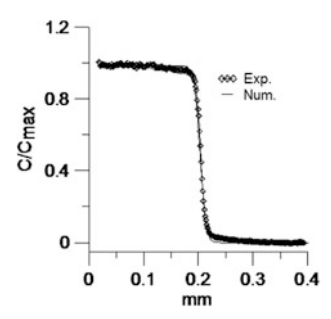


Fig. 4.41 Averaged experimental and computed concentration fields in the central streamwise section of the mixer

Fig. 4.42 Comparison of the experimental and computed concentration profiles in the central streamwise section of the mixer



4.6 Modeling of Two-Phase Flows in a T-Type Micromixer

Two-phase flows are extremely important for numerous microfluidic applications, in particular, in micromixers. Actually, systematic investigations have only started recently, though a number of interesting results have already been obtained. However, a comprehensive review cannot be provided here, because of the limited volume of the present chapter. Here, we consider and analyze only typical difficulties encountered in modeling two-phase flows.

The first problem is related to modeling the flow of a water-oil mixture in a T-type micromixer. The channel height is 100 μ m, and the width of the upper channel is 50 μ m. Oil is fed through the right side channel, and water is fed through the narrow upper channel. The computations were performed for various ratios of the mass flow rates of water and oil $Q_w/Q_o = 0.3 \div 2$, where $Q_w = 0.14$ ml/s, for two wetting angles. A typical flow pattern for a certain prescribed ratio of the water and oil mass flow rates is shown in Fig. 4.43. Here, the mass flow rates are identical $(Q_w/Q_o = 0.3)$, whereas the contact angle is 90° in the upper picture and 150° in the lower picture. The flow character is determined by the wetting angle. A film flow is observed in the microchannel in the case with a contact angle of 90°. The limiting value of the wetting angle at which water droplets start to form is approximately 120°.

At the same time, the shape of water droplets formed in oil is determined by the capillary number $Ca = \mu U/\sigma$. Here, μ , U, and σ are the viscosity coefficient, average velocity determined on the basis of the flow rate, and surface tension coefficient of

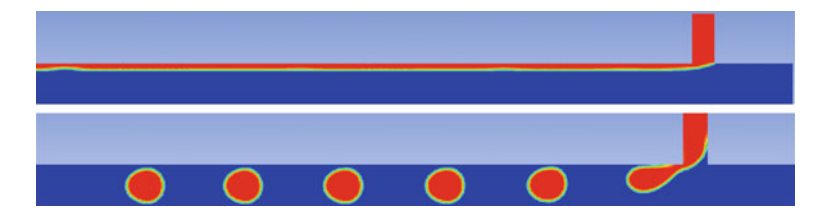


Fig. 4.43 Visualization of numerical simulation of the water-oil flow in a microchannel for two wetting angles

oil. As the surface tension coefficient decreases, the droplets become more and more extended, and begin to resemble a slug flow. The evolution of the flow with the parameter Ca is shown in Fig. 4.44. Here, the contact angle is 150° in all pictures, but the values of Ca are different: $Ca = 18.47 \times 10^{-3}$ in the upper picture, 12.67×10^{-3} in the next picture, 7.92×10^{-3} in the third picture, 4.22×10^{-3} in the fourth picture, and 3.168×10^{-3} in the last picture.

Figure 4.45 shows the pressure isolines in the central section of the channel. Here, the values of the flow rate ratio Q_w/Q_o are 0.3, 0.5, 0.8, 1.5, and 2 from top to bottom, which correspond to the same values of the capillary number and wetting angle in Fig. 4.44. This flow was studied experimentally in Garstecki (2006).

A quantitative comparison of the numerical and experimental data was performed for the dependence of the dimensionless length L' = L/W of the water droplet on the ratio of the water and oil mass flow rates (here, $W = 100 \, \mu m$ is the width of the channel through which oil is fed). The results of this comparison are shown in Fig. 4.46. As could be expected, the droplet length depends, to a large extent, on the wetting angle θ . Here, the experimental data are represented by the crosses (1); the squares (2) and plus signs (3) are the data computed for the wetting angles of 150° and 180°, respectively.

The next problem is modeling a gas-liquid flow in a T-type micromixer with a circular cross-section. The channel is schematically shown in Fig. 4.47. The mixing channel length is $18,000~\mu m$, its diameter is $d=300~\mu m$, and the input channels have the same diameter and the length $1800~\mu m$. Water and air were fed through the upper and lower input channels, respectively. The ratio of the mass flow rates of water and air at the channel entrance was varied in the computations. The solid walls were subjected to the no-slip condition. The wetting angle was 90° .

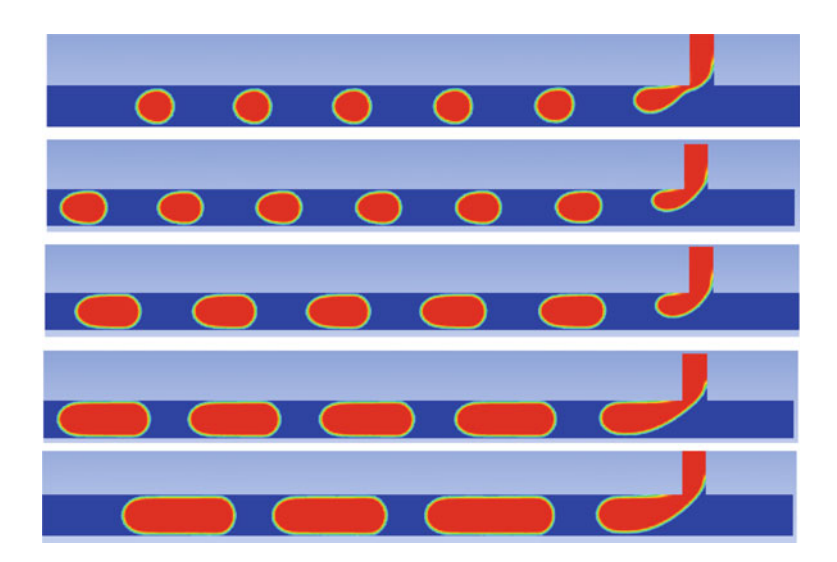


Fig. 4.44 Shape of the water droplets with decreasing Ca

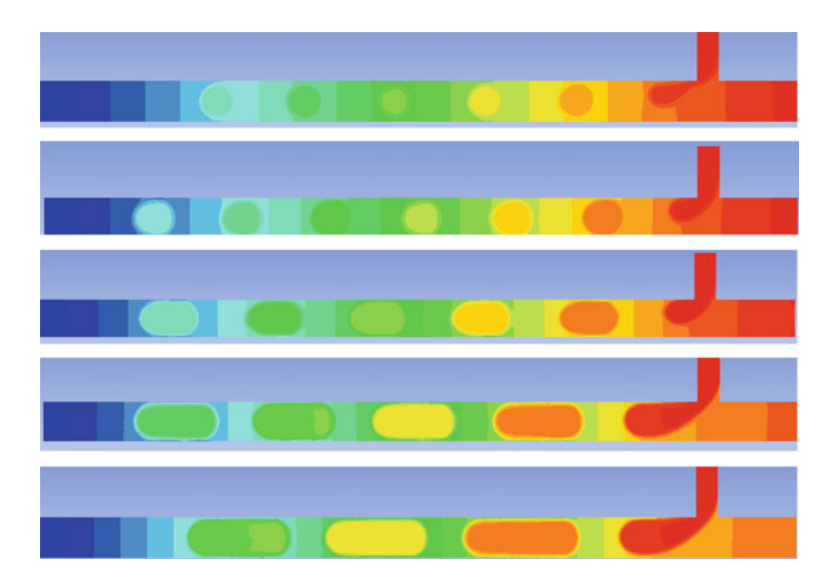
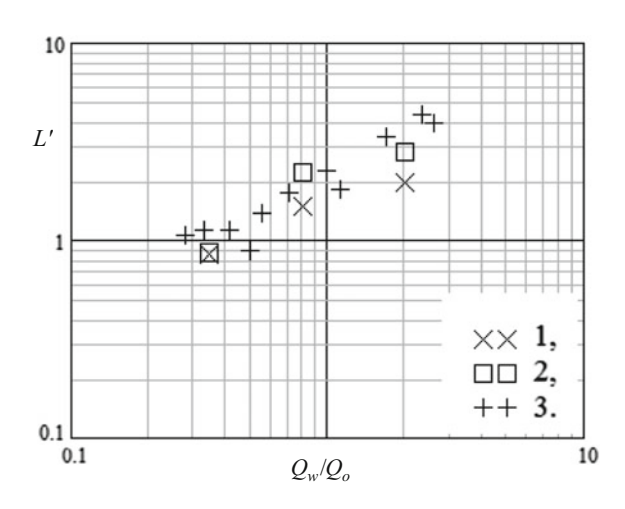


Fig. 4.45 Pressure isolines in the water-oil flow

Fig. 4.46 Dimensionless length of the water droplet versus the ratio of the water and oil mass flow rates Q_w/Q_o



A typical structure of the flow formed in the micromixer is shown in Fig. 4.48. Three situations were considered: gas velocity 0.05 m/s and water velocity 0.02 m/s (upper picture); identical gas and water velocities 0.05 m/s (middle picture); gas velocity 0.05 m/s and water velocity 0.1 m/s (lower picture). The droplet shape is determined by the velocities of water and air supply.

The simulated and experimental results (Quin and Lawal 2006) are quantitatively compared in Fig. 4.49, which shows the dimensionless length of the water droplet L = L/d as a function of the dimensionless velocity of the liquid

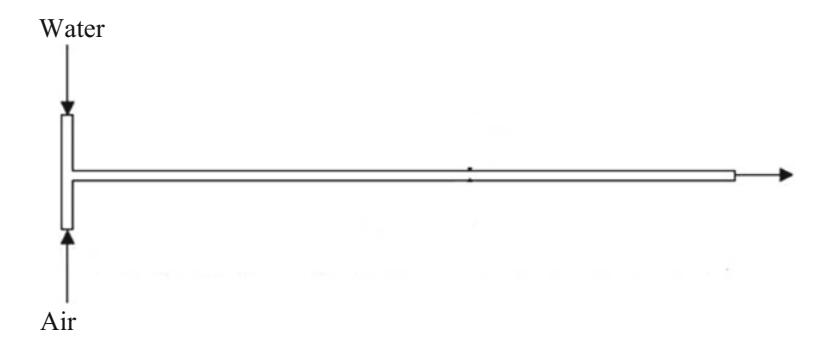


Fig. 4.47 Gas-liquid flow in a cylindrical micromixer

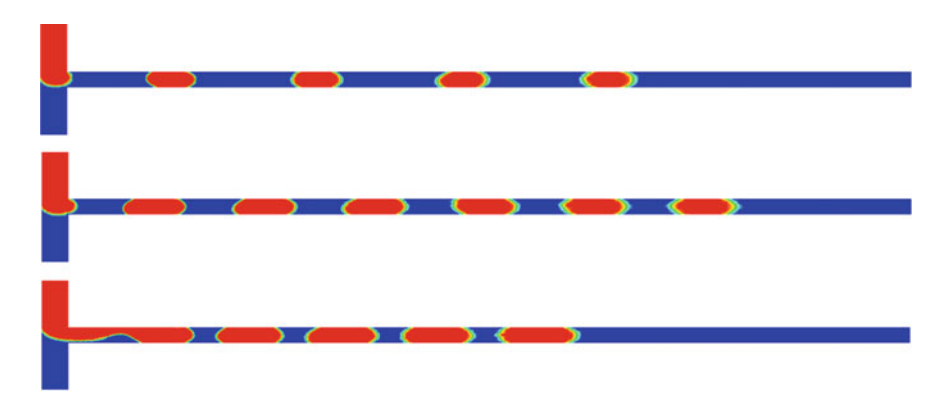


Fig. 4.48 Density isolines in the micromixer

 $\tilde{V} = V_L/(V_L + V_G)$, where V_L and V_G are the water and air velocities. The experimental data are significantly scattered; nevertheless, the numerical data (filled points) ensure an adequate description of the experimental results.

It is of interest to consider the behavior of pressure along the channel. It is clear from the general considerations that it should decrease because of friction. The calculated behavior of pressure (Fig. 4.50) shows that this really is so. However, the monotonic decrease in pressure due to viscous friction is combined with pressure changes induced by capillary forces.

The slug regime of the two-phase mixture flow is involved in many engineering and industrial devices. It is not an easy task to study this flow regime, especially in channels with non-circular cross-sections and sharp angles. In this flow regime, capillary forces exert a dominating effect on the velocity of motion of gas bubbles; therefore, the experimental data (Kuznetzov et al. 2005) on the velocity of emergence of gas bubbles in various channels can serve as a good test for the algorithm developed for calculating flows with free surfaces. The numerical calculation of emergence of gas bubbles described below was performed for an open rectangular

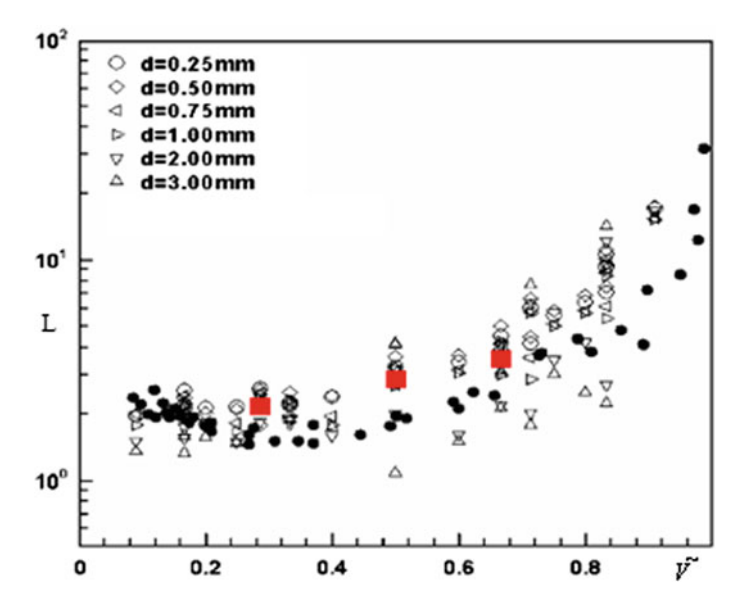


Fig. 4.49 Dimensionless length of the water droplet formed in the micromixer versus the ratio of the water and air velocities

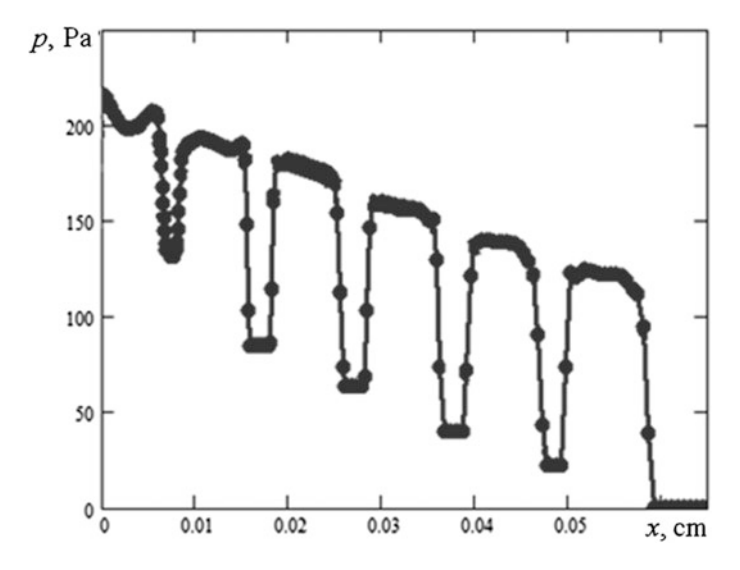


Fig. 4.50 Evolution of pressure along the central line of the channel for the gas velocity of 0.05 m/s and water velocity of 0.1 m/s

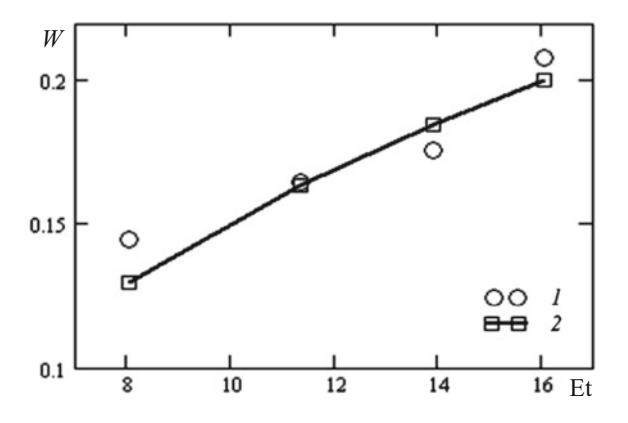
channel with a height of 500 mm and cross-sectional area of 2×7 mm. At the initial time, the existence of an air bubble shaped like a parallelepiped with a volume of about 300 mm³ in a channel filled with acetone was assumed. Approximately 1 s after the beginning of the computation, the bubble acquired the shape of a gas slug, which remained almost unchanged at later times. The variable measured in the computation was the velocity of bubble emergence U as a function of the channel slope relative to the horizontal line Θ . This velocity was practically constant; therefore, it was determined to be the distance covered by the bubble center in one second. Figure 4.51 shows the dimensionless velocity of bubble emergence $W = U/\sqrt{gb \sin \Theta}$ as a function of the Eotvos number $Et = \rho g \sin \Theta b^2/\sigma$ for four angles of the channel: 30° , 45° , 60° , and 90° . Here, b is the width of the narrow part of the channel. The circular and square points in the figure correspond to the experimental and numerical data, respectively. Thus, the simulated results are in good agreement with the experimental data.

One more example of the numerical simulation of the slug flow is presented in the last part of this section. The scheme and geometry used in the computation are shown in Fig. 4.52. Water was supplied from the top with a velocity of 0.2 m/s. Air was injected through a narrow tube. A quasi-stationary gas slug was formed in the channel after a certain time depending on the flow rate of air. A typical pattern of a steady slug flow is also shown in Fig. 4.52 in eight consecutive pictures. The first four pictures show the experimental data (Kashinskii et al. 2010), and the next four pictures are the results of numerical simulations. In all cases, the data are given for four values of the slug length.

In the upper part of the slug, the flow is almost steady. At the slug bottom, gas bubbles are periodically shed, which is clearly visible in Fig. 4.52, both in the experimental photographs and in the visualized numerical patterns. Entrainment of the gas with the bubbles is compensated by gas injection through the tube. As a result, the slug size remains almost constant.

The process studied in the experiment (Kashinskii et al. 2010) was the friction on the channel wall as a function of the length of the gas slug. In this case, the friction

Fig. 4.51 Dimensionless velocity of emergence of water slugs versus the Eotvos number



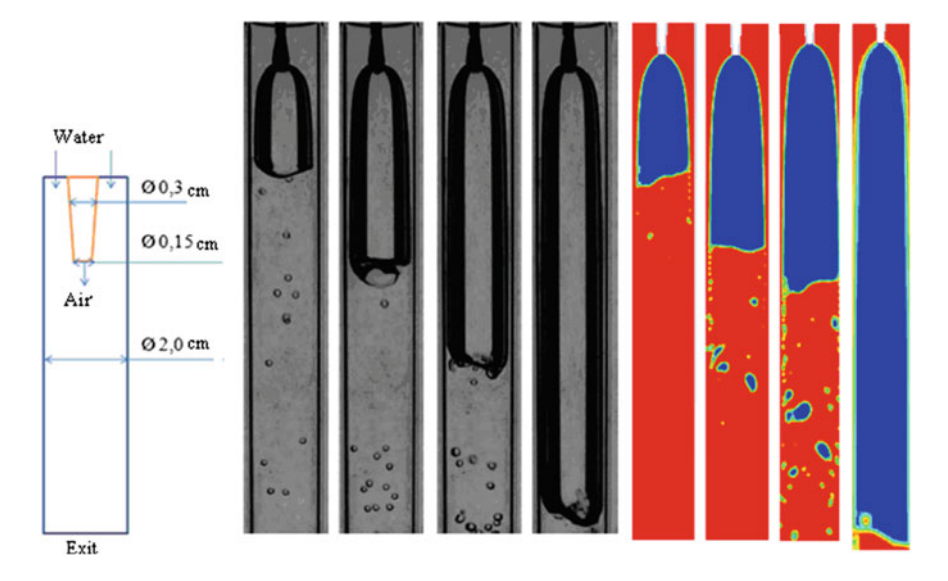


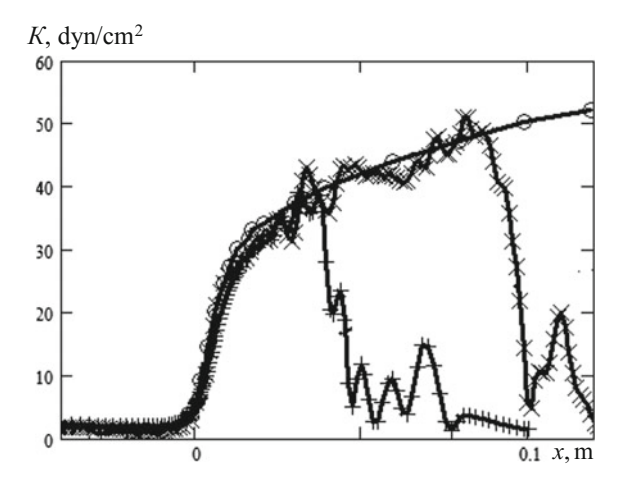
Fig. 4.52 Scheme of the test section and comparisons of the experimental patterns of a steady slug flow in a circular channel with those obtained in numerical simulations

is almost completely determined by the thickness of the liquid film formed between the gas bubble and the channel wall.

The friction was also determined in the numerical simulations. The results of the simulated and experimental results for two values of the slug length (4 and 10 cm) are compared in Fig. 4.53, which shows the specific friction K (dyn/cm²) along the channel. The experimental curve (curve passing through the circular points) was obtained for a slug with a length greater than 12 cm. Therefore, reasonable agreement can be expected only on the part of the friction curve for the corresponding slug length. Indeed, the friction on the wall is independent of the slug length until the end of the slug. The plus signs and crosses in Fig. 4.53 show the simulated results for the slug lengths of 4 and 10 cm, respectively.

It should be noted that this slug flow is only quasi-steady. It is seen in Fig. 4.53 that the liquid film formed between the wall and the bubble becomes unstable approximately after 2 cm. Perturbations develop on this film, leading to the formation of waves moving in the flow direction. These waves are particularly clear on the curve that describes the friction for the shortest slug. The experimental curve shows the friction averaged in time; therefore, this instability is not observed.

Fig. 4.53 Friction in the slug flow along the channel



4.7 Heat Transfer in a T-Type Micromixer

Before studying the processes of thermal mixing in a micromixer, let us consider typical features of the microflow in a cylindrical microchannel with a length of 2000 μ m and radius of 50 μ m. The thermophysical properties of the examined medium are listed in Table 4.4.

A constant heat flux equal to 10 W/mm^2 was imposed on the channel wall (the area of the side surface of the channel was 0.3141 mm^2). The temperature of the medium at the channel entrance was 273 K. In addition, a parabolic velocity profile shown in Fig. 4.54 was set at the channel entrance. The computation was performed on a three-dimensional five-block grid refined toward the channel walls; each block contained $30 \times 30 \times 150$ cells (a total of 675.000 cells).

The calculated velocity and temperature profiles along the channel are shown in Fig. 4.55 and are adequately described by available analytical solutions. At the initial thermal segment $0 \le x \le l_{th}$, whose length is determined by the relation $l_{th} = 0.07dPe$, the local value of the heat transfer coefficient decreases along the channel (with increasing x).

Table 4.4 Thermophysical properties of the medium

Viscosity coefficient	0.001 Pa s
Thermal conductivity	1.4 W/(m K)
Specific heat	4200 J/(kg K)
Density	1000 kg/m ³
Prandtl number	3
Mass flow rate	0.7854 mg/s
Mean mass velocity	0.1 m/s

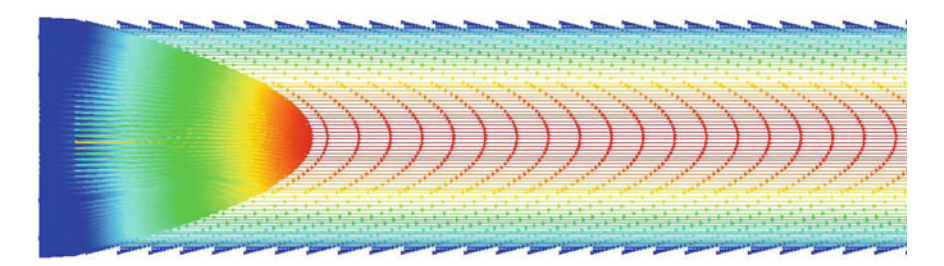


Fig. 4.54 Velocity profile at the channel entrance

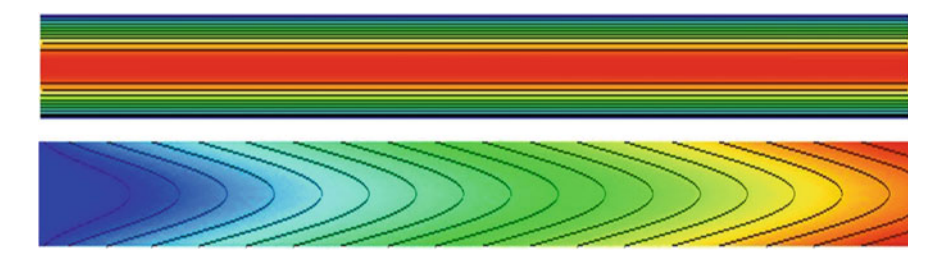


Fig. 4.55 Velocity (upper picture) and temperature (lower picture) distributions along the channel

A theoretical analysis yields the following approximate relation for the Nusselt number Nu in this region (Tzvetkov and Grigoriev 2005):

$$Nu = 1.31 (dPe/x)^{1/3}. (4.9)$$

The theoretical value is compared with the results of numerical simulations for different Reynolds numbers in Fig. 4.56.

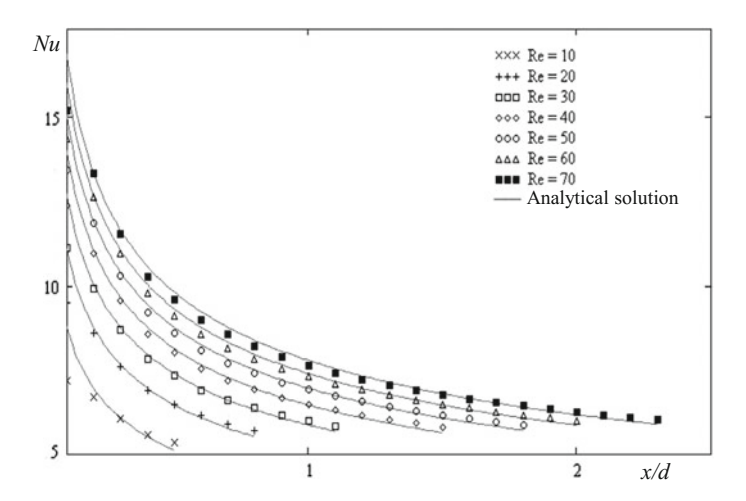


Fig. 4.56 Comparison of the numerical and analytical results

The expression for the Nusselt number, which is valid for the entire heat transfer region, has the form (Tzvetkov and Grigoriev 2005)

$$Nu^{-1} = \frac{11}{48} + \sum_{n=1}^{\infty} A_n \cdot \psi_n \cdot \exp\left(-2\varepsilon_n^2 \cdot \frac{1}{Pe} \cdot \frac{x}{d}\right), \tag{4.10}$$

where A_n , ψ_n , and ε_n^2 are constants depending on n. The first seven values are listed in Table 4.5.

The behavior of the calculated Nusselt number (different points) along the channel for different Reynolds numbers is illustrated in Fig. 4.57. These points are compared with the analytical solution (4.10) (solid curves).

The local Nusselt number asymptotically tends to an integral value, which is constant for a laminar flow and unchanged density of the heat flux on the wall and equal to 4.364. Here, the local Nusselt number is determined by the relation

-1 - 1 - 1 - 1 - 1 - 1 - 1 - 1 - 1 - 1				
n	ε_n^2	$ \psi_n $	A_n	
1	25.680	-0.49252	+0.20174	
2	83.862	+0.39551	-0.087555	
3	174.17	-0.34587	+0.052797	
4	296.54	+0.31405	-0.036640	
5	450.95	-0.29125	+0.027518	
6	637.39	+0.27381	-0.021742	
7	855.85	-0.25985	+0.017799	

Table 4.5 Values of the constants A_n , ψ_n , and ε_n^2 in Eq. (4.10)

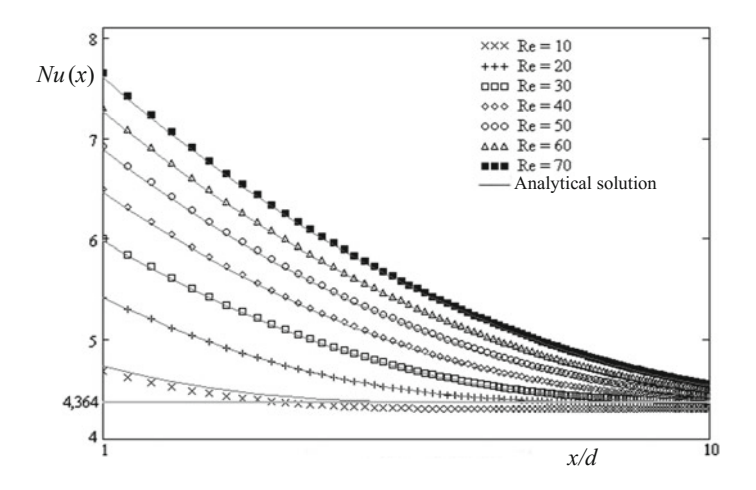


Fig. 4.57 Local Nusselt number versus the Reynolds number

$$Nu(x) = \frac{d}{\lambda} \frac{q}{T_w(x) - T_c(x)},$$

where $T_w(x)$ is the temperature on the wall, $T_c(x) = (4qx)/(\mu \text{Re } C_p)$ is the temperature in the core flow, and q is the density of the heat flux on the wall.

Let us now consider typical features of heat transfer in a T-type rectangular minimizer. Its width was 2h = 0.5 mm, its height was 1 mm, the length of the mixing channel was L = 30 mm, and the length of the input channels was l/2 =1.25 mm. The test fluid was deionized water. A constant mass flow rate equal to 0.025 g/min was set in the input channels. The fluid temperature was 27 °C in one input channel and 55 °C in the other input channel. For a correct description of heat transfer in the rectangular T-type mixer, it is necessary to separate regions of mixing in the T-shaped junction and in the mixing channel. In the region of the T-shaped junction, the hot and cold water flows coaxially in two input channels. Thermal mixing begins after these flows contact each other. Thermal diffusion prevails in this region. The Reynolds number is smaller than unity, and the flow is laminar. Thermal diffusion and convection prevail in the course of thermal mixing in the mixing channel, and the flow regime remains laminar. The computed temperature distribution (left) is compared in Fig. 4.58 with the experimental one (Xu et al. 2010). The temperature distribution along the input channel is shown in Fig. 4.59. The thin and bold curves here are the predicted and experimental (Xu et al. 2010) data. The agreement between the numerical and experimental data is actually within measurement accuracy.

The temperature distributions in the mixer entrance cross-section and at a distance of 7.5 mm from the entrance are shown in Fig. 4.60. Again, the simulated and experimental data are plotted with the solid curve and square points, respectively.

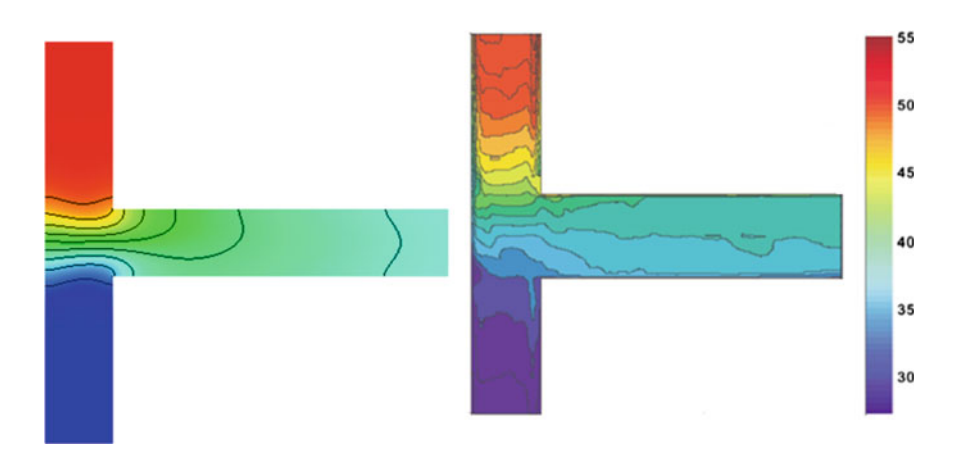


Fig. 4.58 Temperature profile in the T-type micromixer. Results of simulations (left) and experiments (right)

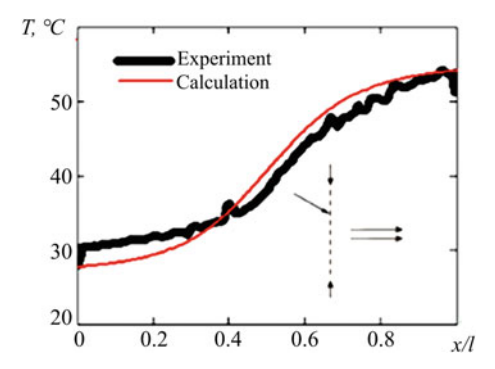


Fig. 4.59 Temperature distribution along the input channel

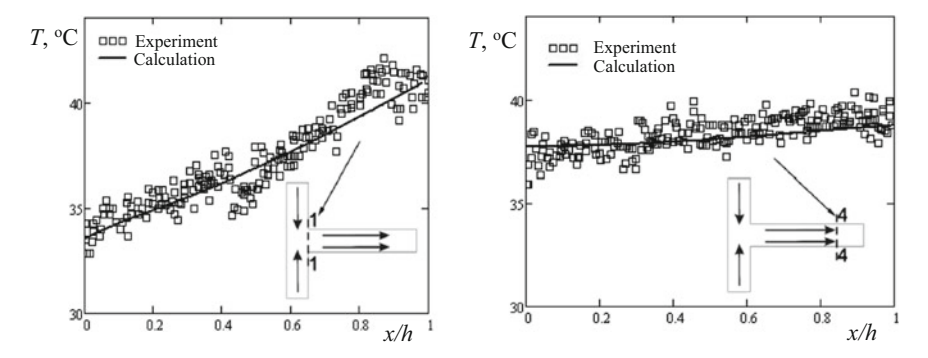


Fig. 4.60 Temperature distributions at the mixing channel entrance (left) and at a distance of $7.5 \mu m$ from the entrance

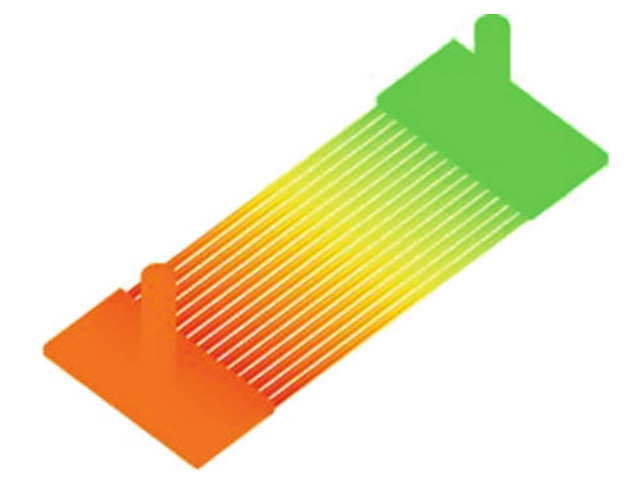
The temperature gradients are appreciably different in these cases, but the temperature levels off fairly rapidly.

The above-described simulations of the T-type micromixer are readily extended to simulations of rather complicated Thermophysical systems. Figure 4.61 shows a microphotograph of a multichannel block of heat transfer in a microscopic heat exchanger consisting of 15 microchannels with rectangular cross-sections. The microchannels have the following dimensions: channel height 772 μ m, channel width 1100 μ m, and channel length 5000 μ m; one block contained 15 microchannels. The geometry of the considered heat exchanger is schematically presented in Fig. 4.62, which shows the distribution of the temperature isolines for the Reynolds number Re = 100. Cooling water is supplied through a circular channel 5 mm in diameter (see Fig. 4.61), subsequently passing to a distributing

Fig. 4.61 Photograph of a minichannel heat exchanger (Khandekar et al. 2010)



Fig. 4.62 Temperature isolines on the microscopic heat exchanger walls



manifold with a cross-sectional size of $30 \times 15 \text{ mm}^2$ and 2.5 mm high. Then, water moves in the microchannels whose lower wall touches the cooled surface. After that, heated water enters a collecting manifold and is removed through the second circular channel. The area of the cooled surface of this heat exchanger is approximately equal to 1500 mm^2 , which corresponds to the size of typical microchip elements; therefore, it is convenient to use such systems, e.g., for cooling computer processors.

This microscopic heat exchanger was experimentally studied in Khandekar et al. (2010). In our numerical calculations, the Reynolds number was varied from 100 to 2000. It was determined on the basis of the flow rate of water at the heat exchanger entrance and input channel diameter. The examined variables were the decrease in pressure between the entrance and exit of the heat exchanger and the average heat transfer coefficient. A constant heat flux density equal to 10 kW/m² was prescribed on the lower wall in each microchannel. The remaining walls were assumed to be adiabatic. The computations were performed on a structured multiblock grid consisting of 400,000 nodes.

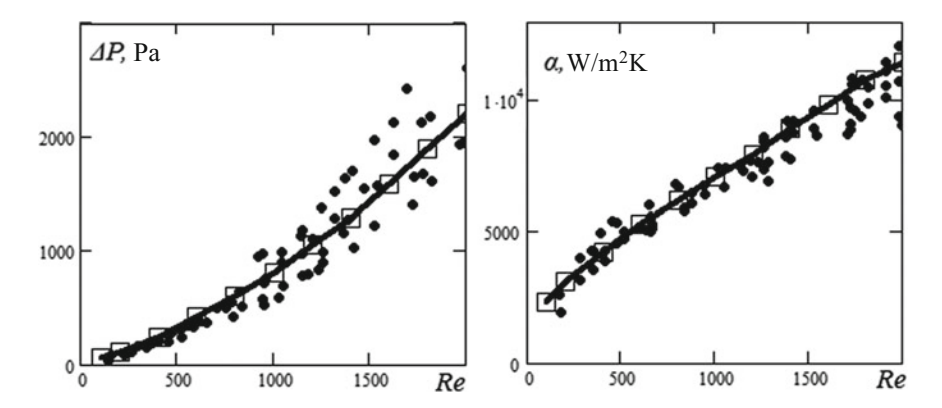


Fig. 4.63 Pressure difference (left) and average heat transfer coefficient (right) versus the Reynolds number

The results of numerical simulations (large squares and curves connecting them) are compared in Fig. 4.63 with the experimental data (Khandekar et al. 2010) (filled points). The figure shows the pressure drop between the entrance and exit of the heat exchanger and the average heat transfer coefficient as functions of the Reynolds number. The heat transfer coefficient was determined by the formula $\alpha = q/(T_w - T_f)$, where T_w is the average temperature of the microchannel wall and T_f is the mean arithmetic temperature of the fluid at the entrance and exit of the heat exchanger.

A comparison of these results shows that simulations ensure an adequate description of the experimental curves within the entire considered range of the Reynolds numbers in terms of both the pressure difference and the heat transfer coefficient. The scatter of the experimental data, which is enhanced as the Reynolds number increases, is caused by the fact that the flow in the collecting manifold of the heat exchanger is no longer steady at Reynolds numbers of 800 and higher. Therefore, the data calculated at high Reynolds numbers were averaged in time. It should also be mentioned that the values of the heat transfer coefficient for this microscopic heat exchanger reach 13,000 W/m² K. Such extremely high values of the heat transfer coefficient under standard conditions cannot be reached in macroscopic single-phase heat exchangers. Thus, we again see that microscopic heat exchangers offer significant prospects for effective utilization of thermal energy.

4.8 Active Method of Mixing

To finalize this chapter, we give one example of an active mixer, which implies variations of the flow rates of the fluids in the input channels. In the presented series of computations, the ratio of the flow rates in the upper and lower input channels

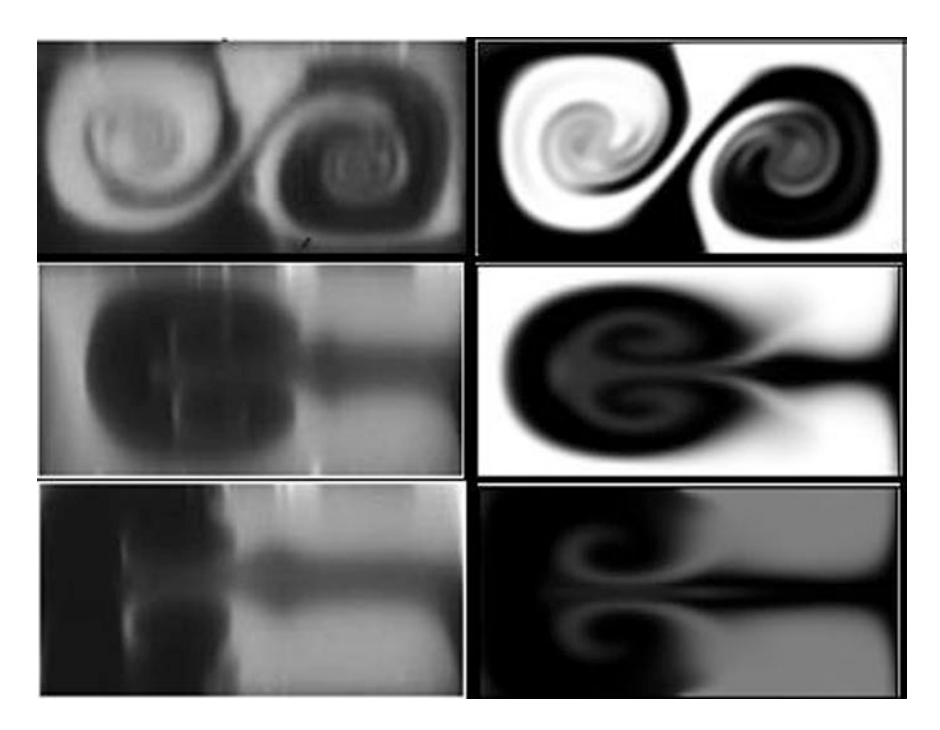


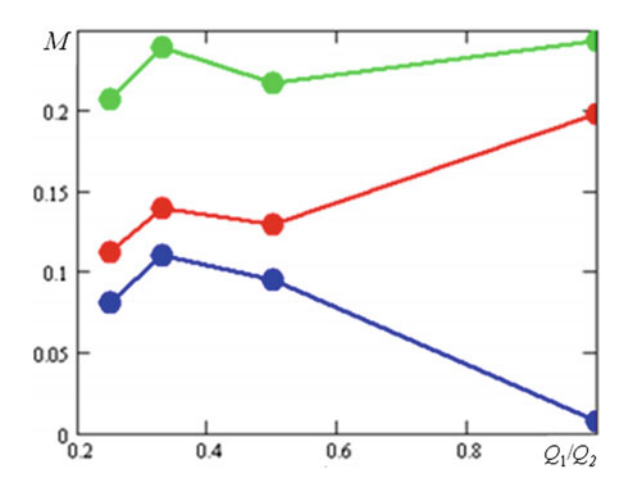
Fig. 4.64 Qualitative comparison of the mixing regime observed in the experiment (Hoffmann et al. 2006) (left) with the computed data (right) for the Reynolds number Re = 186 and different ratios of the flow rates: $Q_1/Q_2 = 1$ (upper picture), $Q_1/Q_2 = 1/2$ (middle picture), and $Q_1/Q_2 = 1/3$ (lower picture) steady regime with Re = 186

 Q_1/Q_2 was varied from 0.25 to 1. Three flow regimes were considered (see Sect. 4.4): symmetric steady regime with Re = 120, asymmetric and periodic unsteady regime with Re = 250. Different regimes of mixing in the microchannel cross-section obtained in the simulations and experiments (Hoffmann et al. 2006) with the Reynolds number Re = 186 and different ratios of the flow rates are qualitatively compared in Fig. 4.64.

The mixing efficiency is shown in Fig. 4.65 as a function of the ratio of the flow rates at the channel entrance for different Reynolds numbers. The behavior is significantly affected by the Reynolds number. For Re = 120 (lower curve), the asymmetry of the input conditions allows for substantial enhancement of mixing (by a factor of 15). The maximum intensity of mixing is observed at $Q_1/Q_2 = 1/3$. For Reynolds numbers greater than 150, at which an S-shaped structure is formed in the mixing channel, artificial asymmetry leads to disintegration of this structure, resulting in worse mixing.

One of the simplest methods of active mixing in Y- and T-type mixers is the method with periodic variations of the flow rate in one of the input channels. The parameter varied in Rudyak et al. (2010) was the velocity U_Q determined by the flow rate Q in the upper input channel at the T-type micromixer entrance:

Fig. 4.65 Mixing efficiency versus the ratio of the flow rates at the mixer entrance for different values of the Reynolds number: Re = 120 (blue curve), Re = 186 (red curve), and Re = 250 (green curve)



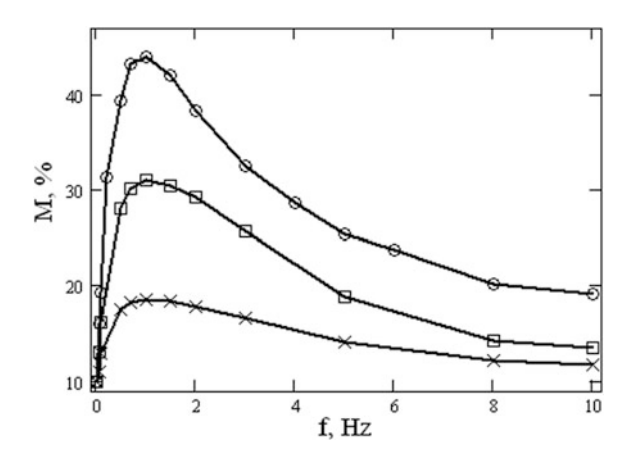
 $U_Q = Q/\rho S$, where ρ is the fluid density and S is the cross-sectional area of the microchannel. It was described by the relation

$$U_O = U_0 + V \sin 2\pi f t. (4.11)$$

The parameters involved into Eq. (4.11) are determined, in the general case, by the characteristic size of the channel where the mixing process occurs and by the flow characteristics (Reynolds and Peclet numbers). Obviously, if the characteristic time of mixing is much shorter than the period of the flow rate variation $\tau_m \ll (2\pi f)^{-1} = T_f$, the mixing efficiency will be almost the same as that in the case of steady mixing. Therefore, the situation with $\tau_m \gg T_f$ is preferable. On the other hand, the period of flow rate variation should be smaller than the characteristic time of the flow $T_f < \tau_L$. Certainly, it is rather difficult from the engineering viewpoint to ensure very high frequencies in microchannels. Therefore, a good compromise would be $\tau_m \ge (2\pi f)^{-1}$. The optimal amplitude of oscillations can be easily estimated by considering the volume of the mixing fluid during the period T_f .

These qualitative considerations are supported by direct computations. As an example, we can consider the mixing of two fluids in a T-type micromixer. Its width is 200 μ m, its height is 120 μ m, its length is 2000 μ m, and $U_0=10^{-3}$ m/s. Mixing of a fluid with the viscosity coefficient $\mu=6.67\times10^{-4}$ Pa s and diffusion coefficient $D=7\times10^{-11}$ m²/s is analyzed, which corresponds to Re = 0.3 and Pe=3000. For these parameters, we have $\tau_m\sim560$ s and $\tau_L\sim2$ s. Therefore, the optimal frequency should satisfy the conditions $T_f<2$ s and $\tau_m\geq T_f$.

Fig. 4.66 Mixing efficiency in the T-type mixer versus the frequency f and amplitude V of the flow rate in one of the input channels. The amplitude is V=1 (crosses), 5 (Square), and 10 mm/s (circle)



The corresponding frequency is found from the condition $f_{op} > 0.08$ Hz. This estimate yields the frequency $f_{op} \sim 1$ Hz. Figure 4.66 shows the mixing efficiency in this mixer as a function of the frequency f and amplitude V.

Indeed, optimal mixing is reached at frequencies on the order of 1 Hz.

References

Aubina J, Fletcherb DF, Xuereb C (2005) Design of micromixers using CFD modeling. Chem Eng Sci 60:2503–2516

Bothe D, Stemich C, Warnecke H-J (2004) Theoretische und experimentelle Untersuchungen der Mischvorgänge in T-förmigen Microreaktoren. Teil 1. Numerische Simulation und Beurteilung des Strömungsmischens. CIT 76:1480–1484

Bothe D, Stemich C, Warnecke H-J (2006) Fluid mixing in a T-shaped micro-mixer. Chem Eng Sci 61:2950–2958

Brackbill JU, Kothe DB, Zemach C (1992) A continuum method for modeling surface tension. J Comput Phys 100:335–354

Cao J, Cheng P, Hong FJ (2008) A numerical study of an electrothermal votex enhanced micromixer. Microfluid Nanofluid 5:13–21

Dreher S, Kockmann N, Woias P (2009) Characterization of laminar transient flow regimes and mixing in T-shaped micromixers. Heat Transf Eng 30:91–100

Engler M, Kockmann N, Kiefer T, Woias P (2004) Numerical and experimental investigations on liquid mixing in static micromixers. Chem Eng J 101:315–322

Ferziger JH, Peric M (2006) Computational methods for fluid dynamics. Springer, Berlin

Garstecki P (2006) Formation of droplets and bubbles in a microfluidic T-junction-scaling and mechanism of breakup. Lab Chip 6:437–446

Gavrilov AA, Minakov AV, Dekterev AA, Rudyak VY (2011) A numerical algorithm for modeling laminar flows in an annular channel with eccentricity. J Appl Ind Math 5(4):1–12

Gobert C, Schwert F, Manhart M (2006) Lagrangian scalar tracking for laminar micromixing at high Schmidt numbers. In: Proceedings of ASME joint U.S.-European fluids engineering summer meeting, Miami, USA, Paper No. FEDSM2006-98035, pp 1053–1062

Grigoriev IS, Meilikhova EZ (eds) (1991) Physical values. Handbook. Energoatomizdat, Moscow

References 183

Hirt CW, Nichols BD (1981) Volume of Fluid (VOF) method for the dynamics of free boundaries. J Comput Phys 39:201–225

- Hoffmann M, Schluter M, Rubiger N (2006) Experimental investigation of liquid–liquid mixing in T-shaped micro-mixers using μ-LIF and μ-PIV. Chem Eng Sci 61:2968–2976
- Hong CC, Choi JW, Ahn CH (2004) A novel in-plain passive microfluidics mixer with modified Tesla structures. Lab Chip 4:109–113
- Jiménez J (2005) The growth of a mixing layer in laminar channel. J Fluid Mech 535:245–254 Karnidakis G. Beskok A. Aluru N (2005) Microflows and nanoflows. Interdisciplinary applied
- Karnidakis G, Beskok A, Aluru N (2005) Microflows and nanoflows. Interdisciplinary applied mathematics, vol 29. Springer, Berlin
- Karnik R (2008) Microfluidic mixing. In: Li D (ed) Encyclopedia of microfluidics and nanofluidics. Springer, Berlin, pp 1177–1186
- Kashinskii ON, Kurdyumov AS, Lobanov PD (2010) Perturbation of a downward liquid flow by a stationary gas slug. Fluid Dyn 45(4):591–598
- Kelleher MD, Flentie DL, McKee RJ (1980) An experimental study of the secondary flow in a curved rectangular channel. Trans J Fluids Eng 102:92–96
- Khandekar S, Agarwal G, Moharana MK (2010) Thermo-hydrodynamics of developing flow in a rectangular mini-channel array. In: Proceedings of 9th international and 20th national ISHMT-ASME heat and mass transfer conference, pp 1342–1349
- Kim BJ, Liu YZ, Sung HJ (2004) Micro PIV measurement of two-fluid flow with different refraction indices. Measur Sci Technol 15(6):1097–1103
- Koshizuka S, Nobe A, Oka Y (1998) Numerical analysis of breaking waves using the moving particle semi-implicit method. Int J Numer Methods Fluids 26(7):751–769
- Kuznetzov VV, Shamirzaev AS, Ershov IN (2005) Motion of gas shells in small size rectangular channels. In: Proceedings of XXVIII Siberian thermophyasical seminar, IT SB RAS, Novosibirsk, pp 145–149
- Lauga E, Brenner MP, Stone HA (2005) Microfluidics: the no-slip boundary condition. In: Foss J, Tropea C, Yarin A (eds) Handbook of experimental fluid dynamics, Ch 15, Springer, New York
- Leonard BP (1979) A stable and accurate convective modeling procedure based on quadratic upstream interpolation. Comput Methods Appl Mech Eng 19:59–98
- Lin YC, Chung YC, Wu CY (2007) Mixing enhancement of the passive microfluidic mixer with J-shaped baffles in the tee channel. Biomed Microdevices 9:215–221
- Liu GR, Liu MB (2003) Smoothed particle hydrodynamics: a meshfree particle method. World Scientific, Singapore
- Mansur EA, Mingxing YE, Yundong W, Youyuan D (2008) A state-of-the-art review of mixing in microfluidic mixers. Chin J Chem Eng 16(4):503–516
- Marchuk GI (1990) Splitting and alternating direction methods. Handbook of numerical analysis, vol 1. Elsevier, Amsterdam, pp 197–462
- Martin JC, Moyce WJ (1952) An experimental study of the collapse of a liquid column on a rigid horizontal plane. Philos Trans Roy Soc Lond 244:312–324
- Menter FR (1993) Zonal two equation k-w turbulence models for aerodynamic flows. AIAA Paper 93-2906-2917
- Minakov AV, Gavrilov AA, Dekterev AA (2008) Numerical algorithm for solving space hydrodynamical problems with moving hard bodies and free surface. Siberian J Ind Math 4 (36):94–104
- Minakov AV, Rudyak VY, Gavrilov AA, Dekterev AA (2010) On optimization of mixing process of liquids in microchannels. J Siberian Fed Univ Math Phys 3(2):146–156
- Minakov AV, Rudyak VY, Gavrilov AA, Dekterev AA (2012) Mixing in a T-shaped micromixer at moderate Reynolds numbers. Thermophys Aeromech 19(3):385–395
- Minakov A, Rudyak V, Yagodnitsina A, Bilsky A (2013a) Micro-LIF and numerical investigation of mixing in microchannel. J. Siberian Fed Univ Eng Technol 1(6):15–27
- Minakov A, Rudyak V, Dekterev A, Gavrilov A (2013b) Investigation of slip boundary conditions in the T-shaped microchannel. Int J Heat Fluid Flow 43:161–169

- Minakov A, Yagodnitsina A, Lobasov A, Rudyak V, Bilsky A (2013c) Study of fluid flow in micromixer with symmetrical and asymmetrical inlet conditions. La Houille Blanche 5:12–21
- Monaghan JJ (1994) Simulation of free surface flows with SPH. J Comput Phys 110:399-406
- Monaghan JJ (2005) Smoothed particle hydrodynamics. Rep Prog Phys 68:1703-1759
- Morris JP (1997) Modeling low Reynolds number incompressible flows using SPH. J Comput Phys 136:214–226
- Ou J, Perot B, Rothstein P (2004) Laminar drag reduction in microchannels using ultrahydrophobic surfaces. Phys Fluids 16:4635–4643
- Podryabinkin EV, Rudyak VY (2011) Moment and forces exerted on the inner cylinder in eccentric annual flow. J Eng Thermophys 20(3):320–328
- Quin D, Lawal A (2006) Numerical study on gas and liquid slugs for Taylor flow in a T-junction microchannel. Chem Eng Sci 61(23):7609–7625
- Reid RC, Prausnitz JM, Sherwood TK (1977) The properties of gases and liquids. McGraw-Hill Company, New York
- Rudyak VY, Minakov AV, Gavrilov AA, Dekterev AA (2008) Application of new numerical algorithm of solving the Navier-Stokes equations for modeling the work of a viscometer of the physical pendulum type. Thermophys Aeromech 15(2):333–345
- Rudyak VY, Minakov AV, Gavrilov AA, Dekterev AA (2010) Modeling the flows in micromixers. Thermophys Aeromech 17(4):45–56
- Stroock AD, Dertinger SK, Whitesides GM, Ajdari A (2002) Patterning flows using grooved surfaces. Anal Chem 74(20):5306–5312
- Tabeling P (2005) Introduction to mivrofluidics. Oxford University Press, Oxford
- Telib H, Manhart M, Iollo A (2004) Analysis and low-order modeling of the inhomogeneous transitional flow inside a T-mixer. Phys Fluids 16:2717–2731
- Tzvetkov FF, Grigoriev BA (2005) Heat and mass transfer. MEI, Moskow
- Vanka SP, Luo G, Winkler CM (2004) Numerical study of scalar mixing in curved channels at low Reynolds number. AIChE J 50:2359–2368
- Wang Y, Su T-C (1993) Computation of wave breaking on sloping beach by VOF method. In: Proceedings of the 3rd international offshore and polar engineering conference (ISOPE). Golden, CO, pp 96–101
- Wing TL, Rajan KM (2004) Flow measurements in microchannels using MicroPiIV system. In: Behnia M, Lin W, McBain GD (eds) Proceedings of the 15th Australasian fluid mechanics conference (CD-ROM), University of Sydney, Australia. Paper AFMC00150
- Wong SH, Ward MCL, Wharton CW (2004) Micro T-mixer as a rapid mixing micromixer. Sens Act B 100:359–379
- Xu B, Wong TN, Nguyen N-T, Che Z, Chai JKC (2010) Thermal mixing of two miscible fluids in a T-shaped microchannel. Biomicrofluidics. https://doi.org/10.1063/1.3496359
- Zaleski S, Li J, Succi S (1995) Two-dimensional Navier-Stokes simulation of deformation and breakup of liquid patches. Phys Rev Lett 75(2):244–247

Chapter 5 Modeling of Nanoflows



Abstract By definition, nanoflows are flows in channels with a characteristic size (height of a plane channel or diameter of a cylindrical channel) smaller than (or equal to) one hundred nanometers. Depending on the cross-sectional configuration, nanochannels are usually classified as follows. A plane channel is a 2D channel and has only one nanosize (distance between the plates); it is also called a nanoslit. There are also cylindrical nanochannels (1D). Short cylindrical nanochannels are often called nanopores. These flows have been studied for about forty years. However, up to now, there were no algorithms that would permit us to model real nanoflows. In addition, in recent years, many new problems have appeared in this area. To solve these problems, we need correspondent techniques. In this chapter, we propose new molecular dynamics algorithms, which allow one to simulate a real plane Poiseuille-type flow characterized by a certain pressure gradient, and discuss specific features of plane flows in nanochannels. This is the subject of the first four sections of the chapter. In Sects. 5.5 and 5.6, the self-diffusion of the fluid molecules in nanochannel and in porous media is studied. Finally, the last section deals with modeling the separation of nanofluids through the use of nanomembranes.

5.1 Molecular Dynamics Simulation of a Channel Flow Generated by an External Force

Interest in nanoflows first appeared back in the 1980s. It was primarily inspired by the development of increasingly compact and effective devices for various biochemical analyses. However, beginning from the 1990s, this topic was diversified. More applications appeared, including those in the fields of medicine, pharmacology, biology, catalysis, etc. This is related not only to the development of nanotechnologies for various purposes, but also to more detailed investigations in fairly traditional fields: biology, geophysics, thermal engineering, etc. There are also intense investigations aimed at creating various nanoporous materials, including nanoceramics. Typical pore sizes in carrier formations vary from tens of nanometers to tens or even hundreds of microns (Nelson 2009). Thus, nanoflows are involved here as well.

Nanochannels, in particular, are used as nanosensors for recognition of DNA and other complex molecules. Nanofilters used for separation of molecules and nanoparticles or as electro-osmotic pumps consist of a tremendous number of long nanochannels. Long nanochannels are also used for fabrication of nanowires, electrodes for supercapacitors, etc. Certainly, in addition to very high applied significance, the interest in flows in nanochannels is also motivated by academic aspects, because new physical phenomena occur here and the transport processes are not described by the classical macroscopic theories.

A review of various methods of nanochannel fabrication can be found in the encyclopedia (Li 2008). There is a special class of nanochannel called carbon nanotubes fabricated by graphene rolling. Their diameter is on the order of several nanometers. Carbon nanotubes have unique properties: high strength, high thermal conductivity (which exceeds that of metals by an order or even several orders of magnitude), high electrical conductivity, etc.

As was already mentioned, the conventional hydrodynamic approach cannot be applied for modeling gas and liquid flows in sufficiently small channels. Actually, the only method that raises no conceptual objections is the method of molecular dynamics (MD). This method has been actively applied for studying microflow properties since the 1980s (see, e.g., Karnidakis et al. 2005 and references therein), and many interesting results have been obtained. The main objects of simulation have been nanoscopic analogs of the known Couette and Poiseuille flows.

The Couette flow is usually modeled by a cell bounded by plates moving in opposite directions. Fluid molecules are located between them. Velocity profiles and other characteristics of the flow were obtained for this system (see, e.g., Thompson and Robbins 1990). In reference to the correspondence between the Couette flow and real flows of this kind, it should be borne in mind that shear velocities in MD simulations exceed realistically achievable values by a factor of hundreds, which is caused by the limited performance of modern computers. In other aspects, MD simulations of this flow are consistent with the real Couette flow.

At the same time, a certain fictitious force is introduced in MD simulations for generation of the Poiseuille flow (see, e.g., Koplik et al. 1989; Heinbuch and Fischer 1989; Thompson and Robbins 1990; Karnidakis et al. 2005 and references therein). This force is often called the gravity force, but it is greater than the latter by orders of magnitude. On the other hand, the presence of a permanently acting force leads to molecule acceleration, which is absent in nature; therefore, various methods for correcting their velocities, such as the so-called thermostat and others (see, e.g., Heinbuch and Fischer 1989; Karnidakis et al. 2005), should be used. Because of the use of such artificial procedures, the real flow arising in a channel under the action of a pressure difference cannot be adequately modeled.

Obviously, MD simulations of fluid flows are rather complicated. Molecules are in the state of random thermal motion with fairly high velocities. The problem is to make all molecules move along the channel with a prescribed hydrodynamic velocity, which is usually smaller than the thermal velocity. In typical macroscopic fluid flows in tubes and channels, this velocity reaches several meters or several tens of meters per second, which is smaller than the thermal velocity by at least an order

of magnitude. The real velocity in microchannels cannot exceed several centimeters per second, and the velocity in nanochannels is even smaller by several orders of magnitude. Thus, to simulate such a flow, it is insufficient to organize directed macroscopically observed motion of molecules on the background of their thermal motion. The velocity of this organized motion should be smaller than the thermal velocity by many orders of magnitude. In the absence of Maxwell's demon, there are two obvious solutions to this problem. The first one is to control the velocities of all molecules at each step of the algorithm. This is an extremely complicated procedure. It can be implemented in principle for a system of hard spheres with only binary collisions. It cannot be implemented for real potential, because the problem for three bodies is not integrable, and it is impossible to recalculate the velocities correctly.

The second solution is to introduce a certain mass force \mathbf{F}_e that would make molecules move in a necessary direction. In this case, we have

$$m_i \frac{d^2 \mathbf{r}_i}{dt^2} = \mathbf{F}_i + \mathbf{F}_e, \quad i = 1, 2, \dots, N,$$
 (5.1)

where N molecules considered here include n molecules of the fluid and (N-n) molecules of the channel walls. In this case, the channel walls are modeled by several layers of the wall material packed in this or that way (body-centered lattice, face-centered lattice, etc.).

This algorithm was developed more than 20 years ago (see, e.g., Koplik et al. 1988, 1989, 1996; Heinbuch and Fischer 1989; Bitsanis et al. 1990 and references therein). This force is often called the gravity force, but it is greater than the latter by orders of magnitude. Thus, e.g., in (Koplik et al. 1988; Heinbuch and Fischer 1989), the acceleration acquired by the molecule at each step is $g = 0.1\varepsilon/(m\sigma)$, which is easily seen to be greater than the freefall acceleration by many orders of magnitude. The thus-generated flow velocities are many times greater than those observed in practice. This drawback was obvious to researchers who used this algorithm. Thus, it was noted (Heinbuch and Fischer 1989) that it would be useful to make the driving force more realistic, i.e., substantially smaller; in this case, however, the flow becomes indiscernible on the background of thermal noise. It was also shown there that the flow characteristics in a nanochannel change as the external force decreases.

On the other hand, the presence of a permanently acting force gives rise to acceleration of molecules, which is absent in nature; therefore, various methods for correcting these velocities should be used. In particular, this is done by using various methods of temperature correction (Heinbuch and Fischer 1989). Sometimes this is done with the use of the Nose-Hoover thermostat described in Chap. 1. In all cases, simulated flows are fairly sensitive to all described technologies. Because of the use of such artificial procedures, the real flow arising in a channel under the action of a pressure or flow rate difference cannot be adequately modeled.

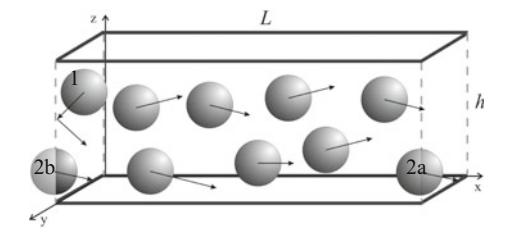
5.2 Algorithm of Modeling a Plane Nanoflow Under Pseudo-periodic Conditions

An algorithm that does not involve an external force for flow generation was proposed in (Rudyak et al. 2008a, 2010). A plane flow (along the x axis, see Fig. 5.1) of a molecular fluid in a channel of length L between two parallel plates separated by a distance h is considered. The modeling cell is a rectangular parallelepiped whose lower and upper faces (perpendicular to the z axis) are channel walls. The cell size in the y direction is $b \ge h$, and usual periodic boundary conditions are applied in this direction.

To organize the fluid flow, a special algorithm was developed, which involves the use of specially modified periodic boundary conditions on the left and right faces of the cell (perpendicular to the x axis). Molecules located inside the channel cannot cross the left face of the cell (e.g., molecule 1 in Fig. 5.1), and interaction with this molecule is defined by specular or diffuse boundary conditions (see below). Molecules can cross the right face; for a molecule crossing the right boundary (e.g., molecule 2a in Fig. 5.1), a copy on the left boundary is created (molecule 2b in Fig. 5.1). The x coordinates of the centers of the molecule and its copy differ by L, whereas other coordinates and velocities of these molecules are identical. In solving the equations of motion of such a molecule, its interaction with molecules both on the left boundary and the right boundary is taken into account, which corresponds to periodic boundary conditions. When the molecule crosses the right face of the cell and leaves the channel, its copy at the left boundary remains. The velocity of this molecule is randomly sampled in accordance with the Maxwell distribution (1.54), (1.55). The projection of the molecule velocity onto the x axis is always set to be positive. Thus, the left boundary of the channel can be considered as a source of molecules whose velocities are distributed in accordance with Eq. (1.54). The total number of molecules in the cell in this algorithm is unchanged, which is convenient for its program implementation.

Interaction of fluid molecules can be described by the Lennard-Jones (LJ) potential (1.53) and the hard sphere (HS) potential (1.52). Interaction of fluid molecules with the wall is defined by two different methods, depending on the type of intermolecular potential used. In the first case (LJ potential), each wall is modeled by two (or more) rows of molecules located in nodes of a certain lattice. Interaction of fluid molecules with wall molecules is defined by potential (1.53),

Fig. 5.1 Modeling of the flow in a plane channel with pseudo-periodic boundary conditions



whose parameters are determined from combinatorial relations. The simplest relations are most often used in practice: $\sigma_{12} = \sqrt{\sigma_{11}\sigma_{22}}$ and $\varepsilon_{12} = \sqrt{\varepsilon_{11}\varepsilon_{22}}$, where σ_{11} and ε_{11} are the parameters of interaction of fluid molecules, while σ_{22} and ε_{22} are the parameters of interaction of wall molecules.

For a fluid with the HS potential, the upper and lower walls of the channel are modeled by two parallel solid surfaces. Interaction of fluid molecules with the walls occurs instantaneously; their post-collision velocities are determined by the specular, diffuse, or specular-diffuse law. In the case of specular reflection, the molecule changes the sign of the velocity projection onto the normal to the wall v_z , whereas the projections v_x and v_y remain unchanged. In the case of diffuse reflection, the molecule velocity components are sampled in accordance with Eq. (1.54) with a corresponding temperature. Finally, in the case of specular-diffuse reflection, a fraction θ of molecules interacts in a diffuse manner and the fraction $(1-\theta)$ of molecules interacts in a specular manner. It should be noted that specular boundary conditions correspond to a zero value of the momentum accommodation coefficient of the wall θ , whereas the accommodation coefficient of diffuse walls is equal to unity.

At the initial time, fluid molecules are uniformly arranged in the simulation cell. Their density is determined by the van der Waals parameter $\varepsilon_V = nd^3$ for the HS fluid and $\varepsilon_V = n\sigma^3$ for the LJ fluid, where n is the number density of molecules. The molecule velocities at the initial time are defined in accordance with the Maxwell distribution (1.54). Then, the system's evolution was calculated. When the relaxation processes are finalized (the relaxation time depends on the channel size, fluid density, and conditions of interaction with the wall), a steady fluid flow is formed in the channel. After that, required characteristics (concentration, velocity, pressure, etc.) are calculated.

The described MD algorithm allowed for a flow with a pressure gradient along the channel (analog of a steady Poiseuille flow) to be simulated for the first time. Results of these simulations will be partly described in Sect. 5.4. It should, however, be noted here that this algorithm is not devoid of drawbacks either. The main problem is that the pressure gradient cannot be prescribed directly, though it can be predicted with sufficient accuracy on the basis of the known channel size and properties of the fluid and the wall. One more drawback is the non-physical long-range interaction of molecules located at the channel exit with molecules at the channel entrance. This effect is not very dramatic, because it occurs only in narrow relaxation regions (actually, the flow with a pressure gradient occurs at the exit of these regions).

5.3 Algorithm of Modeling a Plane Nanoflow with a Prescribed Flow Rate

One of the main drawbacks of the algorithm described in the previous section is the fact that the parameters of the flow being formed are determined not only by the fluid density and temperature, but also by the channel geometry. For this reason, it

is difficult to form a flow with a prescribed flow rate. Below, we propose an MD algorithm that allows one to simulate a real plane Poiseuille-type flow characterized by a certain pressure gradient and a prescribed flow rate.

We again consider a plane fluid flow between infinite parallel walls. As in the previous section, the walls are modeled by several rows of densely packed molecules. Interaction of fluid molecules with each other and with wall molecules is defined by a certain potential, e.g., the Lennard-Jones potential (1.53). The computational cell is shown in Fig. 5.2. It consists of four zones. At the channel entrance, there is a zero zone of length L_0 , through which molecules are inserted. With a certain periodicity determined by the fluid flow rate Q, a layer of densely packed molecules is formed here; these molecules move to the right with a constant velocity u (molecules with velocity vectors in Fig. 5.2). Let us call them "heavy" molecules. In fact, these molecules move as solid bodies. Molecules located in the channel cannot pass through densely packed layers of "heavy" molecules, thus pushing the remaining molecules to the right. We may say that a layer of densely packed "heavy" molecules plays the role of a piston forming the flow in the channel.

After the transition from the zero to the first zone (zone of length L_1 in Fig. 5.2), "heavy" molecules transform into usual molecules and are assigned new velocities at the instant of this transition, which are generated on the basis of the Maxwell distribution function (1.54) for a given temperature T. Thus, the temperature T is maintained in this zone. The temperature in zones 1 and 3 (zone of length L_3 in Fig. 5.2) is maintained through a special procedure of regularization of molecule velocities. In fact, it is similar to the Nose-Hoover thermostat. By using the latter in the zone where such regularization is performed, the total kinetic energy is calculated as

$$\widetilde{E}_K = \sum_i \frac{m_i v_i^2}{2}.$$

On the other hand, the kinetic energy corresponding to a given temperature T is determined by the expression $E_K = (3kT/2)$. Thus, for the fluid temperature in this

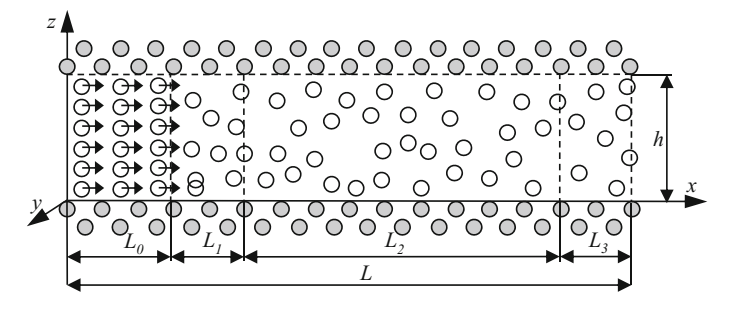


Fig. 5.2 Computational cell for modeling the flow with a prescribed flow rate

zone to be equal to the prescribed temperature, the velocities of all molecules located here are multiplied by the coefficient $k_{\nu} = \sqrt{E_K/\widetilde{E}_K}$. However, the above-described procedure is valid only for the absence of the flow. In the presence of the flow, the kinetic energy of molecules is determined by the relation

$$\widetilde{E}_K = \sum_i \frac{m_i (\overline{\nu}_i - \overline{u})^2}{2},\tag{5.2}$$

where \bar{u} is the flow velocity, which is not known in advance. If formula (5.2) has to be used directly for regularization of molecule velocities, the hydrodynamic velocity of the flow inevitably changes. To avoid this effect, only velocity components normal to the flow direction are recalculated. By virtue of the uniform distribution of the molecule energy over its degrees of freedom, the kinetic energy for two velocity components normal to the flow direction has the form

$$E_K^* = \sum_i \frac{m_i \left(v_{iy}^2 + v_{iz}^2\right)}{2}.$$

The coefficient of molecule velocity recalculation is defined as

$$k_{v} = \sqrt{\frac{E_{Ky} + E_{Kz}}{E_{K}^{*}}} = \sqrt{\frac{2kT}{\sum_{i} m_{i} \left(v_{iy}^{2} + v_{iz}^{2}\right)}}.$$

To generate a flow with a prescribed flow rate, it is necessary to control the fluid density in addition to the flow velocity. For this purpose, the density in the third zone is also kept constant. At each step of integration, the density $\rho = n\sigma^3$ of molecules located in this zone is calculated. If this density is higher than a prescribed value ρ_C , then molecules crossing the right boundary of the channel leave the channel (i.e., are not taken into account in further calculations). Otherwise, molecules crossing the right boundary are reflected from this boundary in a specular manner (v_x changes its sign), and the x coordinate is assigned a value equal to the right wall coordinate. In the second zone, molecules move freely, and no regularization procedures are applied (zone of length L_2 in Fig. 5.2). It is this zone that should be considered as the modeled channel. Thus, the channel length is L_2 .

5.4 Specific Features of Nanoflows in MD Simulations

In this section, the results of modeling a pure argon nanoflow at a temperature T = 300 K are described. The flow is modeled by the algorithm described in Sect. 5.2. The channel height is varied from 6σ to 50σ of the effective diameters of molecules,

the length is varied from 60σ to 250σ , and the width is varied from 6σ to 20σ . Thus, the longest channel is only slightly longer than 70 nm, and its height is varied from 2 to 15 nm. The fluid density is varied within fairly wide limits: $\varepsilon_V = n\sigma^3 = 0.0014 \div 0.88$. Typical features of nanoflows are discussed below.

5.4.1 Flow Velocity Profile

A steady flow is formed in zone 2 (see Fig. 5.2). If the algorithm with pseudo-periodic boundary conditions is used (Sect. 5.2), it is formed at a certain distance from the entrance (left boundary of the channel shown in Fig. 5.1). The flow velocity profile is caused by interaction of fluid molecules with the wall. For the LJ fluid, a parabolic velocity profile is formed, and there is slipping on the wall in all cases. Thus, the velocity profile has the form

$$u = A(z^2 - zh - bh),$$
 (5.3)

where A is a constant and b is the so-called slip length determined by the relation $u(z=0,h)=b(\partial u/\partial z)|_{z=0,h}$. It should also be mentioned that the velocity profile in sufficiently narrow channels at high flow velocities becomes considerably distorted and is no longer parabolic. In fact, the fluid is structured at such a level that each of its layers with the characteristic size on the order of a molecule flows with its own velocity (see Travis et al. 1998; Travis and Gubbins 2000). This effect is less pronounced at low velocities of the flow.

The slip effect was detected previously in almost all activities aimed at MD simulations of the LJ fluid. In the HS fluid flow, a parabolic velocity profile of the form (5.3) is observed only if interaction of molecules with the wall is not specular. In the case of specular reflection, a shock velocity profile is formed over the entire channel length.

In real macroscopic fluid flows, it is usually assumed that the fluid sticks to the wall, i.e., the flow velocity on the wall is equal to the velocity of the wall itself. Slipping is observed for rarefied gas flows only. In this case, we have $b \sim l \sim Kn$, where l is the mean free path of the molecule. Thus, it is usually assumed that slipping should be taken into account beginning from Knudsen numbers $Kn \sim 5 \times 10^{-3}$. As the slip length is proportional to l, it can be neglected in macroscopic flows if the gas is not too rarefied. The error at low Knudsen numbers is small.

The nature of slipping in liquid flows is more complicated that than in gas flows. For gases, a systematic theory determining the slip length was developed; however, there is no corresponding analog for liquids. Nevertheless, the slip length in microflows has been intensely studied in experiments in recent years. As was already noted (see Chap. 4), slip lengths from several nanometers to approximately twenty micrometers are registered (Lauga et al. 2007). The slip length can be even

greater if hydrophobic and especially so-called ultrahydrophobic coatings are used (Watts et al. 1990; Ou et al. 2004). Clearly, such large values (and also small values on the order of several nanometers) of the slip length cannot be explained on the basis of the kinetic theory. A review of available experimental data can be found in publications mentioned above and in Karnidakis et al. (2005), where a list of models proposed for explaining the observed phenomenon is also given (see also Vinogradova 1995; Alexeyev and Vinogradova 1996; Andrienko et al. 2003; Fan and Vinogradova 2005; Vinogradova and Yakubov 2006).

In modeling the LJ fluid by the above-described algorithms, the velocity profile of the steady flow is determined only by the parameters of the potential of fluid interaction with wall molecules. In calculations, the slip length decreased with an increase in the fluid density. In the general case, however, the character of interaction of fluid molecules with the wall and, hence, the slip length depend on the type of crystal lattice of the solid surfaces forming the channel. In particular, it was found (Soong et al. 2007) that the slip length is affected by the type of packing of molecules in the channel walls and the angle of orientation of the fluid flow with respect to the bases of the crystal lattice forming the wall. Thus, by changing the wall topology, it is possible to control the resistance to fluid motion in the nanochannel.

The slip length for the HS fluid flow primarily depends on the accommodation coefficient θ and decreases with an increase in the accommodation coefficient. Thus, the slip length for $\theta=0.5$ is 1.7d (the fluid density is $\varepsilon_V=0.88$); as θ increases up to unity, the slip length decreases by more than a factor of 3 and reaches the value of 0.5d. Naturally, the slip length in the general case increases with a decrease in the fluid density. For instance, for the fluid density $\varepsilon_V=0.0014$, its value is about 10d.

The slip lengths predicted by MD computations are appreciably smaller than those actually observed in experiments, in which the values of tens and even hundreds of nanometers were detected. What is the reason for these large values of the slip length? If we ignore possible "imperfections" of the real fluid, e.g., its saturation with the gas, which produces the effect of "gas lubrication" in some cases, the most realistic reason is the presence of roughness elements on the wall surface. The height of roughness elements on a solid surface is usually several nanometers and more. Naturally, the character of fluid interaction with the wall is changed by the presence of roughness. The study of this issue is one of the most urgent problems of microflow physics. However, the slip length is usually greater than the roughness height.

5.4.2 Decrease in Pressure

A usual steady Poiseuille flow is a flow formed at a prescribed pressure gradient and, as a consequence, prescribed values of input and output pressures. The decrease in pressure along the channel is caused by friction on the walls. The algorithms described in two previous sections allow one to study nanoflows with a

linear gradient of pressure along the channel. The pressure is usually determined on the basis of the virial theorem, which implies that

$$p = \frac{2}{3V} \sum_{i=1}^{N} \frac{\langle \mathbf{p}_{i}^{2} \rangle}{2m} + \frac{1}{6V} \sum_{i=1}^{N} \sum_{j \neq i}^{N} \langle \mathbf{r}_{ij} \cdot \mathbf{F}_{ij} \rangle.$$

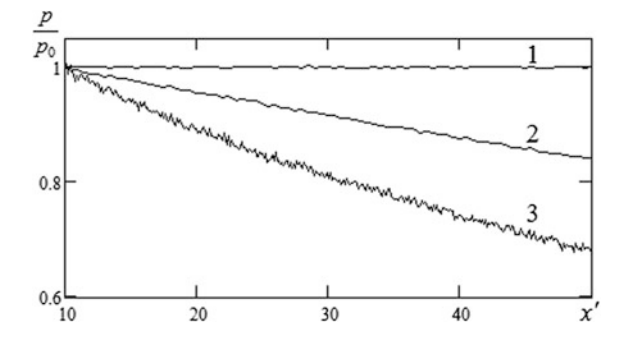
For the HS fluid, the interaction potential and the force \mathbf{F}_{ij} are singular, the virial of the force $\langle \mathbf{r}_{ij} \cdot \mathbf{F}_{ij} \rangle$ is defined by the momentum transferred in collisions, and the pressure is determined as

$$p = \frac{2}{3V} \sum_{i=1}^{N} \frac{\left\langle \mathbf{p}_{i}^{2} \right\rangle}{2m} + \frac{1}{6V} \sum_{i=1}^{N} \sum_{j \neq i}^{N} \left\langle r_{ij}^{*} \frac{\Delta p_{ij}}{\Delta t} \right\rangle.$$

Here, r_{ij}^* is the distance between the molecules (this distance is equal to the molecule diameter at the collision instant) and Δp_{ij} is the change in the absolute value of the momentum of the *i*-th molecule during the time Δt owing to its collision with the *j*-th molecule.

Figure 5.3 shows typical data for the decrease in pressure for different types of interaction of fluid molecules with each other and with the channel walls; the pressure is normalized to its value at the channel entrance p_0 (zone 2). Here, $x' = x/\sigma$. The decrease in pressure along the channel is related to the resistance induced by the interaction of fluid molecules with the wall. Therefore, the pressure in the case of specular reflection of molecules of the HS fluid remains unchanged along the channel (curve 1 in Fig. 5.3). The pressure gradient increases with increasing accommodation coefficient (cf. curves 1 and 2).

Fig. 5.3 Pressure versus the dimensionless streamwise coordinate of the channel. HS fluid, $\theta = 0$ (curve 1); HS fluid, $\theta = 0.5$ (curve 2); LJ fluid, (curve 3). $L = 60\sigma$, $h = 6\sigma$, and $\varepsilon_V = 0.79$



5.4.3 Resistance Coefficient

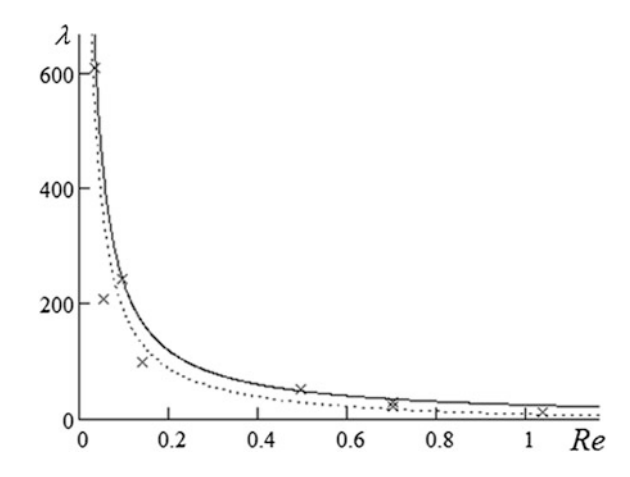
In practice, it is extremely important to find the differences between nanochannel flows and usual hydrodynamic flows. One of the most important characteristics is the hydraulic resistance coefficient determined by the formula

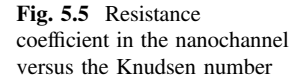
$$\lambda = h \frac{dp}{dx} \frac{2}{\rho \, \bar{u}^2}.$$

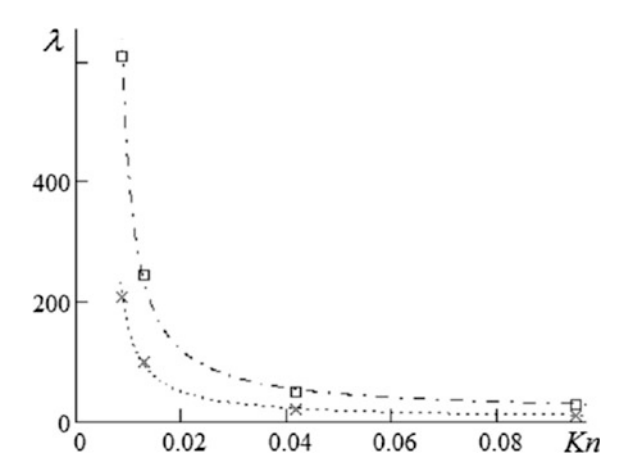
In the flow calculated by the MD algorithm with pseudo-periodic conditions (Sect. 5.2), the relationship between the pressure gradient and the flow rate is not known. Nevertheless, the friction coefficient predicted by MD computations was compared with the hydrodynamic resistance in Rudyak et al. (2011a). These comparisons were performed at identical pressure differences. The results of these comparisons are shown in Fig. 5.4. The solid curve is the hydrodynamic resistance coefficient $\lambda = 24/Re$, and MD predictions are represented by crosses. The dotted curve was obtained through the least squares method on the basis of MD data. Both curves are qualitatively similar, but the hydrodynamic values are slightly higher. It should be noted that these values were obtained for low Reynolds numbers. On the other hand, these Reynolds numbers are typical for nanoflows. It should also be mentioned that the Reynolds number in calculations based on MD data was obtained for the usual value of the viscosity coefficient corresponding to the fluid with a given density. However, the viscosity of the fluid in the nanochannel in the general case is appreciably different from its bulk viscosity (it is significantly higher). If this fact is taken into account, the differences in the resistance coefficients are more pronounced.

Figure 5.5 shows the resistance coefficient as a function of the Knudsen number for the HS fluid with different accommodation coefficients. The squares and crosses correspond to the accommodation coefficients $\theta = 1$ and $\theta = 0.5$, respectively. As

Fig. 5.4 Resistance coefficient in the nanochannel versus the Reynolds number. The solid and dotted curves show the hydrodynamic value and MD predictions, respectively







could have been expected, the resistance coefficient increases with increasing accommodation coefficient. It should be noted that the Reynolds number is a rough and, in a certain sense, more universal similarity parameter. Different Reynolds numbers correspond to different accommodation coefficients.

The algorithm described in Sect. 5.3 also allows for generation of the flow with a given flow rate. The specific flow rate is understood in this section as $Q = \rho u$, where u is the flow velocity, and the fluid density is determined by the formula $\rho_c = n\sigma^3$. Here again, n is the number concentration. The flow rate is measured in meters per second. The relationship between the pressure decrease along the channel and the flow rate is one of the key parameters in hydrodynamics. For Newtonian fluids, the decrease in pressure is a linear function of the flow rate. The same dependence was found for nanoflows in the course of MD simulations. The results simulated for channels of different heights are shown in Fig. 5.6. As the channel height increases, this dependence becomes less steep.

5.4.4 Compressibility of the Fluid in Nanochannels

It is known that the fluid dynamics of usual macroscopic and even microscopic flows is adequately described by the model of an incompressible fluid. However, this model should be used for nanoflows with caution. If there is a pressure decrease in an isothermal nanoflow, it is possible only if the fluid density also decreases along the channel. As the pressure of liquids and dense gases at a fixed temperature is a nonlinear function of density, comparatively large changes in pressure along the channel lead to comparatively small changes in density. This is the pattern observed in MD simulations of nanoflows. Figure 5.7 shows the behavior of pressure along the channel for an argon flow at the temperature T = 300 K in a channel with carbon walls for two values of density. The higher the fluid density, the greater the decrease

Fig. 5.6 Pressure gradient versus the flow rate in a channel of length $L = 60\sigma$; $h = 6\sigma$ (crosses), $h = 12\sigma$ (squares), and $h = 24\sigma$ (circles)

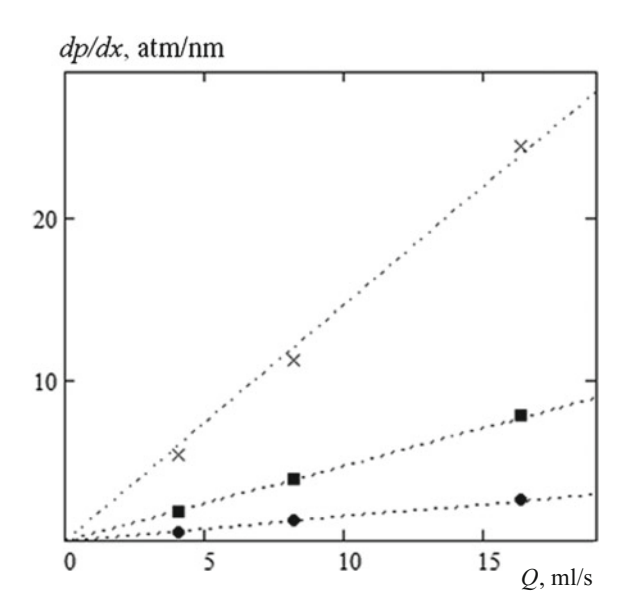
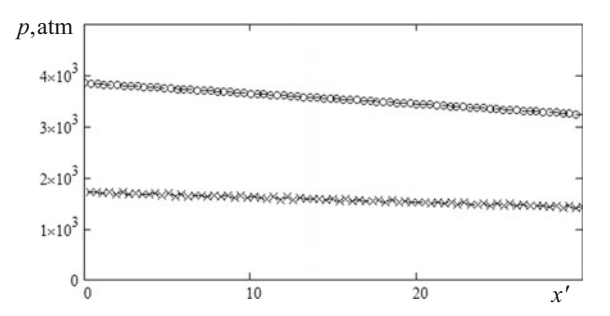


Fig. 5.7 Fluid pressure in the channel versus the streamwise coordinate, $\rho_C=0.6$ (crosses) and $\rho_C=0.8$ (circles)



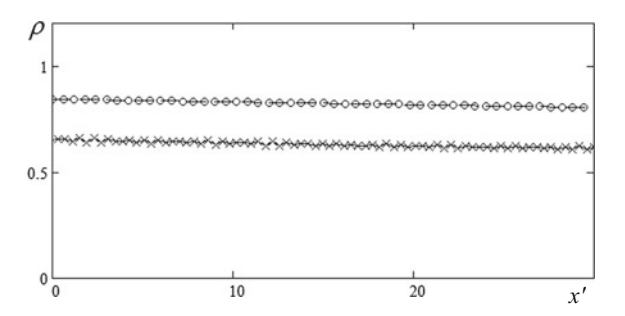
in pressure. The corresponding change in density along the channel is shown in Fig. 5.8 (the streamwise coordinate is measured in units of σ).

It is seen that the density decreases in both cases, but the decrease in density is appreciably smaller than the decrease in pressure. The density on the right boundary of the channel is equal to the prescribed density ρ_C .

5.4.5 Fluid Structure in a Plane Channel

Interaction of fluid molecules with the channel walls is a principally important factor of all nanoflows. For example, in a cylindrical nanochannel 5 nm in diameter, approximately one half of all molecules interact with the wall. Layers of fluid molecules are formed near the channel walls, almost simultaneously interacting

Fig. 5.8 Fluid density in the channel versus the streamwise coordinate, $\rho_C = 0.6$ (crosses) and $\rho_C = 0.8$ (circles)



with each other and with channel wall molecules. As the channel walls consist of molecules of a different nature as compared to fluid molecules, the structure of these near-wall layers of fluid molecules should differ from the structure of the bulk fluid. This is true. Figure 5.9 shows the profiles of the dimensionless density $\rho' = \rho/\bar{\rho}$ (where $\bar{\rho}$ is the mean density in the channel) of the HS and LJ fluids in a plane channel of height 6σ . Here, $z' = z/\sigma$. In both cases, the density exhibits quasi-periodic changes across the channel. In the HS fluid, the maximums and minimums of the density profile are more pronounced; the first peaks of density near the walls are also appreciably higher. This is primarily related to more expressed regions of screening for HS fluid molecules near the wall surfaces. Owing to the presence of these regions, the effective volume occupied by LJ molecules is greater than that occupied by HS molecules. For this reason, the effective density of the HS fluid is somewhat higher than that of the LJ fluid. As the density increases, the effects of fluid structuring become more pronounced.

It should be emphasized that the orderliness of the fluid near the walls is a typical feature of nanochannel flows, and it persists as the distance between the channel walls increases. This fact is illustrated in Fig. 5.10, which shows the density profiles

Fig. 5.9 Density profiles for the HS (plus) and LJ (crosses) fluids. $L=60\sigma$, $h=6\sigma$, and $\varepsilon_V=0.79$

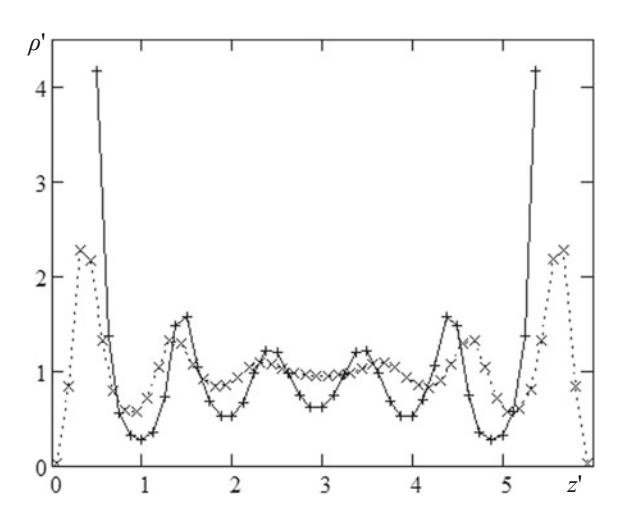
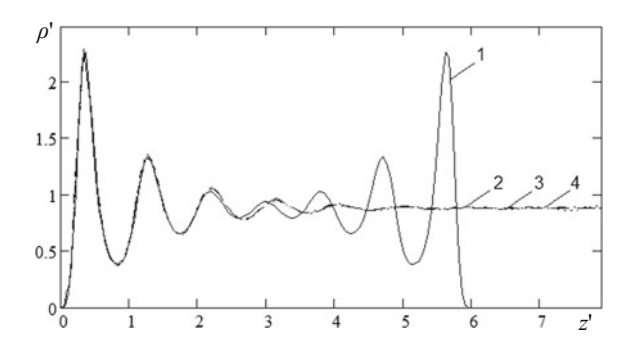


Fig. 5.10 Density profiles in nanochannels of different heights. $\varepsilon_V = 0.88$, $h = 6\sigma$ (1), $h = 12\sigma$ (2), $h = 24\sigma$ (3), and $h = 48\sigma$ (4)



across the channels of different heights: $h = 6\sigma$ (curve 1), $h = 12\sigma$ (2), $h = 24\sigma$ (3), and $h = 48\sigma$ (4). Structuring of the fluid in the channel becomes almost independent of the channel height at $h > 10\sigma$ and is observed at distances on the order of 5–6 σ , i.e., at distances on the order of two nanometers from the wall.

Intense oscillations of the density profile in the nanochannel are universal phenomena that are always observed regardless of the flow generation algorithm used (see, e.g., Zhu and Granick 2001, 2002). The density profile provides local information about the fluid structure. However, the analysis of Figs. 5.9 and 5.10 shows that the short-range order of the fluid in the channel becomes different.

At least, it should occur near the channel walls. The character of the fluid structure is detected by the paired radial distribution function of molecules

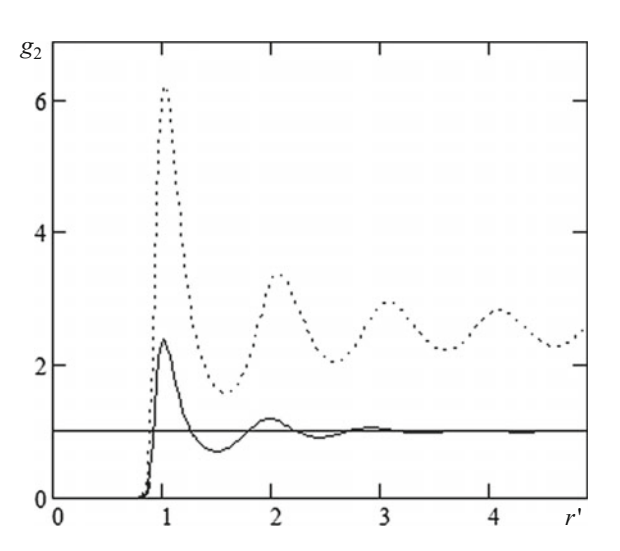
$$g_2(r) = \frac{dN}{4\pi n r^2 dr},\tag{5.4}$$

where dN is the number of molecules in the radial layer of thickness dr at a distance r from the chosen molecule. The radial distribution function (5.4) is a measure of the probability of finding the fluid molecule at a distance r from the chosen molecule. Thus, this function shows how the density of molecules is distributed around an arbitrarily chosen molecule. The density distribution in the nanochannel is not uniform; therefore, to obtain sufficiently objective information about the fluid structure, the radial distribution functions should be constructed in layers of thickness dh parallel to the channel walls and located at different distances from them:

$$g_2(r,h) = \frac{dN}{2\pi nr \, dr dh}.\tag{5.5}$$

The character of the resultant radial distribution function for the first peak of density (see Fig. 5.10) is shown in Fig. 5.11 (dotted curve). For comparison, the figure also shows the radial distribution function for the fluid of the same density in the bulk (solid curve). A comparison of these distribution functions shows that the character of the fluid structure near the surface is appreciably different. In the bulk,

Fig. 5.11 Radial distribution function in the bulk (solid curve) and in the layer of the first maximum of the fluid density in the nanochannel (dotted curve), $h = 6\sigma$, $\varepsilon_V = 0.88$, and $r' = r/\sigma$



the short-range order is manifested at distances on the order of 1 nm $(3\sigma-4\sigma)$; near the surface, however, a quasi-long-range order is actually observed. The radial distribution function decays at distances greater than those in the bulk by at least an order of magnitude.

Thus, there is a nanoscale layer of the fluid (one to several nanometers thick) near the surface, which possesses particular properties. Apparently, it is the presence of this layer that determines the slip length under ideal conditions. This layer plays the role of the Knudsen layer in a rarefied gas. The most important conclusion to be drawn is that the fluid in the nanochannel is not homogeneous. Its density near the walls and in the middle of the channel differs by several degrees. For this reason, the dynamic behavior of the fluid in the nanochannel is appreciably different from its behavior in the bulk.

5.5 Diffusion of Molecules in Nanochannels

Because of the change in the fluid structure in nanochannels and significantly different scales of their spatial sizes, the transport processes in such channels in the general case differ from those in the bulk. This is really so. The importance of studying the transport processes is obvious, because they are responsible for the character of microflows and especially nanoflows. At the same time, the possibility of investigating such flows is rather limited for several reasons. First, experimental studies of these processes are extremely difficult, or even impossible in some cases. Second, perturbations comparable with the measured characteristics can be (and are) inserted in the course of measurements. A similar situation occurs in quantum mechanics, in which a special theory of measurements was developed. Naturally,

specific methods for experimental data interpretation also have to be developed in studying the transport processes in micro- and nanoflows.

An alternative to experimental investigations of the transport processes in such flows is molecular modeling. The only comprehensive method of such modeling is the MD method. At the moment, this method has been successfully used for studying molecular diffusion in nanochannels and porous media, as well as the viscosity of simple fluids. The main results obtained in this field are described below.

Self-diffusion of molecules was studied in (Andryushchenko and Rudyak 2011; Rudyak et al. 2011b) for a system of hard spheres. Diffusion was considered in both plane and rectangular channels. The channel walls were modeled by solid surfaces, and interaction of fluid molecules with the walls was described by a specular, diffuse, or specular-diffuse law. The parameters varied in the simulations were the channel height h (along the z axis), channel width w (along the y axis), and fluid density. The channel height was varied from 2 to 50 nm, and the ratio h/w was varied from unity to infinity. In the latter case, the flow in a rectangular channel reduces to a plane flow. The fluid density nd^3 was also varied within wide limits, from 0.7 to 0.01, so that the low and upper limits corresponded to a liquid and a dense gas, respectively. Here, n is the number density of molecules in the system, and d is the molecule's diameter. The channel was aligned in the x direction so that an extended channel was simulated, and usual periodic boundary conditions were imposed on this axis.

The self-diffusion coefficient D is determined by the Green-Kubo formula

$$D = \frac{1}{3} \int_{0}^{\tau_{p}} \chi(t) dt, \tag{5.6}$$

where χ is the autocorrelation function of velocity (ACFV) of molecules, which is defined by the following relation ($\alpha = x, y, z$):

$$\chi_{\alpha}(t) = \frac{1}{Nl} \sum_{i=1}^{N} \sum_{j=0}^{l-1} \left[v_{i\alpha}(j\Delta t) \cdot v_{i\alpha}(j\Delta t + t) \right]. \tag{5.7}$$

Here, τ_p is the time needed for the ACFV to reach the so-called plateau value (Rudyak et al. 2008b), i.e., the time after which the diffusion coefficient remains almost unchanged, N is the number of particles in the cell, Δt is the integration step, and l is the number of independent phase trajectories over which the averaging is performed.

The self-diffusion coefficient was simultaneously determined by the Einstein relation for the root-mean-square displacement of molecules:

$$\langle R_d^2(t) \rangle = \frac{1}{Nl} \sum_{i=1}^N \sum_{j=0}^{l-1} \left[r_{id}(j\Delta t) - r_{id}(j\Delta t + t) \right]^2 = 2D_d t.$$
 (5.8)

As the behavior of the self-diffusion coefficient is determined by the ACFV relaxation character, it is first necessary to study the ACFV behavior in the nanochannel, as compared to its behavior in the bulk. Relaxation of the ACFV of dense fluids occurs in two stages: exponential decay is observed at the first stage and power-law relaxation takes place at the second stage (Rudyak et al. 2008b). It is only in the dense fluid that a negative tail of the ACFV is observed due to the formation of the short-range order. The ACFV in the nanochannel becomes nonisotropic.

A typical pattern of ACFV evolution for a rectangular channel is shown in Fig. 5.12. Here, the channel height is h = 5d, the channel width is w = 10d, and the fluid density is $nd^3 = 0.047$. The ACFV based on the components of molecule velocities along the channel behaves in the same manner as that in the bulk, whereas two other dependences have a valley whose depth increases as the corresponding geometric size of the channel (height or width) decreases.

The emergence of the negative branch of the ACFV is caused by interaction of fluid molecules with the channel walls and testifies that, first, the diffusion of molecules in the nanochannel is nonisotropic and, second, the diffusion coefficients in the directions normal to the walls should be substantially smaller than the diffusion coefficient along the channel. To find the values of these coefficients, it is convenient to use the information about the behavior of the root-mean-square displacements of molecules (5.8) along and across the channel. For the system presented in Fig. 5.12, the corresponding data are plotted in Fig. 5.13. Two lower curves show that the values of the root-mean-square displacement normal to the

Fig. 5.12 Time evolution of the ACFV components; the time τ is measured in units of the mean free times of molecules

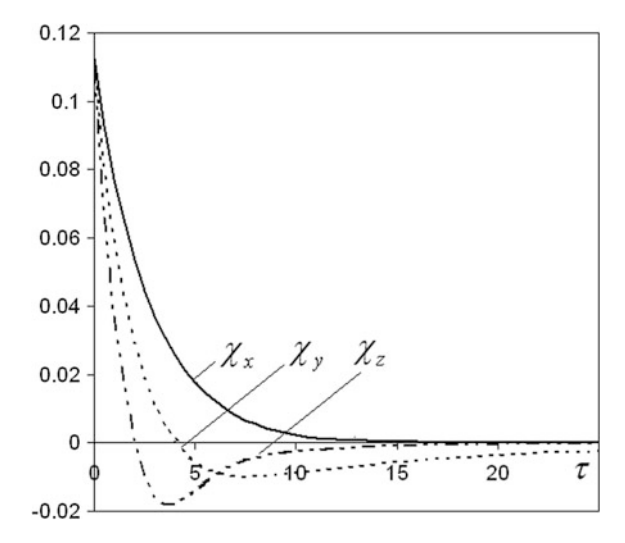
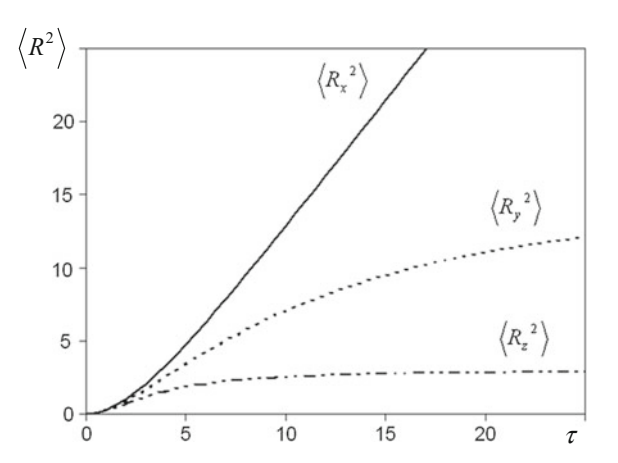


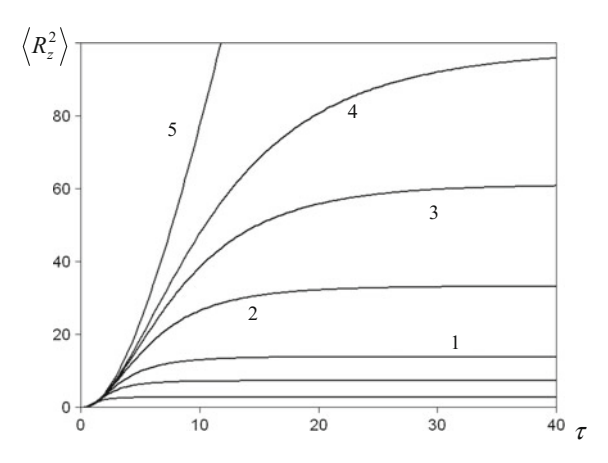
Fig. 5.13 Root-mean-square displacements of molecules in the x (periodic boundary conditions), y, and z directions versus time



channel wall gradually reach a certain constant value, which means zero values of the corresponding diffusion coefficients. The upper curve in Fig. 5.13 almost transforms into a straight line after a certain time, as was predicted by the Einstein theory, and the slope of this curve determines the diffusion coefficient along the channel. It turns out to be $D_b/3$, where D_b is the value of the self-diffusion coefficient in the bulk.

The observed character of the diffusion of fluid molecules is fairly natural from the physical viewpoint and takes place in nanochannels of almost all sizes. This is illustrated in Fig. 5.14, which shows the root-mean-square displacements across the channel for different channel heights. Two lower curves correspond to the channel heights 6d and 12d, and the numbered curves show the data for 18d (curve 1), 24d (2), 30d (3), 36d (4), and 48d (5).

Fig. 5.14 Root-mean square displacements of molecules along the *z* axis versus time



5.6 Self-diffusion of Molecules in Porous Media

The transport processes in micro- and nanochannels help in understanding the transport processes in porous media. The latter play an important role in everyday human life and various engineering processes. The most important examples of such processes are heat and mass transfer in living organisms, motion of moisture in soil, precipitation of impurities on filters of waste treatment facilities, acceleration of reactions by porous catalysts, motion of hydrocarbons in reservoirs, etc. Self-diffusion of fluid molecules is a key process here. It is widely used in practice for obtaining information about the structure of the porous space and its geometry (see, e.g., Kärger and Ruthven 1992; Latour et al. 1993; Cheng and Cory 1999; Song et al. 2000). The importance of self-diffusion has inspired the development of numerous methods for its measurement. The most popular methods are the method of nuclear magnetic resonance, optical methods including neutron radiation scattering, various methods of visualization, and methods using radioactive isotopes (see, e.g., Song et al. 2000). Both laboratory and full-scale experiments are usually performed in porous media with characteristic sizes ranging approximately from ten nanometers to hundreds of micrometers, due to specific features of available experimental techniques. Despite numerous investigations of diffusion in porous media over the last three decades, many issues remain unclear, including those of principal importance. Even the law of molecular diffusion in porous media is not yet clear, though the Einstein law is used in most applications for interpreting experimental data.

MD simulations of the self-diffusion of fluid molecules and investigations of its characteristics in a medium with a nanometer pore size were performed in (Andryushchenko and Rudyak 2011). The matrix porosity $\varphi = V_p/V$, where V_p is the pore volume and V is the total volume of the medium, was varied from 0.5 to 0.9, and the fluid density $n = V_f/V$ was varied from 0.07 to 0.565 (V_f is the volume of the fluid molecules). The characteristic pore size of the simulated medium in those studies varied from several nanometers to several hundreds of nanometers. Self-diffusion of molecules of a dense or moderately dense gas was considered in almost all cases. At the upper limit, the fluid density was close to the liquid density.

A typical porous medium is shown in Fig. 5.15 (left). It is usually simulated by a system of hard spheres (see Fig. 5.15, right). Therefore, the porous matrix in MD simulations was represented by cubic packing of spheres with an identical radius; the packing density and the grain size were varied.

The calculations were performed in a cell (pore) whose boundaries were subjected to periodic boundary conditions, i.e., an infinite porous medium was actually modeled; the cross-section of the simulated porous space is shown in Fig. 5.16. The fluid molecules were arranged in the pore of the simulation cell. Interaction of fluid molecules with each other is always elastic, whereas interaction of fluid molecules with the grain of the porous skeleton could be either elastic (specular) or inelastic (diffuse or specular-diffuse). Moreover, adsorption of fluid molecules on the walls of the porous skeleton could be also modeled.

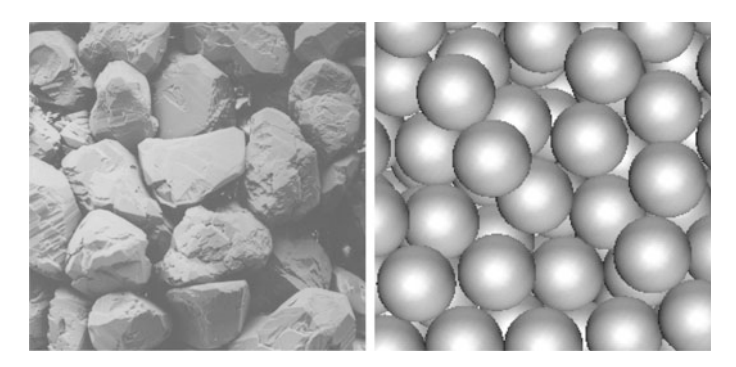
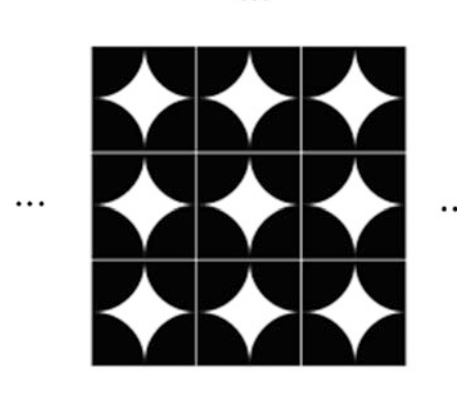


Fig. 5.15 Typical porous medium with large magnification (left) and its simulation by a system of hard spheres (right)

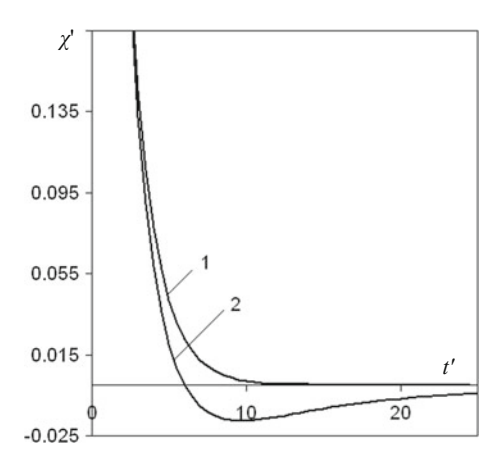
Fig. 5.16 Computational domain for MD simulations of transport processes in a porous medium



A typical shape of the ACFV normalized to the root-mean-square initial velocity $\chi' = \chi/< v^2(0) >$ for a fluid of density n = 0.0707 is shown in Fig. 5.17. In all computations, the ACFV had negative value, which corresponds to a typical valley (cf. Fig. 5.13.) whose depth and position depend on the fluid porosity, fluid density, and ratio of the fluid molecule size to the particle size in the porous medium. The emergence of this valley is caused by interaction of molecules with the solid matrix, similar to the situation in a channel. Significant changes in the ACFV of fluid molecules in the porous medium lead to smaller values of the diffusion coefficient, as compared to its bulk value. This is absolutely natural from the physical points of view; however, it is important to understand what these changes are and how they depend on the medium and fluid parameters.

One of the most important parameters determining diffusion in a porous medium is the ratio of the radius of the transported matter molecules r to the particle size of the porous matrix R. In fact, this ratio determines the characteristic pore size in the medium. The self-diffusion coefficient was calculated as a function of the parameter

Fig. 5.17 Autocorrelation function of velocity versus time (in units of the mean free time). Curves 1 and 2 show the results for bulk self-diffusion and self-diffusion in a porous medium, respectively



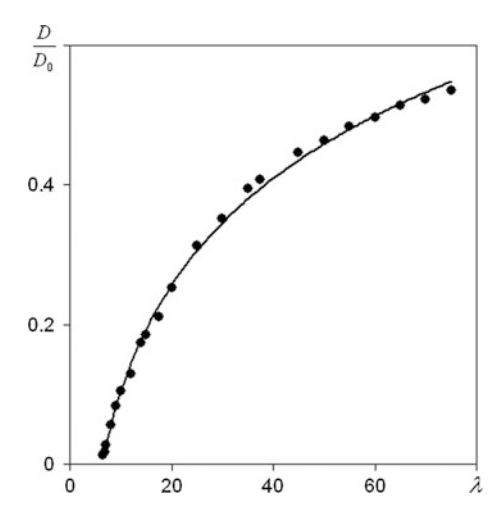
 $\lambda = R/r$ for different values of density, porosity, etc. In all cases, this dependence is accurately described by the function

$$D/D_0 = \alpha \ln \lambda + \beta, \tag{5.9}$$

where the coefficients α and β depend on the system parameters. Hereinafter, the diffusion coefficient is normalized to its bulk value D_0 . An example of the computation for the fluid of density n = 0.0707 is shown in Fig. 5.18.

The results of this computation are adequately approximated by the formula $D/D_0 = 0.22 \ln \lambda - 0.4$. The shape of function (5.9) and the values of the corresponding coefficients were determined from the condition of minimization of the root-mean-square deviation of the considered test function from data obtained in simulations. Dependences of the form (5.9) were also obtained previously in

Fig. 5.18 Normalized self-diffusion coefficient versus λ



experimental investigations. A similar dependence was obtained, e.g., in Kim (1998), in which the experiment was performed in pores with a characteristic size ranging from 50 to 600 µm. The characteristic pore size in the simulations of Andryushchenko and Rudyak (2011) was smaller by several orders of magnitude. Nevertheless, the experimental dependences for the self-diffusion coefficient (Kim 1998) are qualitatively consistent with Eq. (5.9), which apparently testifies to the more or less universal character of this formula.

The next important characteristic of the system is its porosity. The porosity φ of the medium formed by a pack of hard spheres is naturally related to the grain (sphere) radius in the pack. It can be easily seen that $\varphi = 1 - 4\pi n_p R^3/3$, where n_p is the density of the grain in the skeleton (number of particles in a unit volume). As the dependence of the diffusion coefficient on the grain radius is determined by Eq. (5.9), it is almost obvious that its dependence on the porosity is also determined by a logarithmic function. It is so indeed; the dependence of the diffusion coefficient on the skeleton's porosity is determined as $D/D_0 = \gamma \ln \varphi + 1$, where γ is a certain coefficient depending on the parameters of the considered system. In particular, for a fluid with n = 0.0707 and $\lambda = 25$, this dependence has the form

$$D/D_0 = 0.984 \ln \varphi + 1. \tag{5.10}$$

The corresponding data of MD simulations are plotted in Fig. 5.19, where the points are the computed results and the solid curve is their approximation with Eq. (5.10).

As in the bulk, the fluid self-diffusion coefficient significantly depends on the fluid density. The self-diffusion coefficient is a linear function of the Knudsen number Kn for different ratios of the radii and different values of porosity values. An example of such a dependence (for the porosity value $\varphi = 0.5$) for two different values of λ is given in Fig. 5.20.

Fig. 5.19 Normalized self-diffusion coefficient versus the medium porosity

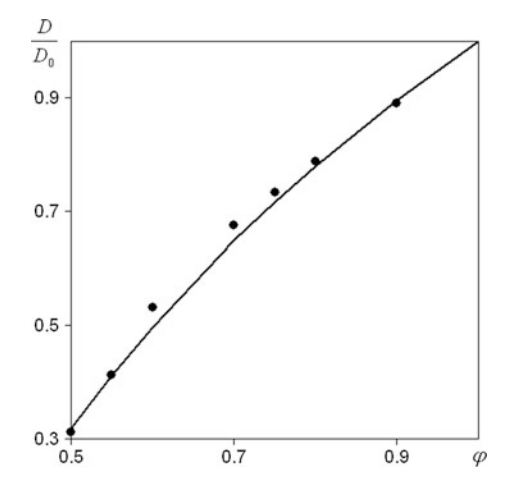
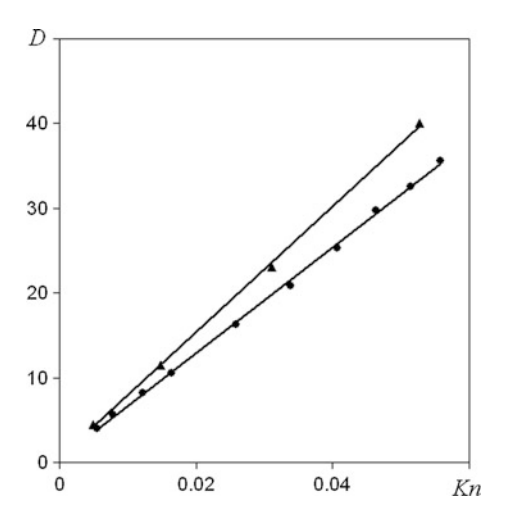


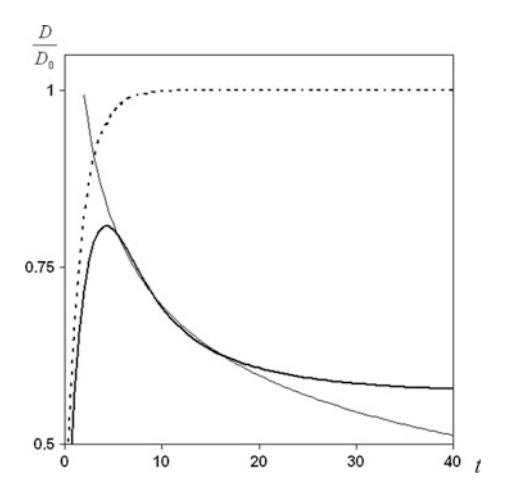
Fig. 5.20 Self-diffusion coefficient versus the Knudsen number. The triangles and circles show the results for $\lambda = 25$ and $\lambda = 30$, respectively



The Knudsen number of the considered system is determined here as the ratio of the molecule mean free path to the grain radius of the porous skeleton Kn = l/R. The behavior illustrated in Fig. 5.20 is typical for ideal gases; in this case, the linear dependence of D on Kn should correspond to an inversely proportional dependence of the self-diffusion coefficient on the fluid density. Indeed, the results of simulations showed that $D/D_0 = \alpha/n$, where α is a coefficient depending on the system parameters. It should be noted that the difference of the self-diffusion coefficient in the porous medium from the corresponding bulk value for less dense fluids is more significant than that for denser fluids. This fact is associated with the increase in the fraction of interactions of fluid molecules with the porous medium in the total number of interactions (certainly, for an identical characteristic pore size).

In accordance with Eq. (5.6), the self-diffusion coefficient calculated according to the MD method depends on time. The self-diffusion coefficient proper is obtained when a plateau value is reached, i.e., when D(t) is no longer time-dependent. Typical dependences of the self-diffusion coefficients in the porous medium and in the bulk are compared in Fig. 5.21. Here, the dotted curve shows the bulk value of the self-diffusion coefficient (n = 0.0707), and the bold solid curve shows the self-diffusion coefficient in the porous medium at $\varphi = 0.5$, $\lambda = 25$, and n = 0.0707. As follows from the presented data, the function D(t) in the porous medium is not monotonic. Nuclear magnetic resonance measurements are usually used to study the self-diffusion coefficient at small times (short-time diffusion) when the molecule covers a distance smaller than the characteristic pore size. At these times, however, the dependence of the root-mean-square distance covered by the molecules is nonlinear (see Fig. 5.21) and is not described by the Einstein-Langevin law. Therefore, experimental data should be interpreted cautiously. The thin solid curve in Fig. 5.21 is the approximation of short-time diffusion, which is described by the relation $D/D_0 \sim t^{-0.22}$. Thus, the root-mean-square distance covered by the

Fig. 5.21 Normalized self-diffusion coefficient versus time (in mean free times)



molecule is not a linear function, as is predicted by the Einstein theory; it is described by the law $\langle L^2 \rangle \sim t^{0.78}$, which corresponds to the so-called subdiffusion.

5.7 Modeling of Nanofluid Separation with the Use of Nanomembranes

The possibility of using nanoporous membranes for separation of gas mixtures has been intensely discussed in recent years (Chen et al. 2008; Bernardo et al. 2009; Rajabbeigi et al. 2009). Here, the MD method is actively used for studying the transport processes, in addition to experimental investigations. In Xu et al. (2000), the membrane was modeled by a three-dimensional network of pores. The transport processes and adsorption of gas molecules were considered, and an optimal configuration of the porous structure to ensure the most effective separation of gases was found. The efficiency of separation of O_2/N_2 and CO_2/N_2 gas mixtures in three zeolite membranes was studied in Jia and Murad (2005). It was found that it is difficult to separate gases having similar adsorption characteristics and molecule sizes. In studying separation of the H₂/CO mixture in nanoporous carbon membranes (Wu et al. 2008), it was demonstrated that the parameter that produces the greatest effect on the mixture separation velocity is the characteristic pore size. Finally, the study of Kozachok (2010) should be mentioned, in which separation of exhaust gases in nanoporous carbon membranes at high temperatures was investigated. In particular, an optimal density of the mixture for effective separation of gases at a temperature of 673 K was determined.

As was noted in previous chapters, interest in the transport processes in nanofluids is rapidly increasing. Separation of nanofluids through the use of nanomembranes is of considerable interest as well. As an example of such

separation, we can mention systems that cleanse air and water of viruses, which are nanoparticles in terms of their size. On the other hand, a nanoporous membrane is a typical tool for separation of various substances in living organisms. However, the main factors responsible for the efficiency of separation of a nanofluid passing through a nanoporous membrane have actually not yet been identified. We try to do this below, following (Rudyak and Andryushchenko 2014). We study the influence of the membrane porosity, type of packing of its granules, ratio of the nanoparticle size to the granule size, ratios of the masses and sizes of the fluid components, and carrier fluid density on the mixture separation velocity. Simulations were performed according to the MD algorithm, which is an extension of the algorithm for a system of hard spheres. Porous membranes were modeled by regular packs of solid particles (granules). In this section, we present the results of modeling a system with the granule diameter 4σ and nanoparticle diameter 5σ , where σ is the diameter of the carrier fluid molecule.

The simulated system is schematically illustrated in Fig. 5.22. The system is a cell shaped like a parallelepiped with solid walls. Its left part (domain 1) was filled with a nanofluid at the initial time. The carrier component could be either a fluid or a gas. Approximately ten thousand molecules were used in a typical computation. Computations with a substantially greater number of molecules were also performed, but the results obtained were almost unchanged. The bulk concentration of nanoparticles varied from 1 to 20%.

In domain 2 of the cell (see Fig. 5.22), a membrane was formed from spheres with an identical diameter. Simple cubic, cubic face-centered, and cubic body-centered types of particle packing were considered. In addition, the packing porosity ϕ could be varied (it was changed from 0.3 to 0.6). The porosity was increased by changing all distances between the pack nodes by an identical factor. At the initial time, the concentration of fluid molecules in the cell to the right of the membrane (domain 3) was equal to zero. The volume of this domain was much greater (by a factor of 100) than the volume of domain 1.

At the initial time, the velocities of molecules and nanoparticles in domain 1 were prescribed in accordance with the Maxwell distribution at a given temperature. The different in pressure between domains 1 and 3 initiated directed motion of the

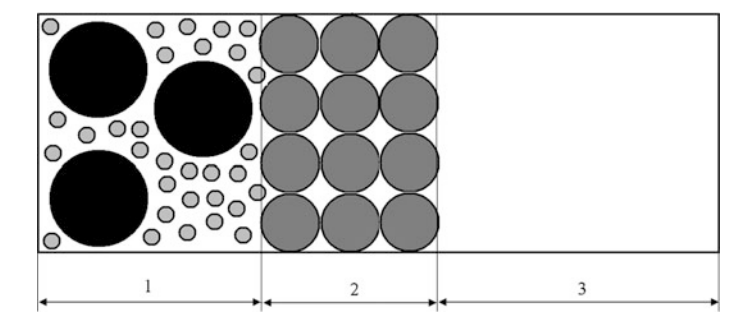


Fig. 5.22 Schematic illustration of the computational domain

nanofluid from left to right. As the nanoparticle diameter was greater than the characteristic pore size, only carrier gas molecules moved in the course of evolution of the process to the domain occupied by the membrane (domain 2 in Fig. 5.22) and then to domain 3, from which practically none of the molecules returned to domains 1 and 2.

The efficiency of nanofluid separation was determined on the basis of the velocity of molecule transportation through the porous membrane. This velocity was found in the following manner. First, filling of the membrane with gas molecules was performed. After that, there was a certain quasi-steady mode of molecule transportation; during this process, the molecule concentration in the membrane fluctuated around some constant value. In this mode, the decrease in the number of molecules in domain 1 was almost equivalent to the increase in the number of molecules in domain 3. As a result, the molecule transportation velocity is defined as the rate of change in the carrier gas mass in a unit volume of domain 3; its value within the time interval dt is Q' = m(dN/dt), where m is the gas molecule mass and dN is the number of molecules that entered domain 3 during this time. For this quantity to be independent of the transverse size of the cell, it should be divided by the cross-sectional area of the channel S. Thus, the molecule transportation rate is $O = m(dN/dt)S^{-1}$. The system evolution was considered at times during which the bulk concentration of molecules in domain 1 changed by less than 3-5%. It is in cases of molecules such as this that the transportation could be considered as a quasi-steady process.

In all cases considered here, the nanofluid separation velocity was proportional to the carrier fluid density gradient along the entire channel: Q = a(dn/dx), where a is a certain coefficient and n is the number density. The total mass flux is a sum of the diffusive Q_d and convective Q_c fluxes: $Q = Q_d + Q_c$. The total flux was calculated in the course of MD simulations. The diffusive flux was estimated as $Q_d = D(dn/dx)$, where D is the diffusion coefficient of molecules in the porous medium. It was found that the convective flux exceeds the diffusive flux by two orders of magnitude in all cases considered here. Thus, we can argue that the process of molecule transportation through the membrane mainly proceeds in the convective mode.

The proportionality of the mass flux of the filtered gas to the gradient of its concentration is fairly natural and expected. However, the coefficient a (see the previous paragraph) defining this proportionality should depend on a number of factors. First of all, the following should be noted: if the volume of domain 1 (Fig. 5.22) is sufficiently large that a stable and almost constant gradient of the carrier gas concentration is formed in the cell, then the filtration velocity should be independent of the bulk concentration of nanoparticles. Indeed, systematic simulations did not reveal this effect. If the membrane thickness H is increased for a given volume of the computational cell (see Fig. 5.22), then the filtration velocity decreases inversely proportionally to the membrane thickness. In our simulations, the membrane thickness was varied from unity to ten diameters of porous skeleton particles, and it was found that $Q \sim H^{-1}$. In this case, the decrease in the filtration

velocity is actually associated with the decrease in the density gradient, which is also inversely proportional to the membrane thickness.

Certainly, the filtration velocity should also depend on the membrane porosity. Figure 5.23 illustrates this dependence for the case when the number concentration of carrier gas molecules in domain 1 is equal to 0.177, and the volume concentration of particles is 20%. Moreover, the data are given for three different types of packing of membrane granules: simple cubic, cubic body-centered, and cubic face-centered packing. In all three cases, the membranes had an identical thickness and cross-section. The dependence of the separation velocity on the membrane porosity is nonlinear and is adequately described in all cases by a quadratic function of ϕ . The greatest separation velocity is provided by the membrane with cubic body-centered packing of granules. For the minimum porosity considered in this study, the filtration velocity for simple cubic and cubic face-centered types of packing of membrane granules is equal to zero, i.e., there is no filtration at all.

The dependence on the packing type is related to the difference in cross-sections of porous media for different types of granule packing, resulting in different effective capacities of membranes, even if they have identical porosity values. As the filtration modeled here is the so-called mechanical filtration (Dimov et al. 2012), the most important parameter characterizing it is the ratio of the size of filtered molecules and porous medium granules: σ/D .

In turn, the pore throats actually determine the characteristic size of channels where molecular motion occurs. The pore throat sizes are significantly different in media with different types of granule packing. For example, for the porosity of 0.5, the pore throat size is 1.12σ for cubic face-centered packing, 1.68σ for simple cubic packing, and 2.12σ for cubic body-centered packing. Thus, body-centered packing is expected to ensure the maximum filtration velocity and face-centered packing is

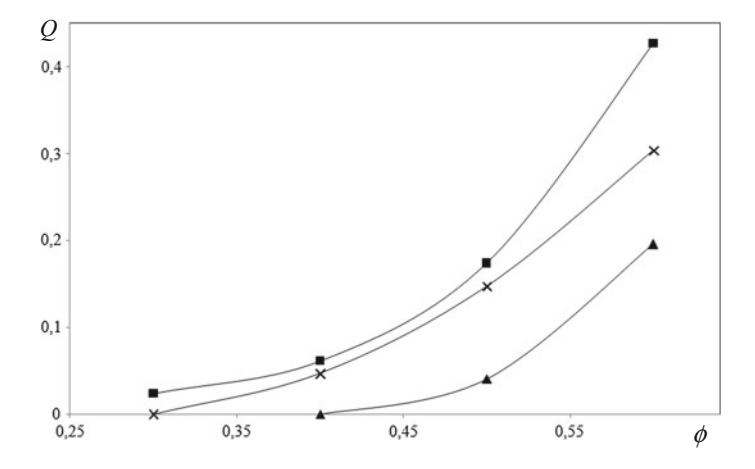


Fig. 5.23 Mixture separation velocity versus the membrane porosity for the simple cubic (crosses), cubic body-centered (squares), and cubic face-centered packing of membrane granules (triangles)

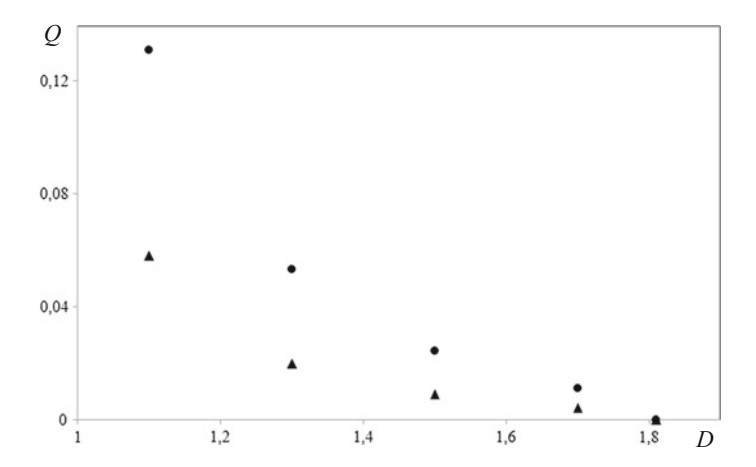


Fig. 5.24 Mixture separation velocity versus the diameter of molecules of the carrier phase of the mixture for different values of the membrane thickness: 3D (circles) and 7D (triangles)

expected to ensure the minimum filtration velocity, which is confirmed here by the computations (see Fig. 5.23).

The pore throat size also determines the threshold from which separation begins. This threshold is also related to the ratio of the sizes of filtered molecules and porous medium granules [it was experimentally studied in Dimov et al. (2012)]. To establish this threshold, filtration of particles of different sizes through a filter with a granule size D was simulated. The results are plotted in Fig. 5.24. Here, the membrane porosity was 0.6, and cubic body-centered packing was used. The separation velocity decreased with increasing diameter of filtered molecules and ceased at $D=1.8\sigma$. For this membrane, the pore throat diameter was 1.81σ . Thus, filtration is terminated only when the size of filtered molecules reaches the order of the pore throat size.

To conclude, it can be noted that the separation process can be controlled by varying the nanofluid and membrane parameters. In particular, for a given density of the carrier gas in domain 1, the concentration gradient and, hence, the separation velocity can be reduced by increasing the membrane's thickness. The type of granule packing in the filter plays the governing role in filtration velocity enhancement.

References

Alexeyev AA, Vinogradova OI (1996) Flow of a liquid in a nonuniformly hydrophobized capillary. Colloids Surf A 108:173–179

Andrienko D, Dünweg B, Vinogradova OI (2003) Boundary slip as a result of a prewetting transition. J Chem Phys 119:13106–13112

- Andryushchenko V, Rudyak V (2011) Self-diffusion coefficient of molecular fluid in porous media. Defect Diffus Forum 312–315:417–422
- Bernardo P, Drioli E, Golemme G (2009) Membrane gas separation: a review/state of the art. Ind Eng Chem Res 48:638–4663
- Bitsanis I, Susan A, Somers SA, Davis HT, Tirrell M (1990) Microscopic dynamics of flow in molecularly narrow pores. J Chem Phys 93(5):3427–3236
- Chen F, Mourhatch R, Tsotsis TT, Sahimi M (2008) Pore network model of transport and separation of binary gas mixture in nanoporous membranes. J Membr Sci 315:48–57
- Cheng Y, Cory DG (1999) Multiple scattering by NMR. J Am Chem Soc 121:7935-7936
- Dimov SV, Kuznetsov VV, Rudyak VY, Tropin NM (2012) Experimental investigation of microsuspension filtration in a highly-permeable porous medium. Fluid Dyn 47(2):178–185
- Fan TH, Vinogradova OI (2005) Hydrodynamic resistance of close-approached slip surfaces with a nanoasperity or an entrapped nanobubble. Phys Rev E 72:066306
- Heinbuch U, Fischer J (1989) Liquid flow in pores: slip, no-slip, or multilayer sticking. Phys Rev A 40:1144–1146
- Jia W, Murad S (2005) Separation of gas mixtures using a range of zeolite membranes: a molecular-dynamics study. J Chem Phys 122:234708
- Kärger J, Ruthven DM (1992) Diffusion in zeolites and over microporous solids. Wiley, New York Karnidakis G, Beskok A, Aluru N (2005) Microflows and nanoflows. Interdisciplinary applied mathematics, vol 29. Springer Science+Business Media, Berlin
- Kim KH (1998) Experimental measurement of restricted diffusion. Chem Ind Technol 16(6):562–567
- Koplik J, Banavar J, Willemsen J (1988) Molecular dynamics of Poiseuille flow and moving contact lines. Phys Rev Lett 60:1282–1285
- Koplik J, Banavar JR, Willemsen JF (1989) Molecular dynamics of fluid flow at solid surfaces. Phys Fluids A 1:781–794
- Koplik J, Vergeles M, Keblinski P, Banavar J (1996) Stokes drag and lubrication flows: a molecular dynamics study. Phys Rev E 53:4852–4864
- Kozachok MV (2010) Equilibrium molecular dynamics and mean first passage time analysis of the separation of exhaust gases at high temperatures by silica nanoporous membranes. Model Simul Mater Sci Eng 18:025009
- Latour LL, Mitra PP, Kleinberg RL, Sotak CH (1993) Time-dependent diffusion coefficient of fluids in porous media as a probe of surface-to-volume ratio. J Magn Reson A101:342–346
- Lauga E, Brenner MP, Stone HA (2007) Microfluidics: the no-slip boundary condition. Handbook of experimental fluid dynamics, Ch 19. Springer, New York, pp 1219–1240
- Li D (eds) (2008) Encyclopedia of microfluidics and nanofluidics. Springer Science+Business Media, Berlin
- Nelson PH (2009) Pore-throat sizes in sandstones, tight sandstones, and shales. AAPG Bull 93 (3):329-340
- Ou J, Perot B, Rothstein JP (2004) Laminar drag reduction in microchannels using ultrahydrophobic surfaces. Phys Fluids 16(12):4635–4643
- Rajabbeigi N, Tsotsis TT, Sahimi M (2009) Molecular pore-network model for nanoporous materials. II: application to transport and separation of gaseous mixtures in silicon-carbide membranes. J Membr Sci 345:323–330
- Rudyak VY, Andryushchenko VA (2014) Molecular dynamics simulation of the nanofluid separation be means of nanomembrane. J Math Mech 4(30):88–94 (Vestnik of Tomsk State University)
- Rudyak VY, Belkin AA, Egorov VV, Ivanov DA (2008a) Modeling of plane flow with a pressure gradient in a nanochannel. In: Proceedings of 1st European conference on microfluidics, Universita di Bologna, Bologna, pp 263–272
- Rudyak VY, Belkin AA, Ivanov DA, Egorov VV (2008b) The simulation of transport processes using the method of molecular dynamics. Self-diffusion coefficient. High Temp 46(1):30–39

References 215

Rudyak V, Belkin A, Egorov V, Ivanov D (2010) The characteristics and structure of plane Poiseuille type flow in a nanochannel. In: Proceedings of 2nd European conference on microfluidics (μFlu-24), SHF, Toulouse

- Rudyak V, Belkin A, Egorov V, Ivanov D (2011a) Modeling the flow in nanochannels by molecular dynamics method. Nanosystems Phys Chem Math 2(4):1–16
- Rudyak VY, Belkin AA, Egorov VV, Ivanov DA (2011b) About fluids structure in microchannels. Int J Multiphys 5(2):145–155
- Song Y-Q, Ryu S, Sen PN (2000) Determining multiple length scales in rock. Nature 406:178–181 Soong CY, Yen TH, Tzeng PY (2007) Molecular dynamics simulation of nanochannels flows with effects of wall lattice-fluid interactions. Phys Rev E 76:036303
- Thompson PA, Robbins MO (1990) Shear flow near solids: epitaxial order and flow boundary conditions. Phys Rev A 41:6830–6837
- Travis KP, Gubbins KE (2000) Poiseuille flow of Lennard-Jones fluids in narrow slit pores. J Chem Phys 112(4):1984–1994
- Travis KP, Todd BD, Evans DJ (1998) Departure from Navier Stokes hydrodynamics in confined liquids. Phys Rev E 55(4):4288–4295
- Vinogradova OI (1995) Drainage of a thin liquid film confined between hydrophobic surfaces. Langmuir 11:2213–2220
- Vinogradova OI, Yakubov GE (2006) Surface roughness and hydrodynamic boundary conditions. Phys Rev E 73:045302
- Watts ET, Krim J, Widom A (1990) Experimental observation of interfacial slippage at the boundary of molecularly thin films with good substraite. Phys Rev B 41(6):3466–3472
- Wu Z, Liu Z, Wang W, Fan Y, Xu N (2008) Non-equilibrium molecular dynamics simulation on permeation and separation of H₂/CO in nanoporous carbon membranes. Sep Purif Technol 64:71–77
- Xu L, Sahimi M, Tsotsis TT (2000) Nonequilibrium molecular dynamics simulation of transport and separation of gas mixtures in nanoporous materials. Phys Rev E 62(5):6942–6948
- Zhu Y, Granick S (2001) Rate-dependent slip of Newtonian liquid at smooth surfaces. Phys Rev Lett 87:096105
- Zhu Y, Granick S (2002) Limits of the hydrodynamic no-slip boundary condition. Phys Rev Lett 88:106102

Chapter 6 Fluid Transport Under Confined Conditions



Abstract The viscosity and thermal conductivity of the fluid are determined by the transport of the impulse and energy in the system considered. In turn, these transports are defined by and depend on the interaction of the fluid molecules. The situation in the fluid under confined conditions (e.g., in a nanochannel) is more complicated, because the transport of the impulse and energy in fluids is highly dependent on the interaction of the fluid molecules with the wall atoms (or molecules). Therefore, the viscosity and thermal conductivity of such a fluid are the properties of the entire "fluid+wall" system. In this chapter, the statistical theory of transport processes in fluids under confined conditions is proposed. The considered system is the specific two-fluid system consisting of fluid and wall molecules. In the chapter, the new constitutive relations for the fluid under confined conditions are proposed. As a result, the Green-Kubo formulas were generalized. Using this new formula and the molecular dynamics method, the viscosity coefficient of the fluid in a nanochannel was studied. It is shown that the viscosity coefficient depends, to a large extent, on the properties of interaction of fluid molecules with channel wall atoms.

6.1 Physics of the Transport Processes in Fluid

The analysis of methods used to describe flows in microchannels, and especially in nanochannels (see Chap. 1), shows that it is impossible to use the traditional hydrodynamic description of the fluid in some typical situations. First, there are significant fluctuations of density, momentum, and energy in sufficiently small channels in a physically infinitesimal volume, which does not even allow for adequate introduction of the hydrodynamic variables themselves. Moreover, there is one more reason. It was demonstrated in Sect. 5.5 that the flow structure in a nanochannel is essentially different from the flow structure in a larger volume. In particular, the fluid density is inhomogeneous, and well-ordered nanolayers of the fluid are formed near the surface. In fact, there is a quasi-long-range order here. However, as one of the mechanisms (and the most important one!) determining the

fluid viscosity is local failure of the short-range order, the presence of such layers suggests the following conclusion. The fluid viscosity in nanochannels is inhomogeneous and may differ significantly from the fluid viscosity in a larger volume. The same conclusions can be drawn for other transport processes: those of mass and energy.

The idea that transport processes in nanochannels should differ from the usual transport processes has been approved long ago. During the last decade, several attempts were made to calculate or measure the fluid viscosity coefficient in nanochannels, or even to propose a new model for its description (Popov 2011). Calculations are usually performed according to the molecular dynamics method (see, e.g., Travis 2004; Liu et al. 2004; Zhu et al. 2002, 2004; Zhu and Schulten 2003; Kumar et al. 2007; Zhang and Ye 2009; Thomas and McGaughey 2009; Rudyak et al. 2011 and references therein). The results obtained were versatile and poorly correlated with each other, but the main idea is fairly obvious: the fluid viscosity in nanochannels is not equal to its bulk viscosity.

Experimental data (see the review of Abdullaeva and Nagiev 2011) are rather speculative for reasons that are easy to understand. First of all, it is impossible to measure the fluid viscosity in sufficiently small channels. Therefore, some integral data on the flow are used, which are then interpreted from a macroscopic viewpoint. Nevertheless, it should be noted that available experimental data confirm the higher effective viscosity of the fluid in nanovolumes, as compared to its macroscopic value (Li et al. 2007).

It was noted above that the formation of fluid viscosity occurs at mesoscales whose characteristic scale is on the order of at least ten nanometers. Therefore, some caution is needed in discussing the fluid viscosity in nanochannels whose characteristic size is smaller than that at which fluid viscosity is formed. The same goes for other transport processes, though the energy (heat) transfer mechanisms differ from that of momentum. However, before trying to develop a theory of such processes, we have to define how these processes are understood. Let us consider an arbitrary molecular system: gas, liquid, or solid. As molecules are permanently moving, there are always local fluctuations of density, momentum, and energy in any system. In the general case, because of a very large number of molecules and the absence of correlations of molecular states, these fluctuations have a random character. In the equilibrium state, these fluctuations are inversely proportional to the square root of the number of particles in the system: $N^{-1/2}$. Therefore, there are no visible fluctuations in equilibrium macroscopic systems with $N \gg 1$. In nonequilibrium systems, however, there are fluctuations of observed variables at scales much greater than the molecular scale. Fluctuations of the quantity ϕ are schematically shown in Fig. 6.1 (left picture) in the form of a dark region. The gradient of this variable is leveled off with time, until the entire domain becomes

¹Strictly speaking, in solids, there is some correlation of motion of crystal lattice atoms by virtue of the orderliness of the configurations. Nevertheless, the number of molecules is also so large that the motion of atoms can be considered as stochastic.

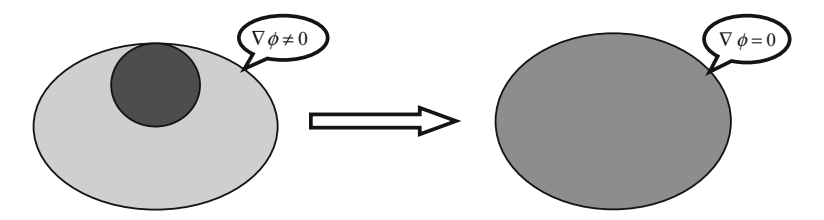


Fig. 6.1 Illustration of level-off of the gradient of a macroscopic variable ϕ in a closed system

homogeneous (Fig. 6.1, right picture). Thus, the transition to the equilibrium state means elimination of large-scale fluctuations.

Reaching the equilibrium state is accompanied by transport processes, i.e., processes of level-off of various macroscopic characteristics of the system (density, momentum, or energy). Let us again recall that transport processes are processes that lead to elimination of large-scale fluctuations.

Weakly nonequilibrium transport processes are characterized by linear constitutive relations, where the fluxes J_i are proportional to gradients of macroscopic variables:

$$\mathbf{J}_{1\alpha} = -\sum_{\beta} \mu_{11}^{\alpha\beta} \nabla v_{\beta} - \mu_{13}^{\alpha\beta} \nabla T, \quad \mathbf{J}_{2} = p\mathbf{U} - \mu_{22}^{0} (\nabla \cdot \mathbf{u}) \mathbf{U} - \mu_{22} (\nabla \mathbf{u})^{s},$$

$$\mathbf{J}_{3} = -\mu_{33} \nabla T - \sum_{\alpha} \mu_{31}^{\alpha} \nabla v_{\alpha}.$$

$$(6.1)$$

Here, $\mathbf{J}_{1\alpha}$, \mathbf{J}_2 , and \mathbf{J}_3 are the diffusion vector, stress tensor, and heat flux vector, respectively, T is the temperature, \mathbf{u} is the macroscopic velocity, and $v_{\alpha} = \zeta_{\alpha}/T$, where ζ_{α} is the chemical potential of the component α and μ_{ij} are the transport coefficients.

Transport processes in rarefied gases are easily interpreted; they are induced by transfer of the corresponding microscopic quantity at scales on the order of the mean free path of molecules. Transport processes in liquids are more complicated. For example, viscosity is caused not only by momentum transfer in molecular collisions, but also by failure of the short-range order and by diffusion processes of momentum transfer in the system. Near the surface, an important factor of momentum equalization in the flow is interaction of fluid molecules with molecules of the surface. In a nanochannel with a characteristic transverse size on the order of 5 nm, almost 50% of all interactions of fluid molecules are their collisions with molecules of the channel wall. Under such conditions, it makes no sense to talk about the viscosity of an individual fluid. Fluid viscosity should be considered as a property of the entire system consisting of the fluid and nanochannel walls. Certainly, it is not easy to study such "viscosity" experimentally. To develop appropriate tools, it is first necessary to create an adequate theory of transport processes, which will be used for interpreting experimental data and their modeling.

6.2 Statistical Theory of Transport Processes

Transport processes in micro- and nanochannels are multi-scales processes. On the one hand, they are formed at mesoscales; on the other hand, they also proceed at both macro- and nanoscales. Therefore, an adequate theory can be developed only with the use of formalism that is suitable for all of these scales. This can be done only on the basis of the first principles. Such formalism was constructed in (Rudyak and Belkin 2014, 2015) through methods of nonequilibrium statistical mechanics. Our considerations presented below are based on these publications.

6.2.1 Dynamic Description of the Fluid-Surface System

As the states of the molecules of the fluid and channel walls are essentially different (in particular, the walls are stationary, whereas the fluid moves), the system is a kind of two-fluid medium. It is proposed below to describe the properties of such a medium by using tools developed earlier for disperse systems (Rudyak and Belkin 1994, 1996). In this case, the system consisting of the fluid and channel walls is considered as a two-phase medium, in which each phase consists of molecules of the same type and is characterized by its own macroscopic variables: density, velocity, and temperature. The system dynamics is described by an N-particle distribution function F_N , which satisfies the Liouville equation (see Rudyak 2005)

$$\partial F_N/\partial t + L_N F_N = 0, (6.2)$$

where the Liouville operator is defined as

$$L_{N} = \sum_{\alpha=1}^{2} \sum_{i=1}^{N_{\alpha}} \left[\frac{\mathbf{p}_{i}}{m_{\alpha}} \cdot \frac{\partial}{\partial \mathbf{r}_{i}} + \frac{1}{2} \sum_{\varphi=1}^{2} \sum_{j=1}^{N_{\varphi}} \left\{ \mathbf{F}_{ij} \cdot \left(\frac{\partial}{\partial \mathbf{p}_{i}} - \frac{\partial}{\partial \mathbf{p}_{j}} \right) \right\} \right].$$

Here, m_i , \mathbf{r}_i , and \mathbf{p}_i are the mass, coordinate of the center of mass, and momentum of the *i*-th molecule of phase α . The force \mathbf{F}_{ij} of intermolecular interaction may be non-potential in the general case, which does not alter the structure of the Liouville operator.

The state of the system is characterized by partial values of the number density of particles n_{α} , momentum \mathbf{p}_{α} , and energy E_{α} . These are averaged values of the corresponding dynamic variables, which can be written by virtue of their additivity in the form of local (at the point \mathbf{r}) densities of these variables:

$$\hat{n}_{\alpha}(\mathbf{r}) = \sum_{i=1}^{N_{\alpha}} \delta(\mathbf{r}_{i} - \mathbf{r}), \quad \hat{\mathbf{p}}_{\alpha}(\mathbf{r}) = \sum_{i=1}^{N_{\alpha}} \hat{\mathbf{p}}_{i} \delta(\mathbf{r}_{i} - \mathbf{r}), \quad \hat{E}_{\alpha}(\mathbf{r}) = \sum_{i=1}^{N_{\alpha}} \hat{E}_{i} \delta(\mathbf{r}_{i} - \mathbf{r}) \quad (6.3)$$

Acting with the Liouville operator on the dynamic densities (6.3), we can derive transport equations for them (Rudyak 2005):

$$\hat{\hat{n}}_{\alpha} = -\nabla \cdot \hat{\mathbf{J}}_{1\alpha}, \quad \hat{\hat{\mathbf{p}}}_{\alpha} = -\nabla \cdot \hat{\mathbf{J}}_{2\alpha} + \hat{\mathbf{j}}_{2\alpha}, \quad \hat{\hat{E}}_{\alpha} = -\nabla \cdot \hat{\mathbf{J}}_{3\alpha} + \hat{j}_{3\alpha}.$$
(6.4)

The operators of the flux of the number of molecules $\hat{\bf J}_{1\alpha}$, momentum flux $\hat{\bf J}_{2\alpha}$, and energy flux $\hat{\bf J}_{3\alpha}$, and also the operators of the interphase forces $\hat{\bf J}_{2\alpha}$ and $\hat{\bf J}_{3\alpha}$, are defined as follows:

$$\begin{split} \hat{\mathbf{J}}_{1\alpha} &= \sum_{i=1}^{N_{\alpha}} \frac{\mathbf{p}_{i}}{m_{\alpha}} \delta(\mathbf{r}_{i} - \mathbf{r}), \\ \hat{\mathbf{J}}_{2\alpha} &= \sum_{i=1}^{N_{\alpha}} \left[\frac{\mathbf{p}_{i} \mathbf{p}_{i}}{m_{\alpha}} \delta(\mathbf{r}_{i} - \mathbf{r}) + \frac{1}{2} \sum_{\varphi}^{f,b} \sum_{j=1}^{N_{\varphi}} \mathbf{r}_{ij} \mathbf{F}_{ij} \int_{0}^{1} d\eta \delta(\mathbf{r}_{j} - \mathbf{r} + \eta \mathbf{r}_{ij}) \right], \\ \hat{\mathbf{J}}_{2\alpha} &= \frac{1}{2} \sum_{i=1}^{N_{\alpha}} \sum_{j=1}^{N_{\varphi \neq \alpha}} \mathbf{F}_{ij} \left[\delta(\mathbf{r}_{i} - \mathbf{r}) + \delta(\mathbf{r}_{j} - \mathbf{r}) \right], \\ \hat{\mathbf{J}}_{3\alpha} &= \sum_{i=1}^{N_{\alpha}} \frac{\mathbf{p}_{i} E_{i}}{m_{\alpha}} \delta(\mathbf{r}_{i} - \mathbf{r}) + \frac{1}{4} \sum_{i=1}^{N_{\alpha}} \sum_{\varphi=1}^{l} \sum_{j=1}^{N_{\varphi}} \left(\frac{\mathbf{p}_{i}}{m_{\alpha}} + \frac{\mathbf{p}_{j}}{m_{\varphi}} \right) \cdot \mathbf{r}_{ij} \mathbf{F}_{ij} \int_{0}^{1} d\eta \delta(\mathbf{r}_{j} - \mathbf{r} + \eta \mathbf{r}_{ij}), \\ \hat{\mathbf{J}}_{3\alpha} &= \frac{1}{4} \sum_{i=1}^{N_{\alpha}} \sum_{j=1}^{N_{\varphi \neq \alpha}} \mathbf{F}_{ij} \cdot \left(\frac{\mathbf{p}_{i}}{m_{\alpha}} + \frac{\mathbf{p}_{j}}{m_{\varphi}} \right) \left[\delta(\mathbf{r}_{i} - \mathbf{r}) + \delta(\mathbf{r}_{j} - \mathbf{r}) \right]. \end{split}$$

The macroscopic values of the density $n_{\alpha}(\mathbf{r},t)$, momentum $\mathbf{p}_{\alpha}(\mathbf{r},t)$, and energy $E_{\alpha}(\mathbf{r},t)$ of the system are obtained by averaging of the local densities (6.3) over the ensemble F_N :

$$n_{\alpha}(\mathbf{r},t) = \int dx \hat{n}_{\alpha}(\mathbf{r}) F_{N}(t),$$

$$\mathbf{p}_{\alpha}(\mathbf{r},t) = m_{\alpha} n_{\alpha}(\mathbf{r},t) \mathbf{u}_{\alpha}(\mathbf{r},t) = \int dx \hat{\mathbf{p}}_{\alpha}(\mathbf{r}) F_{N}(t),$$

$$E_{\alpha}(\mathbf{r},t) = \int dx \hat{E}_{\alpha}(\mathbf{r}) F_{N}(t),$$
(6.5)

The macroscopic velocities of the fluid (marked by f) and body walls (marked by b) are defined as $\mathbf{u}_f(\mathbf{r},t) = \mathbf{p}_f(\mathbf{r},t)/m_f n_f$ and $\mathbf{u}_b(\mathbf{r},t) = 0$, because the walls are at rest.

The transport equations for macroscopic variables are obtained by averaging of the transport equations for local dynamic densities (6.3) over the ensemble F_N . Passing for the fluid to a local fluid-fitted coordinate system, which moves with respect to the laboratory coordinate system with the velocity \mathbf{u}_f , we obtain

$$\frac{dn_f}{dt} = -n_f \nabla \cdot \mathbf{u}_f, \quad \frac{dn_b}{dt} = 0, \quad \frac{d}{dt} = \frac{\partial}{\partial t} + \mathbf{u}_f \cdot \nabla,$$

$$\rho_f \frac{d\mathbf{u}_f}{dt} = -\nabla \cdot \mathbf{J}'_{2f} + \mathbf{j}_{2f}, \quad \frac{d\mathbf{u}_b}{dt} = 0,$$

$$\frac{dE'_f}{dt} = -E'_f \nabla \cdot \mathbf{u}_f - \nabla \cdot \mathbf{J}'_{3f}$$

$$- (\mathbf{J}'_{2f} + \mathbf{J}_{fb}): \nabla \mathbf{u}_f - \mathbf{j}_{fb} \cdot \mathbf{u}_f + j'_{3f},$$

$$\frac{dE'_b}{dt} = -\nabla \cdot \mathbf{J}'_{3b} - j'_{3f} + \mathbf{J}_{fb}: \nabla \mathbf{u}_f.$$
(6.6)

Here, $\mathbf{A} = \left\langle \hat{\mathbf{A}} \right\rangle$, the angular brackets denote averaging over the ensemble F_N , and all primed quantities are obtained from the corresponding non-primed quantities by means of the momentum transformation: $\mathbf{p}'_i = \mathbf{p}_i - m_{\alpha}\mathbf{u}_{\alpha}$. We also introduce additional microscopic densities

$$\hat{\mathbf{J}}_{fb} = -rac{1}{4}\sum_{i=1}^{N_f}\sum_{j=1}^{N_b}\mathbf{r}_{ij}\mathbf{F}_{ij}\int\limits_0^1d\eta\deltaig(\mathbf{r}_j-\mathbf{r}+\eta\mathbf{r}_{ij}ig),\;\hat{\mathbf{j}}_{fb} = rac{1}{2}\sum_{i=1}^{N_f}\sum_{j=1}^{N_b}\mathbf{F}_{ij}\delta(\mathbf{r}_i-\mathbf{r}),$$

typical for multi-fluid systems (Rudyak and Belkin 1996; Rudyak 2005).

6.2.2 Nonequilibrium Distribution Function

Derivation of the transport equations and constitutive relations reduces to finding the solution to Eq. (6.2) for an appropriately chosen shortened description. By virtue of the linearity of Eq. (6.2), its solution can be sought as a sum of the quasi-equilibrium distribution function F_{N0} and the dissipative function F_{N1} : $F_N = F_{N0} + F_{N1}$. The function F_{N0} is found from the condition of the extremum of the information entropy

$$S = -k \int d\Gamma_N F_{N0} \ln F_{N0}$$

for prescribed mean values of the parameters of the number of particles, momentum, and energy of particles of each phase, i.e., from the condition of the extremum of the functional

$$-k\sum_{eta}\int d\Gamma_{N}\Bigg[F_{N0}\ln F_{N0}-(lpha_{0eta}+1)F_{N0}+\sum_{i}\int d\mathbf{r}lpha_{ieta}\widehat{A}_{ieta}(\mathbf{r})F_{N0}\Bigg],$$

where $\alpha_{i\beta}$ are the Lagrangian multipliers. The resultant distribution function corresponds to the two-fluid quasi-equilibrium description of the system. In finding F_{N0} , it should be taken into account that the macroscopic velocity of the walls is

equal to zero, whereas the temperatures of the walls and the fluid can differ from each other. As a result, we easily see that

$$F_{N0} = Q_0^{-1} \exp\left\{-\int d\mathbf{r} \left[\beta_f(\mathbf{r},t)\hat{E}'_f(\mathbf{r}) - v_f(\mathbf{r},t)\hat{n}_f(\mathbf{r}) + \beta_b(\mathbf{r},t)\hat{E}_b(\mathbf{r}) - v_b(\mathbf{r},t)\hat{n}_b(\mathbf{r})\right]\right\},$$

$$Q_0 = \left\langle \exp\left\{-\sum_{\alpha=1}^l \sum_{k=1}^3 \int g_{k\alpha}(\mathbf{r},t)\hat{G}'_{k\alpha}(\mathbf{r})\right\}\right\rangle.$$
(6.7)

The Lagrangian multipliers $g_{k\alpha}$ are chosen so that $g_{3\alpha} = \beta_{\alpha} = 1/kT_{\alpha}$ is the local inverse temperature of the component α , $g_{1\alpha} = \beta_{\alpha} \left(-\mu_{\alpha} + m_{\alpha} \mathbf{u}_{\alpha}^{2}/2\right)$, $g_{2\alpha} = -\beta_{\alpha} \mathbf{u}_{\alpha}$, $v_{\alpha} = -\beta_{\alpha} \varsigma_{\alpha}$, and ς_{α} is the local chemical potential. The mean values of the number density of particles of the component α and its energy calculated over the quasi-equilibrium ensemble (6.7) are

$$\langle \hat{n}_{\alpha}(\mathbf{r}) \rangle_{0} = \frac{\delta \ln Q_{0}}{\delta \nu_{\alpha}(\mathbf{r})}, \ \langle \hat{E'}_{\alpha}(\mathbf{r}) \rangle_{0} = \frac{\delta \ln Q_{0}}{\delta \beta_{\alpha}(\mathbf{r})}.$$

Here, averaging over the ensemble (6.7) is marked by the zero subscript at the angular brackets. For the thermodynamics of the system to be determined by the function F_{N0} , we have to require that the macroscopic variables coincide with their quasi-equilibrium values:

$$n_{\alpha}(\mathbf{r},t) = \langle \hat{n}_{\alpha}(\mathbf{r}) \rangle_{0}, \ E'_{\alpha}(\mathbf{r},t) = \langle \hat{E}'_{\alpha}(\mathbf{r}) \rangle_{0}.$$

As F_{N0} is an even function with respect to the momentum \mathbf{p}'_i and relative coordinates \mathbf{r}_{ij} , the mean values of non-diagonal elements of the stress tensor and the tensor \mathbf{J}_{fb} calculated on the basis of this function are equal to zero:

$$\mathbf{J}_{2f}^{\prime 0}(\mathbf{r},t) = \frac{1}{3} \left\langle \hat{\mathbf{J}}_{2f}^{\prime}(\mathbf{r}):\mathbf{U} \right\rangle_{0} = p_{f}(\mathbf{r},t)\mathbf{U}, \quad \mathbf{J}_{fb}^{0}(\mathbf{r},t) = \frac{1}{3} \left\langle \hat{\mathbf{J}}_{fb}^{\prime}(\mathbf{r}):\mathbf{U} \right\rangle_{0} = p_{fb}(\mathbf{r},t)\mathbf{U}.$$

Here, p_f is the partial pressure of the fluid, which is assumed to be isotropic, and **U** is the unit tensor of the second rank. For the same reason, other fluxes and interphase forces are also set to zero. As a result, the transport equations for the considered fluid in the quasi-equilibrium approximation (which corresponds to the Euler equations in conventional fluid dynamics) have the form

$$\frac{dn_f}{dt} = -n_f \nabla \cdot \mathbf{u}_f, \quad \rho_f \frac{d\mathbf{u}_f}{dt} = -\nabla p_f, \quad \frac{dE'_f}{dt} = -\left(E'_f + p_f + p_{fb}\right) \nabla \cdot \mathbf{u}_f, \tag{6.8}$$

Equation (6.8) are derived on the basis of the ensemble F_{N0} and do not describe dissipative processes in the system. To construct the nonequilibrium distribution function, we have to solve the linear inhomogeneous equation

$$\partial F_{N1}/\partial t + L_N F_{N1} = -(\partial F_{N1}/\partial t + L_N F_{N1}). \tag{6.9}$$

The right-hand side of this equation contains derivatives with respect to the time of hydrodynamic variables, which are determined from the transport equation (6.6) with the use of the total distribution function (marked by the subscript 1):

$$\begin{split} &\left(\rho_f \frac{d\mathbf{u}_f}{dt}\right)_1 = -\nabla \cdot \mathbf{J'}_{2f}^1 + \mathbf{j}_{2f}^1, \quad \left(\rho_b \frac{d\mathbf{u}_b}{dt}\right)_1 = -\nabla \cdot \mathbf{J'}_{2b}^1 - \mathbf{j}_{2f}^1 = 0, \\ &\left(\frac{dE'_f}{dt}\right)_1 = -\nabla \cdot \mathbf{J'}_{3f}^1 - \left(\mathbf{J'}_{2f}^1 + \mathbf{J}_{fb}^1\right) : \nabla \mathbf{u}_f - \mathbf{j}_{fb}^1 \cdot \mathbf{u}_f + j'_{3f}^1, \\ &\left(\frac{dE'_b}{dt}\right)_1 = -\nabla \cdot \mathbf{J'}_{3b}^1 + \mathbf{J}_{fb}^1 : \nabla \mathbf{u}_f + \mathbf{j}_{fb}^1 \cdot \mathbf{u}_f - j'_{3f}^1. \end{split}$$

The method for solving Eq. (6.9) was developed and described in detail by Rudyak (1987). Omitting cumbersome transformations, we present the final explicit form of the nonequilibrium distribution function for the system of nonspherical particles considered here:

$$F_{N1}(t) = \pi(t, t_0) S_{-(t-t_0)}^{(N)} F_{N1}(t_0)$$

$$+ \sum_{\alpha}^{f,b} \sum_{k=1}^{5} \int_{t_0}^{t} dt_1 \int d\mathbf{r} \int d\mathbf{r}' \pi(t, t_1) S_{-(t-t_1)}^{(N)} F_{N0}(t_1) \Delta \mathbf{I}_{k\alpha} \cdot \mathbf{Y}_{k\alpha}(\mathbf{r}', t_1),$$

$$\Delta \mathbf{I}_{k\alpha} = \hat{\mathbf{I}}_{k\alpha}(\mathbf{r}, \mathbf{r}') - \mathbf{I}_{k\alpha}^{0}(\mathbf{r}, \mathbf{r}').$$

$$(6.10)$$

Here, $S_{-(t-t_1)}^{(N)}$ is the displacement operator over the trajectory of N particles. The operator $\pi(t,t_1)$ has the form of an infinite series in thermodynamic forces (Rudyak and Belkin 1996; Rudyak 2005). For weakly nonequilibrium systems (which correspond to the Navier-Stokes approximation in conventional fluid dynamics), it is sufficient to retain only the first term of this series, which is equal to unity. The fluxes $\hat{\mathbf{I}}_{k\alpha}$ and thermodynamic forces $\hat{\mathbf{Y}}_{k\alpha}$ are defined as

$$\hat{\mathbf{I}}_{1f} = \hat{\mathbf{J}}'_{1f}(\mathbf{r}) \left(\delta(\mathbf{r} - \mathbf{r}') - \frac{\beta_f(\mathbf{r})}{n_f(\mathbf{r})} \left(\frac{\delta p_f(\mathbf{r})}{\delta v_f(\mathbf{r}')} \right) \right), \quad \hat{\mathbf{I}}_{1b} = \hat{\mathbf{J}}'_{1b}(\mathbf{r}) \delta(\mathbf{r} - \mathbf{r}'), \quad \mathbf{Y}_{1\alpha} = -\nabla' v_{\alpha}, \\
\hat{\mathbf{I}}_{2f} = \left(\hat{\mathbf{J}}'_{2f}(\mathbf{r}) + \hat{\mathbf{J}}_{fb}(\mathbf{r}) \right) \beta_f \delta(\mathbf{r} - \mathbf{r}') \\
- \left[E'_f(\mathbf{r}') + p_f(\mathbf{r}') + p_{fb}(\mathbf{r}') \right] \left[\hat{n}_f(\mathbf{r}) \left(\frac{\delta v_f(\mathbf{r})}{\delta E'_f(\mathbf{r}')} \right)_{n_f} - \hat{E}'_f(\mathbf{r}) \left(\frac{\delta \beta_f(\mathbf{r})}{\delta E'_f(\mathbf{r}')} \right)_{n_f} \right] \mathbf{U} \\
- n_f(\mathbf{r}') \left[\hat{n}_f(\mathbf{r}) \left(\frac{\delta v_f(\mathbf{r})}{\delta n_f(\mathbf{r}')} \right)_{n_f} - \hat{E}'_f(\mathbf{r}) \left(\frac{\delta \beta_f(\mathbf{r})}{\delta n_f(\mathbf{r}')} \right)_{n_f} \right] \mathbf{U}, \\
\hat{\mathbf{I}}_{2b} = p_{fb}(\mathbf{r}') \left[\hat{n}_b(\mathbf{r}) \left(\frac{\delta v_b(\mathbf{r})}{\delta E'_b(\mathbf{r}')} \right)_{n_b} - \hat{E}'_b(\mathbf{r}) \left(\frac{\delta \beta_b(\mathbf{r})}{\delta E'_b(\mathbf{r}')} \right)_{n_f} \right] \mathbf{U}, \quad \mathbf{Y}_{2\alpha} = -\nabla' \cdot \mathbf{u}_{\alpha}, \\
\hat{\mathbf{I}}_{3f} = \hat{\mathbf{J}}'_{3f}(\mathbf{r}) \delta(\mathbf{r} - \mathbf{r}') + \hat{\mathbf{p}}'_f(\mathbf{r}) \frac{\beta_f(\mathbf{r})}{m_f n_f(\mathbf{r})} \left(\frac{\delta p_f(\mathbf{r})}{\delta \beta_f(\mathbf{r}')} \right)_{v_f}, \quad \hat{\mathbf{I}}_{3b} = \hat{\mathbf{J}}'_{3b}(\mathbf{r}) \delta(\mathbf{r} - \mathbf{r}'), \\
\mathbf{Y}_{3\alpha} = -\nabla' \beta_{\alpha}, \\
\hat{\mathbf{I}}_{4f} = -\hat{\mathbf{J}}_{2f}(\mathbf{r}) \beta_f \delta(\mathbf{r} - \mathbf{r}'), \quad \mathbf{Y}_{4f} = \mathbf{u}_f, \quad \mathbf{Y}_{4b} = 0, \\
\hat{\mathbf{I}}_{5f} = \left(\hat{\mathbf{J}}'_{3f} + \frac{1}{2} \hat{\mathbf{J}}_{2f}(\mathbf{r}) \cdot \mathbf{u}_f \right) \delta(\mathbf{r} - \mathbf{r}'), \quad \mathbf{Y}_{5f} = \beta_f - \beta_b, \quad \mathbf{Y}_{5b} = 0. \\
(6.11)$$

In these expressions, the subscript n_f at the brackets means that the expression in brackets is determined at a fixed value of the concentration of fluid molecules.

6.2.3 Constitutive Relations and Transport Coefficients

The nonequilibrium ensemble (6.10) allows one to obtain close transport equations of fluid in flows confined by channel walls, based on Eq. (6.6). The constitutive relations for the stress tensor, heat flux vector, and interphase forces involved in these equations are non-local and delaying in the general case:

$$\mathbf{f}_{ia}(\mathbf{r},t) = \mathbf{f}_{ia}(\mathbf{r},t_0) + \mathbf{f}_{ia}^0(\mathbf{r},t)$$

$$+ \sum_{k=1}^{5} \sum_{\beta,\phi}^{l} \int_{t_0}^{t} dt_1 \int d\mathbf{r}' \int d\mathbf{r}'' \mathbf{M}_{ia}^{k\beta}(\mathbf{r},\mathbf{r}',\mathbf{r}'',t-t_1) \cdot \mathbf{Y}_{k\beta}(\mathbf{r}'',t_1), \quad (6.12)$$

where
$$i = 1, 2, ..., \mathbf{f}_{ia}^{0}(\mathbf{r}, t) = \left\langle \hat{\mathbf{f}}_{ia}(\mathbf{r}, t) \right\rangle_{0}$$

$$\hat{\mathbf{f}}_{1a} = \hat{\mathbf{J}}'_{1a}, \quad \hat{\mathbf{f}}_{2a} = \hat{\mathbf{J}}'_{2a}, \quad \hat{\mathbf{f}}_{3a} = \hat{\mathbf{J}}'_{3a}, \quad \hat{\mathbf{f}}_{4a} = \hat{\mathbf{j}}_{2a}, \quad \hat{f}_{5a} = \hat{j}'_{3a}, \\
\hat{\mathbf{f}}_{6f} = \hat{\mathbf{J}}_{fb}, \quad \hat{\mathbf{f}}_{7f} = \hat{\mathbf{j}}_{fb}, \quad \hat{\mathbf{f}}_{6b} = \hat{\mathbf{f}}_{7b} = 0.$$

The relaxation transport kernels in these formulas are defined as

$$\mathbf{M}_{ia}^{k\beta}(\mathbf{r},\mathbf{r}',\mathbf{r}'',t-t_1) = \left\langle \hat{\mathbf{f}}_{ia}(\mathbf{r})\pi(t,t_1)S_{-(t-t_1)}^{(N)}\hat{\mathbf{f}}_{k\beta}(\mathbf{r})\Delta\mathbf{I}_{k\beta}(\mathbf{r}',\mathbf{r}'')\right\rangle_0, \tag{6.13}$$

As the quasi-equilibrium distribution function is an even function over the momentum and relative coordinates of molecules, it can be demonstrated that the transport kernels (6.13), which are odd over these variables, are equal to zero. Moreover, the constitutive relations (6.12) are simplified if the bulk viscosity is neglected, i.e., only the symmetric nondivergent part (denoted below by s in superscript) of the stress tensor and the tensor \mathbf{J}_{tb} is left:

$$\mathbf{J}_{2f}^{\prime s}(\mathbf{r},t) = \mathbf{J}_{2f}^{\prime s}(\mathbf{r},t_{0}) + \int_{t_{0}}^{t} dt_{1} \int d\mathbf{r}' \left\langle \hat{\mathbf{J}}_{2f}^{\prime s}(\mathbf{r})\pi(t,t_{1})S_{-(t-t_{1})}^{(N)}\Delta(\hat{\mathbf{J}}_{2f}^{\prime s}(\mathbf{r}') + \hat{\mathbf{J}}_{fb}^{\prime s}(\mathbf{r}'))\right) : \beta_{f} \nabla \mathbf{u}_{f}(\mathbf{r}') \Big\rangle_{0},$$

$$\mathbf{j}_{2f}(\mathbf{r},t) = \mathbf{j}_{2f}(\mathbf{r},t_{0}) + \frac{1}{2} \int_{t_{0}}^{t} dt_{1} \int d\mathbf{r}' \left\langle \hat{\mathbf{j}}_{2f}(\mathbf{r})\pi(t,t_{1})S_{-(t-t_{1})}^{(N)}\Delta\hat{\mathbf{j}}_{2f}(\mathbf{r}') \cdot (\beta_{f} + \beta_{p})\mathbf{u}_{f}(\mathbf{r}') \right\rangle_{0},$$

$$\mathbf{J}_{3f}'(\mathbf{r},t) = \mathbf{J}_{3f}'(\mathbf{r},t_{0}) - \int_{t_{0}}^{t} dt_{1} \int d\mathbf{r}' \left\langle \hat{\mathbf{J}}_{3f}'(\mathbf{r})\pi(t,t_{1})S_{-(t-t_{1})}^{(N)}\Delta(\hat{\mathbf{J}}_{3f}'(\mathbf{r}') + \hat{\mathbf{p}}_{f}(\mathbf{r}') \frac{\beta_{f}(\mathbf{r}')}{m_{f}n_{f}(\mathbf{r}')} \right) - \nabla \beta_{f}(\mathbf{r}'') \Big\rangle_{0},$$

$$\mathbf{J}_{3f}'(\mathbf{r},t) = \mathbf{J}_{3f}^{\prime s}(\mathbf{r},t_{0}) + \int_{t_{0}}^{t} dt_{1} \int d\mathbf{r}' \left\langle \hat{\mathbf{J}}_{3f}'(\mathbf{r})\pi(t,t_{1})S_{-(t-t_{1})}^{(N)}\Delta(\hat{\mathbf{J}}_{3f}'(\mathbf{r}') + \hat{\mathbf{J}}_{fb}'(\mathbf{r}') - \beta_{b}(\mathbf{r}')) \right\rangle_{0},$$

$$\mathbf{J}_{fb}^{\prime s}(\mathbf{r},t) = \mathbf{J}_{fb}^{\prime s}(\mathbf{r},t_{0}) + \int_{t_{0}}^{t} dt_{1} \int d\mathbf{r}' \left\langle \hat{\mathbf{J}}_{fb}'(\mathbf{r})\pi(t,t_{1})S_{-(t-t_{1})}^{(N)}\Delta(\hat{\mathbf{J}}_{2f}'(\mathbf{r}') + \hat{\mathbf{J}}_{fb}'(\mathbf{r}')) \right\rangle_{0},$$

$$\mathbf{J}_{fb}^{\prime s}(\mathbf{r},t) = \mathbf{J}_{fb}^{\prime s}(\mathbf{r},t_{0}) + \frac{1}{2} \int_{t_{0}}^{t} dt_{1} \int d\mathbf{r}' \left\langle \hat{\mathbf{J}}_{fb}(\mathbf{r})\pi(t,t_{1})S_{-(t-t_{1})}^{(N)}\Delta(\hat{\mathbf{J}}_{2f}'(\mathbf{r}') + \hat{\mathbf{J}}_{fb}'(\mathbf{r}')) \right\rangle_{0},$$

$$\mathbf{J}_{fb}^{\prime s}(\mathbf{r},t) = \mathbf{J}_{fb}^{\prime s}(\mathbf{r},t_{0}) + \frac{1}{2} \int_{t_{0}}^{t} dt_{1} \int d\mathbf{r}' \left\langle \hat{\mathbf{J}}_{fb}(\mathbf{r})\pi(t,t_{1})S_{-(t-t_{1})}^{(N)}\Delta(\hat{\mathbf{J}}_{2f}'(\mathbf{r}') + \hat{\mathbf{J}}_{fb}'(\mathbf{r}')) \right\rangle_{0},$$

$$\mathbf{J}_{fb}^{\prime s}(\mathbf{r},t) = \mathbf{J}_{fb}^{\prime s}(\mathbf{r},t_{0}) + \frac{1}{2} \int_{t_{0}}^{t} dt_{1} \int d\mathbf{r}' \left\langle \hat{\mathbf{J}}_{fb}(\mathbf{r})\pi(t,t_{1})S_{-(t-t_{1})}^{(N)}\Delta(\hat{\mathbf{J}}_{2f}'(\mathbf{r}') + \hat{\mathbf{J}}_{fb}'(\mathbf{r}')) \right\rangle_{0},$$

$$\mathbf{J}_{fb}^{\prime s}(\mathbf{r},t) = \mathbf{J}_{fb}^{\prime s}(\mathbf{r},t_{0}) + \frac{1}{2} \int_{t_{0}}^{t} dt_{1} \int d\mathbf{r}' \left\langle \hat{\mathbf{J}}_{fb}(\mathbf{r})\pi(t,t_{1})S_{-(t-t_{1})}^{(N)}\Delta(\mathbf{J}_{2f}'(\mathbf{r}') + \hat{\mathbf{J}}_{fb}'(\mathbf{r}')\right) \right\rangle_{0},$$

In the general case, the constitutive relations (6.14) are nonlinear, nonlocal, and delaying rheological relations. Several types of nonlocality can be identified. Spatial nonlocality is caused by nonlocality of molecular interaction, retaining of correlations, and statistical effects, which are induced by interaction of physically small volumes of the fluid. Two types of nonlocality in the generalized constitutive relations should be distinguished: nonlocality associated with spatial correlations of

dissipative fluxes and thermodynamic forces and nonlocality caused by the nonlocal character of relaxation transport kernels.

The characteristic scale of nonlocality of the first type l_c has the order of the correlation length, i.e., the length at which the relaxation transport kernels have nonzero values. For gases far from the critical point, the correlation length turns out to be on the order of the mean free path of molecules. The characteristic scale of nonlocality of the second type is related to the sizes of the internal structural elements of the medium. Therefore, depending on the considered medium, it varies from $r_0 \ll l$ to a certain value $l_n \geq l$, or even $l_n \sim L$. Thus, $l_n \neq l_c$ in the general case.

The delay of the generalized constitutive relations is caused by the finite velocity of propagation of disturbances in the medium and by the finite time of interaction of its structural elements. As in the case of spatial nonlocality, two types of temporal nonlocality can be identified: nonlocality associated with the time correlations of fluxes and thermodynamic forces and nonlocality caused by temporal nonlocality of the evolution operator and, hence, relaxation transport kernels. The characteristic scales of the first τ_c and second τ_n types of temporal nonlocality in the general case are not equal to each other either. Under standard conditions in gases and liquids, the second type of temporal nonlocality has the characteristic scale on the order of the time of molecular interaction (Rudyak 1987). For this reason, this type of nonlocality at the hydrodynamic level of the flow description can be neglected if the gradients of the hydrodynamic variables are not very large. However, under extreme conditions, in which the changes in the macroscopical variables are significant at scales on the order of r_0 and times on the order of τ_0 , taking into account the nonlocality of this type is principally important. In particular, unusual equations of the state of the medium can be obtained by taking into account the temporal nonlocality of relaxation transport kernels.

Transport coefficients can be introduced into the constitutive relations only if nonlocality and delay of thermodynamic forces can be neglected by means of taking them away from the integral sign in Eq. (6.14). Moreover, in the linear approximation in terms of thermodynamic forces, it may be assumed that $\pi(t,t_0)=1$ and the initial values of the fluxes and interphase forces can be ignored. In this case, the fluid transport equations take the form

$$\begin{split} \frac{dn_{f}}{dt} &= -n_{f}\nabla \cdot \mathbf{u}_{f}, \quad \rho_{f}\frac{d\mathbf{u}_{f}}{dt} = -\nabla p_{f} - \nabla \cdot \left(\mathbf{\mu}_{ff}^{s} + \mathbf{\mu}_{fb}^{s}\right) : \nabla \mathbf{u}_{f}^{s} - \mathbf{v}_{fb} \cdot \mathbf{u}_{f}, \\ \frac{dE'_{f}}{dt} &= -E'_{f}\nabla \cdot \mathbf{u}_{f} - \nabla \cdot \lambda_{ff} \cdot \nabla \beta_{f} - \nabla \cdot \lambda_{fb} \cdot \nabla \beta_{b} - \left(\mathbf{\mu}_{ff}^{s} + \mathbf{\mu}_{fb}^{s} + \mathbf{\mu}_{bf}^{s} + \mathbf{\mu}_{bb}^{s}\right) : \nabla \mathbf{u}_{f} : \nabla \mathbf{u}_{f} \\ &+ \sigma_{fb} : \mathbf{u}_{f} \mathbf{u}_{f} + \sigma_{fb} \left(\beta_{f} - \beta_{b}\right), \end{split} \tag{6.15}$$

For simplicity, we do not write the stress tensor components responsible for bulk viscosity here, and the remaining coefficients in the general case are tensors: $\mu_{ff}^s, \mu_{fb}^s, \mu_{bf}^s$, and μ_{bb}^s are tensors of the fourth rank, $\mathbf{v}_{fb}, \lambda_{ff}$, and σ_{fb} are tensors of the second rank, and ϖ_{fb} is a scalar. All of these quantities depend on the spatial coordinate and are determined by the formulas

$$\begin{split} & \mathbf{\mu}_{ff}(\mathbf{r}) = \beta_{f} \int d\mathbf{r}_{1} \int_{t_{0}}^{\mathbf{r}} dt_{1} \left\langle \hat{\mathbf{J}}_{2f}^{s}(\mathbf{r}) S_{-(t-t_{1})}^{(N)} \Delta \hat{\mathbf{J}}_{2f}^{s}(\mathbf{r}_{1}) \right\rangle_{0}, \\ & \mathbf{\mu}_{fb}(\mathbf{r}) = \beta_{f} \int d\mathbf{r}_{1} \int_{t_{0}}^{t} dt_{1} \left\langle \hat{\mathbf{J}}_{2f}^{s}(\mathbf{r}) S_{-(t-t_{1})}^{(N)} \Delta \hat{\mathbf{J}}_{fb}^{s}(\mathbf{r}_{1}) \right\rangle_{0}, \\ & \mathbf{\mu}_{bf}(\mathbf{r}) = \beta_{f} \int d\mathbf{r}_{1} \int_{t_{0}}^{t} dt_{1} \left\langle \hat{\mathbf{J}}_{fb}^{s}(\mathbf{r}) S_{-(t-t_{1})}^{(N)} \Delta \hat{\mathbf{J}}_{fb}^{s}(\mathbf{r}_{1}) \right\rangle_{0}, \\ & \mathbf{\mu}_{bb}(\mathbf{r}) = \beta_{f} \int d\mathbf{r}_{1} \int_{t_{0}}^{t} dt_{1} \left\langle \hat{\mathbf{J}}_{fb}^{s}(\mathbf{r}) S_{-(t-t_{1})}^{(N)} \Delta \hat{\mathbf{J}}_{fb}^{s}(\mathbf{r}_{1}) \right\rangle_{0}, \\ & \lambda_{ff}(\mathbf{r}) = \int d\mathbf{r}_{1} \int_{t_{0}}^{t} dt_{1} \left\langle \hat{\mathbf{J}}_{3f}^{s}(\mathbf{r}) S_{-(t-t_{1})}^{(N)} \hat{\mathbf{J}}_{3f}^{s}(\mathbf{r}_{1}) + \hat{\mathbf{p}}_{f}^{s}(\mathbf{r}_{1}) \frac{\beta_{f}(\mathbf{r}_{1})}{m_{f}n_{f}(\mathbf{r}_{1})} \left(\frac{\delta p_{f}(\mathbf{r}_{1})}{\delta \beta_{f}(\mathbf{r}_{1})} \right)_{v_{f}} \right\rangle_{0}, \\ & \lambda_{fb}(\mathbf{r}) = \int d\mathbf{r}_{1} \int_{t_{0}}^{t} dt_{1} \left\langle \hat{\mathbf{J}}_{3f}^{s}(\mathbf{r}) S_{-(t-t_{1})}^{(N)} \hat{\mathbf{J}}_{3b}^{s}(\mathbf{r}_{1}) \right\rangle_{0}, \\ & \sigma_{fb}(\mathbf{r}) = \frac{1}{2} \left(\beta_{f} + \beta_{p} \right) \int d\mathbf{r}_{1} \int_{t_{0}}^{t} dt_{1} \left\langle \hat{\mathbf{J}}_{2f}(\mathbf{r}) S_{-(t-t_{1})}^{(N)} \hat{\mathbf{J}}_{2f}^{s}(\mathbf{r}_{1}) \hat{\mathbf{J}}_{2f}^{s}(\mathbf{r}_{1}) \right\rangle_{0}, \\ & \mathbf{v}_{fb}(\mathbf{r}) = \frac{1}{2} \left(\beta_{f} + \beta_{p} \right) \int d\mathbf{r}_{1} \int_{t_{0}}^{t} dt_{1} \left\langle \hat{\mathbf{J}}_{2f}(\mathbf{r}) S_{-(t-t_{1})}^{(N)} \hat{\mathbf{J}}_{2f}^{s}(\mathbf{r}_{1}) \hat{\mathbf{J}}_{2f}^{s}(\mathbf{r}_{1}) \right\rangle_{0}. \end{aligned} \tag{6.16}$$

It should be noted that the hydrodynamic velocity \mathbf{u}_b in the case of incompressible channel walls is equal to zero. From the conditions of equality of the absolute value of the interphase forces $\mathbf{j}_{2f} = \mathbf{j}_{2b}$ and the equation

$$\rho_b \frac{d\mathbf{u}_b}{dt} = -\nabla \cdot \mathbf{J}'_{2b} + \mathbf{j}_{2b} = 0,$$

it follows that $\mathbf{j}'_{2f} = -\nabla \cdot \mathbf{J}'_{2b}$, and the fluid velocity evolution equation can be written in the divergent form as

$$\rho_f \frac{d\mathbf{u}_f}{dt} = -\nabla p_f - \nabla \cdot \left(\mathbf{\mu}_{ff}^s + \mathbf{\mu}_{fb}^s + \mathbf{\mu}_b^s \right) : \nabla \mathbf{u}_f^s. \tag{6.17}$$

Thus, the fluid viscosity under confined conditions is not only determined by interaction of fluid molecules with each other (which is the responsibility of the tensor coefficient μ_{ff}^s); the effective viscosity coefficient also includes contributions that describe interaction with the surface; the latter is determined by the relation

$$\boldsymbol{\mu}_b^s(\mathbf{r}) = \beta_b \int d\mathbf{r}_1 \int_{t_0}^t dt_1 \left\langle \hat{\mathbf{J}}_{2b}^{\prime s}(\mathbf{r}) S_{-(t-t_1)}^{(N)} \Delta \hat{\mathbf{J}}_{fb}^{s}(\mathbf{r}_1) \right\rangle_0.$$
 (6.18)

The transport equations can be further simplified in systems possessing the properties of symmetry. For an isotropic medium, the transport kernels (6.13) and the corresponding transport coefficients (6.16) are scalar quantities multiplied by isotropic tensors. Thus, for an isotropic medium, the local constitutive relations reduce to

$$\mathbf{J}'_{2f}(\mathbf{r},t) = p_f(\mathbf{r},t)\mathbf{U} - \left(\mu_{ff}^s + \mu_{fb}^s + \mu_b^s\right)\nabla\mathbf{u}_f^s, \quad \mathbf{J}'_{3f}(\mathbf{r},t) = \lambda_{ff}\nabla\beta_f + \lambda_{fb}\nabla\beta_b,
\mathbf{j}_{2f}(\mathbf{r},t) = 0, \quad j'_{3f}(\mathbf{r},t) = \omega_{fb}(\beta_f - \beta_b),
\mathbf{J}_{fb}(\mathbf{r},t) = -\left(\mu_{bf}^s + \mu_{bb}^s\right)\nabla\mathbf{u}_f^s, \quad \mathbf{j}_{fb}(\mathbf{r},t) = -\sigma_{fb}\mathbf{u}_f.$$
(6.19)

The scalar transport coefficients are obtained by applying the convolution of the tensor coefficients; for example, the components of the shear viscosity and thermal conductivity coefficients that take into account interaction of fluid molecules with each other are determined by the formulas

$$\mu_{ff}^{s} = \frac{\beta_{f}}{5} \int d\mathbf{r}_{1} \int_{t_{0}}^{t} dt \left\langle \hat{\mathbf{J}}_{2f}^{rs}(\mathbf{r}) : S_{-(t-t_{1})}^{(N)} \hat{\mathbf{J}}_{2f}^{rs}(\mathbf{r}_{1}) \right\rangle,$$

$$\mu_{fb}(\mathbf{r}) = \beta_{f} \int d\mathbf{r}_{1} \int_{t_{0}}^{t} dt_{1} \left\langle \hat{\mathbf{J}}_{2f}^{rs}(\mathbf{r}) : S_{-(t-t_{1})}^{(N)} \Delta \hat{\mathbf{J}}_{fb}^{s}(\mathbf{r}_{1}) \right\rangle_{0},$$

$$\mu_{b}^{s}(\mathbf{r}) = \beta_{b} \int d\mathbf{r}_{1} \int_{t_{0}}^{t} dt_{1} \left\langle \hat{\mathbf{J}}_{2b}^{rs}(\mathbf{r}) : S_{-(t-t_{1})}^{(N)} \Delta \hat{\mathbf{J}}_{fb}^{s}(\mathbf{r}_{1}) \right\rangle_{0},$$

$$\lambda_{ff}(\mathbf{r}) = \frac{1}{3} \int d\mathbf{r}_{1} \int_{t_{0}}^{t} dt_{1} \left\langle \hat{\mathbf{J}}_{3f}^{r}(\mathbf{r}) \cdot S_{-(t-t_{1})}^{(N)} \hat{\mathbf{J}}_{3f}^{r}(\mathbf{r}_{1}) + \hat{\mathbf{p}}_{f}^{r}(\mathbf{r}_{1}) \frac{\beta_{f}(\mathbf{r}_{1})}{m_{f}n_{f}(\mathbf{r}_{1})} \left(\frac{\delta p_{f}(\mathbf{r}_{1})}{\delta \beta_{f}(\mathbf{r}_{1})} \right)_{v_{f}} \right\rangle_{0},$$

$$\lambda_{fb}(\mathbf{r}) = \int d\mathbf{r}_{1} \int_{t_{0}}^{t} dt_{1} \left\langle \hat{\mathbf{J}}_{3f}^{r}(\mathbf{r}) \cdot S_{-(t-t_{1})}^{(N)} \hat{\mathbf{J}}_{3b}^{r}(\mathbf{r}_{1}) \right\rangle_{0},$$

$$\sigma_{fb}(\mathbf{r}) = \frac{1}{2} \left(\beta_{f} + \beta_{p} \right) \int d\mathbf{r}_{1} \int_{t_{0}}^{t} dt_{1} \left\langle \hat{\mathbf{J}}_{fb}^{r}(\mathbf{r}) \cdot S_{-(t-t_{1})}^{(N)} \Delta \hat{\mathbf{J}}_{2f}^{r}(\mathbf{r}_{1}) \right\rangle_{0}.$$

$$(6.20)$$

Thus, in the simplest situation, the fluid transport equations under confined conditions have the following form:

$$\frac{d\mathbf{n}_{f}}{dt} = -n_{f} \nabla \cdot \mathbf{u}_{f}, \quad \rho_{f} \frac{d\mathbf{u}_{f}}{dt} = -\nabla p_{f} - \nabla \cdot \left[\left(\mu_{ff}^{s} + \mu_{fb}^{s} + \mu_{b}^{s} \right) \nabla \mathbf{u}_{f}^{s} \right],$$

$$\frac{dE'_{f}}{dt} = -E'_{f} \nabla \cdot \mathbf{u}_{f} - \nabla \cdot (\lambda_{ff} \nabla \beta_{f}) - \nabla \cdot (\lambda_{fb} \nabla \beta_{b}) - \left(\mu_{ff}^{s} + \mu_{fb}^{s} + \mu_{bf}^{s} \right) \nabla \mathbf{u}_{f} : \nabla \mathbf{u}_{f}$$

$$+ \sigma_{fb} \mathbf{u}_{f}^{2} + \overline{\omega}_{fb} \left(\beta_{f} - \beta_{b} \right).$$
(6.21)

Here, the continuity equation has a traditional form. In the momentum equation, the shear viscosity coefficient $(\mu_{ff}^s + \mu_{fb}^s + \mu_b^s)$ is now a complex variable, which is determined not only by momentum transfer in the fluid volume, but also by interaction of fluid molecules with confining surface molecules. In fact, the viscosity coefficient of the fluid is only the first term in this expression. The second term, μ_{fb} , has the same structure as μ_{ff} , but is determined by interaction of fluid molecules with atoms of the channel walls. Moreover, there arises one more term, μ_b , which has no analogs in traditional statistical mechanics of transport processes in a simple fluid. It is caused by correlation of intermolecular forces of the fluid and channel walls. Therefore, it is clear that the transport coefficients in sufficiently small channels are significantly different from the transport coefficient in the bulk of the fluid.

The energy transport equation is principally different from the traditional equation. It contains three additional source terms caused by interaction of fluid molecules with atoms of the channel walls. The first source term is induced by the change in the kinetic energy of fluid motion due to interaction of its molecules with ambient surfaces. Two other terms are caused by heat fluxes arising due to a possible difference in temperature between the walls and the fluid. If the walls and the fluid have identical temperatures, the last equation of system (6.21) is simplified and reduces to

$$\frac{dE_f'}{dt} = -E_f' \nabla \cdot \mathbf{u}_f - \nabla \cdot \left[(\lambda_{f\!f} + \lambda_{f\!b}) \nabla \beta_f \right] - \left(\mu_{f\!f}^s + \mu_{f\!b}^s + \mu_{b\!f}^s \right) (\nabla \mathbf{u}_f)^2 + \sigma_{f\!b} \mathbf{u}_f^2.$$

The thermal conductivity of the fluid and its viscosity are now also determined by interaction of fluid molecules with atoms of the channel wall.

Thus, the transport coefficients of the liquid or gas in the nanochannel do not coincide with the corresponding bulk values; moreover, they are determined by certain other parameters in addition to those of the fluid. Studying the fluid momentum and energy transport processes, it is necessary to introduce the viscosity and thermal conductivity of the "fluid-surface" system.

On the other hand, the constitutive relations (6.14) in the general case have a rather complicated structure and, possibly, look strange to specialists working in terms of transport coefficients. Typical aspects of the traditional CFD approach are scalar, homogeneous, and isotropic transport coefficients. It should be borne in mind that they cannot be used for the flow, e.g., in a carbon nanotube, where all fluid molecules permanently interact with molecules of the tube wall. Spatial and temporal nonlocality of transport processes and their anisotropy are properties of principal importance for such systems. Nevertheless, the influence of these effects becomes more pronounced as the system's size increases. In the limiting case of macroscopic systems, the classical hydrodynamic equations are naturally obtained, and interaction of the fluid with the surface is taken into account only by boundary conditions (e.g., slip or no-slip conditions). Let us consider which relations are valid in systems of various sizes.

As was already noted, for nanochannels several nanometers in diameter or similar nanoporous systems, it is necessary to use Eq. (6.14). Probably, the only alternative for detailed studies of transport processes is the use of molecular dynamics (MD) simulations, and there are many recent investigations of this kind. Nevertheless, the MD method does not provide a direct answer to the question as to what the viscosity or thermal conductivity coefficient is and whether it is possible to determine this parameter for this or that system. In activities in which MD simulations were used to study nanoflow characteristics, attempts were sometimes made to write the usual CFD equations and Green-Kubo formulas for transport coefficients. Obviously, the use of this approach is not grounded for such small systems.

In nanochannels about ten nanometers in diameter, it is possible to identify a near-wall region and a region where fluid molecules do not directly interact with the wall. Here, it becomes possible to neglect the nonlocality and delay of thermodynamic forces and to introduce transport coefficients; however, it should be taken into account that these coefficients are anisotropic (i.e., these coefficients are tensors) and inhomogeneous.

The influence of anisotropy and inhomogeneity becomes less pronounced as the system's size increases; apparently, the transport Eq. (6.21) will be valid for channels and pores with characteristic sizes of several tens of nanometers. Nevertheless, the volume of near-wall regions of intense fluid-wall interaction is not infinitesimal either. Therefore, a correct description of transport processes may require a hybrid description with different equations for the near-wall and internal regions.

Within the framework of the developed approach, the transport equations for the near-wall regions determine the boundary conditions for the classical CFD equations for the fluid in the internal region. It is because of the presence of the near-wall region that the no-slip boundary condition on the channel walls is replaced by the slip condition typical for microflows. Thus, the results of this work can be used to analyze the influence of various characteristics of microflows on the slip length and on the momentum and energy accommodation coefficients.

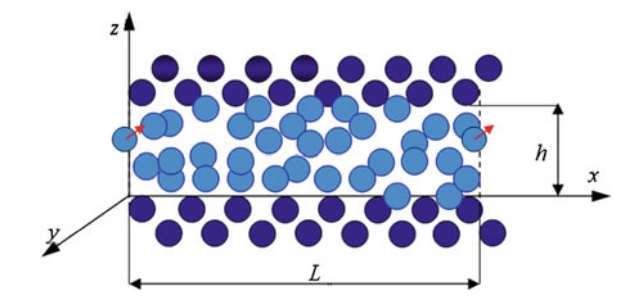
Even if the stress tensor and the heat flux vector can be expressed via the effective coefficients of viscosity and thermal conductivity, the constitutive relations contain additive terms corresponding to fluid-fluid and fluid-surface interactions. Thus, the transport coefficients of the liquid or gas in the nanochannel do not merely fail to coincide with the corresponding bulk values; they are not determined by the fluid parameters alone. Studying the fluid momentum and energy transport processes, it is necessary to take into account the viscosity and thermal conductivity of the fluid-surface system.

6.3 On Fluid Viscosity in the Nanochannel

In the first section of the present chapter, we described a statistical theory of transport processes under confined conditions. Using this theory, it is possible to derive closed transport equations and constitutive relations for transport coefficients; analogs of these equations in unconfined systems are the Green-Kubo relations. It was shown that momentum and energy transport in fluid flows in nanochannels and, possibly, in sufficiently small microchannels cannot be described on the basis of the fluid properties alone. Viscosity and thermal conductivity are no longer properties of the fluid itself; they become properties of the fluid-surface system. The only method that can be used to study these properties is the molecular dynamics method. The viscosity of fluids in nanochannels is studied below according to this method.

It is further assumed that the fluid and the walls of the plane channel constraining the fluid have an identical temperature. In this case, the stress tensor is determined by the formula

Fig. 6.2 Computational cell. The dark and light circles show the molecules of the channel walls and of the fluid, respectively. The arrows show the velocities of the molecule located at the channel boundary with periodic boundary conditions and of its copy



$$\mathbf{J}_{2} = -\left(\mu_{ff}^{s} + \mu_{fb}^{s} + \mu_{b}^{s}\right) \nabla \mathbf{u}_{f}^{s} \cong -\mu_{eff} \nabla \mathbf{u}_{f}^{s}, \tag{6.22}$$

where the viscosity coefficients are determined by the fluctuation-dissipative theorems (6.20).

To calculate the temporal correlation functions included in the fluctuation-dissipative relations (6.20), it is necessary to use the MD method. This method is applied below to calculate the effective viscosity coefficient μ_{eff} of the fluid in a plane nanochannel between two parallel plates (Fig. 6.2). The channel walls are two square plates parallel to the xy plane and consisting of two rows of atoms. The atoms are located in nodes of a cubic face-centered lattice. Periodic boundary conditions are applied to the channel boundaries parallel to the yz and xz planes.

The plate length L is chosen in such a manner that the results remain unchanged as the plate length increases. The main parameters of the channel walls are the distance between them or the channel height h and the constants of the interaction potential between the wall and fluid molecules.

All intermolecular interactions are described below by the truncated Lennard-Jones potential

$$\Phi(r) = \begin{cases}
4\varepsilon_{\alpha\beta} \left(\left(\frac{\sigma_{\alpha\beta}}{r} \right)^{12} - \left(\frac{\sigma_{\alpha\beta}}{r} \right)^{6} \right) - \Phi_{0}, & r \leq R_{C} \\
0, & r > R_{C}
\end{cases}$$
(6.23)

where σ is the effective diameter, ε is the depth of the potential well, R_C is the radius of action of the potential, $r = |\mathbf{r}_i - \mathbf{r}_j|$ is the distance between the molecule centers, and $\alpha, \beta = f, b$. The radius of action of the potential is taken to be $R_c = 2.5\sigma_{ff}$, and the shift of the potential Φ_0 is determined from the condition $\Phi(R_C) = 0$. The parameters of interaction of fluid molecules with the walls' atoms are calculated on the basis of the constants of interaction of individual substances by the following combination relations: $\sigma_{fb} = \sqrt{\sigma_{ff}\sigma_{bb}}$ and $\varepsilon_{fb} = \sqrt{\varepsilon_{ff}\varepsilon_{bb}}$.

The effective viscosity coefficients calculated for such systems are compared with the viscosity coefficient of the corresponding fluid in an unconfined system modeled by a cubic cell filled with molecules with periodic boundary conditions in all directions. Here, an additional problem arises, which is often not mentioned in publications aimed at modeling transport coefficients in nanochannels. This is determination of the effective concentration of molecules in the channel. Obviously, zones inaccessible for molecules are formed near the walls. In this case, the effective volume of the channel decreases, and it is not clear with which open system the fluid in the nanochannel should be compared and what the reduced concentration of molecules $n\sigma^3$ should be. For this reason, the results obtained in the nanochannel and in the bulk are compared below for an identical pressure (and, naturally, identical temperature). This is consistent with a typical experimental situation.

First, let us consider the influence of variations of the wall's material properties on the effective viscosity coefficient of the fluid, i.e., the influence of the interaction constants σ_{bb} and ε_{bb} . For this purpose, we calculate the viscosity coefficients of argon with $\sigma_{ff} = 3.405$ Å and $\varepsilon_{ff}/k = 119.8$ °K in channels with different properties of the walls. The fluid temperature is 160 K, and the reduced concentration of molecules is $n\sigma^3 = 0.4$. The parameters of the wall molecules are varied.

Variations of the effective size of wall molecules σ_{bb} are found to produce a minor effect on the viscosity coefficient. However, the latter is significantly affected by variations of ε_{bb} and ε_{fb} . The left-hand picture in Fig. 6.3 shows the viscosity coefficient $\eta^* = \eta/\eta_0$ normalized to the fluid viscosity coefficient in the bulk η_0 as a function of ε_{bb} in the channel with h = 20.4 Å and $\sigma_{bb} = 3.405$ Å. If the values of the parameter ε of the fluid and wall molecules are close to each other, the viscosity coefficient in the channel increases by several tens of percent. However, as interaction between the fluid atoms and wall molecules becomes less intense, the

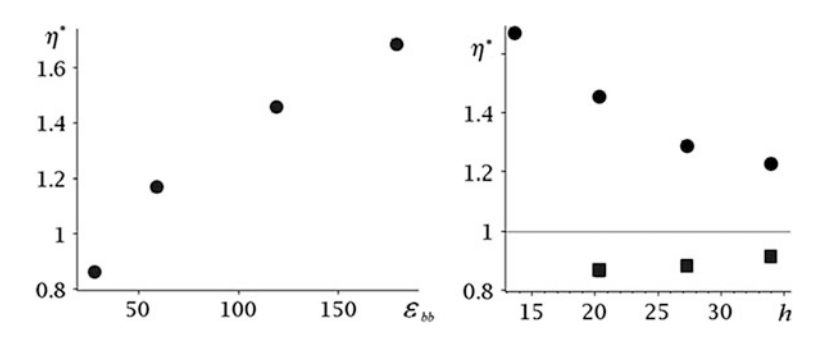
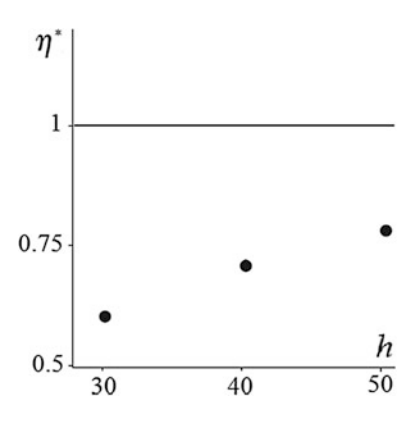


Fig. 6.3 Normalized viscosity coefficient of argon versus the parameter of the interaction potential of the wall and fluid molecules, $h=20.4~\text{\AA}$ (left). Normalized viscosity coefficient of argon versus the height h (Å) of the channel composed of argon molecules (circles) and carbon molecules (squares)

Fig. 6.4 Normalized viscosity coefficient of benzene versus the channel height h (\mathring{A}) for carbon walls



viscosity coefficient decreases, and even becomes smaller than η_0 . This behavior is caused by the fact that the number of intermolecular interactions of the fluid molecules in the channel becomes smaller than that in the volume. Thus, the viscosity of the fluid placed in the nanochannel can be expected to decrease in systems with $\varepsilon_{bb} \ll \varepsilon_{ff}$ and to increase in systems with $\varepsilon_{bb} \geq \varepsilon_{ff}$. This conclusion is confirmed in Fig. 6.3 (right), which shows the viscosity coefficient as a function of the channel height for channels whose walls are made of different materials. It is seen that the viscosity really decreases in the nanochannel with walls made of carbon whose molecules have a small value of $\varepsilon(\sigma_{bb} = 3.4 \text{ Å} \text{ and } \varepsilon_{bb}/k = 28 \text{ K})$. At the same time, if the constants of interaction of the fluid and wall molecules are identical, the viscosity increases. In both cases, the difference of the viscosity coefficient from η_0 monotonically increases with decreasing channel height.

Figure 6.4 shows the normalized viscosity coefficient of benzene (σ_{bb} = 5.04 Å and ε_{bb}/k = 440 K) as a function of the channel height for carbon walls. As in the previous case, the small value of the parameter ε of the channel for all molecules leads to a decrease in viscosity, which is fairly considerable.

Thus, the viscosity of the fluid in the nanochannel in the general case differs from its bulk viscosity. The viscosity coefficient depends, to a large extent, on the properties of interaction of fluid molecules with channel wall atoms; enhanced interaction leads to an increase in viscosity. However, a decrease in viscosity can also be observed in the case of small values of the interaction constant ε_{fb} . Therefore, in channels with identical shapes as those of the walls and identical roughness, it is possible to control the properties of fluid transport in the channel and the flow characteristics by varying the wall's material. It should be noted that the above-mentioned reduction of the effective viscosity coefficient will also lead to reduction of hydraulic resistance on the walls, which is usually attributed to the slip effect. However, we can see that the physical nature of the observed reduction of hydraulic resistance is absolutely different.

References

- Abdullaeva S, Nagiev F (2011) Nanohydrodynamics. Scientific Center of Higher Technology, Baku
- Kumar P, Starr FW, Buldyrev SV, Stanley HE (2007) Effect of water-wall interaction potential on the properties of nanoconfined water. Phys Rev E 75:011202
- Li T-D, Gao J, Szoszkeiwicz R, Landman U, Riedo E (2007) Structured and viscous water in subnanometer gaps. Phys Rev B 75:115415
- Liu Y-C, Wang Q, Lu L-H (2004) Transport properties of fluids in micropores by molecular dynamics simulation. Chin J Chem 22:238–242
- Popov IY (2011) Statistical derivation of modified hydrodynamic equations for nanotube flows. Phys Scr 83:045601
- Rudyak VY (1987) Statistical theory of dissipative processes in gases and liquids. Nauka, Novosibirsk
- Rudyak VY (2005) Statistical aerohydromechanics of homogeneous and heterogeneous media. Hydromechanics, vol 2. NSUACE, Novosibirsk
- Rudyak VY, Belkin AA (1994) Statistical hydromechanics of two-phase media. J Aerosol Sci 25 (1):S387–S388
- Rudyak VY, Belkin AA (1996) The equations of multi-fluid hydrodynamics. Math Model 8 (1):33–37
- Rudyak VY, Belkin AA (2014) Fluid viscosity under confined conditions. Dokl Phys 59(12):604–606
- Rudyak VY, Belkin AA (2015) Statistical mechanics of transport processes of fluids under confined conditions. Nanosystems Phys Chem Math 6(3):366–377
- Rudyak VY, Belkin AA, Ivanov DA, Andrushenko VA (2011) Self-diffusion and viscosity coefficients of fluids in nanochannels. In: Proceedings of 3rd micro and nano flows conference, Thessaloniki, Paper 1-74
- Thomas JA, McGaughey AJH (2009) Water Flow in carbon nanotubes: transition to subcontinuum transport. Phys Rev Lett 102:184502
- Travis KP (2004) Viscosity of confined inhomogeneous nonequilibrium fluids. J Chem Phys 121 (21):10778–10786
- Zhang ZH, Ye H (2009) Pressure-driven flow in parallel-plate nanochannels. Appl Phys Lett 95:154101
- Zhu F, Schulten K (2003) Water and proton conduction through carbon nanotubes as models for biological channels. Biophys J 85:236–244.
- Zhu F, Tajkhorshid E, Schulten K (2002) Pressure-induced water transport in membrane channels studied by molecular dynamics. Biophys J 83:154–160
- Zhu F, Tajkhorshid E, Schulten K (2004) Collective diffuision model for water permeation through microscopic channels. Phys Rev Lett 93:22450

Chapter 7 Conclusions



Abstract Though micro- and nanoflows have been successfully investigated for several decades, we can honestly say that we are still at the very beginning of the road. The goal of this chapter is to discuss the main problems which have to solve in future. The experimental problems of the micro and nanoflows studying and their modeling are analyzed. Then the transport processes in nanochannels and nanopores are considered. Complexity of these processes in general case is their nonlocality. Finally, the last part deals with discussing the applicability of the similarity parameters to model the nanofluid flow.

Though micro- and nanoflows have been successfully investigated for several decades, we can honestly say that we are still at the very beginning of the road, a fact that will require a lot of effort to overcome. Nevertheless, it is clear that the currently existing paradigm of development of microsystem technologies and nanotechnologies in the 21st century requires this path to be explored as quickly as possible. It is obvious, however, that this path will not be easy to traverse and there will be unpredictable obstacles. Even now, after at least three decades of serious effort, there are still no clear criteria for what can and cannot be considered as a microflow. In this aspect, the situation with nanoflows is more definite: all flows with a characteristic size smaller than one hundred nanometers are nanoflows by definition. It seems reasonable to consider microflows in the same manner. For example, all flows with a characteristic size smaller than five hundred micrometers could be considered as microflows. However, many of these flows may exhibit the classical behavior. On the other hand, it is almost always possible today to predict the situations in which the nonclassical behavior of microflows can be expected.

It is also important to understand that experimental data obtained for microflows, and especially nanoflows, should be treated cautiously. The point is that the majority of experimental techniques are based on the classical relations derived for macroscopic flows. Moreover, only integral information can be obtained in nanoflows (and often in microflows), and its interpretation can be less than unique. Therefore, the success in studying these problems depends on the tools used for investigations and on the methods used for interpretation of the experimental data.

238 7 Conclusions

On the other hand, results of simulations can also be rather conventional. In fact, the absolute majority of data obtained in microflow simulations are the results of traditional computational fluid dynamics. Usually, nobody even raises the question as to whether such simulations are justified in such situations. It was mentioned above that fluid dynamics modeling is somewhat rough and is often used far beyond the area of its formal applicability. If the results of such modeling are definitely outside the area of applicability of CFD, their importance and reliability should not be overestimated.

Because of limitations of both experimental research and simulations, it is obviously necessary to use both methods for studying microsystems. Examples of such combined modeling (both physical and mathematical) are given in this book. We can even say that combining experimental investigations of microflows with simultaneous simulations is the only method for obtaining reliable information. In particular, this is caused by the fact that methods of adequate interpretation of experimental data are developed in the course of formulating the problem for mathematical modeling and solving this problem.

The situation with nanoflows is even more complicated. First of all, experimental investigations of such flows are extremely difficult for several reasons. On the one hand, there are no necessary tools available. On the other hand, if such tools were available, it would be necessary to develop an appropriate theory of measurements, as was done in quantum mechanics. Perturbations, which are inevitably inserted into the nanoflow in the course of measurements, may drastically change the flow's character. Let us emphasize again that only some integral information about nanoflows can be obtained today; moreover, when we say "integral information," we do not even mean obtaining data on integral properties of the flow (e.g., flow rate), which is obviously implied. The situation is aggravated by the fact that such investigations provide information about an ensemble of nanoflows, rather than about an individual nanoflow. A typical example is a system of nanochannels. The flow rate is measured throughout the entire system. A similar situation is observed for the decrease in pressure, i.e., with the force of resistance along the channel. In such situations, the classical hydrodynamic theories are usually used for data interpretation. For example, the pressure drop is described by the Darcy law relating the filtration velocity **u** with the pressure drop as

$$\mathbf{u} = -(k/\eta)\nabla p,\tag{7.1}$$

where η is the viscosity coefficient of the filtered fluid and k is the so-called permeability. Here, we make two mistakes simultaneously. First, it is implied that the fluid viscosity has the same value in microchannels, nanochannels, and macrochannels. It is clear today that this is not so, but the differences in these situations are not yet understood. Interpretation of measured results with the use of Eq. (7.1), for example, may yield different values of permeability. The final result is determined by the fluid viscosity coefficient used. The error may be several times or several orders of magnitude. Thus, for example, in the experiments (Holt et al. 2006) with water filtration through a nanoporous membrane, its permeability turned

7 Conclusions 239

out to be higher by three orders of magnitude than the value predicted in CFD simulations.

Such an unusual result (Holt et al. 2006) is caused, in particular, by the important role of transport processes in microflows, and especially in nanoflows. Moreover, the main problem is not the fact that transport processes are no longer isotropic and homogeneous like the corresponding processes in the volume. The problem is that momentum and energy transfer under confined conditions and, hence, the fluid viscosity and thermal conductivity are no longer the properties of the fluid itself. These properties are determined, to a large extent, by interaction of fluid molecules with channel wall atoms. As a result, as is demonstrated in Chap. 6, the processes of fluid transport under confined conditions are described by a set of fluctuation-dissipative theorems, which are principally different from the known Green-Kubo formulas.

The fluid in the nanochannel is always structured, and there is a near-wall layer with a characteristic size on the order of several nanometers, where the transport processes are essentially different. In this sense, both the fluid viscosity and thermal conductivity under confined conditions are inhomogeneous.

There is one more point that should be borne in mind in considering micro- and nanoflows. It does not make much sense to describe such flows through the use of usual global parameters of similarity. The characteristic sizes of a microchannel may be significantly different. The Reynolds numbers based on the width and height of a rectangular channel may also significantly differ from each other. For example, the flow in a rectangular channel whose width is one hundred times greater than its height and whose height is equal to 1 µm cannot be considered as a plane channel, though such a situation is admissible in macroscopic flows. The roughness of the channel wall also plays an extremely important role in such flows. The presence of roughness elements can essentially alter the flow's character. This fact can be illustrated by the following simple example. The typical height of roughness elements in well-treated macroscopic channels (e.g., glass tubes) is usually several micrometers. Through use of special treatment, the roughness height can be further reduced several more times. In macroscopic channels, this roughness is mainly considered as being negligibly small. However, it generates perturbations that trigger the laminar-turbulent transition (though roughness is not the only reason for that). In a plane channel with the characteristic distance between the plates on the order of 0.1 m, perturbations generated by roughness elements several micrometers high are small for this kind of flow. In this case, the laminar-turbulent transition will follow the classical scenario. However, if such roughness elements are present in a microchannel with the characteristic size of 100 µm, they generate perturbations of finite amplitude, and the transition to turbulence occurs in an absolutely different manner. It is clear from this example that local criteria of similarity should be taken into account in microflows in addition to global criteria.

A large part of this book deals with nanofluids, in particular, nanoflows. What conclusions can be drawn here? First, a nanofluid is not a standard fluid, and its properties are not described by the classical relations. Certainly, this could be expected. Fluids with coarse particles are macroscopic objects. The carrier fluid and

240 7 Conclusions

the disperse particles are macroscopic objects, both individually and as a whole, as long as the properties of the carrier fluid are described by methods of dynamics of continuous media. At the same time, a nanofluid is a mesoscopic object, and disperse particles occupy an intermediate position between the usual molecules (microscopic objects) and macroscopic particles. The main difference separating nanofluids from fluids with coarse particles is their unusual thermophysical properties, which depend not only on the nanoparticle concentration, but also on the nanoparticle size and material. The current state of research allows for simulation of nanofluid flows on the basis of reliable data on transport coefficients. After all, adequate modeling of such flows will become possible. It should be borne in mind, however, that the traditional hydrodynamic description of flows, even in sufficiently large microchannels, may fail. Concerning small microchannels, and especially nanochannels, standard hydrodynamic methods, including the two-fluid description, are inapplicable. It is necessary to use a hybrid kinetic-hydrodynamic description or molecular dynamics method.

The second important fact that should be taken into account in modeling and interpreting experimental data is the fact that the use of similarity parameters traditionally used in physics and fluid dynamics may yield inadequate results. Among popular similarity parameters, probably the only parameter that can be definitely used is the Reynolds number $\text{Re} = (\rho U L)/\eta$. However, it should be borne in mind that different nanofluids may correspond to identical Reynolds numbers. The situation with the Prandtl number $\text{Pr} = (C_p \eta)/\lambda$ is extremely severe. Here, the viscosity and thermal conductivity coefficients exhibit the opposite dependences on the nanoparticle size. In the general case, they also exhibit the opposite behaviors due to temperature variation. Therefore, similarity in terms of the Prandtl number may mean nothing at all: it is just that different nanofluids correspond to different Prandtl numbers (Rudyak et al. 2017). A similar situation in the general case also refers to the Nusselt number.

References

Holt JK, Park HG, Wang Y, Stadermann M, Artyukhin AB, Grigoropoulos CP, Noy A, Bakajin O (2006) Fast mass transport through sub-2-nanometer carbon nanoturbes. Science 312 (5776):1034–1037

Rudyak VY, Minakov AV, Pryazhnikov MI (2017) Thermal properties of nanofluids and their similarity criteria. Tech Phys Lett 43(1):23–26

Index

C Computational Fluid Dynamics (CFD), 127–129, 131, 145, 231, 232, 238, 239 D Dispersed fluid, 1	Microflow, 9, 97, 107, 173, 186, 193, 237 Micromixer, 128, 139, 140, 142, 144, 145, 147–151, 153–155, 157, 159, 161, 163, 165–171, 173, 175–177, 179–182 Molecular dynamics, 1, 15, 16, 21, 28, 29, 34–36, 40, 43–45, 47, 49, 51, 185, 187, 217, 218, 240
E	
Experiment, 5, 12, 13, 15, 19, 28, 29, 42–44,	N
50, 57, 59, 60, 62, 74–76, 79, 87, 88, 93,	Nanochannel, 185–187, 193, 195–200, 202,
97, 98, 107–110, 113, 115–117, 120,	217, 219, 231–235, 239
121, 136, 139, 150, 151, 160, 161, 163,	Nanoflow, 188, 189, 191, 196, 231, 238
171, 176, 180, 192, 193, 204, 207, 238	Nanofluid, 19, 28–31, 33, 35–37, 39–41, 43, 44, 98, 209, 210, 211, 213, 239
F	
Fluid flows, 1, 2, 17, 18, 97, 98, 102, 105, 109,	S
111–116, 120, 122, 123, 131	Subsonic and supersonic microjets, 57–61, 70
M	V
Microchannel, 6, 9, 13, 15, 16, 18, 19, 97–124,	Viscosity, 5, 9, 14–16, 20, 31, 36–42, 43, 46,
128–131, 133, 138, 140, 141, 145, 148,	114, 131, 139, 140, 146, 147, 151, 166,
160, 161, 166, 173, 177–181, 187, 217,	181, 195, 201, 217–219, 226, 227,
232, 238–240	229–235, 238–240
232, 230-240	227-233, 230-240